Abstract

The south western Barents Sea has a complex burial and uplift history with episodes linked both to local extension and regional episodes affecting the entire area. The most significant exploration problem relates to the severe uplift and erosion that took place during Cenozoic times.

The Cenozoic events have had important implications for the hydrocarbon potential of the area. During uplift and erosion the geometry of the basins and the properties of the buried rocks changed. This caused hydrocarbon leakage from traps, cooling of source rocks, change in reservoir quality and redistribution of hydrocarbons. In the Barents Sea recent discoveries have shown that these effect are still not fully understood.

Different methods, including analysis of shale compaction trends from well logs, analysis of vitrinite reflectance, sandstone diagenesis, apatite fission track analysis and analysis of pyrolysis T-max results, have been used to estimate net erosion. The various methods can give different results and in this way lead to increased uncertainties in prospect evaluation.

To quantify uplift and erosion in this study, we tested methods using both property-depth trends in addition to a modelling technique combining porosity and cement volume calculations with burial history. Data from wells as well as seismic data were used in the estimations. We also modelled the effects uplift and erosion have had on seismic AVO signatures, and used this to better understand the structural development and hydrocarbon potential in the area.

We found that net erosion estimates varies from more than 2000 meters in the north east to no net erosion in the westernmost areas. Net erosion estimates are to some extent linked to structural elements, and range from approximately 800 to 1400 meters within the Hammerfest Basin, 1000 to 1500 meters on the southern Loppa High, 800 to 1500 meters within the Bjørnøya Basin, around 1700 to 1900 meters in the Fingerdjupet sub-basin, 1300 to 1700 meters on the Bjarmeland Platform and 1300 to 2000 meters on the northern Bjarmeland Platform. Maximum burial occurred in Middle Eocene time and the main depocenter was in the Tromsø basin. The first major net erosion event took place in late Eocene time, and the second main erosion event is linked to glacial erosion in the Quaternary period.

When testing various methods for quantifying net erosion we found that shale velocity trends and sandstone modelling gave consistent results across the study area. This was also the case when using seismic velocities to estimate net erosion. We found that combining an extensive regional seismic velocity cube with mapped seismic horizons highly improved the horizontal resolution of the net erosion distribution. Further we tested velocity- and resistivity trends for sandstones. These

net erosion estimates varied too much and are probably not reliable. Generally we saw that combining and cross testing methods increased reliability in the net erosion estimations.

Relatively small changes in reference trends could produce significantly different net erosion estimates, and since there are few good reference wells in the Barents, the North Sea was used as reference area. We established references trends for shale velocity, shale resistivity, sandstone velocity, sandstone resistivity and smectite-illite rich shales. Before they were used for estimating net erosion, the North Sea trends were compared to single wells in an area with no uplift in the Barents Sea.

Testing resistivity trends for shales showed geographical variations as for the other methods, but these net erosion estimates were unrealistically high. We interpret this to be caused mainly by cooling due to uplift of the formations. The effect of cooling can be estimated by combining velocity trends and resistivity trends. This work flow can potentially also be used to estimate the temperature gradient for the actual area.

When including net erosion estimates in modelling of seismic AVO signatures for the Stø reservoir formation, we found that AVO signatures are strongly influenced by the amount of net erosion. The AVO modelling demonstrated that both the fluid content in the reservoirs and the maximum burial depth have strong influence on which AVO class the responses belong to. The modelled AVO signatures were compared to real AVO responses at the south western margin of the Loppa High. Here the real AVO responses were calibrated to wells, and the modelled results gave good match with the real responses.

Sammendrag

Sørvestlige deler av Barentshavet har en kompleks begravningshistorie preget av flere perioder med både lokal ekstensjon og regionale episoder som har påvirket hele området. Det viktigste problemet for leting er knyttet til det store oppløftet og den kraftige erosjonen som skjedde i Kenozoikum.

Oppløfts- og erosjonsepisodene i Kenozoikum har hatt implikasjoner for hydrokarbonpotensialet i området. Bassengenes geometri og egenskapene til de begravde bergartene endret seg gjennom disse episodene. Dette har blant annet forårsaket lekkasje av hydrokarboner fra feller, avkjøling av kildebergarter, endringer i reservoarkvalitet og redistribusjon av hydrokarboner. Nylige funn i Barentshavet har vist at disse effektene ikke er fullstendig forstått.

Ulike metoder, som inkluderer blant annet analyser av skiferkompaksjonstrender fra brønndata, analyser av vitrinittreflektans, sandsteinsdiagenese, apatitt fisjonsanalyser og analyser av pyrolyse T-maks resultater har blitt brukt til å estimere netto erosjon. De ulike metodene kan gi varierende resultater og kan igjen føre til økt usikkerhet i prospektevaluering.

For å kvantifisere oppløft og erosjon i dette studiet testet vi ulike metoder som benytter egenskap – dybde trender og en modelleringsteknikk som kombinerer porøsitet og beregninger av sementvolum med begravningshistorie. Både brønndata og seismiske data ble brukt i estimeringene. Vi modellerte også effekten oppløft og erosjon har på seismiske AVO data og brukte dette til bedre å forstå den strukturelle utviklingen og hydrokarbonpotensialet i området.

Estimatene av netto erosjon varierer fra mer enn 2000 meter i nordøst til ingen netto erosjon i de vestlige områdene. Netto erosjon er til en viss grad koblet til strukturelle elementer og varierer fra omtrent 800 til 1400 meter i Hammerfestbassenget, fra 1000 til 1500 meter på sørlige Loppahøyden, fra 800 til 1500 meter i Bjørnøyabassenget, fra 1700 til 1900 meter i Fingerdjupet, fra 1300 til 1700 meter på Bjarmelandplattformen og fra 1300 til 2200 meter på den nordlige Bjarmelandplattformen. Maksimum begraving skjedde i midtre Eocen og deposenteret var da i Tromsøbassenget. Den første store erosjonen skjedde i sen Eocen og den andre store er koblet til den glasiale erosjonen i Kvartær.

Under testing av de ulike metodene for kvantifisering av netto erosjon så vi at skiferhastighetstrender og sandsteinsmodellering gav de mest konsistente resultatene. Dette var også tilfellet når seismiske hastigheter ble brukt. Ved å kombinere en omfattende regional seismisk hastighetskube med tolkede horisonter ble den horisontale oppløsningen av nettoerosjonen kraftig forbedret. Videre testet vi hastighet- og resistivitetstrender for sandsteiner. Disse estimatene varierte for mye og er mest sannsynlig ikke til å stole på. Generelt så vi at ved å kombinere ulike metoder økte påliteligheten til estimatene av netto erosjon.

Relativt små endringer i referansetrendene gav store forskjeller i nettoerosjonsestimatene, og siden det er få gode referansebrønner i Barentshavet, ble Nordsjøen brukt som referanseområde. Vi etablerte referansetrender for skiferhastighet, skiferresistivitet, sandsteiner og for smektitt- og illitskifere. Før disse ble brukt til å estimere netto erosjon, ble de sammenlignet med enkeltbrønner i Barentshavet fra et område uten oppløft.

I likhet med de andre metodene viste resistivitetstrendene for skifer også geografiske variasjoner. Men disse estimatene av netto erosjon var urealistisk store. Vi tolket dette til i hovedsak å være forårsaket av avkjøling på grunn av oppløft av formasjonene. Effekten av avkjøling kan estimeres ved å kombinere hastighetstrender og resistivitetstrender. Denne metoden kan potensielt også brukes til å estimere temperaturgradienter for et gitt område.

Når vi inkluderte netto erosjon i modellering av seismiske AVO signaturer for Støreservoarene, fant vi at AVO signaturene i stor grad er påvirket av oppløft og erosjon. AVO modelleringen viste at både væskeinnholdet i reservoaret og maksimum begravingsdyp har stor innvirkning på hvilken AVO klasse responsen tilhører. De modellerte AVO signaturene ble sammenlignet med reelle AVO responser fra den sørvestlige delen av Loppahøyden. De ekte AVO responsene ble her kalibrert med brønner, og de modellerte resultatene samsvarte godt med de reelle responsene.

.

Acknowledgement

I would like to thank my supervisors Per Åge Avseth (Tullow Oil) and Mai-Britt Mørk (NTNU) for the knowledge and support during the process of writing the master thesis.

I would like to thank employees at Tullow Oil for the help and for providing data. Also, I would like to thank First Geo for interval velocity cubes and TGS for seismic lines and seismic AVO data. Per Åge Avseth has contributed with valuable discussions and guidance throughout the process. I have gained a lot of experience and have been introduced to new views and perspectives.

I would also like to thank my co-supervisor Kenneth Duffaut for inspiring discussions and Pål Gabrielsen for valuable input on the work with resistivity data.

Finally, I would like to thank my family and friends for the motivation and time.

Table of Contents

List of figures

List of tables

Chapter 1 – Introduction

It is of general interest to understand the uplift and erosion history of a sedimentary basin. It is important for understanding the geological history of an area. In addition it is important for understanding the hydrocarbon potential in a sedimentary basin.

The most significant exploration problem in the Western Barents Sea relates to the severe uplift and erosion of the area that took place during Cenozoic times. The uplift and erosion have had important implications for oil and gas exploration. The amounts of sediments removed and the timing of these events are still debated (Faleide et al., 2010).

When rocks are uplifted and eroded both the geometry of the basin and the properties of the rocks will change. Severe uplift can cause hydrocarbon leakage from traps and cooling of source rocks (Doré and Jensen, 1996). It can alter reservoir quality and cause redistribution of hydrocarbons by changing migration pathways (Baig et al., 2016, Henriksen et al., 2011, Ohm et al., 2008).

Knowledge of the burial- and thermal history of a basin, including the uplift and erosional events, are critical to determine the maximum burial depths of the source rock. The time spent at a particular temperature controls the maturation and expulsion of hydrocarbons (Baig et al., 2016, Henriksen et al., 2011).

Many traps in the Barents Sea are underfilled and more gas than oil is found (NPD, 2016). This can be caused by expansion of the gas and expulsion of oil from the traps during uplift. In other places the seals breach and cause leakage from the top of the traps (Nyland et al., 1992).

Before information about net erosion is used in the exploration process it should be estimated as correctly as possible. Many different methods are used to estimate net erosion. Henriksen et al. (2011) give an overview of the most common techniques used in practice: (1) analysis of shale compaction trends from sonic- and density logs, (2) analysis of vitrinite reflectance, (3) sandstone diagenesis, (4) apatite fission track analysis and (5) analysis of pyrolysis T-max results. They also show that the different methods can give different results. This fact, also demonstrated by Baig et al. (2016), can lead to increased uncertainties in the prospect- and play evaluation process. In addition to these techniques that use data from wells, it is also possible to use seismic velocities to estimate uplift and erosion (Richardsen et al., 1993).

In addition to well data, seismic reflection data is the most important data for understanding the geological history of an area. Seismic data is even more important in hydrocarbon exploration were the goal is to understand the geology away from the wells. When interpreting the seismic data it is important to understand the seismic expression, or seismic signature, of the rocks that are imaged

by the seismic. The burial history, including uplift and erosion will have significant influence on seismic signatures. The seismic AVO technique (Amplitude versus Offset) utilizes that the seismic amplitude changes systematically with increasing offset between the source and the receivers (Castagna and Smith, 1994). This information can be used to directly predict the fluid content in a reservoir rock. It is therefore especially important to understand the factors that influence the seismic AVO signatures.

The main objective of this study is to quantify amount of uplift and erosion form several techniques and to compare and evaluate the results. We will test methods using both property-depth trends, and a modelling technique combining porosity and cement calculations with burial history. Methods based on well data as well as seismic data will be used. In this process we will make trend maps and more detailed maps that quantify uplift and erosion in our study area in the south-western Barents Sea (Figure 1.1). Finally, we will estimate and discuss the effects uplift and erosion have on the seismic AVO signatures in the Barents Sea. These results can be used to better understand the structural development of the area. Tectonic development through time has great influence on prospectivity, and better understanding of these processes can potentially also improve the exploration success in the region.

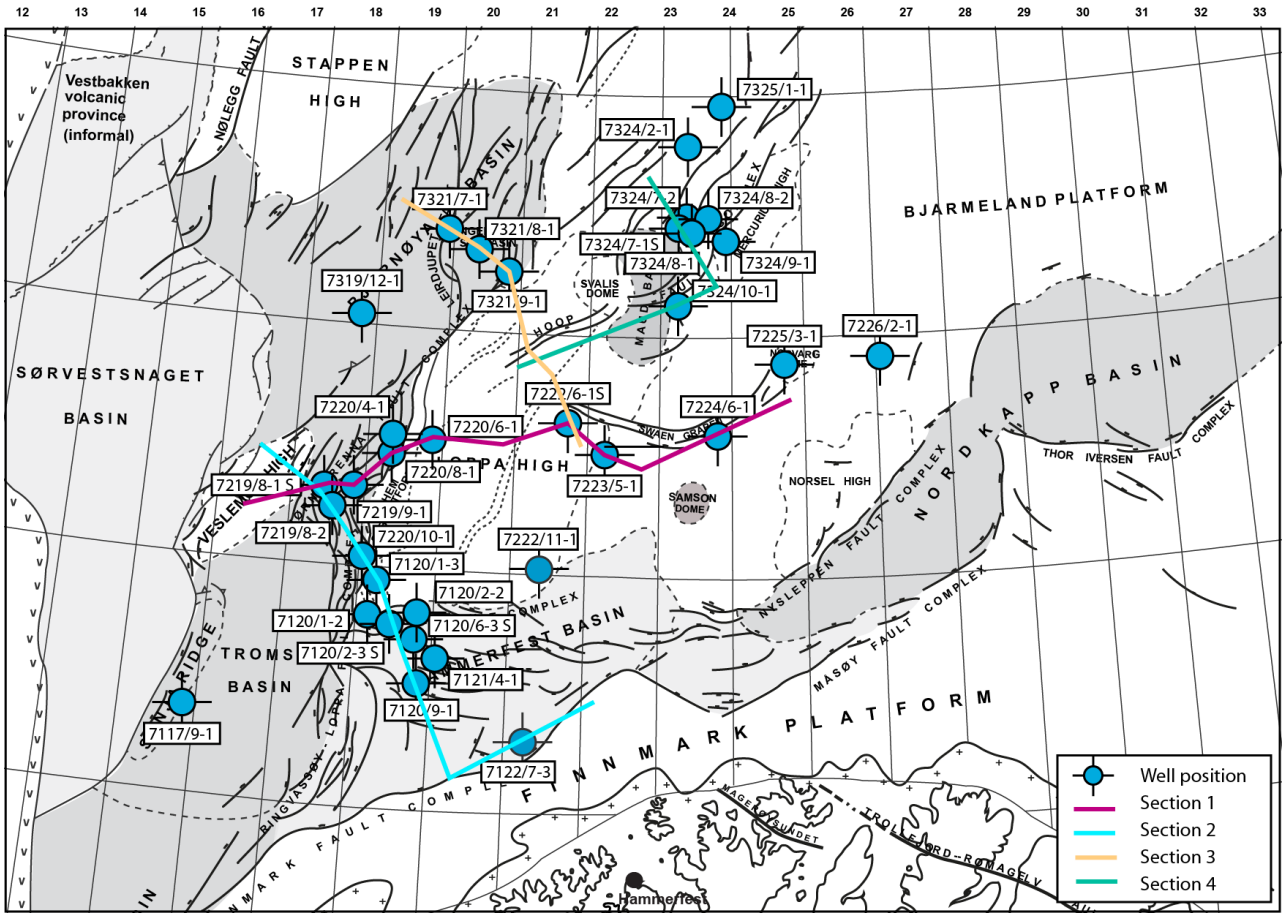

***Figure 1.1**: Study area with well bores and seismic sections in south western Barents Sea. Structural elements are modified from Faleide et al. (2010).*

Chapter 2 – Background and data

2.1 Uplift and erosion

Although the processes often are linked to each other, removal of overburden must be distinguished from uplift of the earth surface (England and Molnar, 1990, Japsen and Chalmers, 2000). Overburden can be eroded by water or ice without any uplift occurring, and it is therefore important to differentiate between the two. In this study the term "net erosion" describes the difference between current day burial and the maximum burial depth with reference to a surface horizon as illustrated in Figure 2.1 (Henriksen et al., 2011).

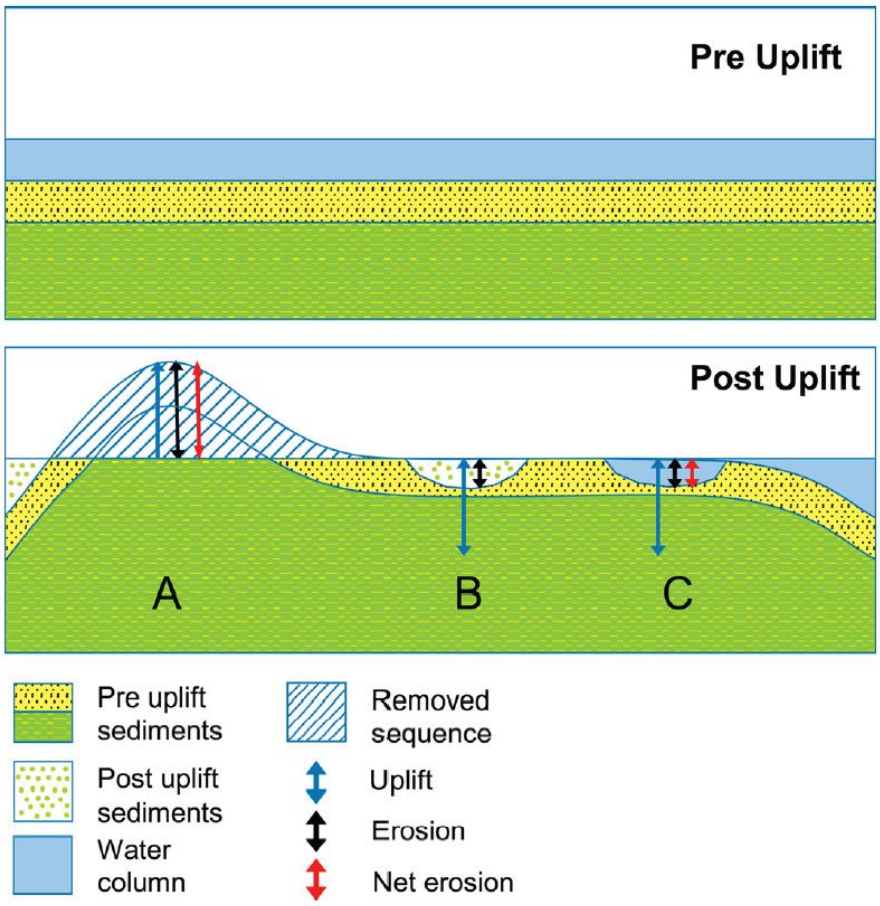

Figure 2.1: *Net erosion is described as the difference between the maximum burial depth (upper figure) and the present day burial depth (lower figure). The figure is modified from Henriksen et al. (2011) and illustrates the differences between net erosion, erosion and uplift.*

2.1.1 Implications of net erosion on rock properties

Rocks are influenced by burial and sediments will generally compact with increased burial depths and loading. The physical properties will change in the rocks, as they undergo both mechanical and chemical compaction with increased burial depth (Bjørlykke and Jahren, 2015). In our study area the most common lithologies are shales and sandstones and Figure 2.2 explains depositional trends of each of them.

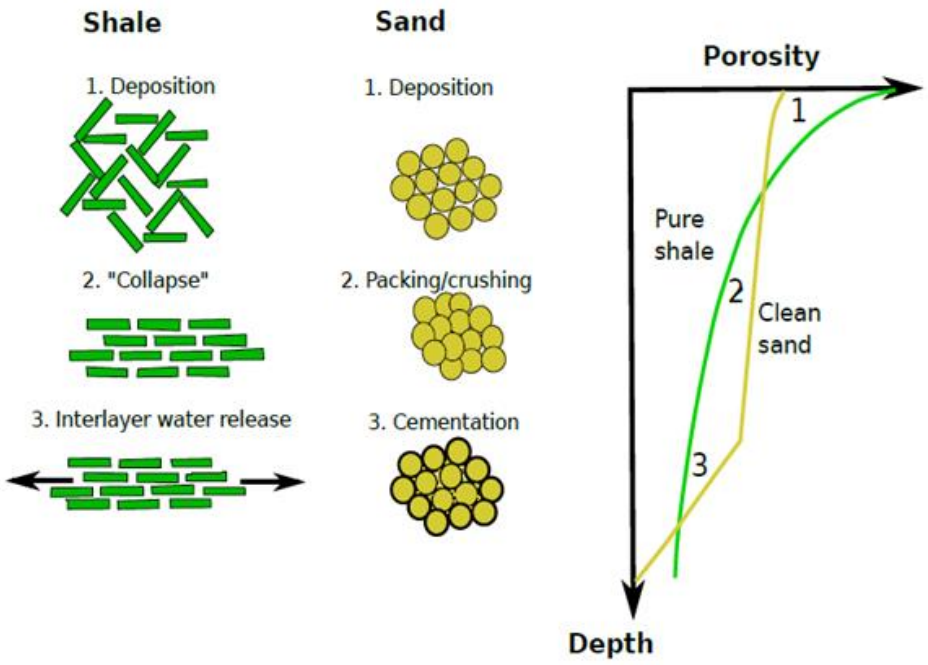

Figure 2.2: *Mechanical and chemical processes in sandstones and shales during burial and compaction. Modified from Marion (1990).*

The shales have higher initial porosities than courser sediments like silt and sandstones, and the mechanical compaction will affect clay rich sediments more than sandstones (Mondol et al., 2007). Sandstones are mechanically compacted through grain crushing and the compaction is generally controlled by grain shape, size and sorting. Chemical compaction is controlled by time, temperature and mineralogy (Bjørlykke and Jahren, 2015, Lander and Walderhaug, 1999, Storvoll et al., 2005). For sandstones chemical compaction starts at approximately 60-70ºC (Bjørlykke and Jahren, 2015). At these temperatures quartz will start precipitate and will further reduce the porosity and increase the stiffness of the rock. Cementation will also continue during uplift, but at a lower rate, as long as the temperatures are high enough (Figure 2.3).

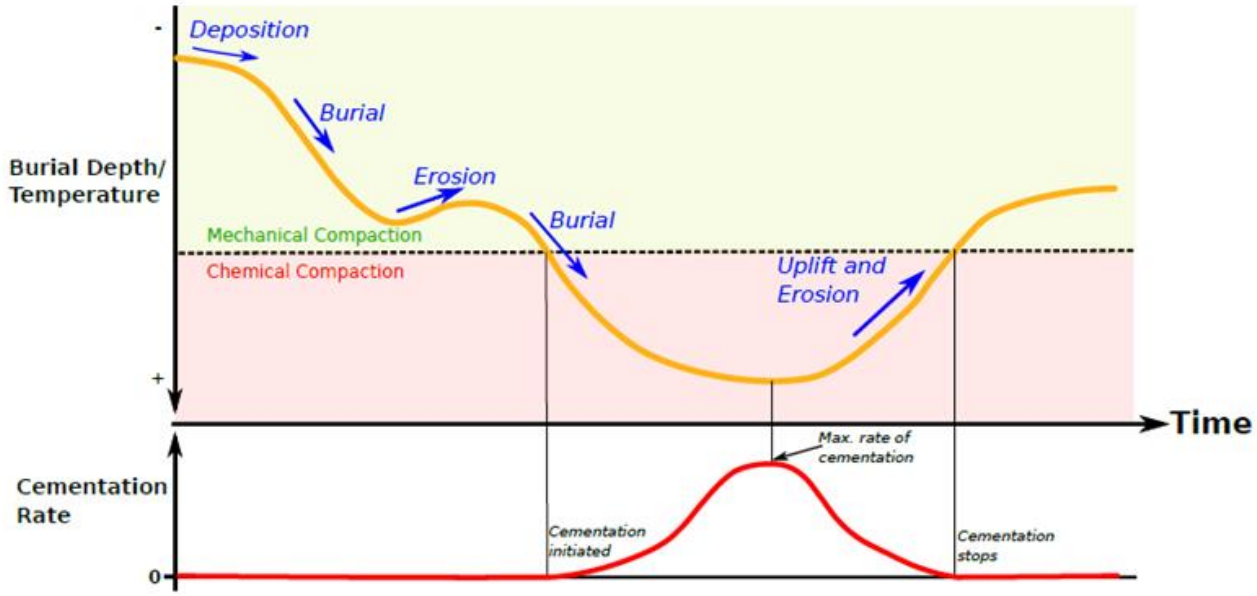

Figure 2.3: *Conceptual illustration showing the cementation rate (bottom) as a function of time and burial. The top graph is showing changing temperature related to mechanical and chemical compaction. Modified from Gatemann (2016).*

Chemical compaction in shales involves mineral transformation in addition to porosity loss due to compaction. The most common alterations of clay minerals is the transformation of smectite to illite starting at around 70-80ºC (Bjørlykke and Jahren, 2015).

Changes in the rock properties with depth are the basis for the methods for estimation of net erosion that is tested in this thesis project.

2.1.2 Net erosion and petroleum prospectivity

To understand and quantify net erosion is important for understanding the geological development of an area. This is again fundamental for understanding the hydrocarbon prospectivity. Uplift and erosion events can have both negative and positive effects on the prospectivity (Baig et al., 2016, Doré and Jensen, 1996).

Henriksen et al. (2011) summarized typical effects on a petroleum system (Figure 2.4).

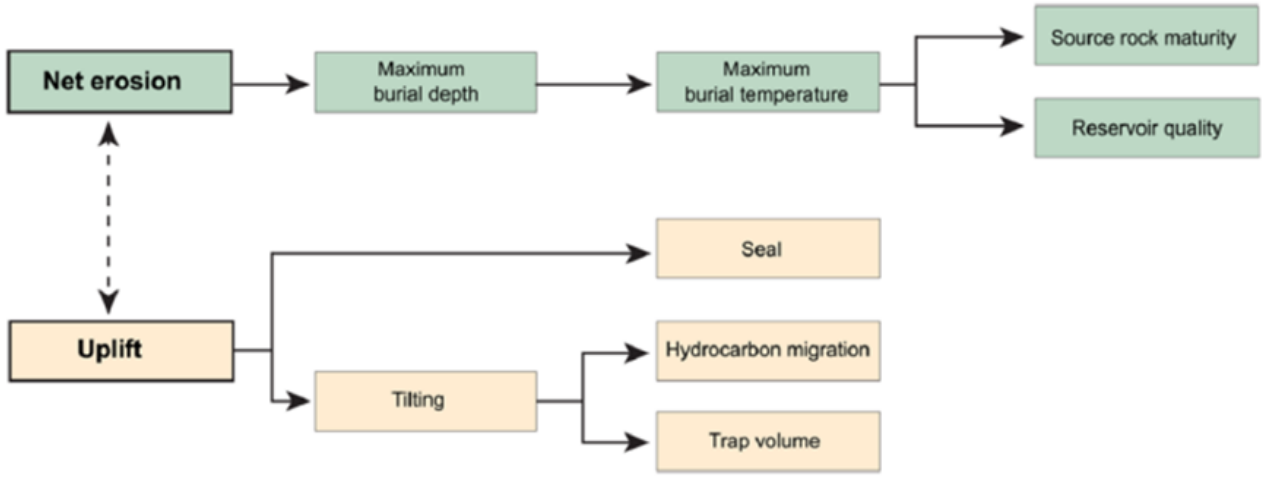

Figure 2.4: *Effects of uplift and erosion on the processes affecting petroleum prospectivity. Modified from Henriksen et al. (2011).*

Negative effects on prospectivity

Reservoir quality: A rock that has been buried and uplifted will have a compaction and diagenetic state that reflects its maximum burial depth. Diagenetic processes are irreversible and will reduce both porosity and permeability, thus this gives poorer reservoir quality than normally expected at the new depth.

Seal capacity: When a sealing rock experience uplift and erosion, failure of the cap rock can happen. This can cause fracturing of the shale and leakage of hydrocarbons through the cap rock. Hydraulic fracturing and seal failure can also happen when there is overpressure.

Petroleum generation, migration and biodegradation: Maturation of a source rock is irreversible, and as for the properties of the reservoir the measured maturity of a source rock reflects its maximum temperature. In uplifted areas source rocks are present on shallower depths than expected from vitrinite measurements. In source rocks with reduced temperatures due to uplift, the hydrocarbon generation has ceased or is reduced. This could lead to underfilled prospects. The chance of biodegradation is also present when oil has moved to shallower depths.

Structural changes: When reservoirs are uplifted a pre-existing hydrocarbon accumulation can be tilted. This will lead to spillage of oil and gas. Structural changes can also create closures that were not present in the past. The result of this could be underfilled structures if no further hydrocarbons were generated after uplift.

Gas expansion and gas release from oil: Removal of overburden and decrease in pressure will cause gas to expand. If the structure was filled to spill point before overburden was removed, this could lead to expulsion from the closure. In a case were the seal is not leaking, it will result in oil spill out of the trap, and the gas being trapped above the oil. In contrast, if gas is leaking from the top of the trap, this could also lead to an underfilled oil trap.

Positive effects on prospectivity

Local redeposition: When uplift occurs there are adjacent areas of subsidence. Rapid deposition causes acceleration in maturation of the source rocks. Rapid burial leads to enhanced hydrocarbon generation and secondary migration. The redeposited sediments can also contain coarser sediments that can be potential reservoir rocks.

Traps: In cases were uplift is associated with extension or compression new structural traps could be formed.

Source rock maturation: Uplifted source rocks will be more mature than expected due to its previous deeper burial. This can also be positive if the timing between maturation, burial and uplift is favorable. Thus, knowing the total net erosion in an area where the source rocks are at shallow depths above the expected present day oil window is important.

Methane gas release from formation water: Formation water has the potential to produce methane when uplift is occurring. Higher concentrations of dissolved methane is formed as a result of thermal maturation of organic matter in the section. The solubility of methane in water increases with pressure, thus an uplifted deep petroleum basin that has experienced decreased pressure and temperatures can liberate methane as a free gas.

Sealing capacity: As a consequence of uplift and erosion many seals fail. Although it has also been observed that cap rocks have kept their sealing capacity during uplift. Ductile seals like evaporates and hot shales can have this capacity.

Fracture enhancement of reservoirs: The amount of strain reservoir rocks are able to withstand before fracturing is often significantly less than a cap rocks can withstand. Thus, fracturing can enhance porosity and permeability. This combined with a cap rock that has kept its sealing capacity is positive. A detailed explanation of the origin and consequence of rock fracturing is given by Sorkhabi (2015).

Remigration: When hydrocarbons are lost due to failure of seals, overpressure and hydrofracturing or spillage, the possibility of remigration is still there. This means that hydrocarbons from a deeper horizon can migrate to a new location and possibly getting trapped in shallower or adjacent structures.

Although these effects will not be studied in any detail in this project, they are a very important part of the background motivation for studying net erosion.

2.2 Geological history and stratigraphy

The Barents Sea has been studied for many year and several authors have contributed to the understanding of the area (Baig et al., 2016, Fiedler and Faleide, 1996, Laberg et al., 2012, Nyland et al., 1992). In the summery given below the focus is on the structural development, and the review by Faleide et al. (2010) is the main source of information.

The western Barents Sea is bounded by passive margins to the west and north. Caledonian rocks are basement in the south western Barents Sea, and the geological history is dominated by rift phases in Carboniferous-, middle Jurassic-early Cretaceous-, and early Tertiary times. These rift systems has gradually shifted westward through time (Figure 2.5).

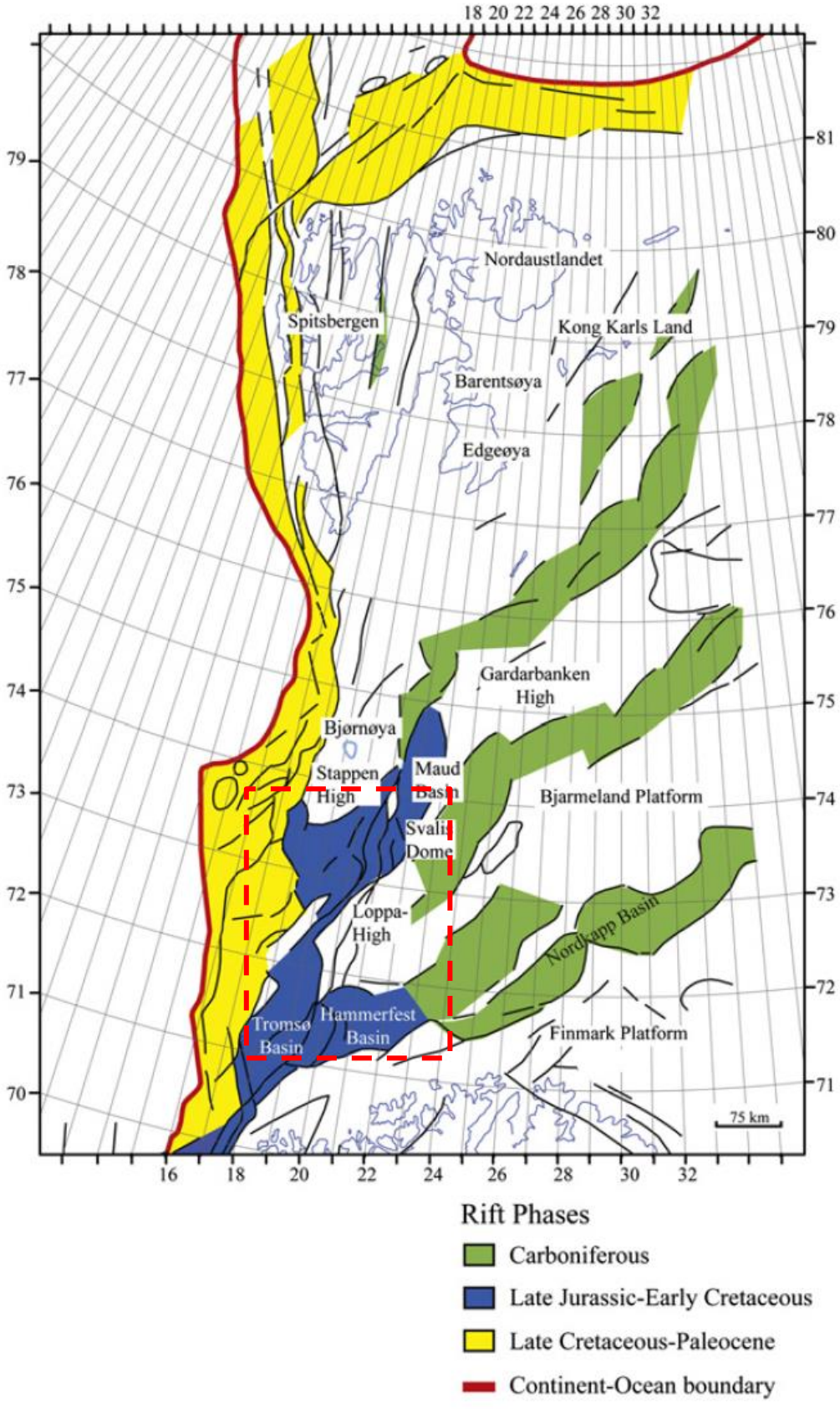

Figure 2.5: *The western Barents Sea is bounded by passive margins to the west and north. The rift phases of different geological ages are illustrated by colours. The geological history is dominated by rift phases in Carboniferous-, middle Jurassic-early Cretaceous-, and early Tertiary times. Our study is focusing on the south western part of the Barents Sea. Modified from Faleide et al. (2010).*

In the first rift face in middle Carboniferous time a large rift zone existed in the entire area and extended several hundred kilometres towards the north east. It consists of many smaller basins and graben systems that later were filled in, and in late Carboniferous- and Permian times the Barents Sea was a large platform area.

In the west and the north-west some of the fault systems were active again in late Permian- and early Triassic times. The Triassic period continued with large scale and rapid subsidence. Thick layers of sediments were deposited. The sediments came from the east and south east, with the Uralian Mountains as the main source.

Lower to Middle Jurassic sandstones (Stø Formation) represent one of the main reservoir intervals in the Barents Sea (Figure 2.6). These rocks most likely covered the entire area, also the Loppa High and other areas that were eroded later due to uplift and tectonic activity.

The next important period with rifting in the Barents Sea occurred in late Jurassic- and early Cretaceous time. The Upper Jurassic Hekkingen source rock was deposited during this period. In the phase after the rifting very deep Cretaceous basins developed and thick sedimentary layers were deposited. In this period also the marine Kolmule shale formation was deposited. The Kolmule Formation is widespread, and in this study it was used for estimation of net erosion. In the western areas subsidence continued in upper Cretaceous time, but in the rest of the area the Upper Cretaceous unit is thin or absent (Figure 2.6).

The Norwegian-Greenland Sea opened in Cenozoic time, and the development of the western area is strongly influenced by this event. In the westernmost areas also volcanism was common in the Eocene time period. Later in Cenozoic time the basins were subsiding, and the entire margin was covered by thick sediment wedges derived from the uplifted Barents Sea area further east. Late Cenozoic uplift and erosion removed most of the Cenozoic sediments, and partly also older strata. In the south western Barents Sea between 1000 and 1500 meters of strata were remove, in some places even more. During the latest development in the area a huge sedimentary wedge of Upper Pliocene to Holocene sediments were deposited along the entire margin.

Generally uplift mechanisms can be divided into four categories; tectonic-, thermal-, isostatic- and stress mechanisms. Typically the four mechanisms leads to density changes in the upper crust or mantel, which again leads to uplift or subsidence until isostatic equilibrium is re-established (Gallagher, 2012).

The uplift mechanisms in the Barents Sea have been debated for a long time and several mechanisms have been suggested. Most of them are liked to thermal changes in the mantel or stress in the lithosphere. Fjeldskaar and Amantov (2016) summarize this debate and proposes a sequence of events that can explain the observed Cenozoic uplift and erosion. In their model uplift started in the west and was caused by lateral plate movements before opening of the Norwegian - Greenland Sea. When the uplifted areas in the west were eroded this triggered isostatic movements and continued erosion that gradually influenced larger areas of the Barents Sea. If this uplift is added to the isostatic response to the glacial erosion the last three million years, most of the uplift and erosion can be explained. To explain the remaining part Fjeldskaar and Amantov (2016) suggested that uplift also could be caused by migration of a phase change (gabbro to eclogite) at the base of the crust at 30-50 km depth. During erosion this phase change will move downwards and cause uplift at the surface.

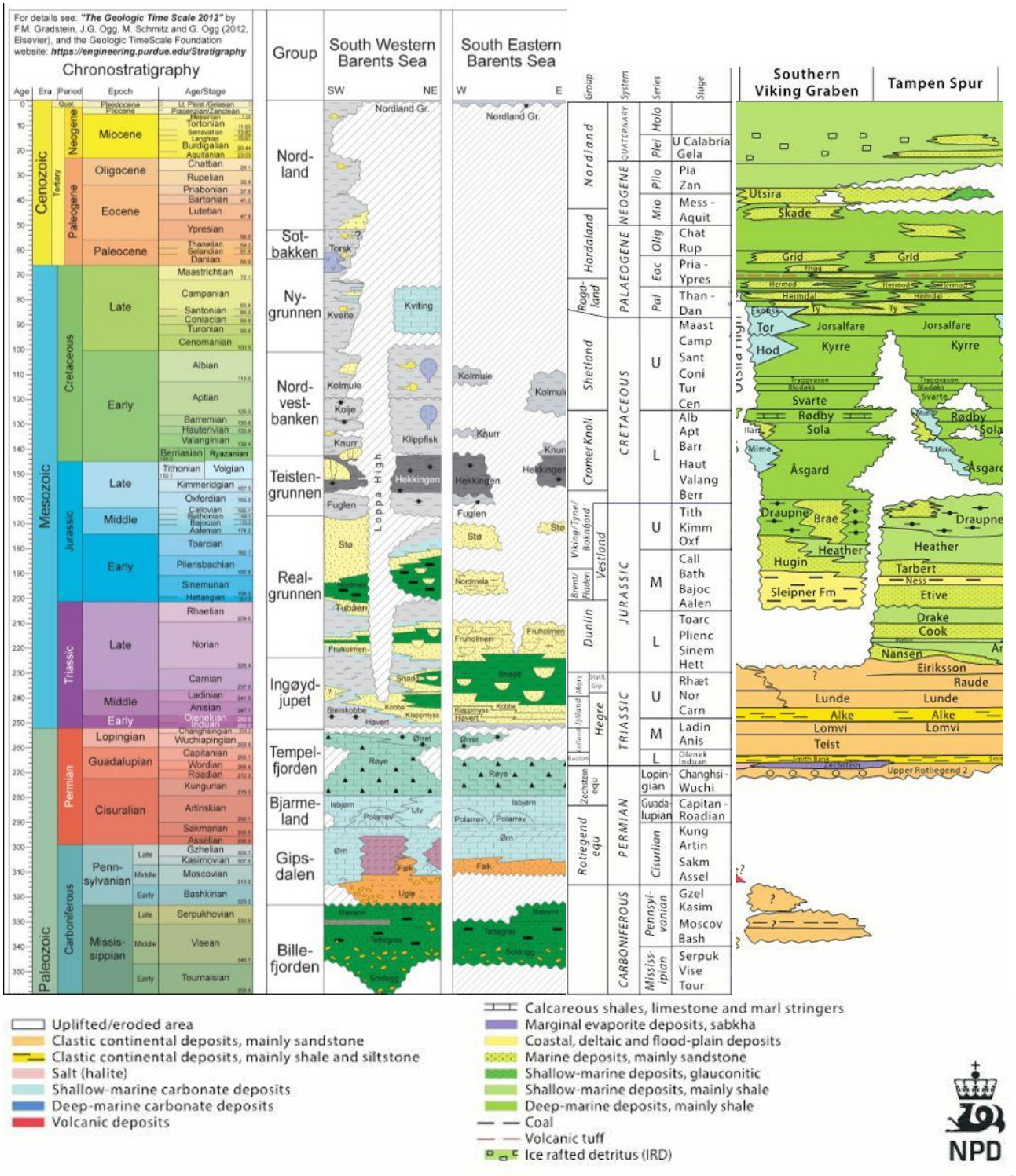

Figure 2.6: *Lithostratigraphic charts for the Barents Sea (left) and the Norths Sea (right). Modified from Gradstein et al. (2012), NPD (2014) and (NPD, 2016).*

2.3 Data and software

For the purpose of estimating the net erosion in this study a comprehensive well data base consisting of well log P-wave velocities, well log resistivities and other petrophysical data has been used. Seismic data sets were used for seismic interpretation and AVO analysis, and seismic velocity data was used to generate net erosion maps. For a full overview of the data base and software, see Figure 1.1 and Table 2.1.

Data	**Software**
Well Log Data Barents Sea and North Sea *Providers: NTNU and Tullow Oil*	Petrel (Schlumberger, 2015)
Seismic Data *Provider: Tullow Oil/TGS*	Hampson Russell – HR-9/R2 (CGG)
Seismic Velocity Cubes *Provider: Tullow Oil/First Geo*	Matlab (MathWorks, R2015a)
NPD Factpages (2016)	Excel (2013)

Table 2.1: *Data and software used in this study. Petrel was used for geological interpretation and generation of net erosion maps. Hampson Russell was used for seismic reservoir characterization. Matlab was used for calculations of net erosion and generation of net erosion maps from seismic velocities. Excel was used for basic calculations.*

Chapter 3 – Theory and Methodology

Several different techniques can be used to study uplift and erosion. Japsen and Chalmers (2000) give an overview and summarizes the methods in five different categories:

(1) Maximum burial studies estimating removed overburden using sonic velocity, density or vitrinite reflectance. Properties of the rock changes during burial and the prediction of how these parameters change is the foundation of how net erosion of sediments can be estimated. Using compacted shale units is one of the most tested and traditional ways of estimating net erosion and has been carried out in many uplift and net erosion studies (Bulat and Stoker, 1987, Henriksen et al., 2011, Baig et al., 2016, Jensen and Schmidt, 1992).

(2) Fission-track studies use apatite fission track data to constrain the erosional and cooling history of a basin. Basin modelling constrained by fission tracks makes it possible to determine uplift and give estimates of net erosion in an area. Apatite fission track thermochronology is a technique based on the decay of uranium and using the number of fission events produced, for analyzing thermal histories and reflects both the level of maximum temperature and its duration (Green, 1989, Hansen, 2000, Johnson and Gallagher, 2000, Mathiesen et al., 2000, Rohrman et al., 1995).

(3) Geomorphological studies of present topography for estimation of uplift and subsidence, by correlation of offshore geology and onshore morphological elements. Using identification of denudation events by recognizing erosional surfaces, marking a lower level of elevation, allows quantification of net erosion and tells us when and where the uplift has occurred (Doré, 1992, Lidmar-Bergstrøm et al., 2000, Riis, 1996).

(4) Sediment supply studies for estimating increased erosion rates and possible related uplift. The changes in sediment distribution and supply from the hinterland indicate regional vertical movements. These vertical movements are mainly related to tectonic processes along the continental margin and is in many cases responsible for generation and removal of sediments. But the tectonic movements cannot be differentiated from sea-level changes using sequence stratigraphy alone. It can also be difficult to recognize where the depositional material is originated (Andersen et al., 2000, Clausen et al., 2000, Evans et al., 2000, Jordt et al., 1995, Stuevold and Eldholm, 1996).

(5) Structural studies for estimation of relative uplift and removal of overburden. These studies apply structural seismic interpretation to evaluate and interpret present structures and relative movements of sedimentary packages of different ages within a basin. Correlating this with morphological studies of exhumation estimations quantifies the net erosion (Andersen et al., 2000, Chalmers, 2000, Riis, 1996).

These five methods address the challenging problem of quantifying uplift and erosion. To obtain the best result possible, several techniques should be applied. The standard deviation narrows with an increasing number of methods (Henriksen et al., 2011).

In this study the technique that uses shale velocities to estimate removed overburden has been utilized. In addition an estimation method using sandstone modelling of cement volume and porosity honoring burial history was used (Avseth et al., 2014). Also an alternative approach, using resistivity data in estimating net erosion, was tested. Structural interpretation of seismic sections was used to link together the results from the mentioned techniques, to document uplift and to understand how the erosion influenced the stratigraphic development and thereby also the prospectivity of the actual area.

3.1 Estimating net erosion from shale depth trends using P-wave velocity

When there is no over-pressure development, the porosity decreases with increased burial depth. This is referred to as normal compaction and is an irreversible process. A shale will thus retain the compaction it has gained at maximum burial depth (Hansen, 1996). By comparing P-wave velocity-depth trends for a reference area that has not experienced uplift or erosion with an area of interest, it is possible to estimate the net erosion that has occurred. Uplifted and eroded rocks will still have approximately the same velocity as when they were at their deepest burial.

By estimating the deviation from a reference velocity-depth trend the net erosion in an area or at a specific location can be given. Figure 3.1 shows a schematic illustration of how to estimate the net erosion. The uplifted area has a higher velocity than normal for the actual depth, and net erosion is here the difference in depth between the reference curve and the actual curve for a specific P-wave velocity.

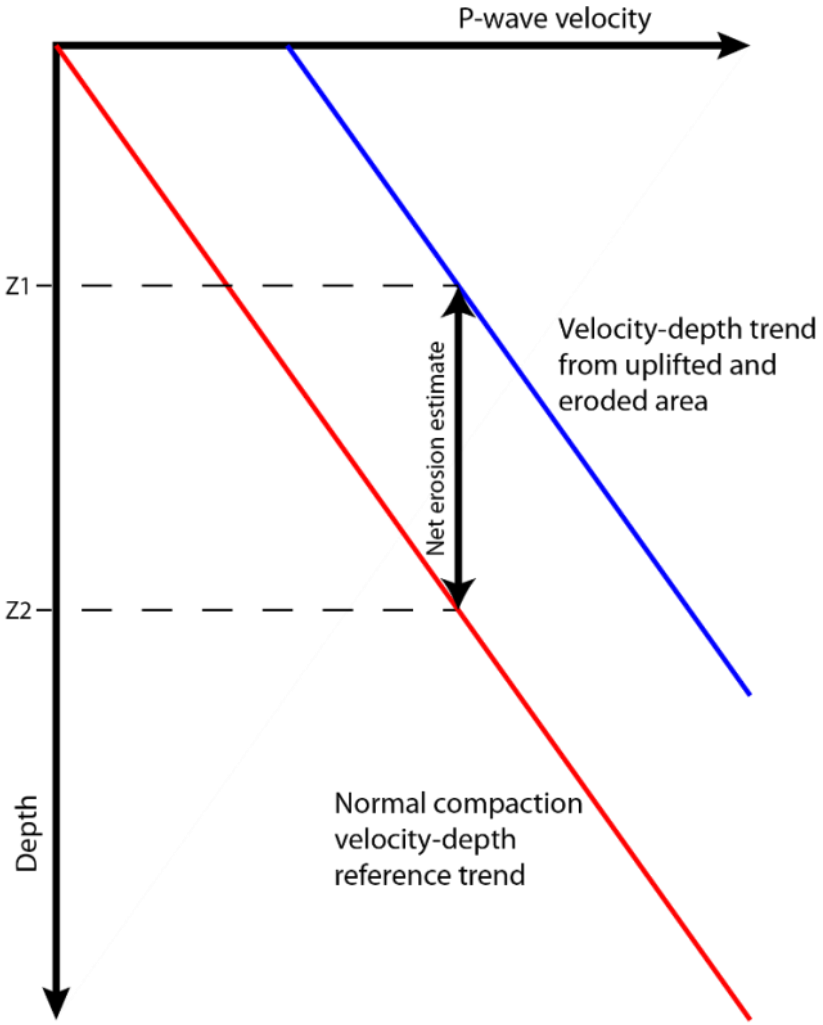

Figure 3.1: *Quantification of net erosion from compaction techniques using P-wave velocity vs. depth trend for shales. The difference between the reference trend (red) and the blue trend line which has undergone uplift and erosion will give the net erosion estimate. The net erosion is the difference between present day burial depth for the formation (Z1) and maximum burial depth (Z2).*

3.1.1 Reference trend

Previous studies of velocity-depth trends by Storvoll et al. (2005) in the northern parts of the North Sea, and by Japsen (2000) further south both based on significant amounts of data, established P-wave velocity-depth trends in areas with no uplift. In this study, a new trend line was stablished based on data from the central Viking Graben in the northern North Sea (Figure 3.2).

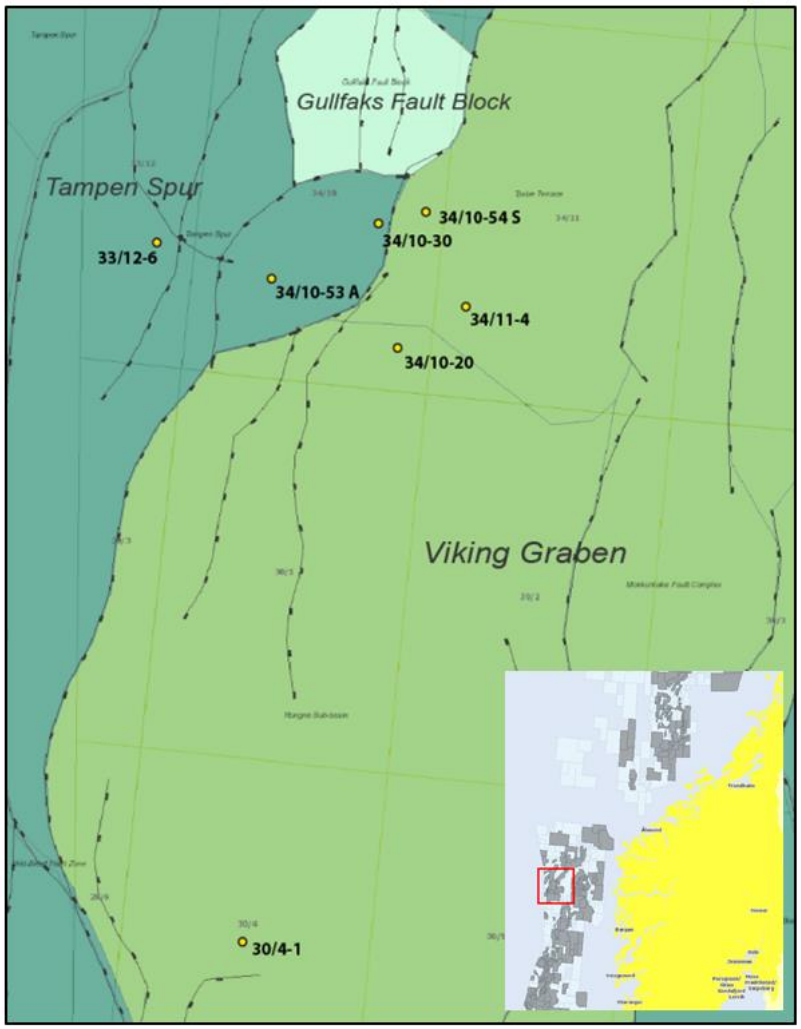

Figure 3.2: *Study area in the Viking Graben. Wells close to or in the graben itself are used in this study to establish a velocity-depth trend. This area is thought to have no or little uplift (Storvoll et al., 2005). Wells are chosen in the same area as Storvoll et al. (2005) established their reference trend for the North Sea.*

Estimating the net erosion in the Western Barents Sea region was based on the velocity-depth reference trend line established for the North Sea. When we want to establish and use a reference trend line from the North Sea to estimate net erosion in the Barents Sea region, two basins quite far apart, we need to make some assumptions.

1) **Velocity-depth trends are linear and increases with depth.** Normally, the velocity increases with depth, and this is the case for both the Barents Sea and the North Sea. Although velocity-depth trends may vary with depth, in this study we have assumed a linear relationship.
2) **Shales in the Barents Sea and the North Sea should ideally be homogenous and of same character.** Change in lithology will occur over a large study area and this will affect the results. So to be able to use the reference trend established for North Sea shales, Barents Sea and North Sea shales should have similar or comparable properties.

3) **Common geological setting.** The North Sea and the Western Barents Sea are comparable sedimentary basins with similar geological development in some periods, but very different in other periods. To use a reference trend established in the North Sea the basins are assumed to be comparable in terms of subsidence history for the relevant intervals.
4) **Similar thermal history:** In order to simplify the study, the same thermal history is assumed across the North Sea and the Barents Sea when estimating net erosion.

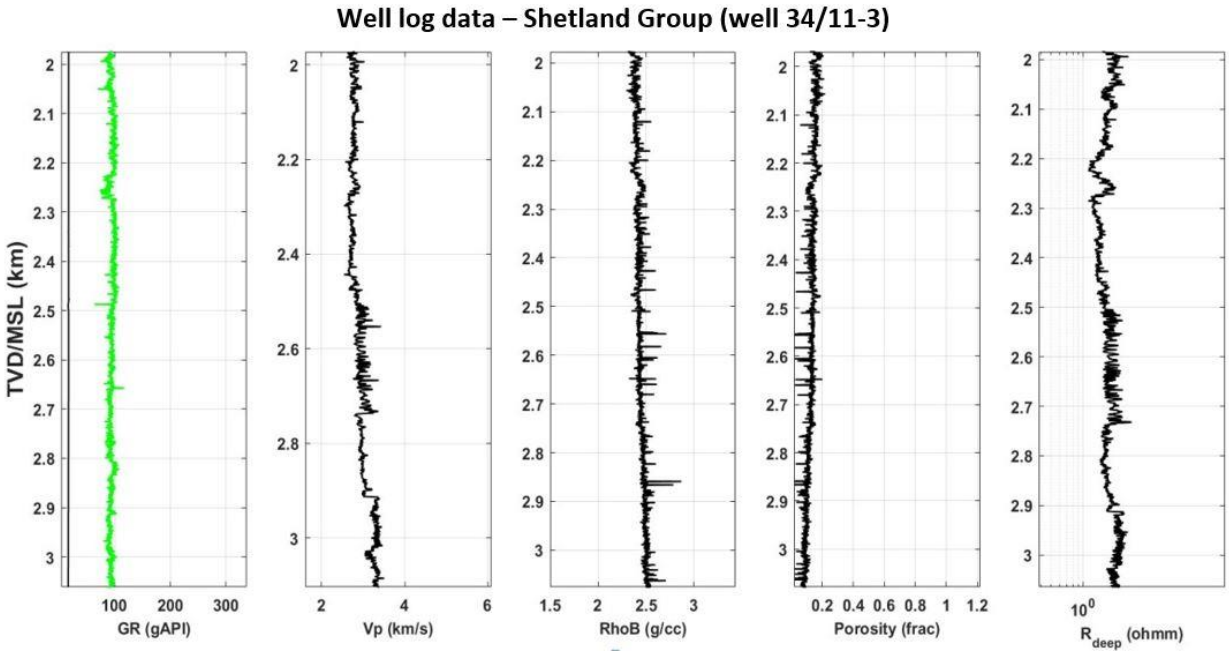

Figure 3.3: *Well log data from well 34/11-3 located in the Viking Graben. Continuous logs indicate a thick package dominated by clay stone with high shale content. See Figure 3.2 for location of the well.*

When selecting wells for the reference trend, seven well bores penetrating the Upper Cretaceous shales in the Shetland Group were chosen (Figure 2.6 and Figure 3.3). These shales were chosen because they have properties comparable to the Lower Cretaceous Kolmule Formation in the Barents Sea (Figure 2.6). Kolmule was used for the actual net erosion estimates, and the two are of approximately the same age, and both have good shale properties according to Storvoll et al. (2005) and NPD (2016). The Kolmule Formation is generally a thick shale unit and is widespread in the Barents Sea. The reference wells were selected from same area where the Storvoll-trend was established (Storvoll et al., 2005). Their study was based on a large amount of data from several formations, and is good for general calibration. The wells chosen in our study are all drilled after 2005 and in this way complements Storvoll et al. (2005)'s work. The Storvoll trend is based on 60 wells from the Norwegian Shelf. Most of the wells are dry which minimize the effect of varying pore-fluids on sonic velocities. The log data have not been corrected for overpressure.

The Storvoll trend is also in fair agreement with other published trend lines like Japsen (2000), Hansen (1996) and Hermanrud et al. (1998). The reference trend is shown in Figure 3.4 and will be discussed and compared to other trend lines in Chapter 5.

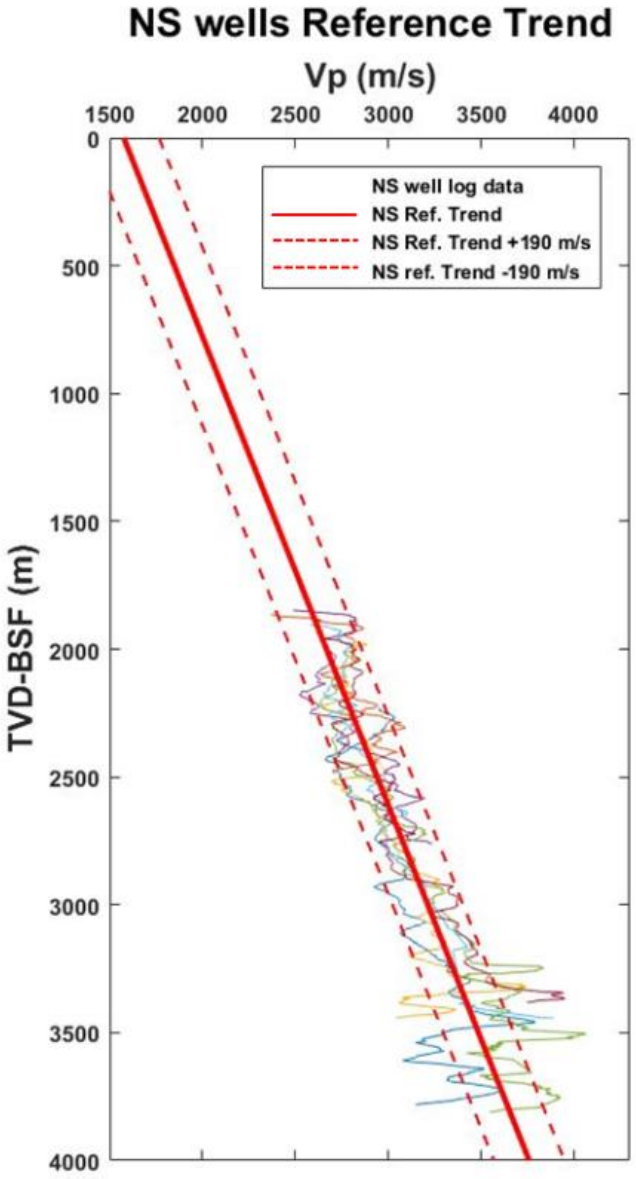

Figure 3.4: *P-wave velocity reference depth trend established from the Viking Graben in the North Sea. See Figure 3.2 for location of wells used to establish the reference trend. Uncertainties (stippled lines) for the reference trend were calculated and are shown in the figure.*

The shales in the Lower Cretaceous Cromer Knoll group were also tested, but were not chosen due to a higher content of marl. Furthermore, the Hordaland Group was considered but is not a favourable shale unit because of a higher content of silt, sand, carbonates or volcanic rocks (Figure 2.6). When the Shetland Group shales were selected for the new reference trend line only the thickest and cleanest shale intervals were chosen. The North Sea Shetland shales are as stated in Storvoll et al. (2005) thought to be dominated by smectite and illite. The effects of lithology on the reference trend will be discussed below. The reference wells were chosen away from the coast, to ensure as little uplift as possible. Moreover, the wells were selected from the northern North Sea, since the Shetland shales have higher carbonate content in the southern areas (Japsen, 2000). Higher carbonate content will increase the P-wave velocity.

A reference velocity-depth trend line could also be calculated from the westernmost parts of the Barents Sea, where no or little uplift has occurred. But the data coverage is sparse and there is less knowledge about these parts of the Norwegian Shelf. However, the North Sea reference line will be compared to wells in the Barents Sea not affect by uplift.

3.1.2 Data processing and net erosion estimation

When establishing the reference trend the well log velocities were edited and outlier points were removed. Such points are caused by abrupt changes in velocity due to lithology changes, in most cases due to chalk or other carbonate stringers. Illitization, at deeper burial depths might also contribute to higher velocities and give erroneous results (Bjørlykke and Jahren, 2015). In addition to the velocity logs; gamma-, density- and porosity logs were used when selecting suitable log intervals for the reference trend. The logs were smoothed to remove the effects of the unwanted lithology stringers. By editing and smoothing the logs in this way the reference trend will approximate a clean shale.

The widespread Kolmule shale is homogenous and has high clay content (Baig et al., 2016, NPD, 2016). Although Kolmule is the better formation choice for doing the calculations, there are places where the formation is not present, for instance on the Loppa High. In these cases the Paleocene Torsk Formation was used (Figure 2.6). Although the Torsk Formation in some areas have slightly higher content of silt than the Kolmule Formation (NPD, 2016) it is still well suited for the purpose.

All data were imported and quality controlled using NPD (2016) and Petrel (2015). The calculations and the processing itself were done in Matlab (R2015a) on imported ASCII (LAS) files. Water depth, kelly bushing height, formation level depth, petrophysical analyses and composite logs were taken from either completion reports or from the NPD website (2016).

The data used in the net erosion calculations should have a clay volume greater than 80 %. This is considered clean shale. The volume of clay was calculated from gamma logs using the following formula (Cannon, 2016):

$$V_{clay} = \frac{GR_{log} - GR_{min}}{GR_{max} - GR_{min}} \tag{3.1}$$

To calculate the volume of clay the maximum and minumum values from the gamma ray log are picked as shown in Figure 3.5. The GR_{max} value is the clay line, with 100 % shale, and the GR_{min} is the sand line, with 100 % sand. GR_{log} is the gamma ray log value for the particular data point in the log were the clay volume is calculated (3.1). The shale- and sand lines were picked at the lower and higher general trend of the log. These lines vary from well to well and were picked in all logs to obtain the best result possible. Some places the gamma ray varies within the spesific interval. In such cases multiple intervals were chosen to adjust the minumum and maximum values selected from the gamma log.

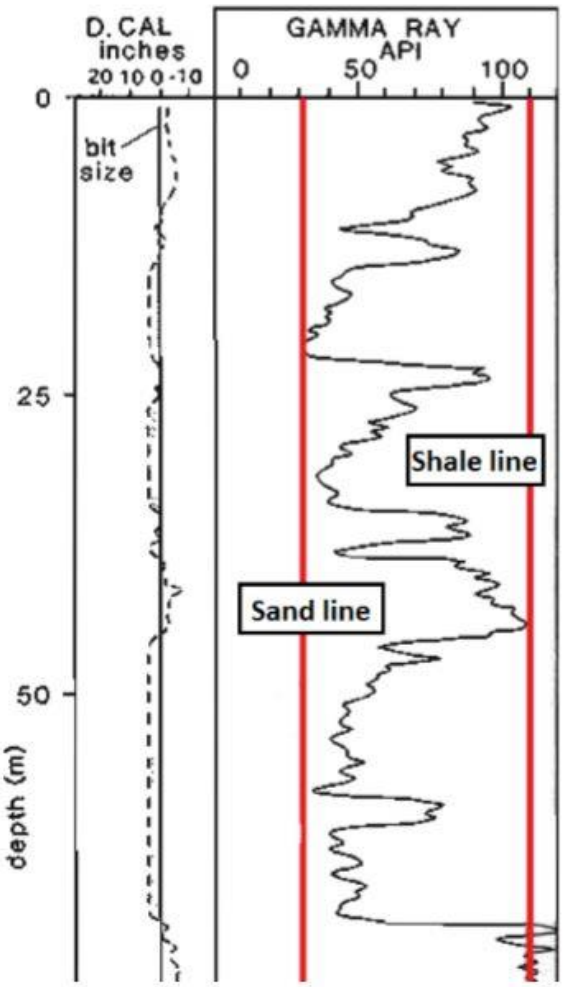

Figure 3.5: *A gamma ray log showing the shale base line and sand base line. Modified from Rider (2000).*

After the processing steps described above, the effects of lithologies like silt, sand and carbonates that could contribute to too high velocities are removed. By using shale lithologies we most likely also minimize the effect potential cracks can have on velocities. The velocity-depth regression line for each specific well log was established using the clay points from the clay volume estimations. This line was then plotted against the established North Sea reference trend (Figure 3.6).

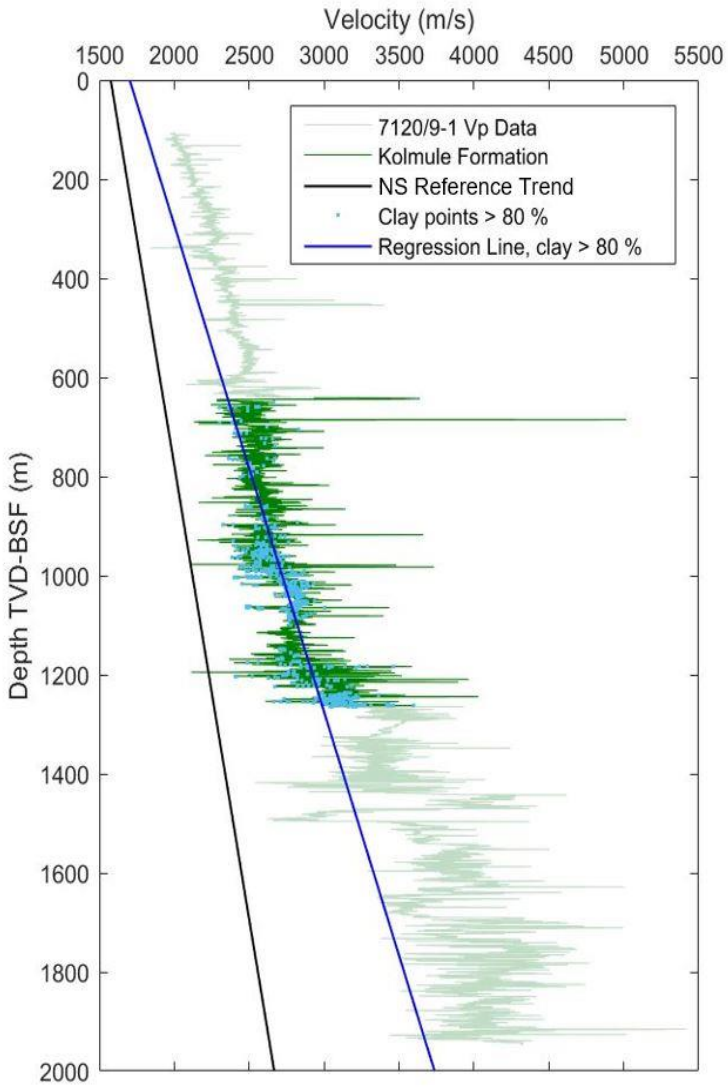

Figure 3.6: *Well log velocity data and clay points with more than 80 % clay for the Kolmule Formation in the Snøhvit well (7120/9-1). A depth-velocity trend line is made through the formation of interest and is used in calculations of net erosion. See Figure 1.1 for location of the well.*

Net erosion was calculated as the difference between the reference trend line and the well log regression line (Figure 3.7). In cases where the two lines have different inclination the net erosion estimate is the average of the maximum and minimum values within the interval. For the velocity data to be plotted correctly against the reference trend the water depth and the kelly bushing height was subtracted.

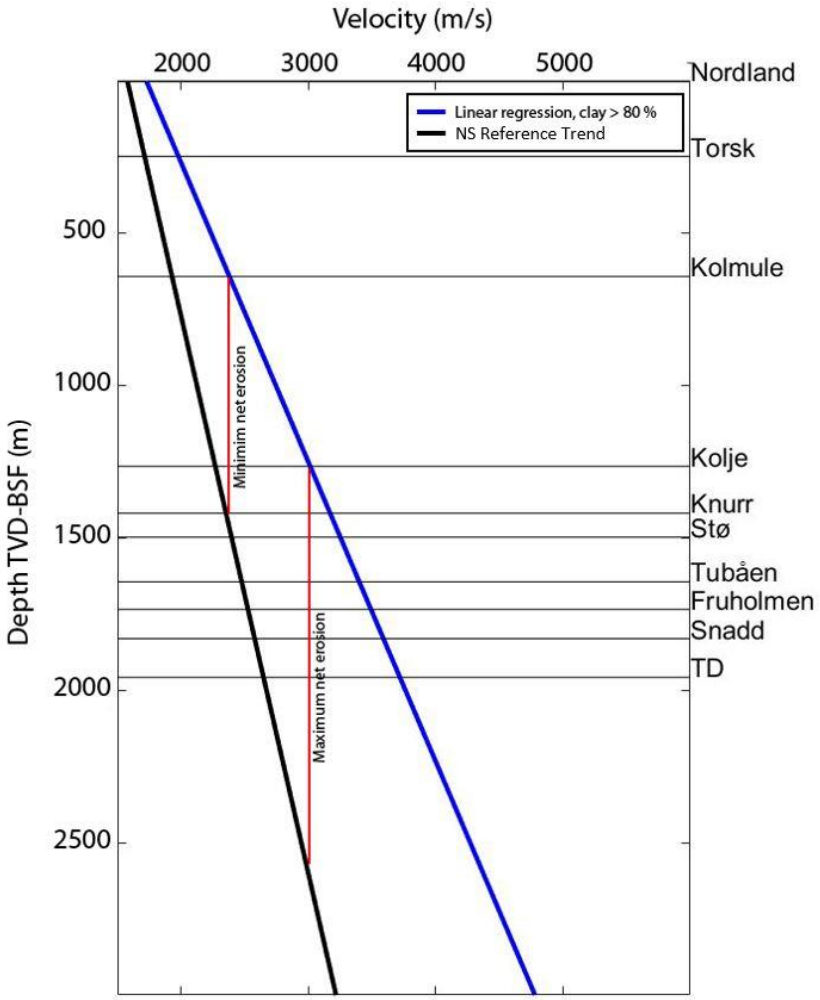

Figure 3.7: *Estimation of net erosion showing the regression trend for Barents Sea well (7120/9-1) from figure 3.6, the established North Sea reference trend and the maximum and minimum net erosion values for the Kolmule formation. The net erosion estimate is the average value for the Kolmule Formation. See Figure 1.1 for location of well.*

3.2 Estimating net erosion from shale depth trends using well log resistivity data

By using resistivity logs for the same shale intervals as used for the velocity method, we want to test if net erosion can be estimated also form resistivity data. This method has not been much used and is a new approach for estimating net erosion in the Barents Sea.

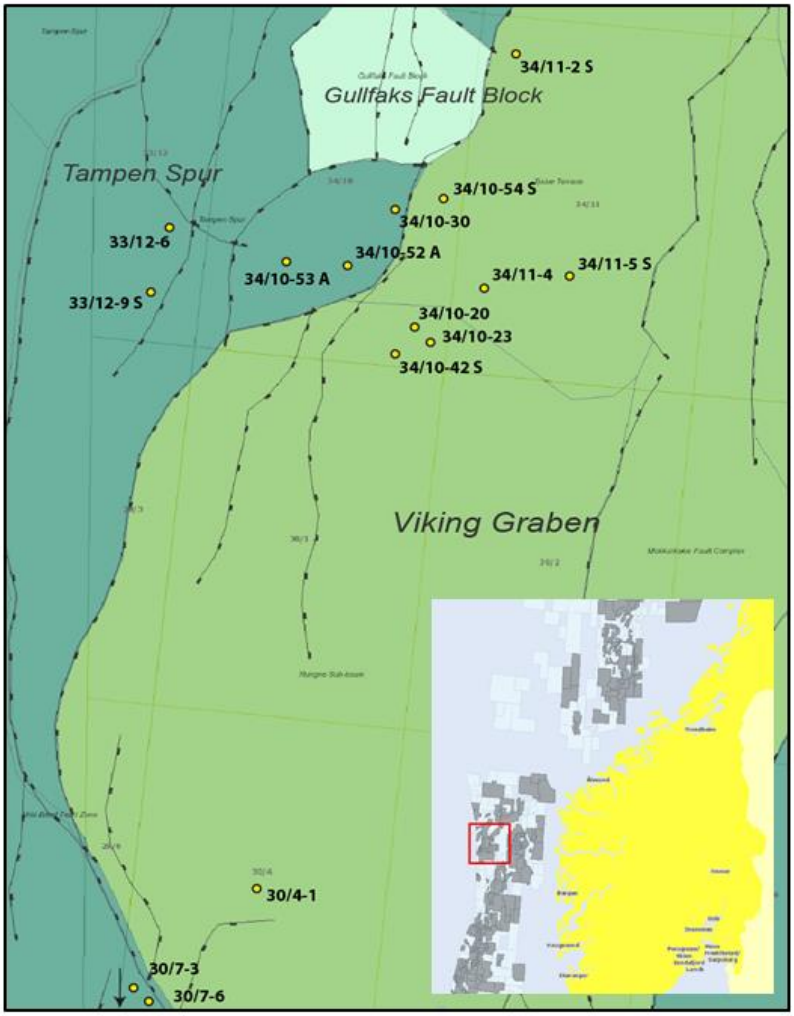

Figure 3.8: *Selected wells in the Viking Graben for the reference resistivity depth trend. Wells close to or in the graben are preferable and are used for this study due to no or little uplift in this area (Storvoll et al., 2005). Wells are from the same area as the velocity depth reference trend line.*

The reference trend was established based on resistivity log data from 15 wells in the Viking Graben. The study area is the same as for the velocity-depth trend analysis (Figure 3.8). The study used a larger number of wells since there are very few studies on resistivity-depth trends. The Shetland Group was used also here, and the resistivity log data were processed in the same way as the velocity logs. The additional wells chosen for the resistivity-depth trend (Figure 3.9) have the best and cleanest shales. High resistivity lithologies, like carbonates or volcanic rocks, will influence the measured resistivity and was therefore avoided. The distance from the potentially uplifted basin margin and a good depth distribution of the selected shale intervals were also taken into account. The well logs were smoothed and some wells had to be removed due to significant lithology effects. However, the resistivity is sensitive to the pore fluids, so changes in pore fluid parameters will normally influence the resistivity more than changes in lithology (Johansen and Gabrielsen, 2015).

The same approach, assumptions and methodology as for velocity data were used when calculating net erosion from resistivity data. A regression line for the specific wells was difficult to establish from the resistivity well log data. Instead an average resistivity value for representative intervals was used. The reference trend line was moved to tangent the point placed in the middle of the actual shale interval. This technique will also be discussed in Chapter 4. Then the distance from the reference trend to the new compaction line for the specific well was measured as for the velocity estimates (Figure 3.1).

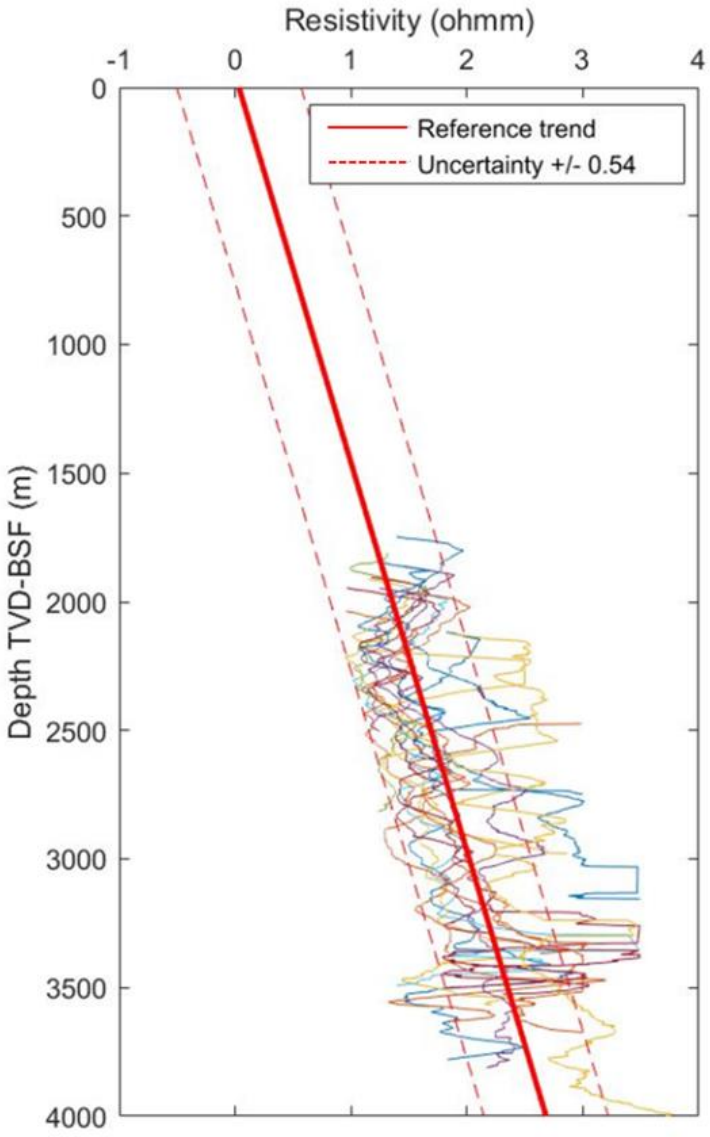

Figure 3.9: *Resistivity reference depth trend established from the Viking Graben in the North Sea. See Figure 3.8 for location of wells used to establish the reference trend. Uncertainty range (stippled red lines) for the reference trend were calculated and are shown in the figure.*

3.3 Estimating net erosion using sandstone depth trends

Using suitable shale units in estimating net erosion in areas that has experienced uplift like in the Barents Sea is a robust and well tested method. The shales are homogenous and widespread, and give consistent estimations. However, in the Western Barents Sea the shale interval used are not always present. For instance the Loppa High is lacking the Kolmule Formation. When this is the case, using sandstones for estimating net erosion is an alternative approach. The sandstone estimates in this study will be compared to the shale estimates for calibration in the wells where both good shale and sandstone intervals are present. When the shale interval is lacking the sandstone estimate will be used in mapping of net erosion.

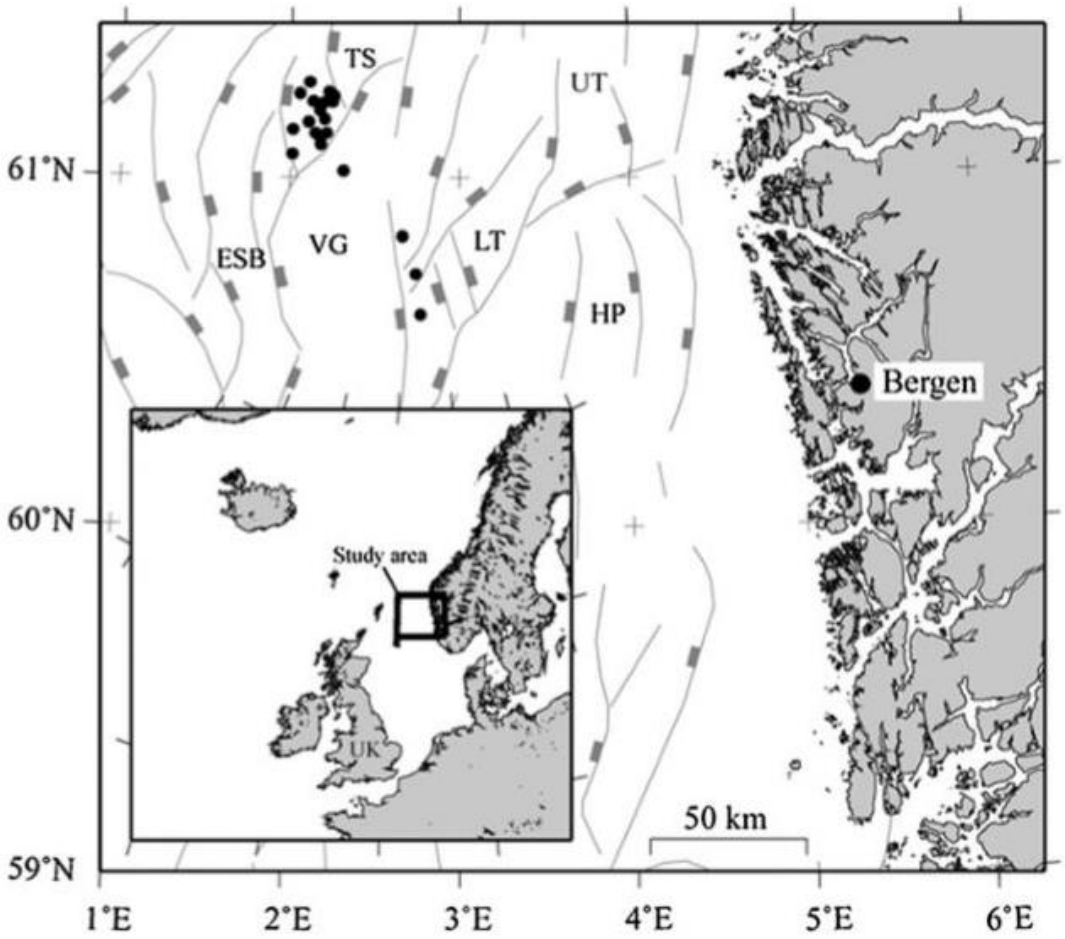

Figure 3.10: *Wells selected for the Etive Sandstone Formation velocity- and resistivity depth trends. Map of the study area in the Viking Graben is modified form Marcussen et al. (2009).*

Also when using sandstones in estimating net erosion, the first step was to establish a depth reference trend. As for the shale estimates we used data from the North Sea. Compaction trends for sandstones for both velocity and resistivity were established based on data from a previous study (Marcussen et al., 2009). Marcussen provided velocity-, density-, resistivity- and porosity data with depth for a number of chosen wells. His study was done on the Etive reservoir sandstone formation in the northern North Sea (Figure 3.10). Marcussen did not establish depth trends himself. Based on his results we estimated trend lines for the Etive sandstone, both for resistivity and P-wave velocity (Figure 3.11). Sandstone reservoir quality of the Etive Formation is good, and the velocity and density increases with depth due to normal compaction and diagenetic processes. Down to the onset of diagenetic processes at approximately 2000 meters the effective stress controls compaction. Below this point, around 60-70ºC (Bjørlykke and Jahren, 2015), the velocity-depth trend will also be influenced by quartz cementation. This was shown for the Etive sandstone by Marcussen et al. (2009). Only small amounts of quartz cement can cause changes in the velocities and porosities with depth. Marcussen et al. (2009) used the Gassmann (1951) equation to do fluid substitution for the Etive reservoir sands. Fluid substitution was only done for the velocity data. The resistivity data has not been fluid substituted, therefore sandstones without hydrocarbons were chosen for the resistivity reference depth trend.

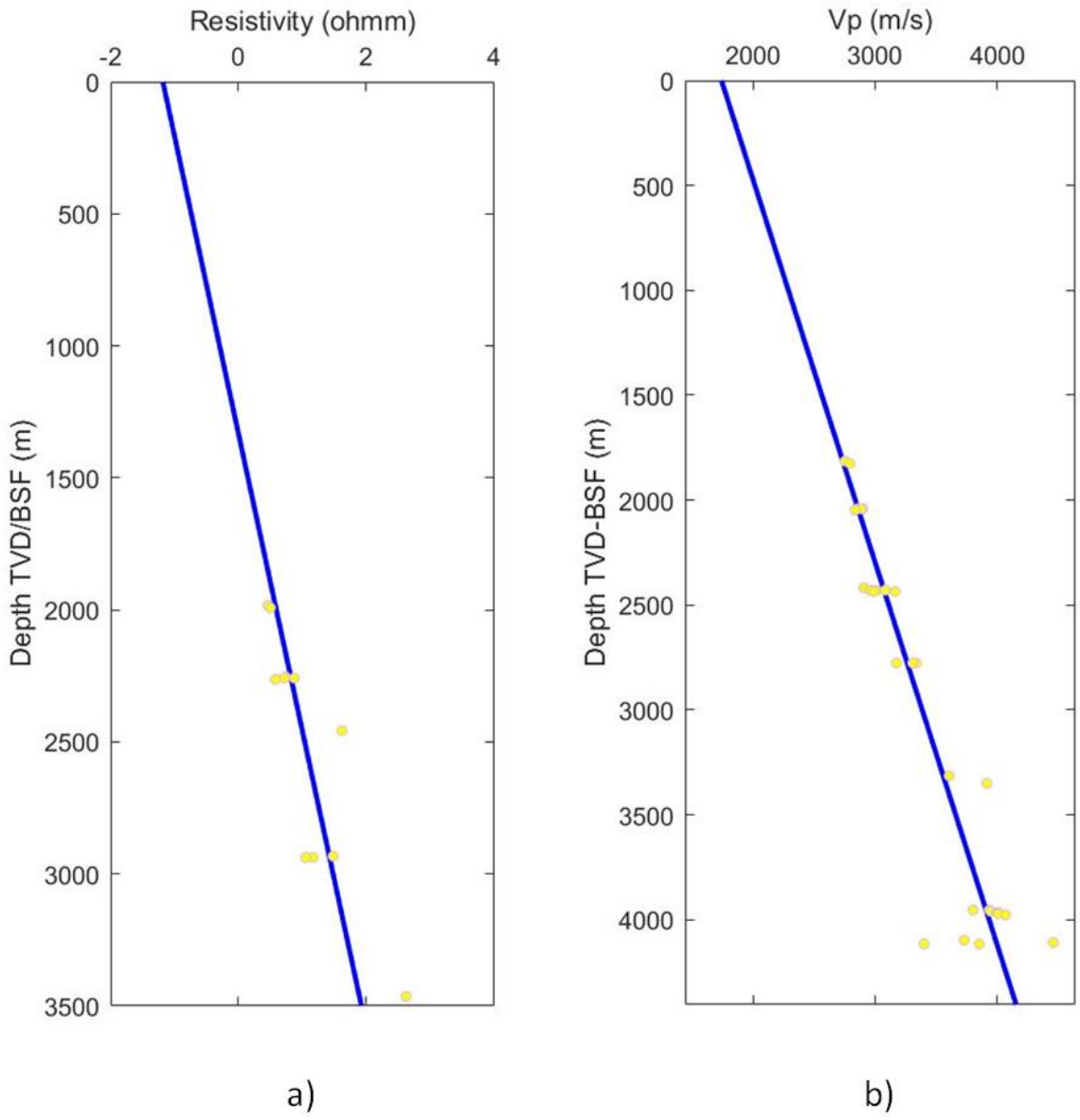

Figure 3.11: *a) Resistivity reference depth trend and b) velocity reference depth trend established for sandstones with data from Marcussen et al. (2009) (yellow points). See Figure 3.10 for location of wells used to establish the reference trends.*

3.4 Sandstone - diagenetic and burial history modelling

A sandstone modelling approach was also tested for calculating net erosion. These results are compared with and evaluated against the results from the other methods. Burial history is controlling diagenetic processes, and these effects have to be taken into account when using sandstones for estimating net erosion.

The sandstone modelling was done using the same approach as Avseth and Lehocki (2016). A method combining porosity and cement calculations with burial history was used to estimate net erosion for selected wells in the study area (Avseth et al., 2014).

As a sandstone is buried it goes through mechanical compaction until it reaches the point where the chemical compaction normally starts at about 60-70ºC (Bjørlykke and Jahren, 2015). In this study, the temperature corresponding to the onset of quartz cementation was chosen to be 70ºC. In the mechanical compaction domain the sediments will to a large degree keep their properties from maximum burial depth when uplifted (Bjørlykke and Jahren, 2015). During mechanical compaction the porosity is gradually reduced with depth. If the rocks experiences uplift this will only have minor effects on the porosity of the rock and the processes are only slightly reversed, due to the pressure release. However, if the same rocks again are buried to the same depth, the previous pressure will reoccur and the porosity will be the same as prior to uplift. When the rocks enter the chemical compaction domain the diagenetic processes will start and cement will be generated. The chemical processes will happen both during burial and uplift as long as the temperature in the rocks is greater than 70ºC. These processes are irreversible.

When performing modelling of mechanical and chemical compaction of sands and shales as a function of burial history, we model porosity and cement volume for the sandstones of interest using the Walderhaug model (Walderhaug, 1996). The relationship between porosity and effective stress is controlling the mechanical compaction (Lander and Walderhaug, 1999). Shale porosities were also modelled by using empirical trends and it takes into account the transition from smectite to illite at approximately 70ºC. Hydrostatic pressure and normal compaction was assumed for both shales and sandstones.

Burial history curves are input to the modelling for different stratigraphic intervals, and were modified to fit the present day porosity and velocity logs (Figure 3.12).

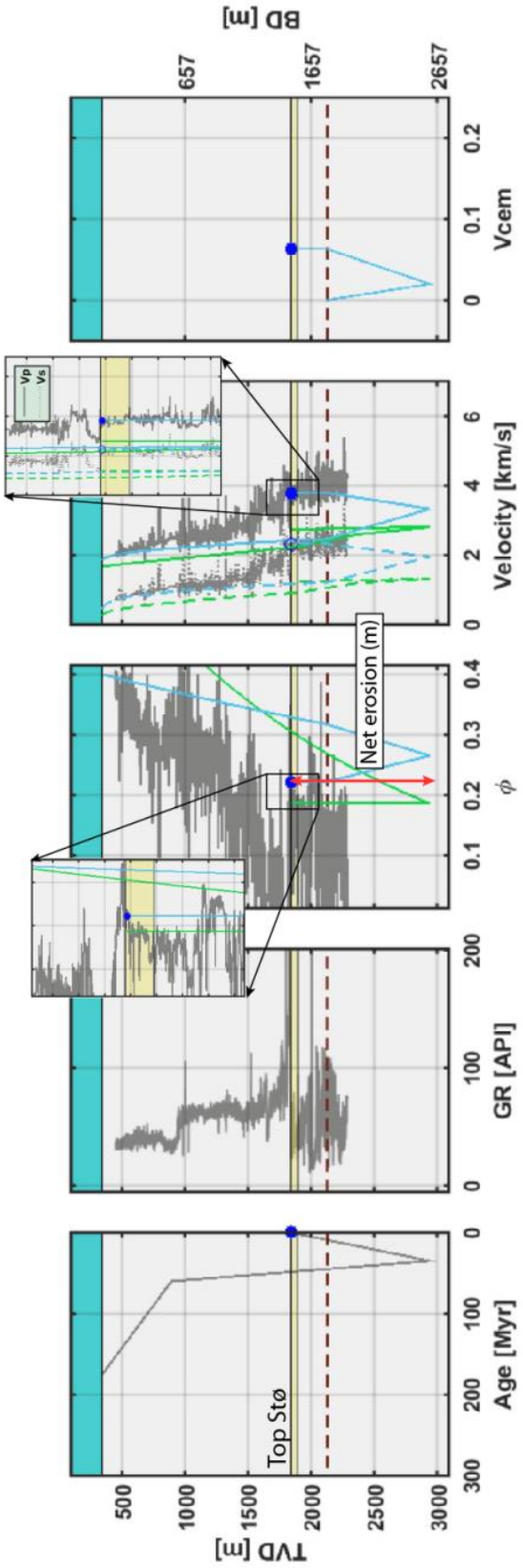

Figure 3.12: *Modelling results and well log data from the Snøhvit Albatross well (7120/9-1). From left to right: input burial history curve for the Stø sandstone (175 Ma), gamma log, well log porosity and modelled sandstone porosity, well log P-wave and S-wave velocity with modelled velocities and the calculated cement volume. The plots show good fit for the sand layer both for porosity and the velocities. The red dashed line is representing 70°C. The green line represents the shale line and the blue line is representing the brine sand.*

The porosity loss due to mechanical compaction is calculated using the formula for inter-granular volume (IGV) (Lander and Walderhaug, 1999). This modelling assumes that the sandstones are perfectly sorted. Thus the modelled sandstone porosity will be the upper limit for the actual porosity. The formula for IGV used in the calculations is:

$$IGV = IGV_f + (\varphi_0 + m_0 - IGV_f)e^{-\beta\sigma_{es}} \quad (3.2)$$

IGV: volume fraction of the pore space, cement and matrix material combined
IGV_f: volume fraction of the stable packing configuration
ϕ_0: volume fraction of the depositional porosity
m_0: volume fraction of the initial proportion of the matrix material
β: exponential rate of IGV decline with increase in effective stress (MPa^{-1})
σ_{es}: maximum effective stress (MPa)

In the sandstone model the clay content (m_0) is assumed to be 5 %, since in reality completely clean sands are very rare. The initial depositional porosity (ϕ_0) is set to be 40 % and as suggested by Lander and Walderhaug (1999) the IGV_f and β constants are set to 28 % and 0.06 respectively. There will normally appear some coating on the grain surface and the volume is assumed to be 10 % in all cases. For the shales in the Barents Sea a lower depositional porosity of 30 % was used. The open to shallower marine (NPD, 2016) Cretaceous shales in the Barents Sea occasionally have higher content of silt and marl than the more marine shales in the North Sea (Avseth and Lehocki, 2016). In shales the transition from smectite to illite can cause stiffening of the rocks as quartz is a byproduct of the transition (Thyberg et al., 2009). However, only the effect of mineralogy is taken into account in the modelling since this stiffening process is very complex and poorly understood.

Sandstones start to cement at approximately 70°C. In the chemical compaction domain the amount of quartz cement is given by the following formula (Walderhaug, 1996):

$$V_{q2} = \varphi_0 - (\varphi_0 - V_{q1})e^{\left(\frac{-MaA_0}{\rho\varphi_0 bcln10}(10^{bT_2} - 10^{bT_1})\right)} \quad (3.3)$$

V_{q2}: amount of quartz cement (cm^3) precipitated from time T_1 to T_2

Φ_0: porosity when quartz cement starts to precipitate

V_{q1}: amount of quartz cement at time T_1

A_0: initial quartz surface area

M: molar mass of quartz (60.09 g/mole)

a = $1.98*10^{-22}$, b = 0.22 (Walderhaug, 1996)

c = heating rate (ºC/Myr) obtained from burial history curves using a geothermal gradient of 3.5 ºC/100m

A_0 is the initial quartz surface area given by:

$$A_0 = (1 - C)6fV/D \quad (3.4)$$

C: fraction of grain surface coated

f: volume fraction of quartz grains

V: sample volume in cm^3

D: quartz grain size (cm)

In the modelling the constants C and D were given depending on the sandstone interval chosen.

An average default temperature gradient was estimated for each sub-basin, ranging between 35ºC/km and 42ºC/km. These gradients were used in the calculation for the Barents Sea wells. The gradients are rough estimates based on data from NPD (2016) and a seabed temperatures of 4°C. The estimated average temperature gradients for the different basins are listed below.

Hammerfest Basin: 35ºC/km

Bjørnøya Basin/Loppa West: 38ºC/km

Bjarmeland Platform South: 38ºC/km

Bjarmeland Platform North/Hoop: 42ºC/km

Fingerdjupet: 36ºC/km

Loppa High: 36ºC/km

When cement volumes and porosity loss related to mechanical and chemical compaction had been calculated using the diagenetic modelling outlined above, these were input parameters to rock physics models for estimation of corresponding velocities as a function of burial history. Net erosion estimates were then obtained by comparing observed and modelled velocities. More details on these estimations are included in the AVO section below.

An example is shown in Figure 3.12. It shows an input burial history curve, porosity and velocity well log data and the calculated cement volume. The imported burial history curves were modified, and the modelled porosity and velocities were changed accordingly, until these matched with the observed porosity and velocities (both Vp and Vs). The age of the sandstone formation of interest was input and by altering the maximum burial depths the net erosion was obtained by finding the best overall fit to the present day porosity- and velocity logs for the chosen sand interval. The difference between the present burial depth and the modelled maximum burial depth will then give the estimate of the net erosion. In most cases the Stø reservoir sandstone was used. In areas where the Stø sandstone did not have the desired qualities, other sandstones like the Tubåen- or the Nordmela Formations were used.

3.5 Net erosion estimates using seismic interval velocities

For better lateral resolution detailed net erosion map can be made using seismic interval velocities. In areas lacking well control this method gives good indications on the relative variations in net erosion. However, the method can give relatively uncertain estimates if well data are sparse. In the approach used here seismic velocities are compared to the North Sea velocity reference depth trend, and then combined with a structural map for the top of the actual stratigraphic interval.

The method is described by Dræge et al. (2015) for seismic 2D lines. Background trend lines and methodology are shown in Figure 3.13.

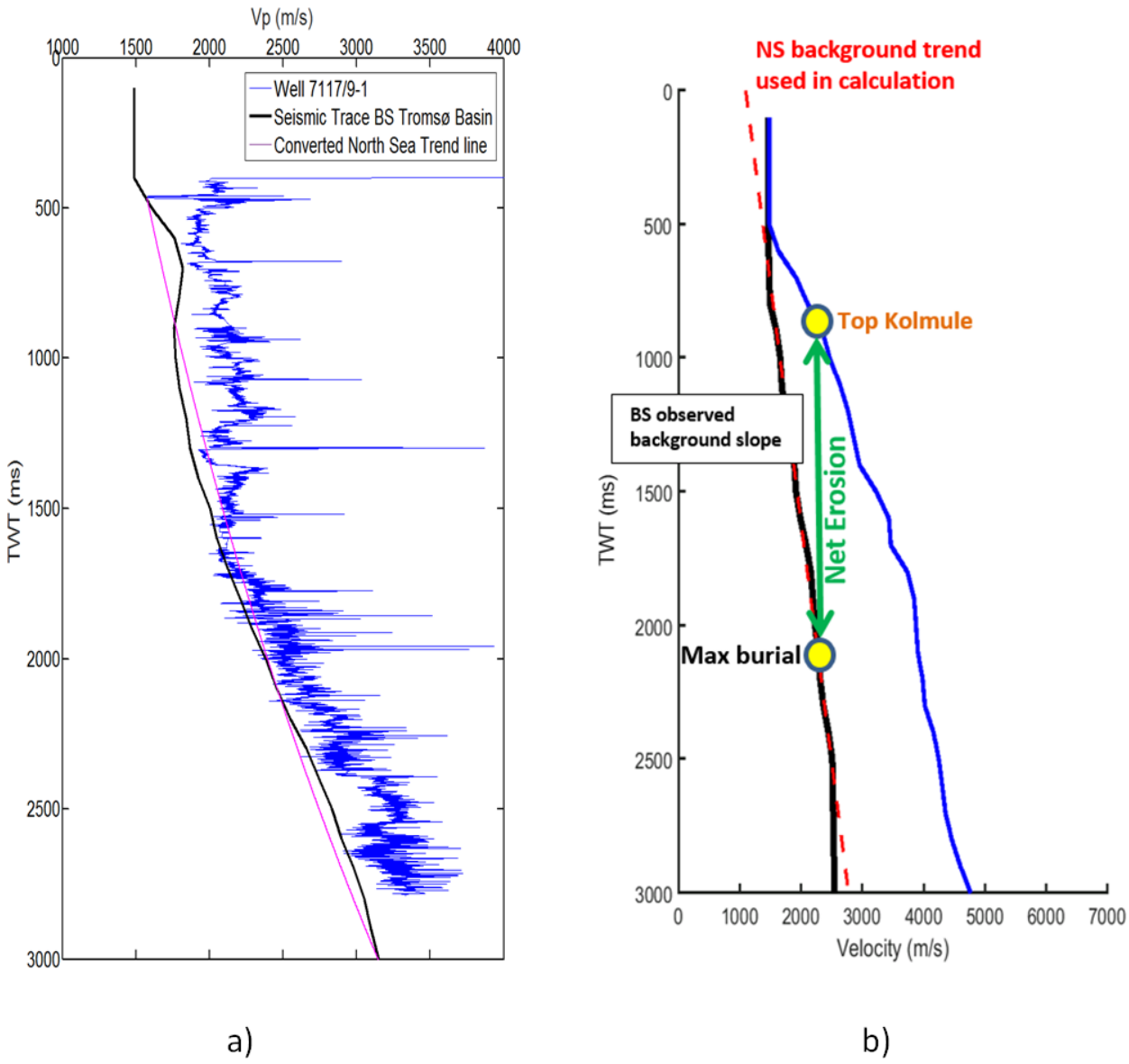

Figure 3.13: *a) The North Sea reference trend converted to TWT for comparison to a seismic trace from the Tromsø Basin and the velocity log from the Senja Ridge well. b) Methodology for estimating net erosion using seismic velocities. The distance between the top Kolmule horizon and maximum burial depth is the estimated net erosion. See Figure 1.1 for location of well.*

Interval velocities were derived from seismic stacking velocities using the Dix (1955) formula given by the equation:

$$V_{n,layer} = \frac{V_n^2 t_n - V_{n-1}^2 t_{n-1}}{t_n - t_{n-1}}^{1/2} \qquad (3.5)$$

Interval velocities, $V_{n,layer}$, for each layer can be derived from stacking velocities. V_{n-1} and V_n are the stacking velocities for the reflectors above and below the layer respectively. The equation is valid if we consider small offsets and flat and parallel layers.

The established velocity-depth trend from the North Sea (Chapter 3.1.1) has the seabed as its reference. When using an interval velocity cube it has its reference at sea level. Hence to use the North Sea trend as reference for seismic velocities in the Barents Sea we added the actual water depth at all locations.

To qualify the North Sea reference trend for comparison with seismic velocity trends from the Barents Sea, we compared it to a well with minimum uplift and a seismic velocity trace. Figure 3.13a shows the Senja ridge well log (7117/9-1) west in the Barents Sea, the time converted (TWT) North Sea reference trend, and a seismic trace from the Tromsø Basin. This trace is from an area with no or minimum net erosion. As seen in the figure the Senja Ridge well could have some minor uplift, when compared to the reference and the seismic trace. Since the seismic trace from the Tromsø Basin has good match with the time converted North Sea reference trend, the net erosion results based on seismic velocities can be compared and integrated with the other net erosion results based on well log data. As for the shale estimates from well log velocities the net erosion was estimated for the Kolmule Formation.

The methodology and principals are the same as when using well log velocities, where the difference between the background trend and the top Kolmule horizon will give the net erosion estimate (Figure 3.13b). The great advantage using seismic velocities from a velocity cube is the density of estimations compared to the few wells available in our study area. From the wells simple trend maps can be constructed, while detailed net erosion maps based on the top Kolmule surface are constructed from the seismic velocity cube. Estimations are performed in a 3 by 3 kilometre grid.

When the Kolmule Formation was not present, an interpreted BCU (Base Cretaceous Unconformity) horizon was used.

The principle of making the net erosion map from seismic velocities is simple, but in practice, due to software settings a more detailed workflow consisting of several steps had to be used (Figure 3.14). The cubes in the figure have two way travel time (TWT) values on the z-axis, while the attributes are changing.

- A Barents Sea average velocity cube was generated from stacking velocities. The stacking velocities are corrected for anisotropy. This means that we now have vertical velocities.
- From the Barents Sea average velocity cube a new volume with interval velocities was calculated (Figure 3.14a).
- The Barents Sea average velocity cube was depth converted using a TWT volume with the simple formula: $\text{Depth} = 0.5 * \text{TWT} * V_{p,avg}$. It is this new depth converted cube that will be used in the estimation of net erosion (Figure 3.14b)
- A new cube with predicted depths from the interval velocity cube was estimated using the North Sea velocity-depth trend line established in this study (Figure 3.14c): $\text{Predicted Depth} = \frac{V_{p,interval} - 1575.9}{0.5457}$. The actual depth conversion was performed as above.
- The net erosion was estimated by subtracting the depth generated from the Barents Sea average velocity cube from the predicted reference depth. The water depth was subtracted to be able to compare the two cubes (Figure 3.14d). Therefore: $\text{Net Erosion} = \text{Predicted Depth} - (\text{Depth} - \text{Water Depth})$
- This new volume is a cube with net erosion estimates in meters and a map can be generated form the Top Kolmule or the BCU horizons.

The depth conversion should compensate for velocity anomalies in the overburden above the top Kolmule horizon. Overburden velocity anomalies will affect the travel times and give erroneous results if not accounted for. For instance as in Figure 3.11a the increased velocities at depths between 500 and 1000 TWT (ms), most likely caused by Pliocene sediments, can influence the layers below and give higher net erosion estimates due to velocity pull-ups.

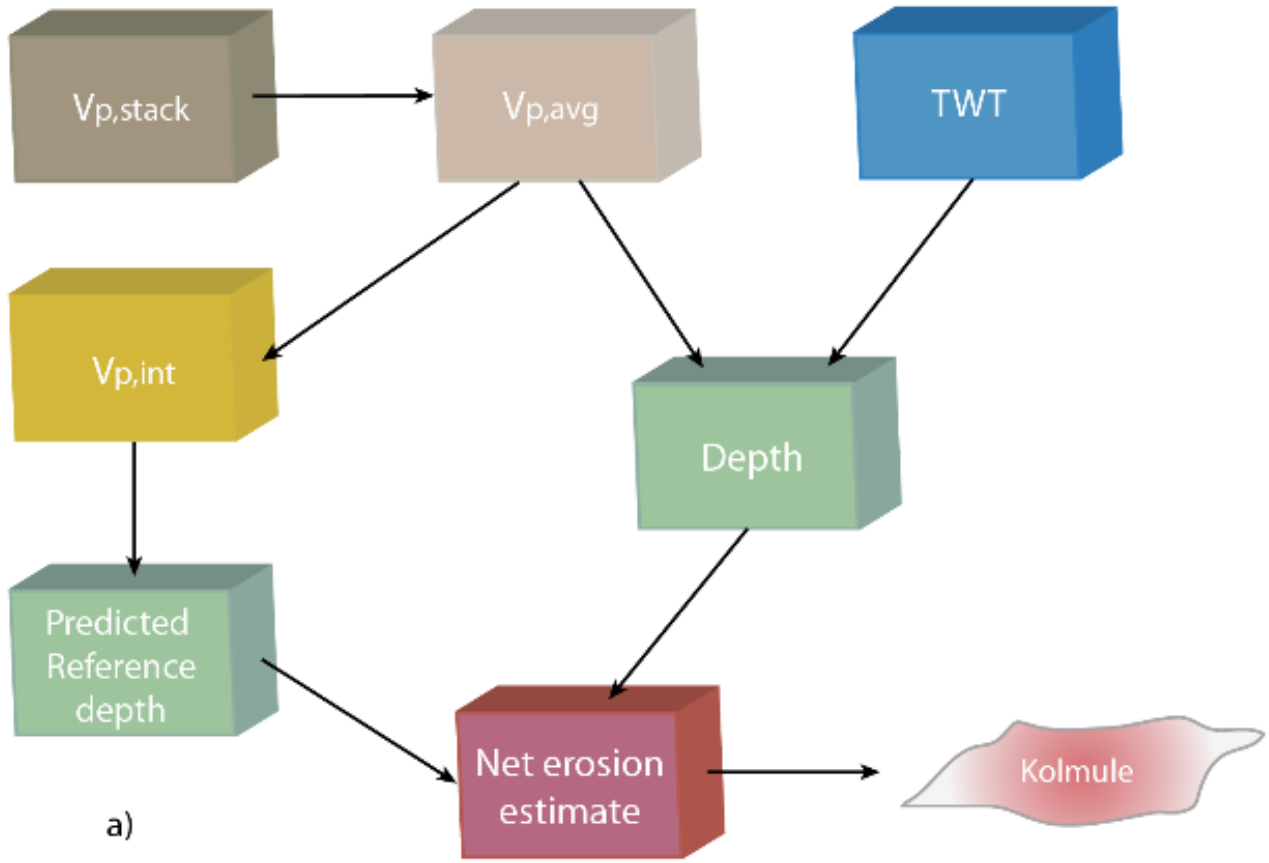
Vp,stack
Vp,avg
TWT
Vp,int
Depth
Predicted Reference depth
Net erosion estimate
Kolmule
a)

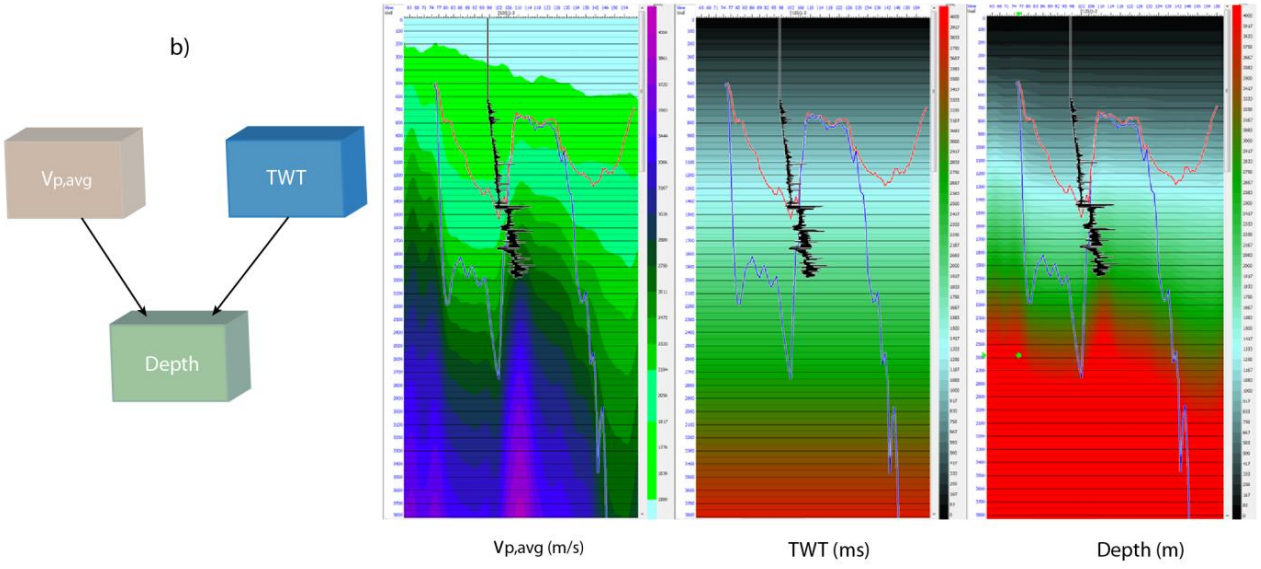
b)
Vp,avg
TWT
Depth
Vp,avg (m/s)
TWT (ms)
Depth (m)

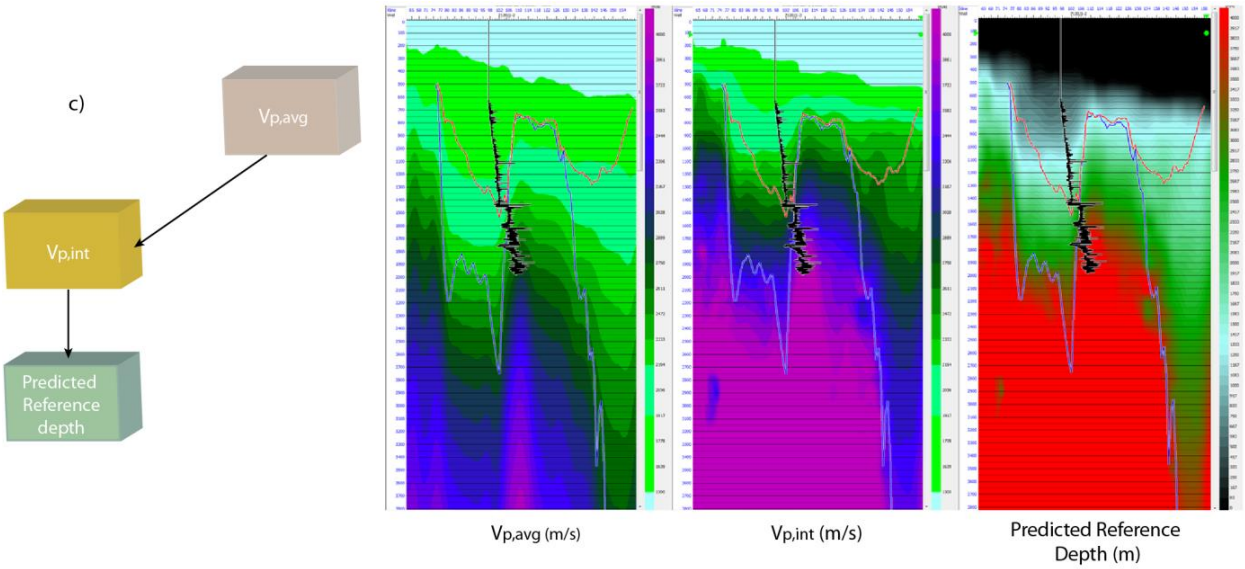
c)
Vp,avg
Vp,int
Predicted Reference depth
Vp,avg (m/s)
Vp,int (m/s)
Predicted Reference Depth (m)

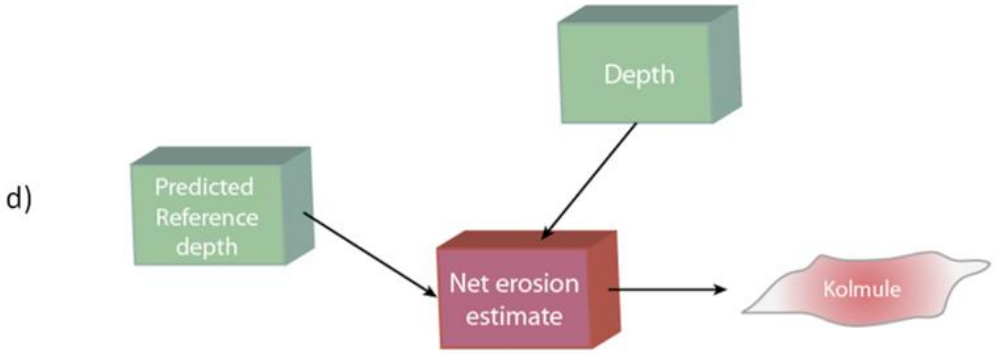
d)
Depth
Predicted Reference depth
Net erosion estimate
Kolmule

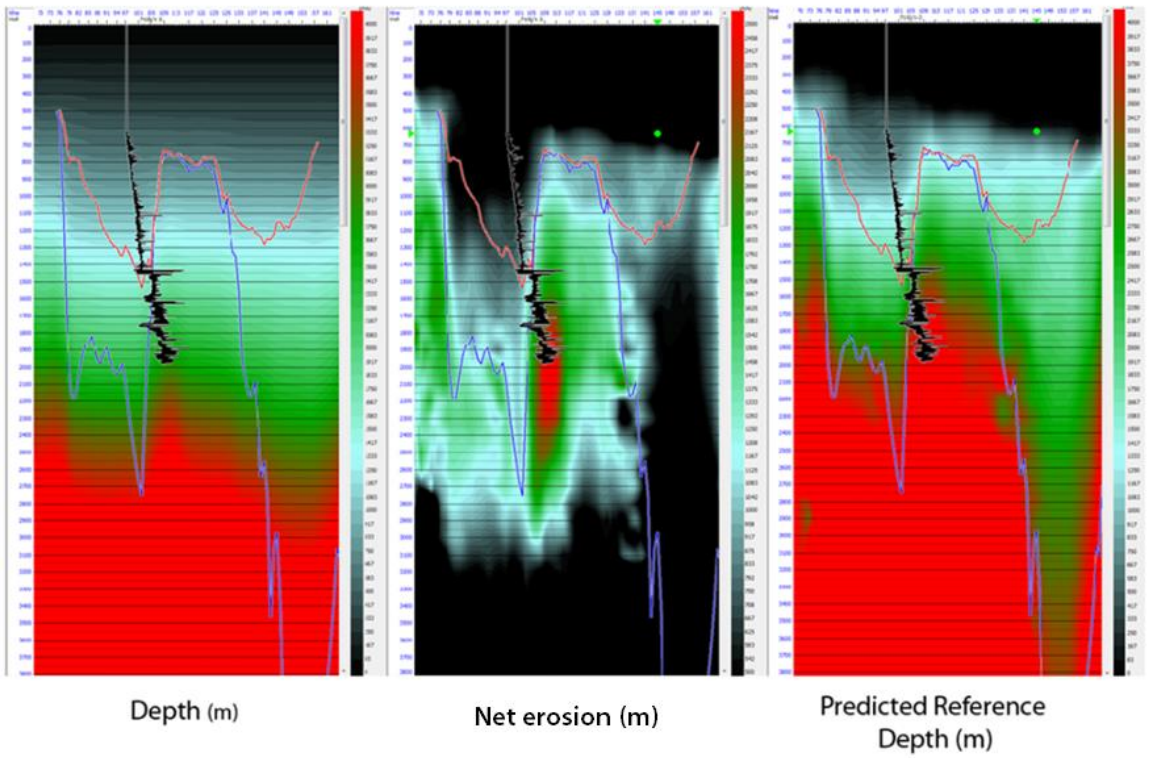
Depth (m)
Net erosion (m)
Predicted Reference Depth (m)

Figure 3.14: *The detailed workflow for making net erosion maps from seismic velocities consists of several steps: a) Overview of work flow. First interval velocities were calculated from the average velocities, b) the average velocity cube was depth converted using a TWT volume and this new volume was used in the estimation of net erosion, together with c) predicted depths from the interval velocity cube, which was estimated using the North Sea velocity-depth trend line established in this study. d) Net erosion was estimated by subtracting the predicted depth, from the depth generated from the Barents Sea average velocity cube. All the cubes have TWT along the vertical axis and geographical positions along the horizontal axis. The cube attributes varies as show in the figures. The Kolmule- (red line) and BCU Horizons (blue line) are also included in the cubes. See text for a more detailed explanation of the work flow.*

3.6 Seismic interpretation

By calculating net erosion for a number of wells in the Barents Sea the uplift- and erosion history was investigated. To further evaluate and being able to couple the net erosion estimates to the geologic development, seismic interpretation was carried out on four regional seismic sections (Figure 1.1). By linking the tectonostratigraphic development of the area and the net erosion estimates from well data, the goal is to better understand the erosional history. This includes the magnitude and timing of the uplift on and around the Loppa High.

Key seismic horizons for understanding the development were selected and tied to the wells, and major faults important for the understanding of the large scale development were interpreted. The focus in the interpretation was to understand the burial history of the study area. Geological models were created based on the interpretation, and packages were defined according to geological age.

Due to lack of shaly intervals and well bores, net erosion estimates from the Loppa High are sparse compared to the surrounding areas. But, some estimates were carried out and give an indication of the net erosion. The interpreted seismic sections will supplement these estimates, and thus the understanding of the geological development in our study areas.

3.7 AVO

The effects burial history has on seismic signatures and rock physics parameters have been addressed in several publications, such as Dræge et al. (2015), Avseth and Dræge (2011) and Brevik et al. (2011). To understand these effects, seismic data and well data must be integrated. This is especially important when predicting rock properties in new areas, and in areas with complex geology. From basic interpretation of seismic data high amplitude anomalies (HAA) can be detected, but to know whether it for example is a diagenetic effect or a fluid effect that creates the HAA, can be difficult. In order to distinguish between such effects, and to evaluate what types of fluids are present, amplitude versus offset (AVO) in the seismic data can be used.

The change in amplitude with offset can represent varying types of fluids in the reservoir rock, and can thus be divided into several recognizable AVO classes. Originally the AVO classes were defined for gas sands (Rutherford and Williams, 1989). Avseth et al. (2005) suggested to use the classifications more as a descriptive system for observed AVO anomalies, without automatically linking them to gas sands.

3.7.1 AVO classification

Standard seismic interpretation gives the stratigraphic and structural development of an area, in addition to definition of prospects. AVO data gives additional information about reservoir properties and fluids. The information AVO gives on lithology and pore fluid properties of a rock is divided into classes (Rutherford and Williams, 1989, Castanga and Smith, 1994, Ross and Kinman, 1995b). AVO responses can be characterized by plotting the reflectivity at zero offset versus the amplitude change with increasing offset, or in this case with angle of incidence with the actual surface (Figure 3.15). The first is known as the intercept and the second as the gradient.

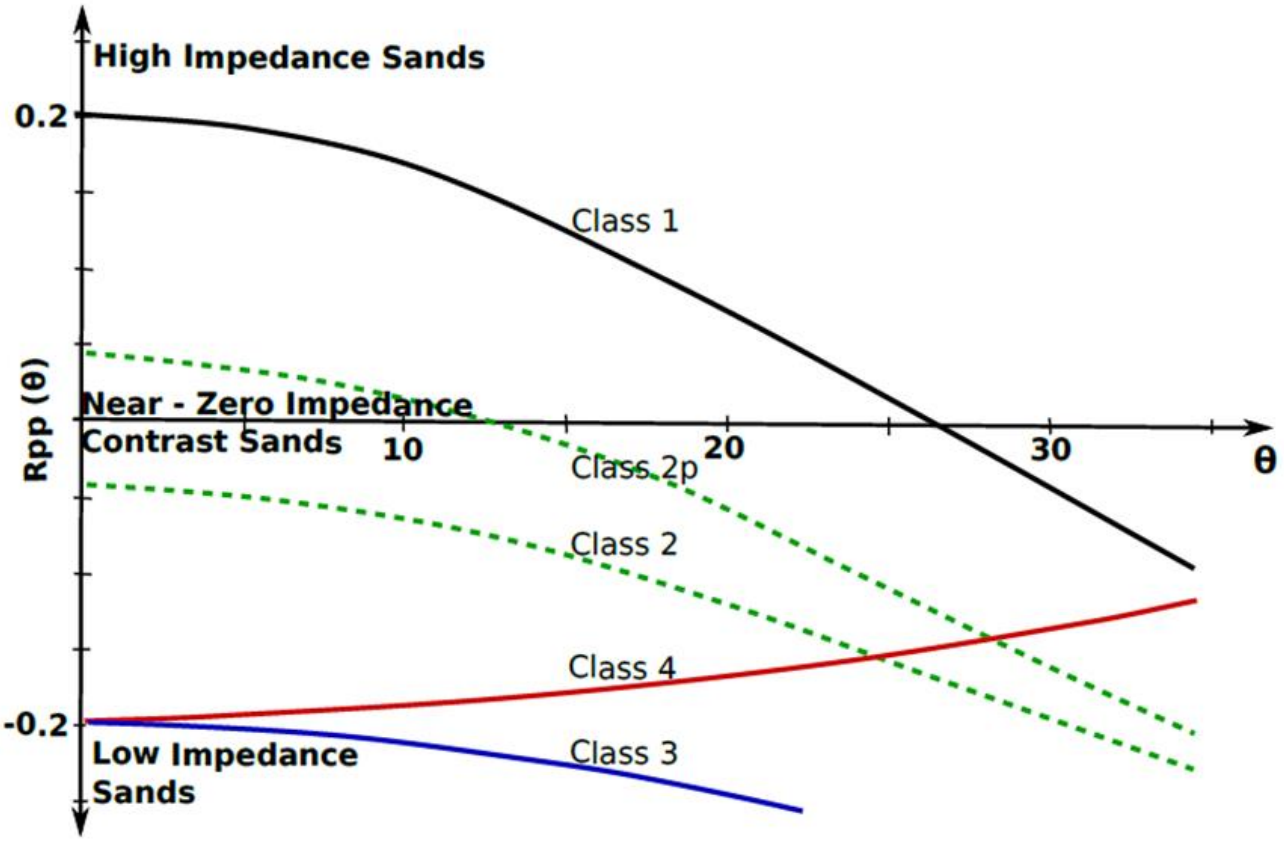

Figure 3.15: *AVO responses are divided into five classes. $R_{pp}(\Theta)$ is the P-wave to P-wave reflection coefficient and Θ is the angle of incidence. The AVO classes are defined by Rutherford and Williams (1989), Castagna and Smith (1994) and Ross and Kinman (1995). Examples of reservoir sands for each class are given* Table 3.1. *The figure is modified from (Gatemann, 2016).*

Class	R(0)	G	Lithology
1	+	-	Hard sands with HC
2	-	-	Small impedance sands with HC
2p	+	-	Small impedance sands with HC
3	-	-	Soft sands with high fluid sensitivity
4	-	+	Soft gas filled sands underneath stiff cap-rock shales.

Table 3.1: *Examples of AVO classes. The classes are defined by Rutherford and Williams (1989), Castagna and Smith (1994) and Ross and Kinman (1995). See Figure 3.15 for illustration of the classes. Modified from Gatemann (2016).*

When the AVO responses are plotted in an intercept versus gradient cross plot, five main classes are defined. In Figure 3.16 a typical intercept-gradient cross plot is shown with the same classes as show in Figure 3.15.

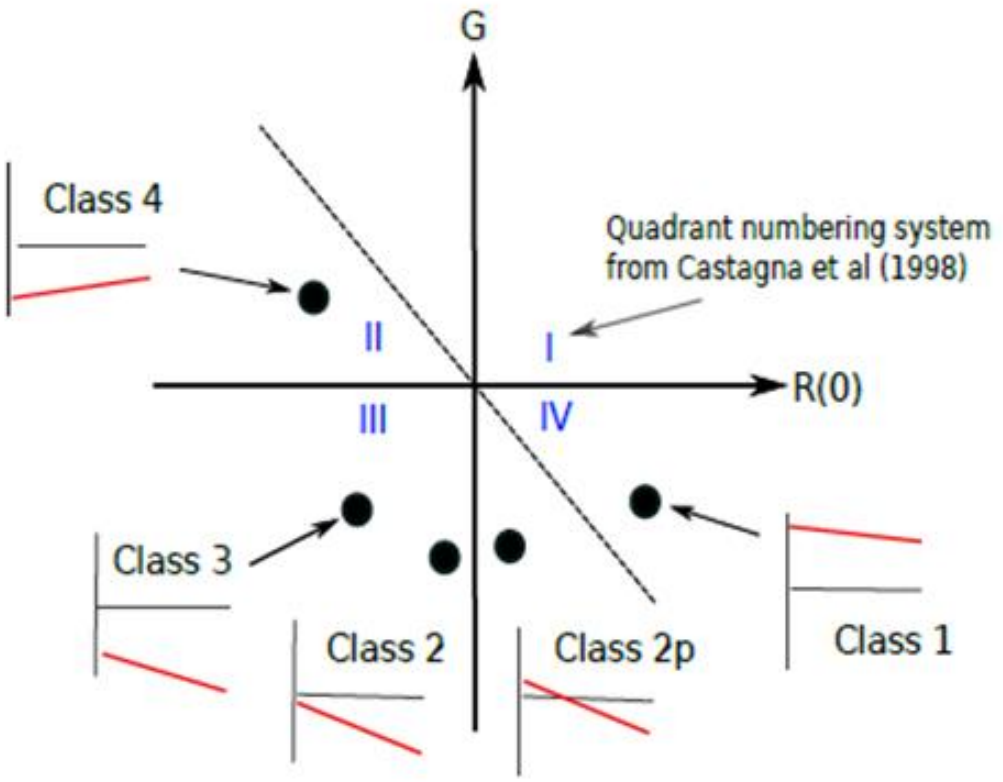

Figure 3.16: *Intercept-gradient cross-plot with location of the AVO classes from Figure 3.15. Modifed from Gatemann (2016).*

To be able to interpret the AVO responses and intercept-gradient cross plot the link between the geophysical domain and the geological domain must be understood. Such links are based on modelling, interpretation of real data case and experience. One simplified interpretation is shown in Table 3.1. Here the AVO classes are linked to likely combinations of reservoir, cap rock and pore fluid. Other combinations can also explain similar anomalies. Another and much used link between the two domains is show in Figure 3.17 (Ødegaard and Avseth, 2004). In this elastic rock properties cross plot the P-wave/S-wave ratio is combined with the P-impedance. Now the AVO classes can be displayed in both domains and a geological interpretation is made easier.

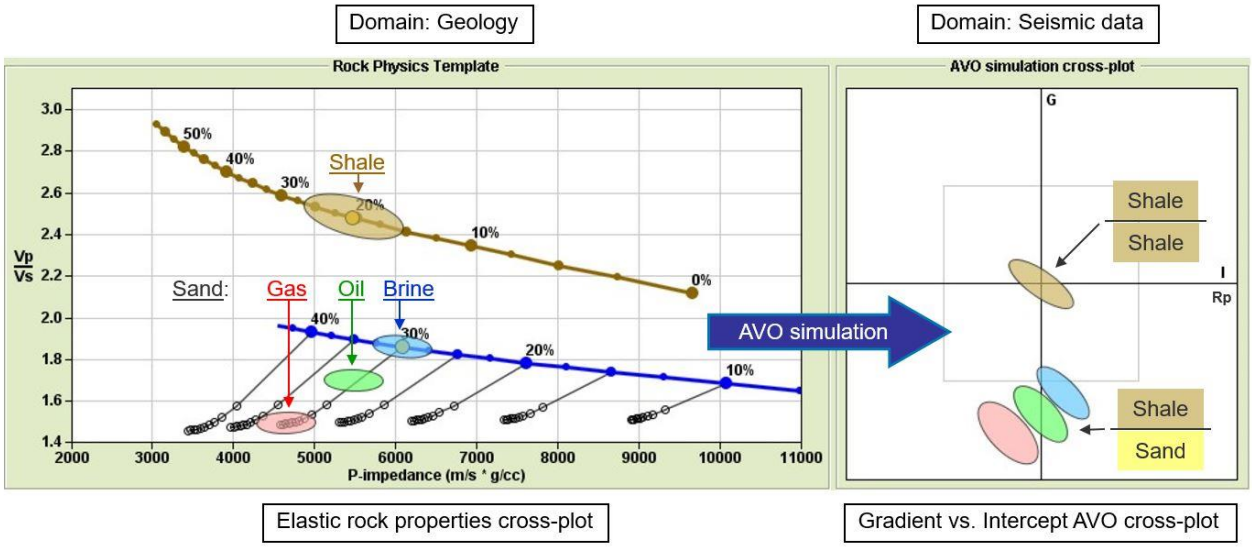

Figure 3.17: *Relationship between rock physics- and the seismic domain showing classification of fluids and lithologies. The rock physics template (left) shows elastic rock properties with P-wave/S-wave ratio combined with the P-impedance. To the right a simulated AVO cross plot with intercept and gradient from the seismic is shown. Figure modified from Ødegaard and Avseth (2004).*

Using AVO data for identification of lithology and fluid responses is not straightforward. In practice, different workflows and plots can be used. In this study we have used a workflow shown in Figure 3.18. The original stack data was subdivided into three different stacks; the near, mid and far stack. Typically, the near stack consists of angles of incidence from approximately 0-10º, the mid stack from 10-20º and the far stack from 20-30º. These angles are not absolute and some variation can occur, due to local conditions. The details for our case are described below. The near stack represents approximately the zero-offset reflection (R0), or intercept, while the gradient (G) describes the slope of the AVO trend at far/intermediate offset. To find the gradient the near and the far stack were combined.

In our work flow the mid stack does not give any additional information, and was not included in the calculations. The gradient (G) was calculated in the following way (Shuey, 1985) and is shown in Figure 3.18a:

$$R(\theta) = R(0) + G\sin^2\theta \qquad (3.6)$$

We then use the assumptions that R(0) ≈ near stack and θ = 30º in the following equation:

$$F = \text{Near Stack} + \text{G} * 0.25 \qquad (3.7)$$

And solve G for:

$$G = \frac{\text{F}-\text{Near Stack}}{0.25} \tag{3.8}$$

The information from the three stacks is plotted in the intercept-gradient cross plot in Figure 3.18b. Now, each small coloured square represents a specific position in TWT (ms). To be able to interpret the cross plot, typical lithology and fluid responses are included as coloured ellipsis in the figure. These are the same ellipses illustrated in the conceptual Figure 3.17. In practice, the different classes are overlapping in the intercept-gradient domain and in the interpretation local conditions of the study area must be taken into account.

Based on the interpretation of the intercept-gradient cross plot the section in Figure 3.18c was created. The principle is that the area covered by coloured ellipses is represented in the seismic section and is resulting in a simplified seismic AVO plot view. This process highlight the areas of interest from the cross plot and simplify the interpretation of the AVO data. For details of interpretations see Chapter 4.6.

Calculations and generation of plots and figures were done using the Hampson-Russell software (CGG).

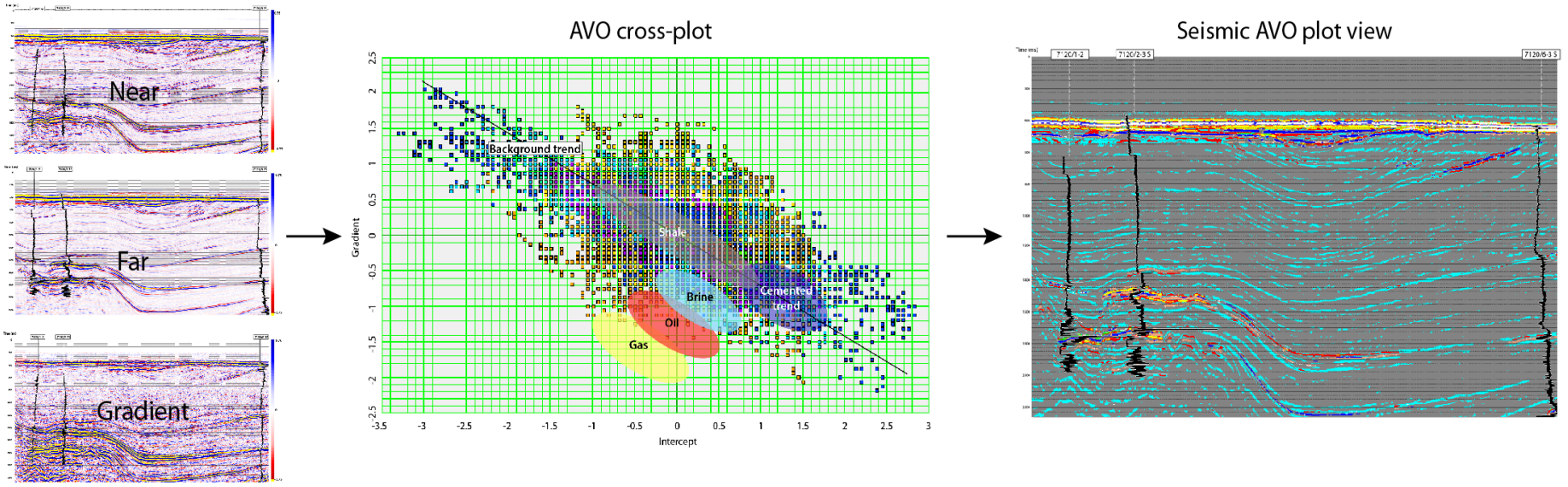
Near
Far
Gradient
AVO cross-plot
Background trend
Shale
Brine
Oil
Gas
Cemented trend
Gradient
Intercept
Seismic AVO plot view
a)
b)
c)

Figure 3.18: *AVO workflow for identification of lithology and fluid responses. a) Original near angle stack-, far angle stack- and gradient data. b) AVO cross plot with intercept (near stack) and gradient. c) Interpretation of the AVO cross plot in a seismic section. See text for more detailed explanations of figures.*

3.7.2 AVO modelling

In the interpretation real AVO responses from seismic data was compared to modelled AVO responses. These modelled AVO responses were obtained using the sandstone modelling approach honoring burial history including net erosion (Chapter 3.4). The AVO modelling is based on rock physics modelling of the sandstone reservoirs of interest.

The mechanical and chemical compaction is modelled as a function of burial history as explained in Chapter 3.4. Based on the modelled porosity and cement volume for sandstones and the porosity for shales, modelling of rock-physics and seismic properties can be done with different fluid types. The rock-physics modelling is necessary as it will be used as input for modelling of seismic AVO signatures. The link between rock physics and the seismic domain is shown in Figure 3.17.

The friable-sand model (Dvorkin and Nur, 1996) and the Hertz-Mindlin (Mindlin, 1949) contact theory is used for the mechanical compaction domain and describes the effect of sorting on the porosity-velocity relation for unconsolidated sandstones. The contact-cement model (Dvorkin et al., 1994) is used for cemented sandstones in the chemical domain.

The rock-physics properties for shales are also modelled using the Hertz-Mindlin contact theory, both for smectite and illite shales (Avseth and Lehocki, 2016). The mechanically compacted porosity for shales is not reversible. But the effective pressure is, and thus the velocities will decrease slightly during uplift when the porosities stay constant. The Gassmann fluid substitution equation (Gassmann, 1951) was used combined with the contact-cement model. The modelled sandstones are assumed to have 5 % clay.

Figure 3.19 shows burial curves for a sandstone case saturated with brine and gas. The figure also shows the burial curve for the shale above the reservoir and the corresponding velocities, impedance and V_p/V_s-ratio for both the shale and the sandstone.

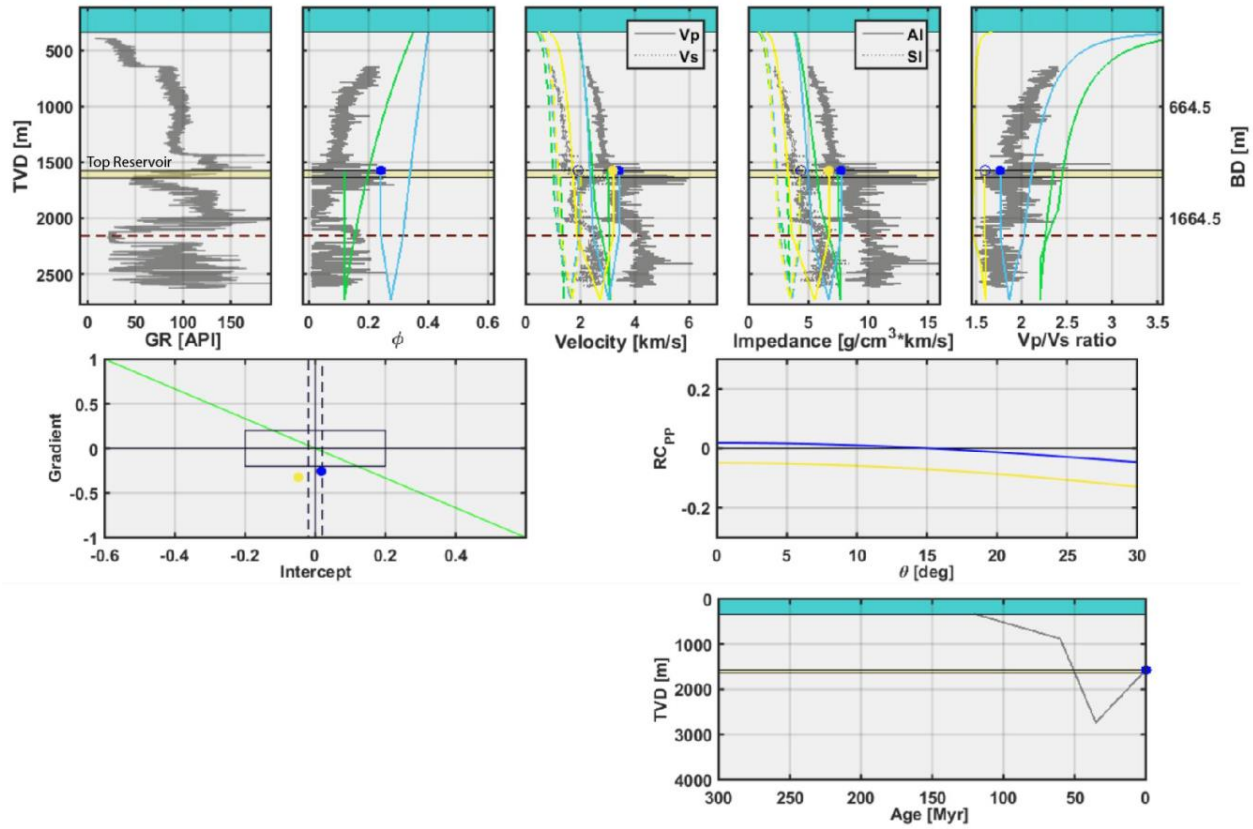

Figure 3.19: *AVO modelling constrained by burial history. The modelling is done in three steps. 1) Modelling of mechanical and chemical compaction of shales and sandstones as a function of burial history (lower right figure). 2) Based on step one rock physics and seismic properties are modelled. This modelling incudes both a HC- and a brine case. 3) Based on the rock physics modelling AVO responses are modelled (Avseth and Veggeland, 2015). The sandstone trends should fit top reservoir, while the shale trend should fit the base of the shale interval. The green line represents the shale trend, while the blue- and yellow lines represent brine sand (100 %) and gas sand (100 %) cases respectively. The dashed red line is 70ºC. The AVO responses are shown in the intercept versus gradient cross plot and the amplitude (RC_{pp}) versus angle plot.*

From rock physics based AVO modelling of a sandstone reservoir interbedded in shales the expected AVO signature can be obtained. Net erosion estimates are included when simulating the expected AVO signatures. This gives a more realistic comparison between the modelled and real AVO responses. The AVO modelling is based on the rock physics modelling of the actual sandstone reservoirs, and the rock properties from the rock physics modelling are input to the AVO estimation. To model the AVO response a simplification of the Zoeppritz equation as described by Shuey (1985) was assumed.

A half-space modelling approach was used in the AVO modelling for the sandstone reservoir located beneath an overburden shale as described in Gatemann (2016). The shale properties of the overburden are based on an empirical shale trend from the North Sea. In the modelling the shale trend (green) was adjusted to fit the observed properties of the cap-rock shale unit, while the sandstone trend was adjusted to fit the top reservoir (Figure 3.19). The AVO signatures can be modelled for different fluid saturations (oil, gas and brine), and in this study we have assumed uniform saturations in the reservoirs. Fluid substitution was done using the Gassmann's equation (Gassmann, 1951). The fluid properties are calculated using (Batzle and Wang, 1992) formulas. The rock physics based AVO modelled responses are shown in Figure 3.19. The intercept versus gradient cross plot and the amplitude (RC_{pp}) versus angle plot show the modelled effect of the fluid substitution.

Chapter 4 - Results

In this chapter results from the different methods for estimation of net erosion are summarized. Results from seismic interpretation and seismic AVO interpretation are also shown.

4.1 Net erosion estimates from p-wave velocity using shales

Net erosion was calculated for the well data set using the methodology explained in Chapter 3.1. Here the net erosion estimates will be displayed in terms of single well results and maps. This gives an overview of the distribution and magnitude of the net erosion occurring in the south western Barents Sea.

Figure 3.4 shows the P-wave versus depth reference trend established in this study. The linear velocity-depth relationship is expressed with the following equation:

$$V_p = 0.55z + 1576 \qquad (4.1)$$

The net erosion results obtained using this depth-velocity reference trend line, are shown in Figure 4.1 and Figure 4.2. A clear trend in net erosion estimates is observed in the data set, with larger net erosion in the northern- and north eastern parts of the Barents Sea compared to the southern and western parts. The bulk of the estimates are between 1000 and 1500 meters. In the north east net erosion is almost 2000 meters, while in the west it is close to zero.

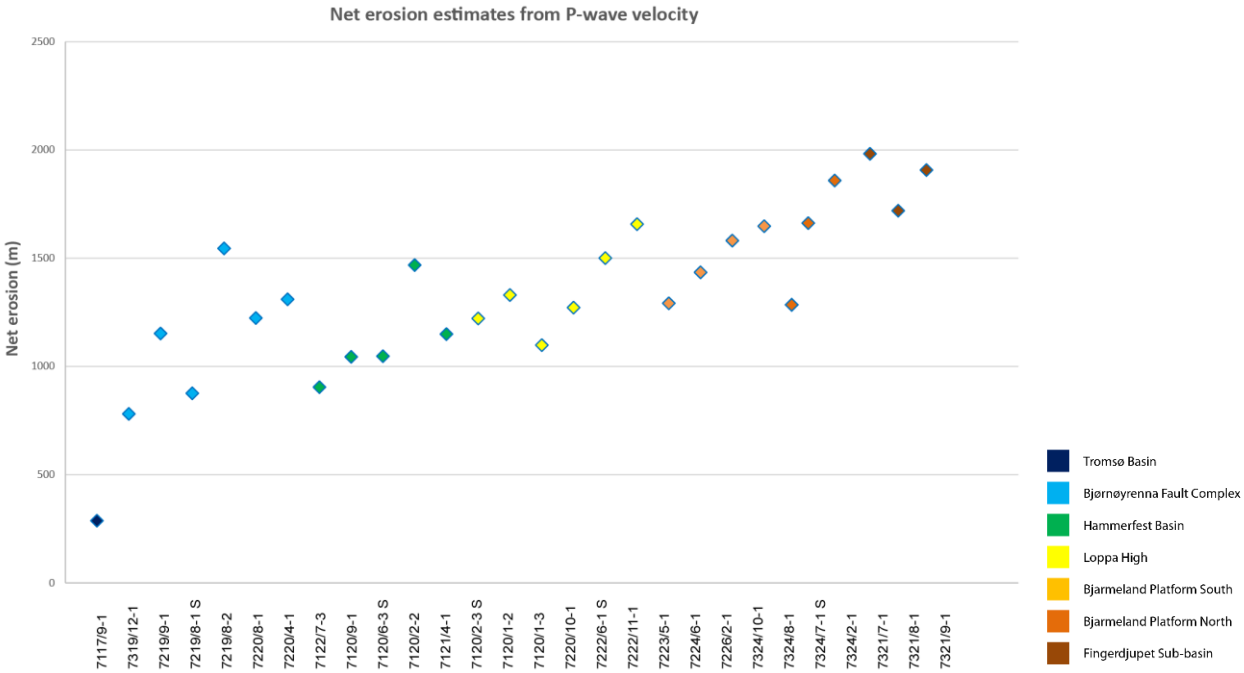

Figure 4.1: *Net erosion estimates from Barents Sea wells showing an increasing trend with increasing well number towards the north and north east. Results are divided into sub basins showing varying net erosion. See Figure 4.2 for location of wells.*

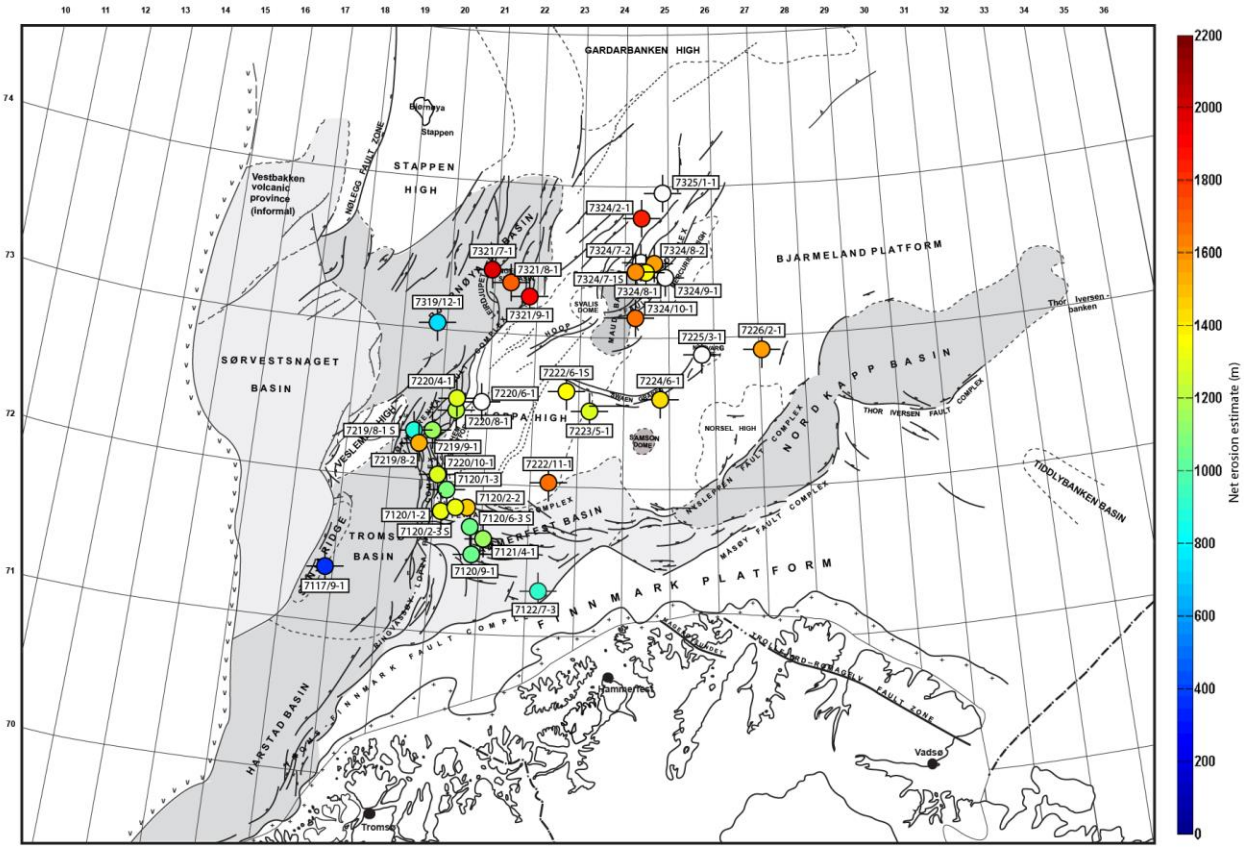

Figure 4.2: *Location of net erosion estimates from Barents Sea wells show an increasing trend towards the north and north east and partial correlation with individual structural elements. Modified from Faleide et al. (2010).*

As explained above the established reference trend was compared to the actual well log, and net erosion was estimated for each well in the data base. Examples of the results from individual wells are shown in Figure 4.3. These are results from edited well logs choosing only the cleanest shales possible in the Kolmule- or Torsk Formations. Shale regression lines were established for each velocity log as shown in the figure.

The Arenaria well (Figure 4.3a) gives a regression line approximately parallel to the reference trend, and the Kolmule interval is of sufficient thickness to give credibility to the result. A parallel line to the reference trend can indicate comparable temperature gradients in the two areas.

The Obesum well (Figure 4.3b) have a regression line that is not parallel to the reference trend. This can be caused by the thin Kolmule interval which makes it difficult to create a reliable regression trend line.

For the Skalle well (Figure 4.3c) the Torsk Formation was used because the Kolmule interval has high velocities in the lower sandy parts of the unit. The regression line is also in this case parallel to the reference trend.

Well 7120/2-2 located east of the Skalle well (Figure 4.3d) also have internal and varying trends in the Kolmule interval. In this case the upper part of the Kolmule unit was used in the calculations due to its higher clay content.

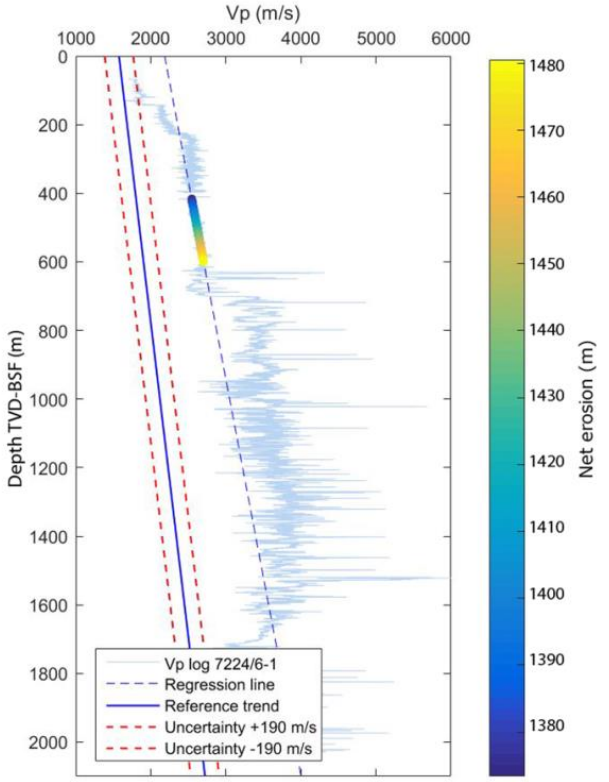
Vp (m/s)
Depth TVD-BSF (m)
Net erosion (m)
Vp log 7224/6-1
Regression line
Reference trend
Uncertainty +190 m/s
Uncertainty -190 m/s

a)

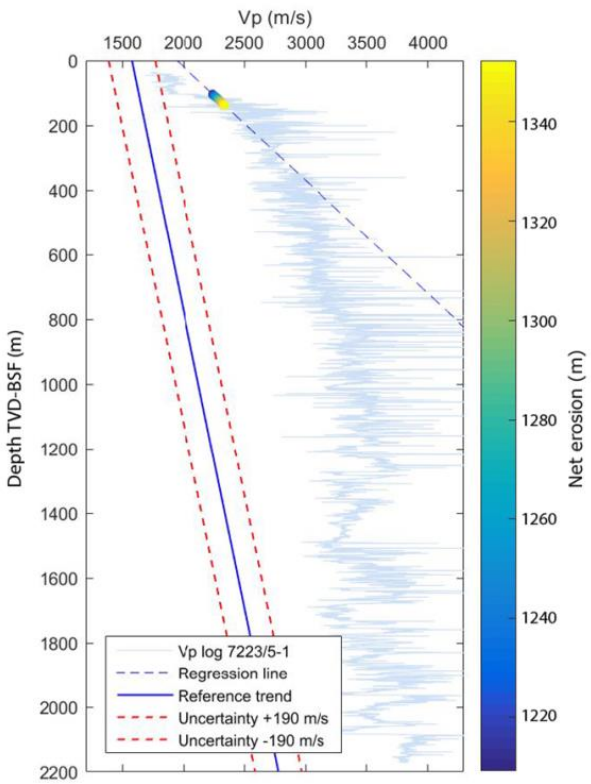
Vp (m/s)
Depth TVD-BSF (m)
Net erosion (m)
Vp log 7223/5-1
Regression line
Reference trend
Uncertainty +190 m/s
Uncertainty -190 m/s

b)

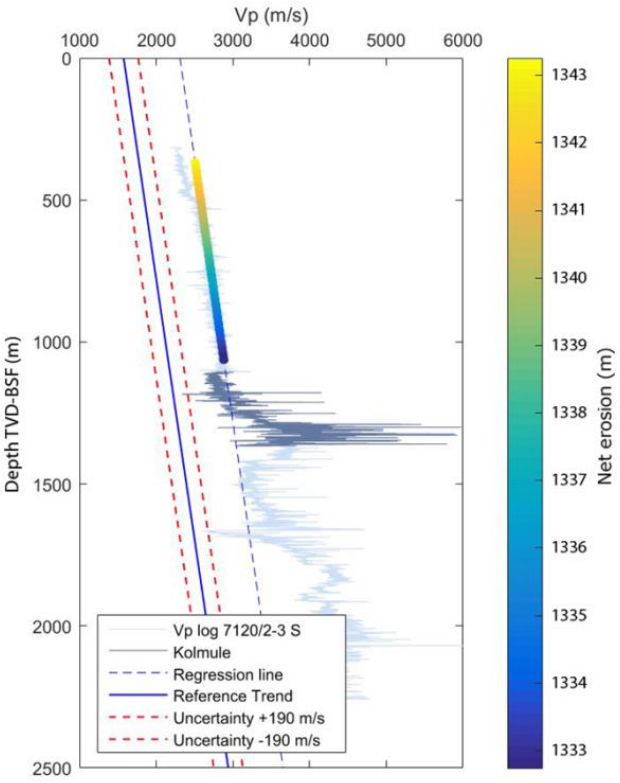
Vp (m/s)
Depth TVD-BSF (m)
Net erosion (m)
Vp log 7120/2-3 S
Kolmule
Regression line
Reference Trend
Uncertainty +190 m/s
Uncertainty -190 m/s

c)

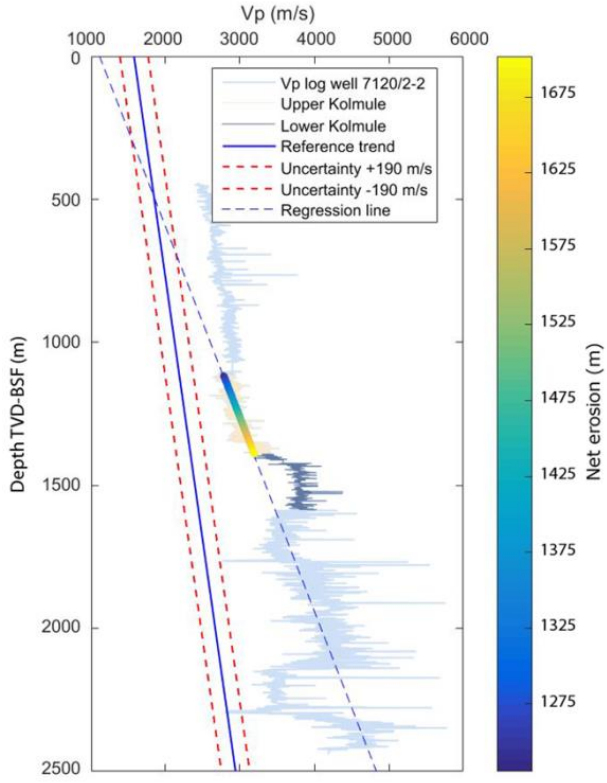
Vp (m/s)
Depth TVD-BSF (m)
Net erosion (m)
Vp log well 7120/2-2
Upper Kolmule
Lower Kolmule
Reference trend
Uncertainty +190 m/s
Uncertainty -190 m/s
Regression line

d)

Figure 4.3: *Examples of net erosion estimates from four well bores in the Barents Sea. Locations are shown in Figure 4.2. The thickness of the used interval and the trend line is highlighted by the coloured thick line on the log itself. a) Arenaria well (7224/6-1), the Kolmule interval was used. b) Obesum Appraisal well (7223/5-1), the Kolmule interval was used. c). Skalle well (7120/2-3 S), the Torsk unit was used. d) Well 7120/2-2 located east of the Skalle well, the upper part of the Kolmule unit was used. Internal trends in the formations are highlighted by the darker colour and show why this part of the log were not used.*

In general the Kolmule interval has high clay content, is wide spread in the Barents Sea and is thick enough for estimation of net erosion. But in cases like the examples above, errors can be introduced if the well logs are not carefully evaluated. This will be discussed further in Chapter 5.

To enhance the value of the net erosion calculations the results are used to create trend maps. Figure 4.4 illustrates the increasing net erosion trend towards the north as summarized in Figure 4.1 and Figure 4.2. Although there is some variation, the amount of net erosion also seems to be linked to the individual structural elements. The net erosion map was created using the Petrel software (Schlumberger, 2015). The trend map was slightly modified to remove unrealistic local variations. This was done by removing outliers in the dataset.

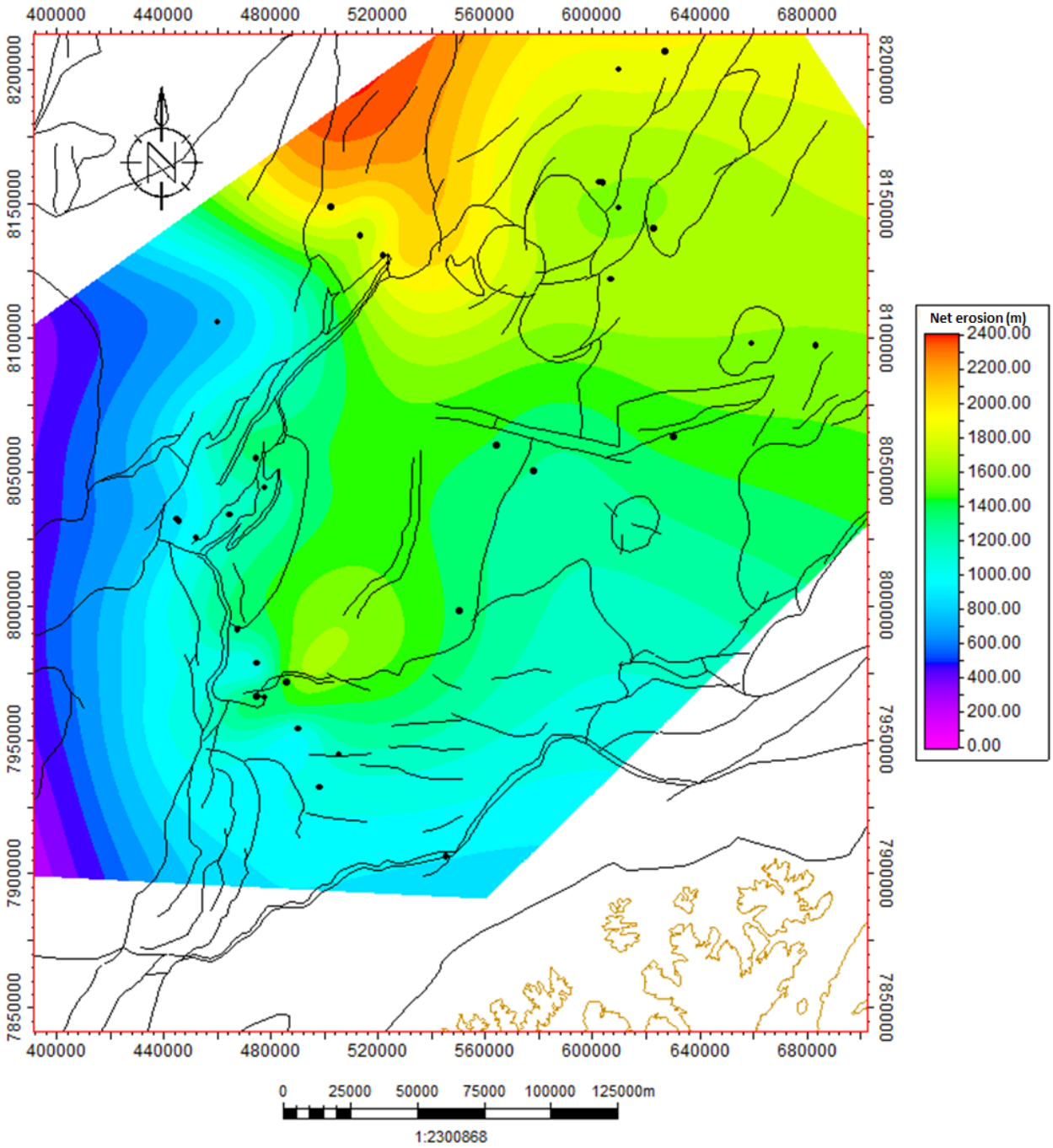

Figure 4.4: *Net erosion map generated from velocity well log data. The estimates show an increasing trend towards the north and north east ranging from approximately 200 meters in the far west to around 2200 meters in the north. Structural elements are modified from Faleide et al. (2010).*

4.2 Net erosion estimates from well log resistivity data

As for the velocity estimates net erosion was also calculated using well log resistivity data. The reference resistivity compaction trend line from the North Sea (Figure 3.9) is given by the following formula:

$$r = 0.03 + 6.6e^{-4}z \qquad (4.2)$$

Using the same method as for velocity the net erosion was calculated using this reference trend established in Chapter 3. Using this method for estimation of net erosion is not previously tested in the Barents Sea. The results from individual well bores are shown in

Figure 4.5. The same general trend as for the velocity based estimation is observed here with increasing net erosion towards north and north east. The difference is that the estimated net erosion is systematically much larger than for estimations based on P-wave velocity. When comparing the results from the two different methods, we see that also the difference in net erosion results from velocity and resistivity increases towards the east and north east.

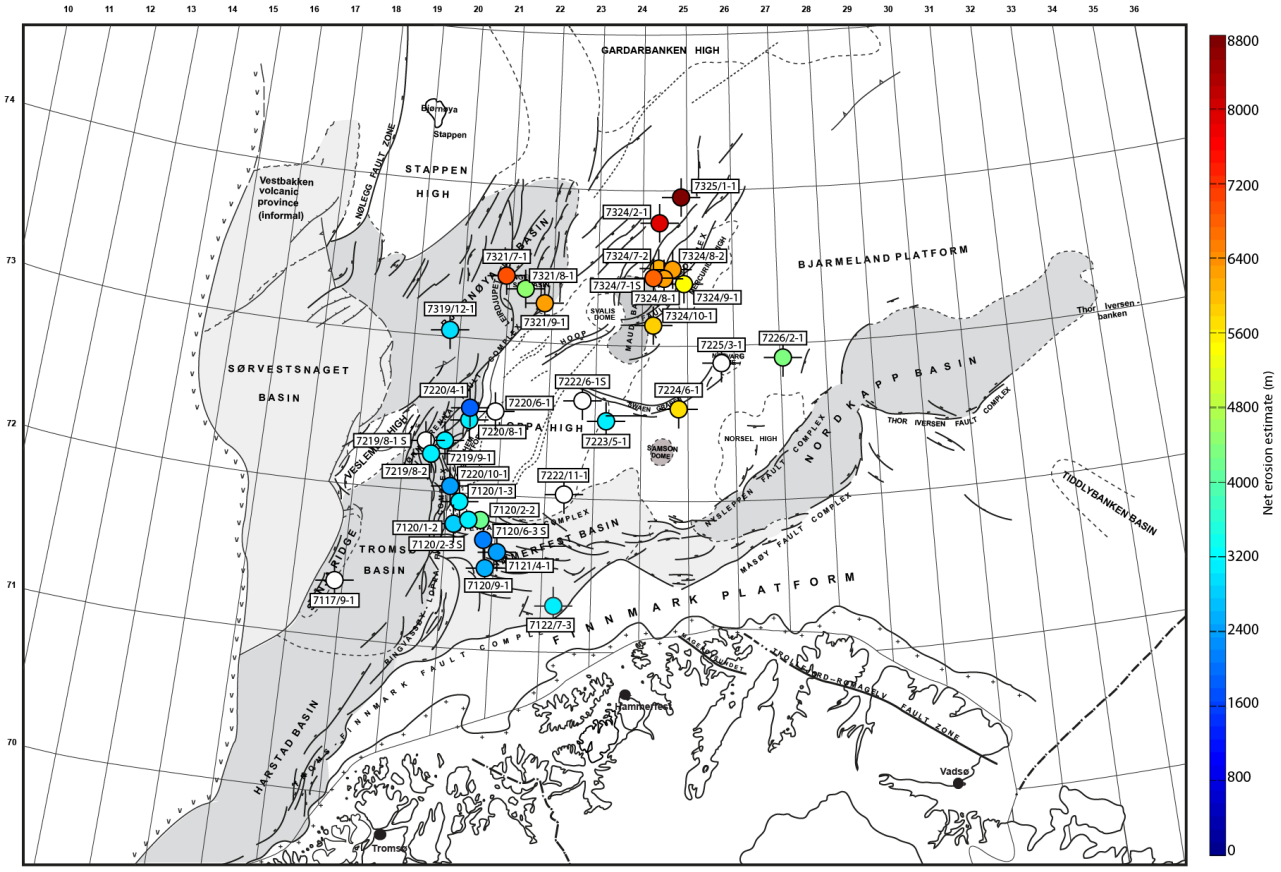

Figure 4.5: *Net erosion estimates from resistivity well log data in the western Barents Sea. The same increasing trend in estimates can be seen here as for the velocity data, but the net erosion calculations from resistivity data are much larger than the estimates from velocity data. Structural elements are modified from Faleide et al. (2010).*

In Figure 4.6 net erosion estimates are shown for two specific Barents Sea wells. The Kolmule interval does not always give good velocity-depth trends, and in some cases the regression line through the Kolmule interval is even negative. Therefore, an average value for the interval was calculated for the uplifted formations. This is further discussed in Chapter 5. It is quite obvious that the resistivity estimates give too large numbers. It is very unlikely that net erosion is more than 6000 meters in the north eastern areas (Figure 4.5), but it seems to be a systematic connection between the two results. Figure 4.7 shows net erosion estimated from velocity data divided by net erosion estimated from resistivity data. The coefficient representing this relationship is decreasing towards the north, which means that the difference between the resistivity estimates and the velocity estimates is increasing in this direction.

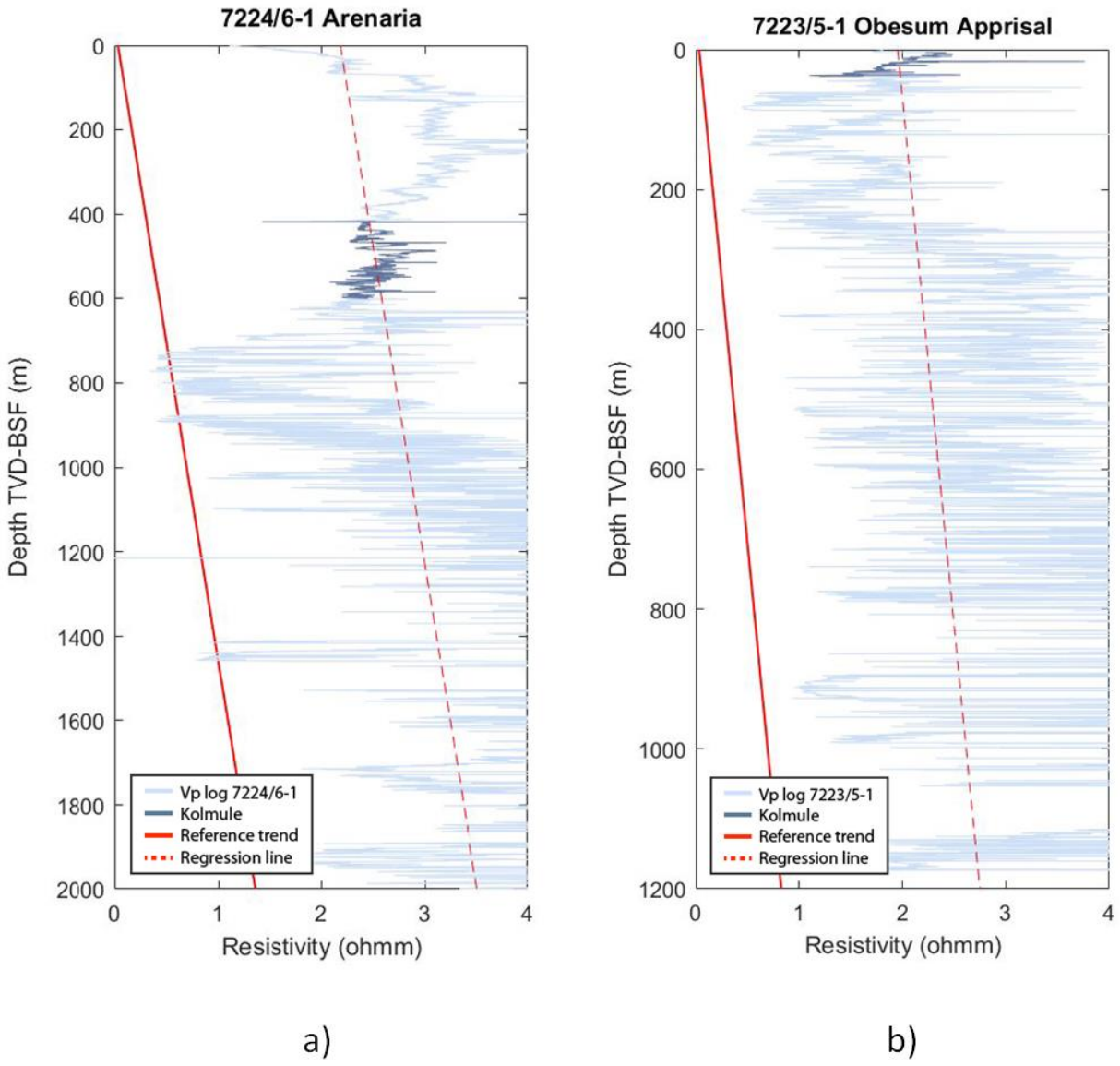

Figure 4.6: *Examples of net erosion estimates from two Barents Sea wells. a) The Arenaria (7224/6-1) well have a Kolmule interval of sufficient length, but the trend in the resistivity data within the interval is varying and slightly negative. Therefore the average value of the resistivity interval was used to do the calculations. b) The Obseum Appraisal (7223/5-1) well has a short Kolmule interval with large variation in resistivity and the average value has also here been used when estimating the net erosion. Internal trends in the formations are highlighted by darker colour. See Figure 4.5 for location of wells.*

Figure 4.8 shows the depth to the middle of the shale unit, either the Kolmule- or Torsk Formations. The depth to the shale units is decreasing towards the north. This means that the difference between the velocity and the resistivity estimates increase with decreasing depth to the actual shale formation.

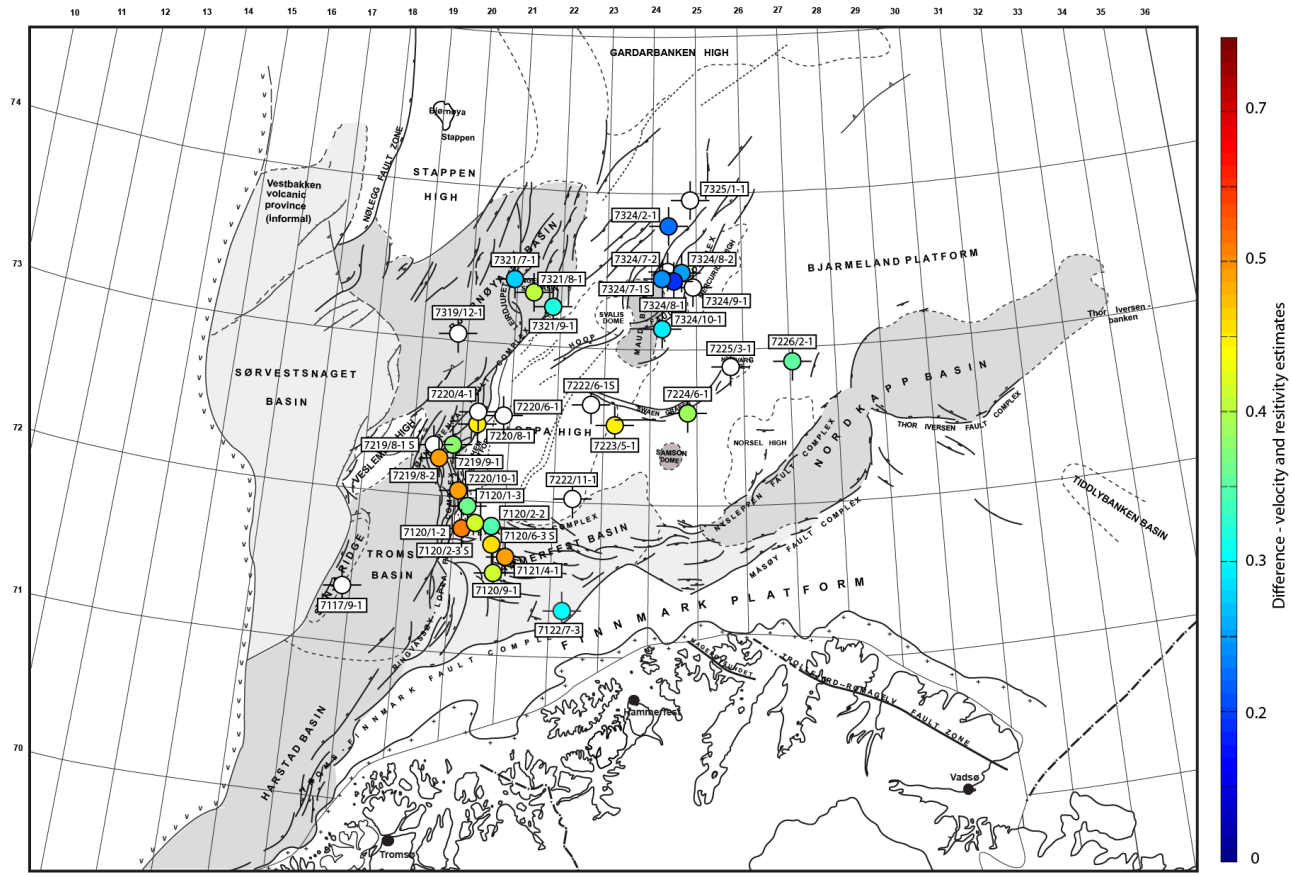

Figure 4.7: *Difference between net erosion estimates from velocity- and resistivity data plotted in every well position. The difference illustrated by using the relationship Vp-estimate/Rh-estimate is decreasing towards the north and north east. Structural elements are modified from Faleide et al. (2010).*

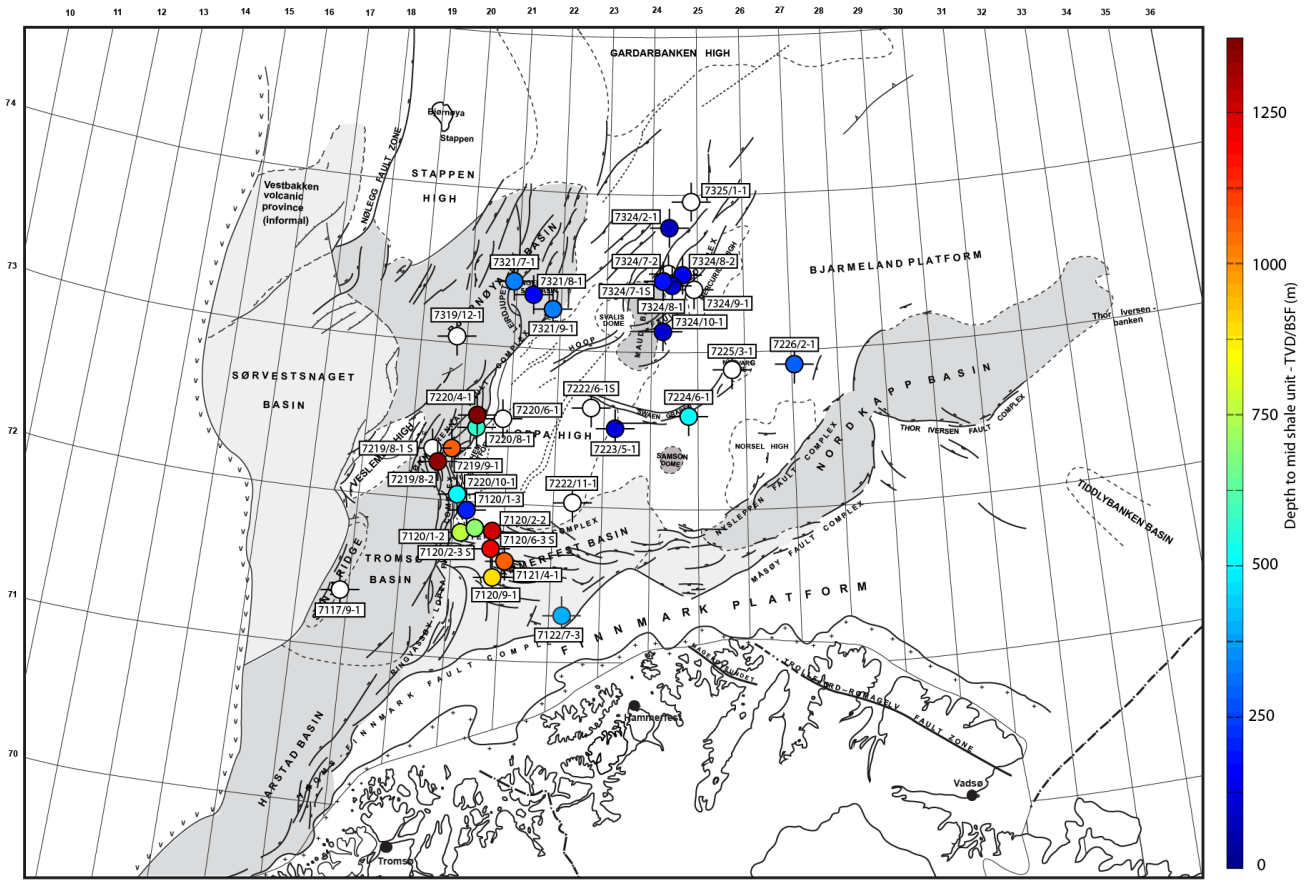

Figure 4.8: *Depth to the formation used for estimation of net erosion. The depth is here the distance from the seabed to the middle of the shale unit, in these cases the Kolmule- and Torsk Formation, The depth is decreasing towards the north and north east. Structural elements are modified from Faleide et al. (2010).*

These results will be discussed in more detail in the discussion chapter.

4.3 Net erosion estimates using sandstone

4.3.1 Empirical depth trends – North Sea

Also when attempting to use sandstones instead of shales in estimating the net erosion in the Barents Sea, the first approach was to establish an empirical reference trends from the North Sea.

The velocity-depth relationship (Figure 3.11a) established based on the Marcussen et al. (2009) data set is given by the following equation:

$$V_p = 1741.5 + 0.55z \quad (4.3)$$

The reference resistivity-depth trend established for the Etive sandstone (Figure 3.11b) is given by the following equation:

$$r = -1.2 + 8.9e^{-4}z \quad (4.4)$$

The results from using these reference trends for five different Barents Sea wells are shown in Figure 4.9. Some of the sandstone velocity estimates are similar to the ones from the shale estimation, but the variation is too large. The resistivity results on the other hand have even larger variations, and have values ranging from almost zero to 3000 meters. The data seems inconsistent, and are not easily incorporated with the other net erosion estimates in the Barents Sea. These results will be compared to the other results in more detail, and further discussed in Chapter 5.

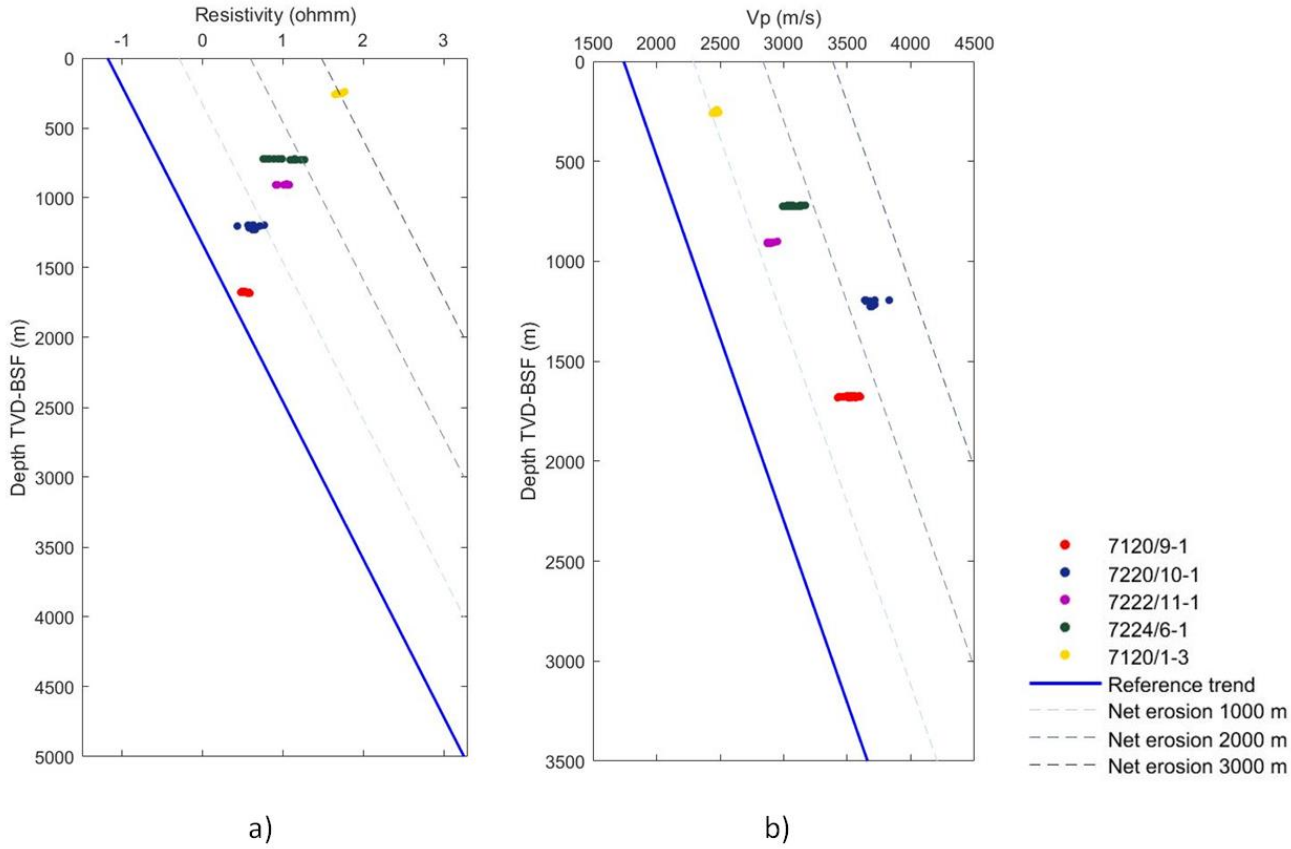

Figure 4.9: *a) Resistivity depth trend for sandstone with selected wells from the Barents Sea showing varying net erosion estimates. b) Velocity depth trend for sandstone with selected wells from the Barents Sea. These results are more consistent than the resistivity estimations, but the values are differing from the net erosion calculations from shales shown in Figure 4.2.*

4.3.2 Sandstone diagenesis and burial history modelling

As explained in Chapter 3, cement volumes and porosity loss related to mechanical and chemical compaction was calculated using diagenetic modelling. The results from this modelling were input parameters to rock physics modelling for estimation of corresponding velocities as a function of burial history. Net erosion estimates was then obtained by comparing observed and modelled velocities. The net erosion results using this modelled approach are shown in Figure 4.10 and Figure 4.11.

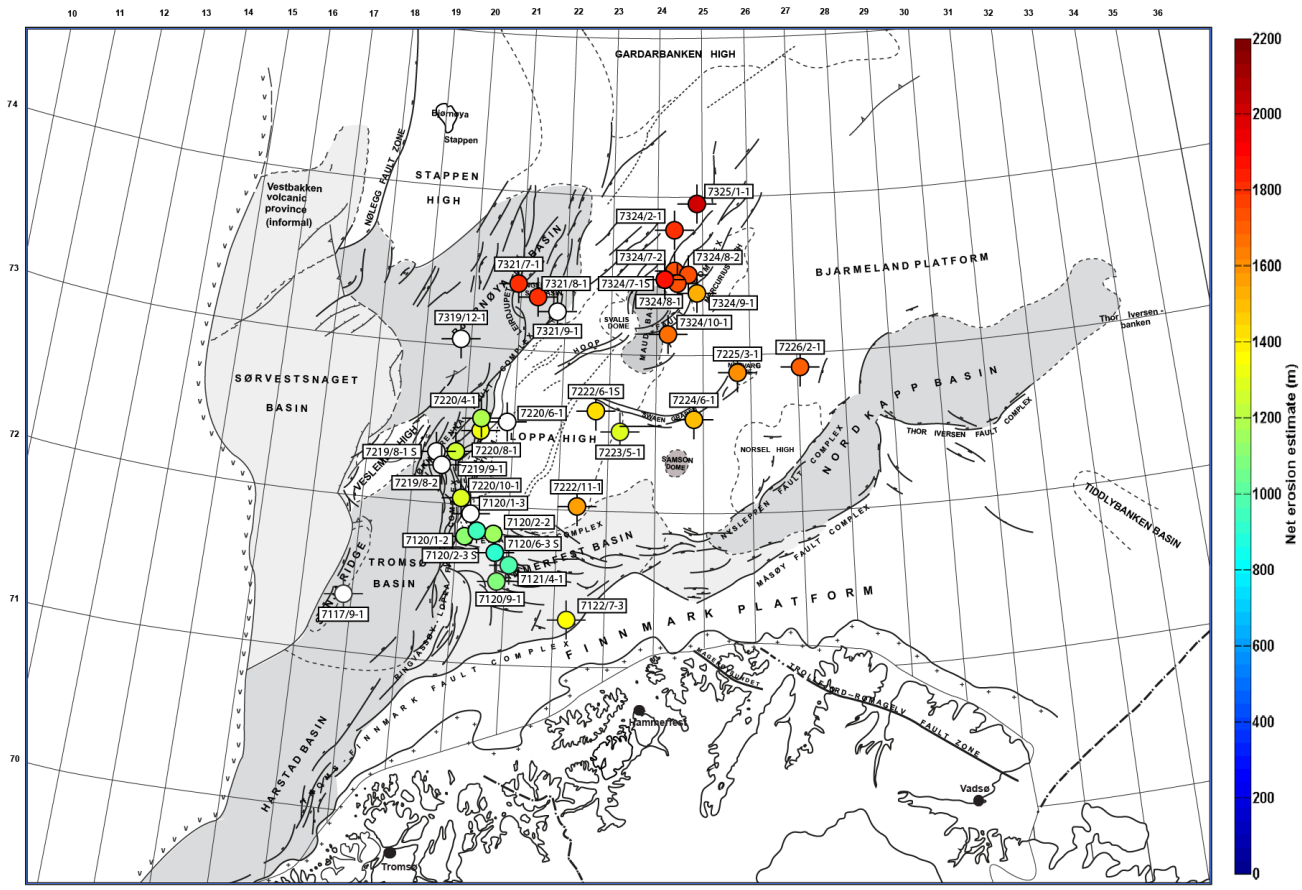

Figure 4.10: *Locations of net erosion estimates from sandstone modelling show an increasing trend towards the north and north east and partial correlation with individual structural elements, similar to the shale estimates in Figure 4.2, modified from Faleide et al. (2010).*

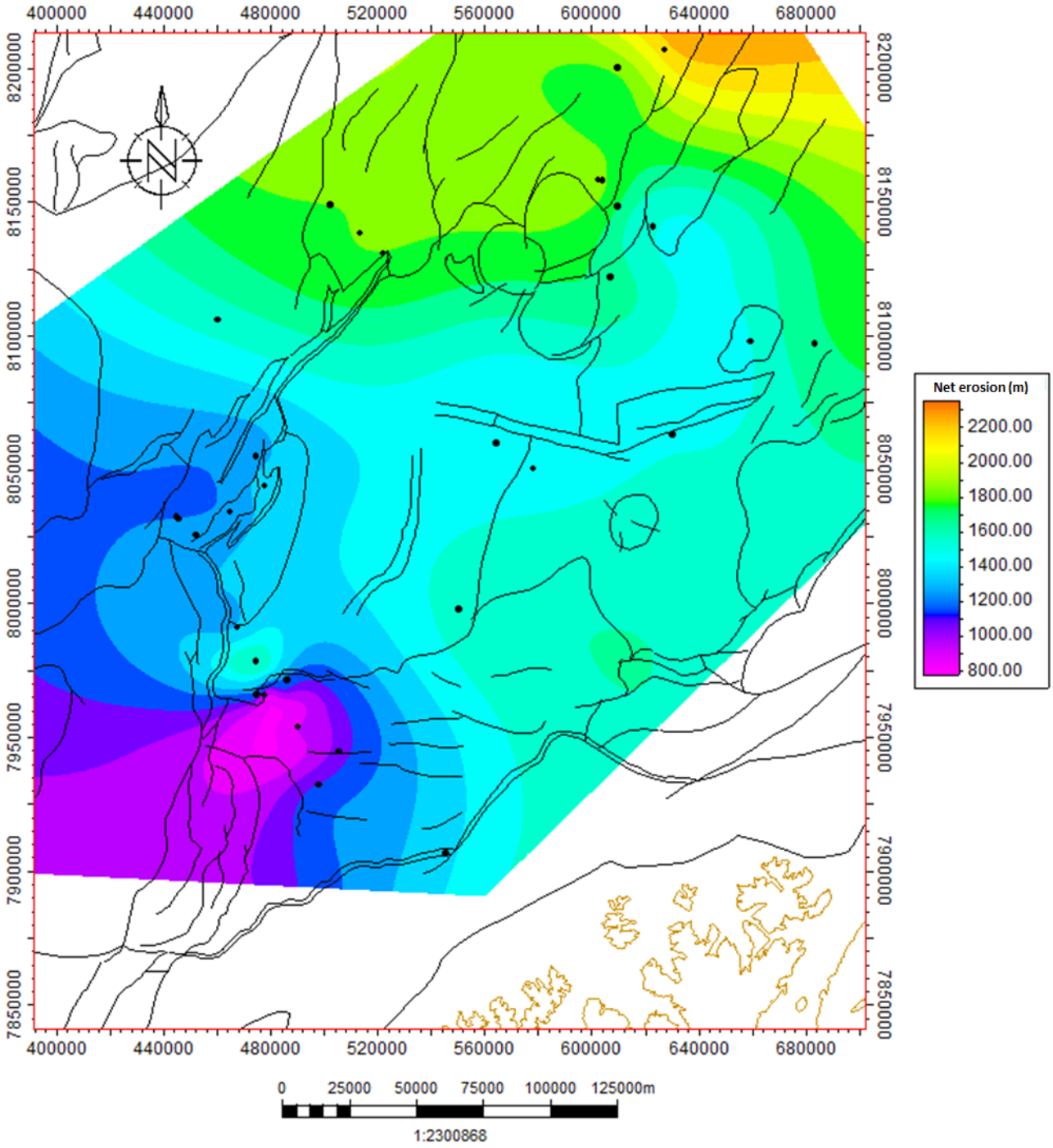

Figure 4.11: *Net erosion map generated from the sandstone modelling results. The estimates show an increasing trend towards the north and north east. This trend is similar to the increasing trend shown in the map in Figure 4.4. The estimates are ranging from about 800 meters, compared to 200 meters in Figure 4.4, to around 2000-2200 m in the north. The difference in the west is due to missing data in this area. Structural elements are modified from Faleide et al. (2010).*

Although these estimates were mainly done for the Jurassic Stø sandstone formation, the results should theoretically coincide with the other estimates since the uplift postdates the time of deposition of the formations. This is most likely also the case for the Torsk Formation, but since the detailed timing of the uplift (Faleide et al., 2010) is uncertain some overlap could occur. This could be a possible explanation if net erosion estimates based on the Torsk Formation differ significantly from estimation based on the Kolmule Formation.

Similar net erosion trends can be seen as for the uplift estimates based on shale trends. In the north east three new net erosion estimates were done to compliment the shale based net erosion estimates. The trend with increasing net erosion in this direction is confirmed. The estimates in the Hammerfest Basin are slightly lower, but the general picture is the same as for the shale trend estimates.

As part of the modelling, cement volume was also calculated for the wells. The volumes vary, mostly depending on maximum burial depths. But it is also dependent on the amount of time the sandstones has been below 70ºC, the grain size of the sand and the temperature gradient of the area. Varying burial curves will thus alter the calculated cement volume.

Of the modelled wells, four representative examples are presented in Figure 4.12. The wells were chosen to represent different areas with different amount of uplift and erosion. The Stø reservoir in the Snøhvit well (7120/9-1) located in the Hammerfest Basin has high porosity and low clay content. This well has good modelling match for both porosity and velocity. A net erosion of 1100 meters was calculated from the sandstone modelling, compared to 1044 meters from the shale trend estimation.

The Kramsnø well (7220/4-1) in the Bjørnøya Basin also show good fits in porosity and velocity. The net erosion estimates for sandstone is 1170 meters compared to a shale estimate of 1323 meters.

The Arenaria well (7224/6-1) is located on the Bjarmeland Platform and was also selected as a good example because of high porosity and low clay content in the studied reservoir zone. The sandstone interval for this well is the Tubåen Formation. The modelled response fits both the velocity and the porosity very well.

Moving further north, the Alpha well (7324/10-1) also shows good modelling match for both velocity and porosity. These two wells on the Bjarmeland platform also have similar results from the sandstone and the shale methods.

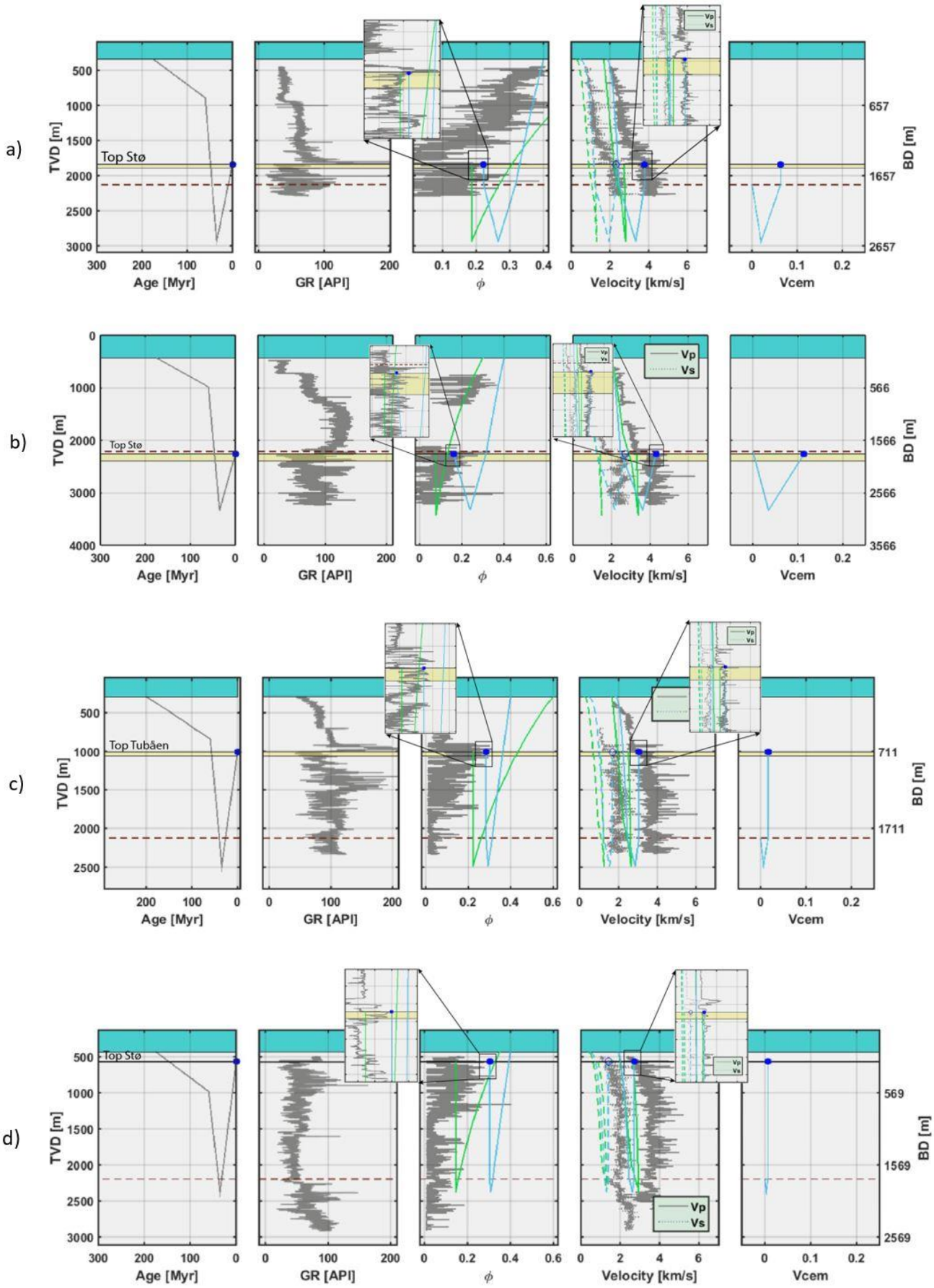
a)
b)
c)
d)
TVD [m]
BD [m]
Top Stø
Top Tubåen
Age [Myr]
GR [API]
ϕ
Velocity [km/s]
Vcem
Vp
Vs

Figure 4.12: *Sandstone modelling results for selected wells from different areas in the western Barents Sea. a) Snøhvit (7120/9-1), b) Kramsnø (7220/4-1), c) Arenaria (7224/6-1) and d) Alpha (7324/10-1). See text for more details on the individual wells. Locations of the wells are shown in Figure 4.10.*

When a Stø reservoir interval with good reservoir quality was absent in the well, other reservoir sand intervals were used, like the Tubåen Formation mentioned above. In the Juksa- (7120/6-3 S) and Skalle (7120/6-2 S) wells on the south western Loppa High, the Kolmule sandstone was used in the modelling. This will be addressed further in the AVO section, where the net erosion estimates are used in AVO modelling.

The estimation of net erosion from sandstone modelling will be compared with the shale estimates and discussed further in Chapter 5.

4.4 Seismic interval velocities – net erosion maps

By using seismic interval velocities as explained in Chapter 3.5, maps showing net erosion distribution were created (Figure 4.13 to Figure 4.15). Compared to the trend maps the spatial resolution is significantly improved. The generated net erosion maps are extracted from the net erosion cube (Figure 4.16) made from the seismic interval velocities. The top Kolmule and BCU Horizons are used as reference horizons when the net erosion values are extracted from the cube.

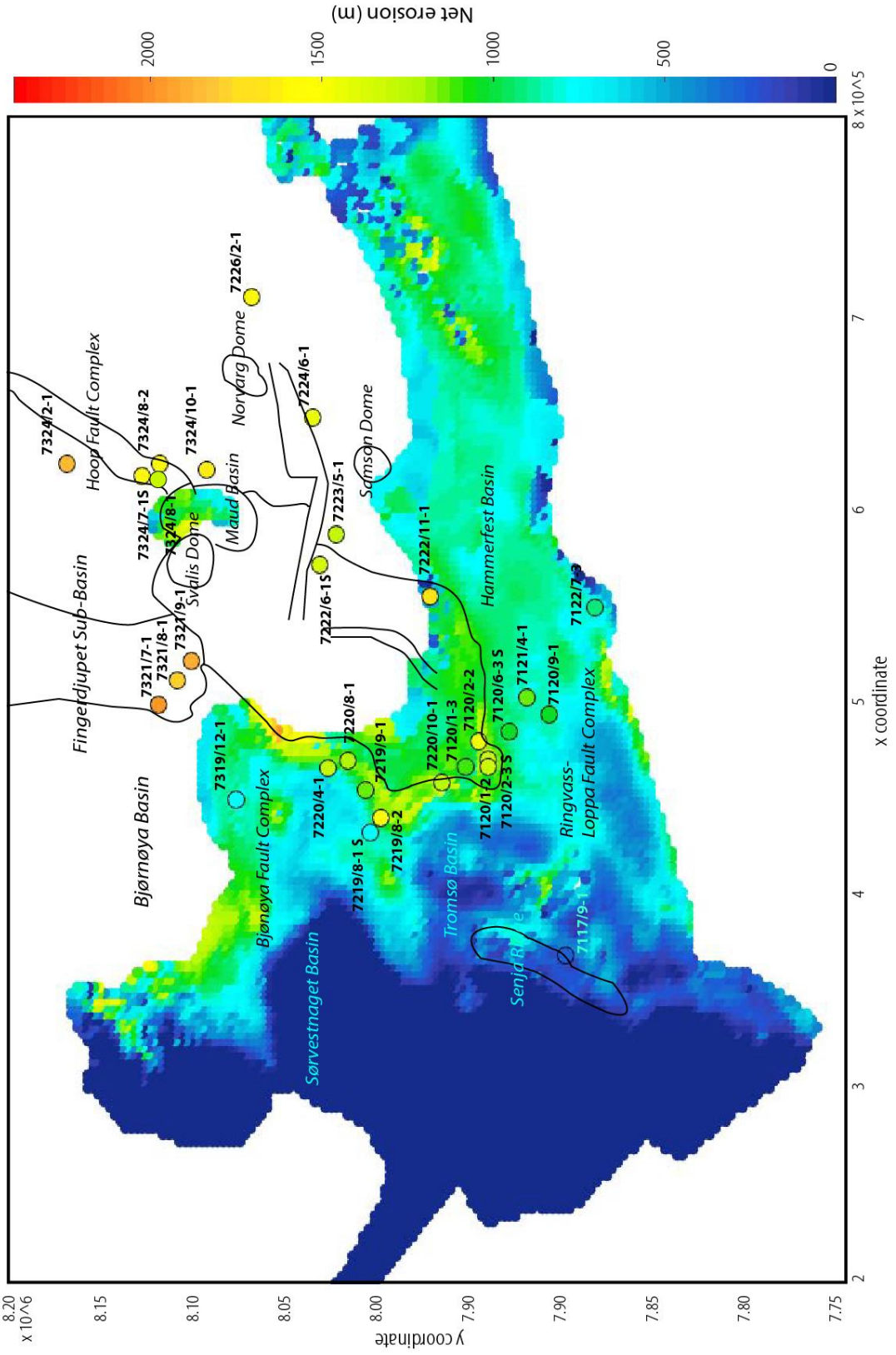

Figure 4.13: *Net erosion map created from seismic interval velocities for the top Kolmule Horizon shows increasing net erosion from south to north and from west to east. Due to the dense velocity grid compared to the well data base this map is much more detailed than the trend maps shown in Figure 4.4 and Figure 4.11. Net erosion results from velocity trends in wells are included for comparison. In the white area the top Kolmule Formation is thin or absent, and the horizon was not mapped on the seismic data.*

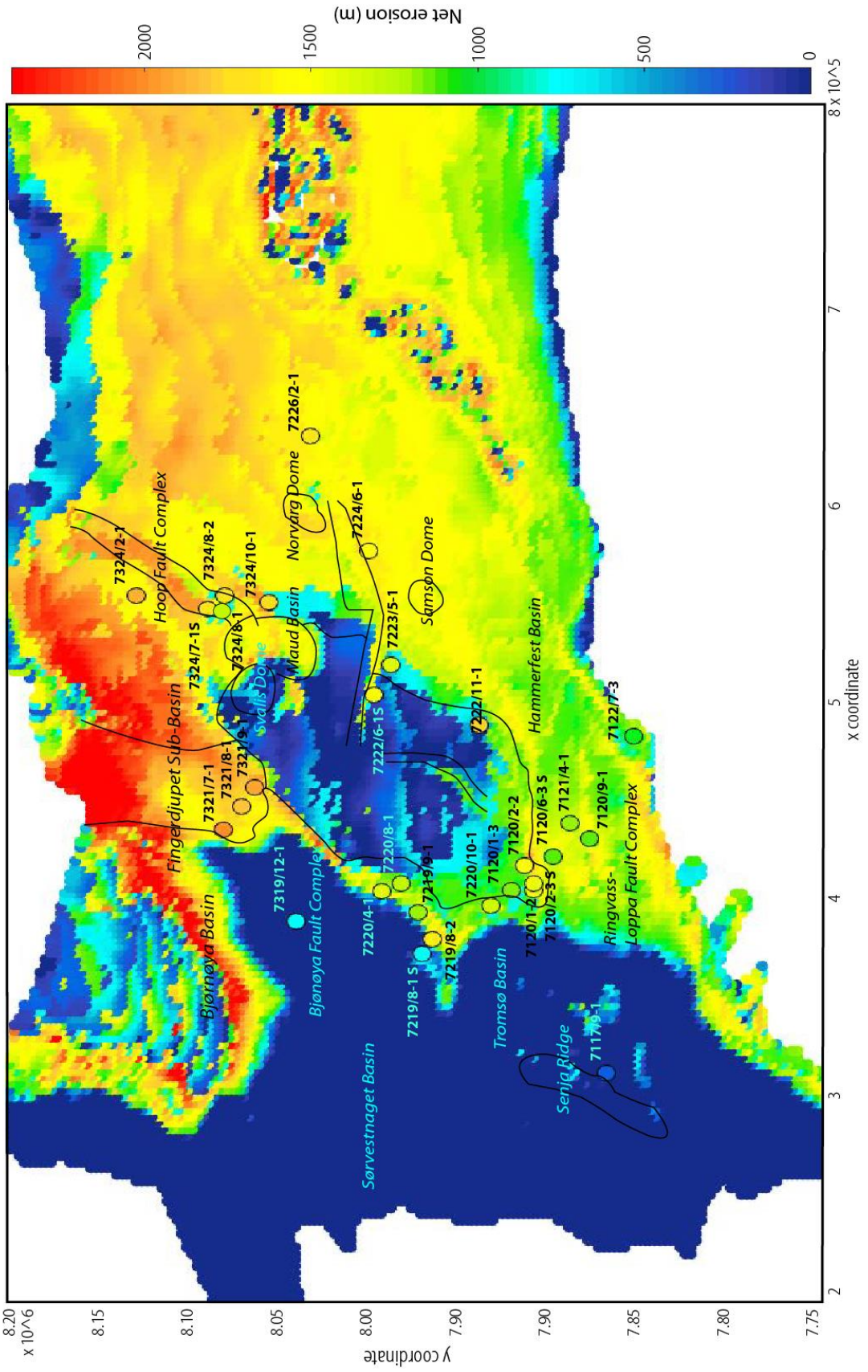

Figure 4.14: *Net erosion map created from seismic interval velocities for the top BCU Horizon shows increasing net erosion from south to north and from west to east. Due to the dense velocity grid compared to the well data base this map is much more detailed than the trend maps shown in Figure 4.4 and Figure 4.11. Net erosion results from velocity trends in wells are included for comparison. In the blue area at the Loppa High net erosion is not estimated.*

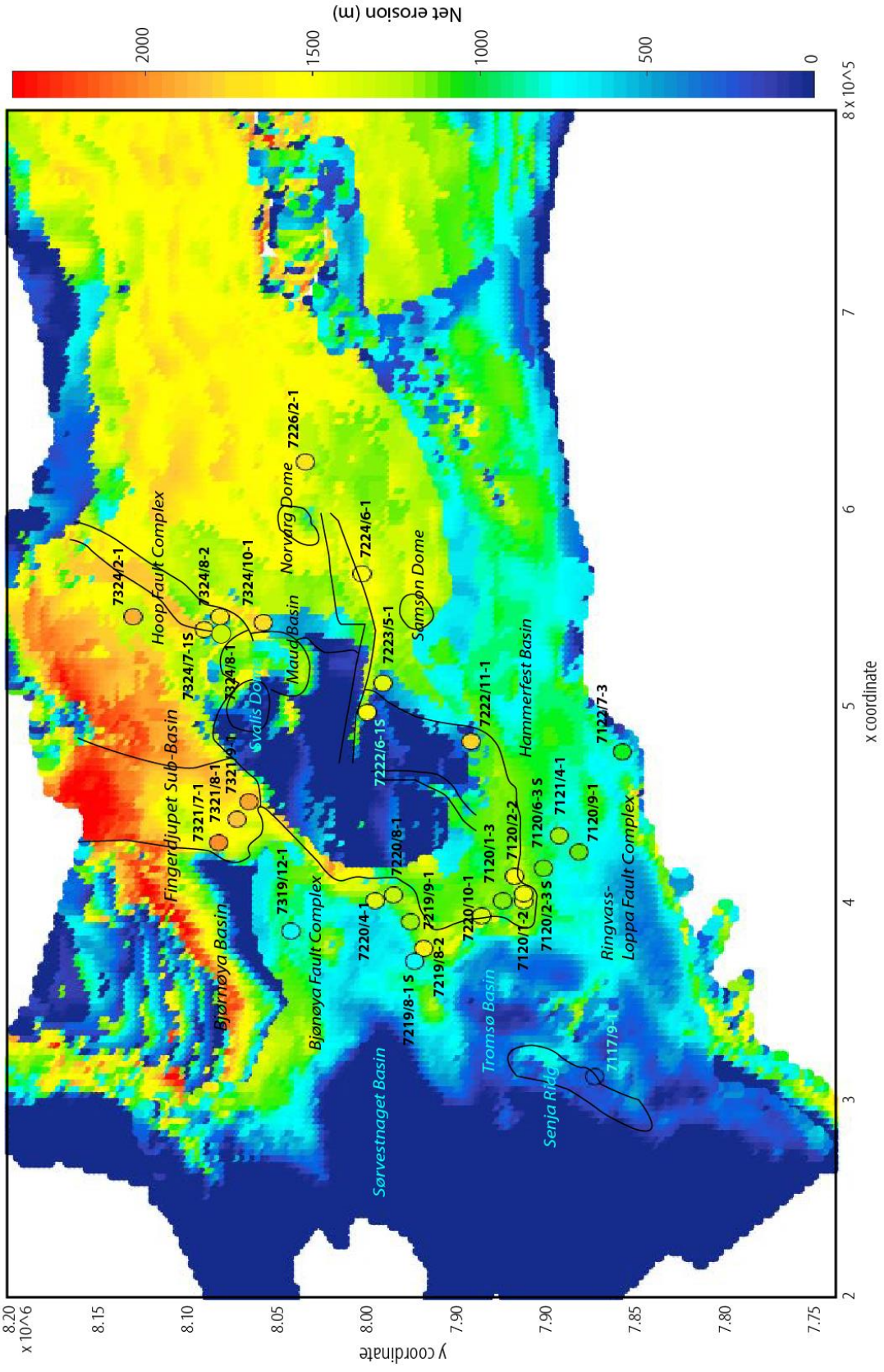

Figure 4.15: *Combined net erosion map created from merging seismic interval velocities maps for the top BCU Horizon (Figure 4.14) and the Top Kolmule Horizon (Figure 4.13). Net erosion results from velocity trends in wells are included for comparison. The BCU map is shifted down 200 meters. See text for a more detailed explanation. The apparently abrupt change in net erosion estimate in the northern Tromsø Basin on this map is caused by the imperfect merge between the two maps. In the blue area at the Loppa High net erosion is not estimated.*

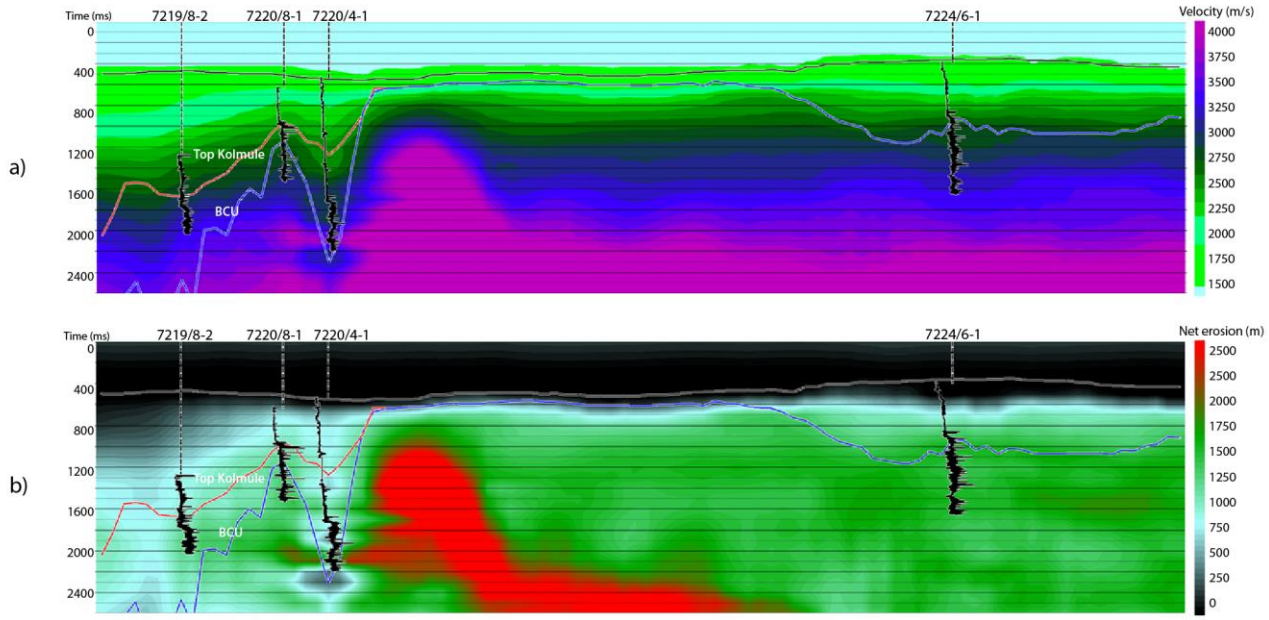

Figure 4.16: *a) Section from the interval velocity cube with the interpreted Kolmule- and BCU Horizons. b) Section from the net erosion cube generated from seismic velocities with the same horizons. The interpreted BCU horizon continues over the Loppa High onto the Bjarmeland Platform, while the top Kolmule interpretation stops at the western edge of the high. See Figure 1.1 for location of cross section (Section 1) and wells.*

The maps were generated by choosing intervals below and above the horizons to obtain good coverage of the units of interest (Figure 4.17). An interval from 0-100 ms below the top Kolmule Horizon was chosen to represent the formation. For the BCU horizon an interval from 0-50 ms was chosen above the horizon. A thicker interval from 100 to 200 ms was first tested, but was influenced by elevated velocities above the BCU horizon.

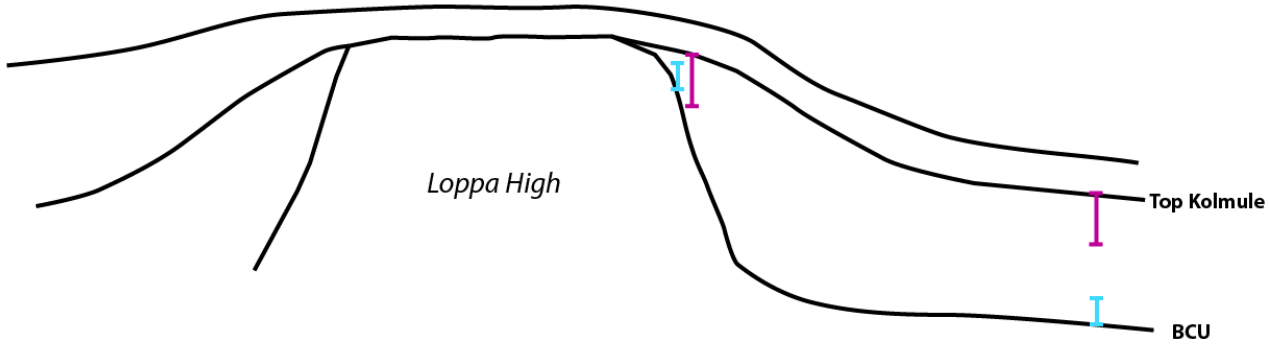

Figure 4.17: *Conceptual sketch showing the selected intervals (vertical bars) below the top Kolmule Horizon and above the BCU Horizon. Near the Loppa High the top Kolmule Horizon and the BCU Horizon are overlapping, while further away from the high the distance between the two horizons is larger causing inconsistent net erosion results in the two maps created from seismic velocities (Figure 4.15). See text for a more detailed explanation of the figure.*

The net erosion map based on the Kolmule Formation alone (Figure 4.13) will not give estimates for the entire area of interest. This is because the top Kolmule horizon is not present in the northern and north eastern parts (Figure 4.13). For these areas the BCU horizon was used.

In the maps generated from seismic velocities, the net erosion estimates from single wells derived from velocity logs are also superimposed. Both these maps have fairly good match with the single well results. We have not tested in any detail why these small differences occur, but velocity dispersion is a typical effect that could explain, at least partly, such differences (Mavko, 1987). Figure 4.14 shows the net erosion map generated from the BCU horizon. The BCU map has slightly larger values than the Kolmule map. To cover the entire area the Kolmule- and the BCU maps were merged (Figure 4.15). In this process 200 meters was subtracted from all BCU estimates.

The most likely reason for the small mismatch between the two maps is illustrated in Figure 4.17. For example at the Loppa High the Kolmule interval is thin, and the two horizons are closer together than in the basin. Near the high the net erosion estimates are almost similar, but when we move away from the high the results from the two maps differ. This can be explained by relatively higher velocities closer to the BCU horizon. This is probably caused by coarser and harder lithologies above the horizon. In the Hammerfest Basin the Knurr sandstones is one example that can give higher net erosion estimates due to elevated velocities. Theoretically an alternative explanation could be that the BCU horizon has experience a different burial history compared to the Kolmule horizon.

The Kolmule net erosion map will most likely give more reliable and consistent results since the Kolmule Formation is thicker and has a more stable shale content compared to the formations associated with the BCU. In addition, an averaging algorithm for the chosen time windows below the Kolmule interval (100 ms) and above the BCU (50 ms), cancelling out small irregularities, was used when making the maps.

4.5 Geological interpretations of net erosion estimates

The results from the seismic interpretation are presented below. The main focus is to understand the burial history of the area by linking the net erosion estimates in wells to the seismic sections. Four regional seismic composite sections were interpreted, and in total seven regional horizons were tied to the wells (Figure 4.18). The locations of the four sections are shown in Figure 1.1.

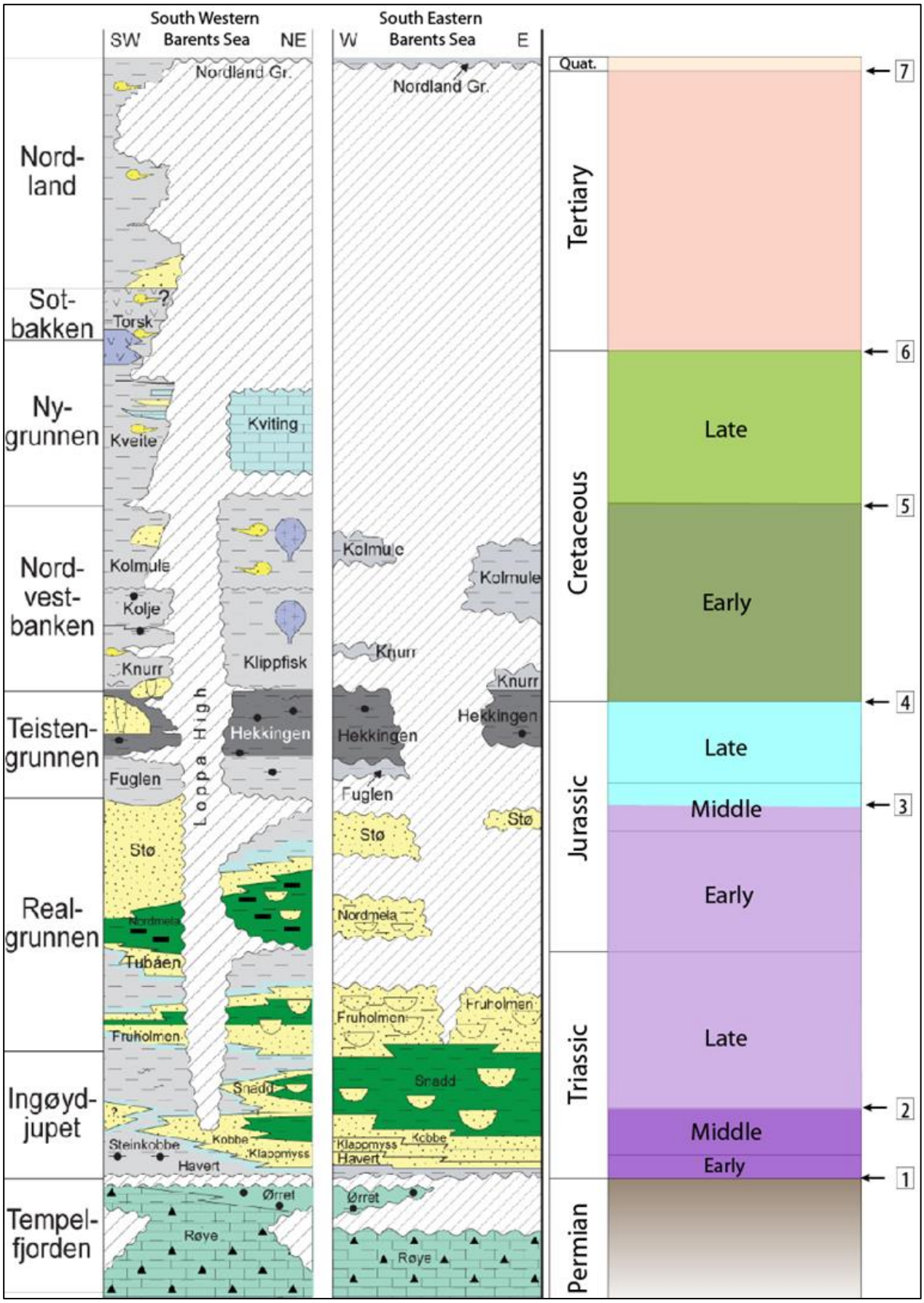

Figure 4.18: *Lithostratigraphic units in the Barents Sea. Approximate ages of the horizons interpreted on the regional seismic sections are shown with numbers 1-7. Modified from Gradstein et al. (2012) and NPD (2016).*

The east-west section across the Loppa High clearly shows the general thickening of the post Paleozoic strata towards the east, and the abrupt change from the Loppa High into the Bjørnøya Basin with great subsidence and deposition of thick sediment packages. It also shows the lack of the Jurassic and Cretaceous sediments on the Loppa High (Figure 4.19).

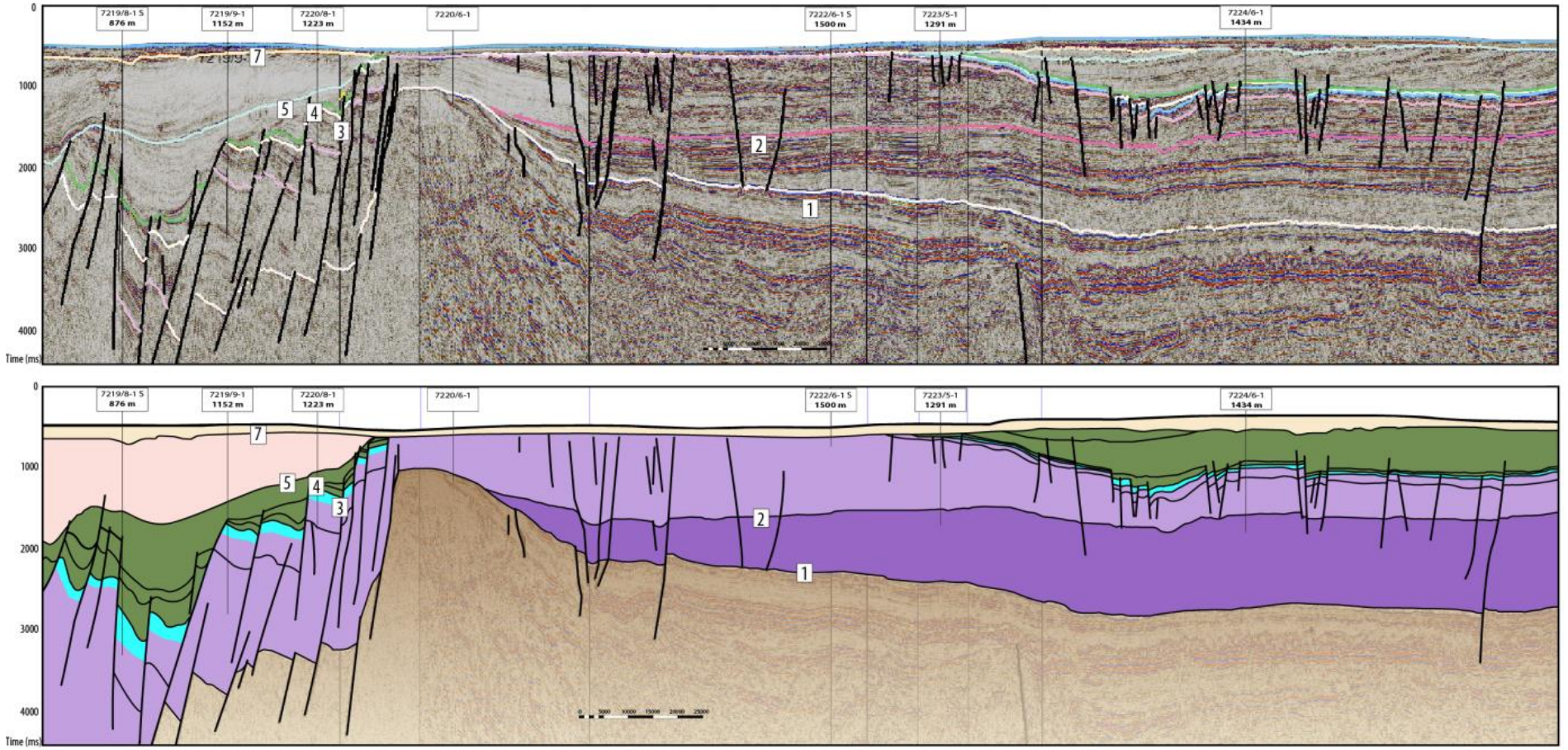
7219/8-1 S
876 m
7219/9-1
1152 m
7220/8-1
1223 m
7220/6-1
7222/6-1 S
1500 m
7223/5-1
1291 m
7224/6-1
1434 m
0
1000
2000
3000
4000
Time (ms)
7
5
4
3
2
1

Figure 4.19: *Interpreted regional seismic section number 1 (upper). Geological model based on the interpreted seismic section (lower). For location of section see Figure 1.1 and Figure 4.18 for ages of seismic horizons. The net erosion estimates from velocity trends in the wells are show in the well positions.*

In the Loppa High area the pre-Triassic strata, the units below Reflector 1, are elevated and show an upward dip. This combined with the faulting shows that the high also was a Paleozoic structural high. It was uplifted and eroded before it was buried by Triassic strata. This erosion is local and much older than the net erosion estimated for the Cretaceous and Cenozoic strata.

In Triassic time the entire area subsided and was covered by thick layers of sedimentary strata (reflector 1 – 3). The Loppa high was still a high, and was not covered by sediments before in late Triassic time, after reflector 2. Between reflector 1 and 2 there are also internal thickening towards the east, interpreted as progradation from east to west in this period. An easterly Triassic sediment source is supported by provenance studies by Mork (1999).

In late Triassic time an important change occurred, and we see thickening of upper Triassic sediments on the Loppa High. The high had changed into a basin, and major subsidence took place. The sediments are now thickening towards the west, and a thick sediment package was also deposited west of the high.

The Jurassic sedimentary unit is thin compared to the Triassic package. The general subsidence had slowed down, and the sediments now contain more sandstones (Figure 2.6 and Figure 4.19). In this period, the western part of the Loppa high is characterized by many faults. The high fault activity continued from late Jurassic- and into early Cretaceous time. During this period the high was again uplifted and eroded.

After the rifting a period with large scale Cretaceous post-rift subsidence occurred. In the east, although the preserved units are thin on this section, the sediments seem to prograde in from the east. The Kolmule Formation (Figure 2.6 and Figure 4.19) that was used for the net erosion estimations in the well positions was deposited during this period.

The present day thickness of the formation varies in the study area, thickest in the west and thinner towards the east. The net erosion estimates in the well positions are included on the top of the geological model. The estimates vary between 1300 and 1500 meters in eastern areas, and in the west from approximately 800 to 1200 meters. This means that the entire region continued to subside also after deposition of the Kolmule Formation. In places the formation reached a maximum burial depth close to 2000 meters deeper than it is buried today before it was uplifted. This interpretation is supported by other regional studies (Baig et al., 2016, Faleide et al., 2010, Henriksen et al., 2011).

When combining net erosion estimates along the line and the model from the seismic interpretation, we subdivided the section into three parts. From the net erosion trend map in Figure 4.4 we see that most of the area had significant net erosion. This widespread event was most active in the eastern part of the section. The middle part was also affected by margin uplift due to the rifting in the west. Since the upper Triassic sediments are thickest on the Loppa high itself, the late Triassic and Jurassic depocenter on the Loppa High has been inverted. This was also reported by Glørstad-Clark et al. (2010). For how long time into the Cretaceous period this episode was active is uncertain. In the west local subsidence most likely occurred simultaneously with the regional uplift. This can explain less uplift towards the west.

The upper regional unconformity (Reflector 7) is present everywhere in the study area. On the Loppa High Triassic strata are sub cropping the unconformity. In the Hammerfest Basin (Figure 4.20), along the western flank of the Loppa High, and in the deep basins in the west, Tertiary strata are sub cropping. Elsewhere in the study area Cretaceous rocks are sub cropping Reflector 7. Above this reflector only Quaternary sediments are present and Quaternary glacial erosion was clearly active. Based on erosion estimates, and quantification of sediment volumes, it has been estimated that the glacial erosion can account for 40-60% of the total estimated net erosion (Baig et al., 2016, Laberg et al., 2012). Isostatic response to the glacial erosion can explain a significant part of this uplift and erosion, but glaciers can also erode without any simultaneous uplift. Vågnes et al. (1992) made an attempt to quantify this effect in the Barents Sea.

Most authors, for example Faleide et al. (2010) date maximum burial and the subsequent onset of uplift to have occurred in middle Eocene time, approximately 40 mill years ago.

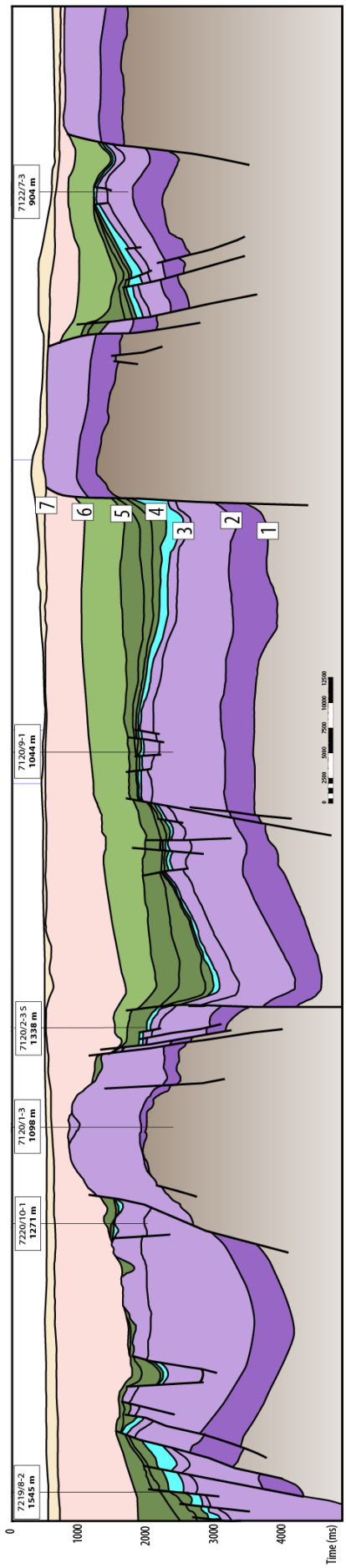
7219/8-2
1545 m
7220/10-1
1271 m
7120/1-3
1098 m
7120/2-3 S
1338 m
7120/9-1
1044 m
7122/7-3
904 m
7
6
5
4
3
2
1
0
1000
2000
3000
4000
Time (ms)

Figure 4.20: *Geological model based on the interpreted seismic section number 2. For location of section see Figure 1.1 and Figure 4.18 for ages of seismic horizons. The net erosion estimates from velocity trends in the wells are show in the well positions.*

This erosion did not affect the westernmost areas, but the rest of the study area was strongly affected by this event (Figure 4.4 and Figure 4.13 to Figure 4.15). It is the northern and north eastern areas that have been eroded the most. In the Fingerdjupet sub basin almost 2000 meter of strata was removed and in the Hoop area more than 1600 meters was eroded (Figure 4.21 and Figure 4.22). The general patterns and events described above are also seen in this area.

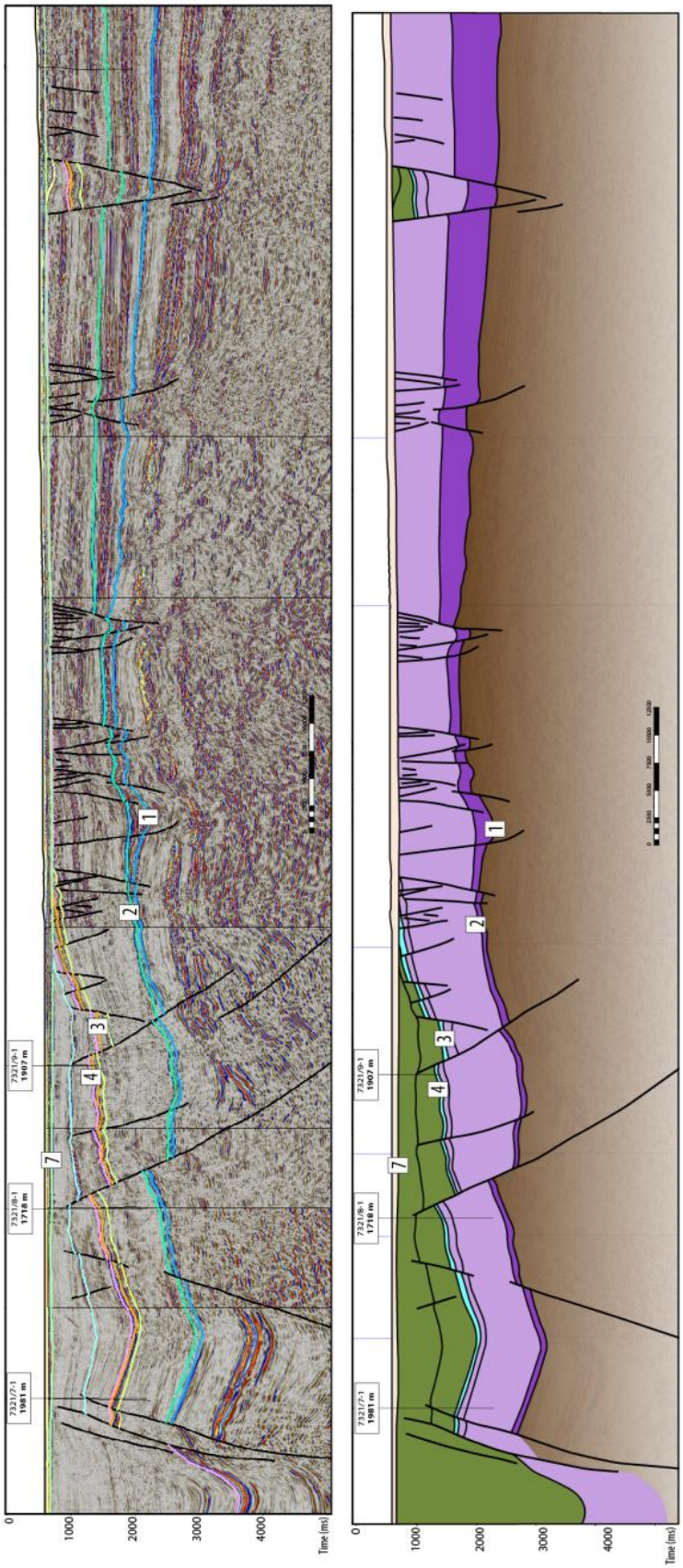

Figure 4.21: *Interpreted regional seismic section number 3 (upper). Geological model based on the interpreted seismic section (lower). The net erosion estimates from velocity trends in the wells are show in the well positions. For location of section see Figure 1.1 and Figure 4.18 for age of seismic horizon. Note that the colours of the reflectors are slightly modified compared to Figure 4.19. The numbering of the reflectors is the same for all the sections.*

Figure 4.22: *Geological model based on the interpreted seismic section number 4. For location of section see Figure 1.1 and Figure 3.18 for age of seismic horizons. The net erosion estimates from velocity trends in the wells are show in the well positions.*

Towards the south west and south the amount of net erosion is smaller. In the Hammerfest Basin and onto the Finnmark Platform it is approximately 1000 meters (Figure 4.20). The most likely explanation for this is that the amount of regional uplift was less in the south. This was combined with local Tertiary subsidence in the basin. The Hammerfest Basin profile continues northwards onto the south western tip of the Loppa High, and higher net erosion here supports this model. The profile (Section 2) follows the fault zone northwards (Figure 1.1). Along the fault zone the net erosion estimates are constantly higher than in the Hammerfest Basin, but also have more variation than normal for the data set.

4.6 Seismic AVO responses

Seismic signatures are affected by uplift and erosion. As the rocks are buried the AVO response will change due to alternations in the reservoir- and the cap rock.

In this chapter real AVO responses from seismic angle stack data will be compared to modelled AVO responses using rock physics modelling and the estimated net erosion results. These analyses were done on three wells on the south western edge of the Loppa High.

Regional analysis of modelled AVO responses was also done across the study area.

4.6.1 Detailed AVO analysis – south western Loppa High

Near and far angle stack data from the Myrsildre (7120/1-2), Skalle (7120/2-3 S) and Juksa (7120/6-3 S) wells were used to perform AVO analysis (Figure 4.23). This was done to classify and compare the individual reservoir responses, and to understand the effect of net erosion compared to the effect of hydrocarbons in the reservoir.

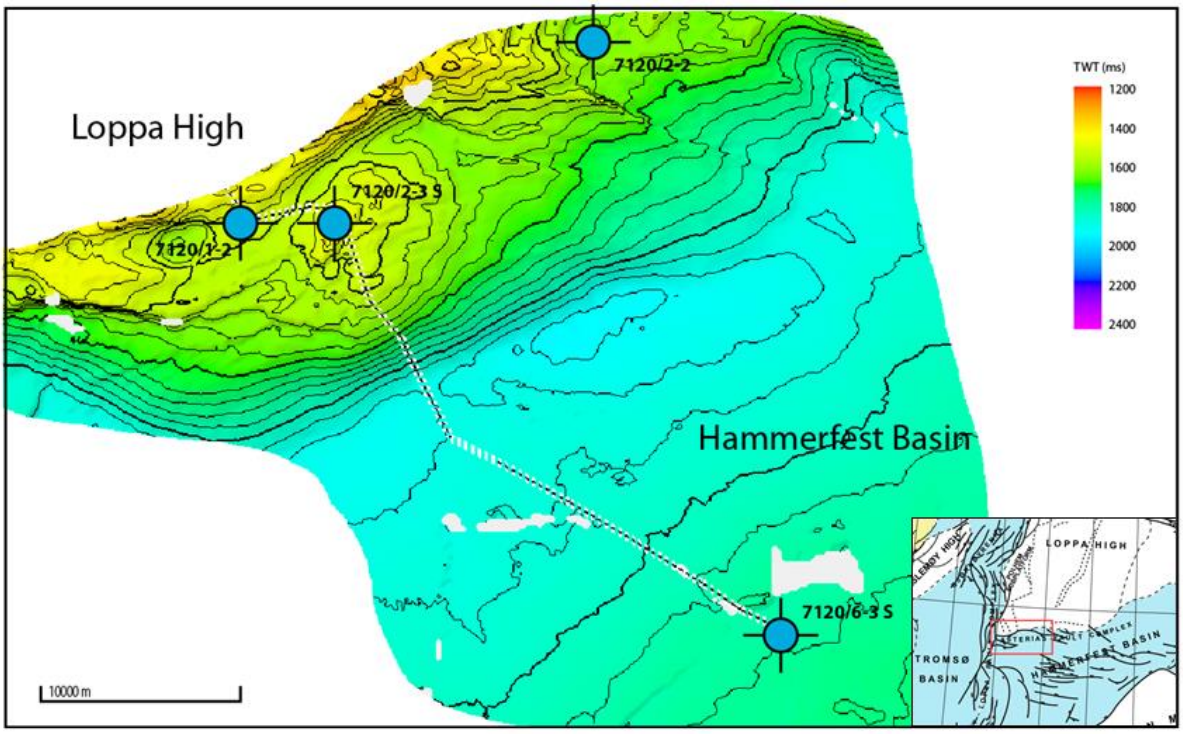

Figure 4.23: *Study area at the south western edge of the Loppa High. The stippled line is the location of a composite seismic section (Figure 4.24) through the Myrsildre- (7120/1-2), Skalle- (7120/2-3 S) and Juksa (7120/6-3 S) wells. Depth to the BCU Horizon (TWT) is also included in the figure.*

Figure 4.24 shows the composite line through the wells of interest and the net erosion estimates generated from the seismic velocities. Net erosion estimates from the sandstone modelling approach are also included on top of the figure. Less net erosion is estimated in the Juksa (7120/2-2) well compared to the Skalle (7120/2-3 S) and Myrsildre (7120/1-2) wells.

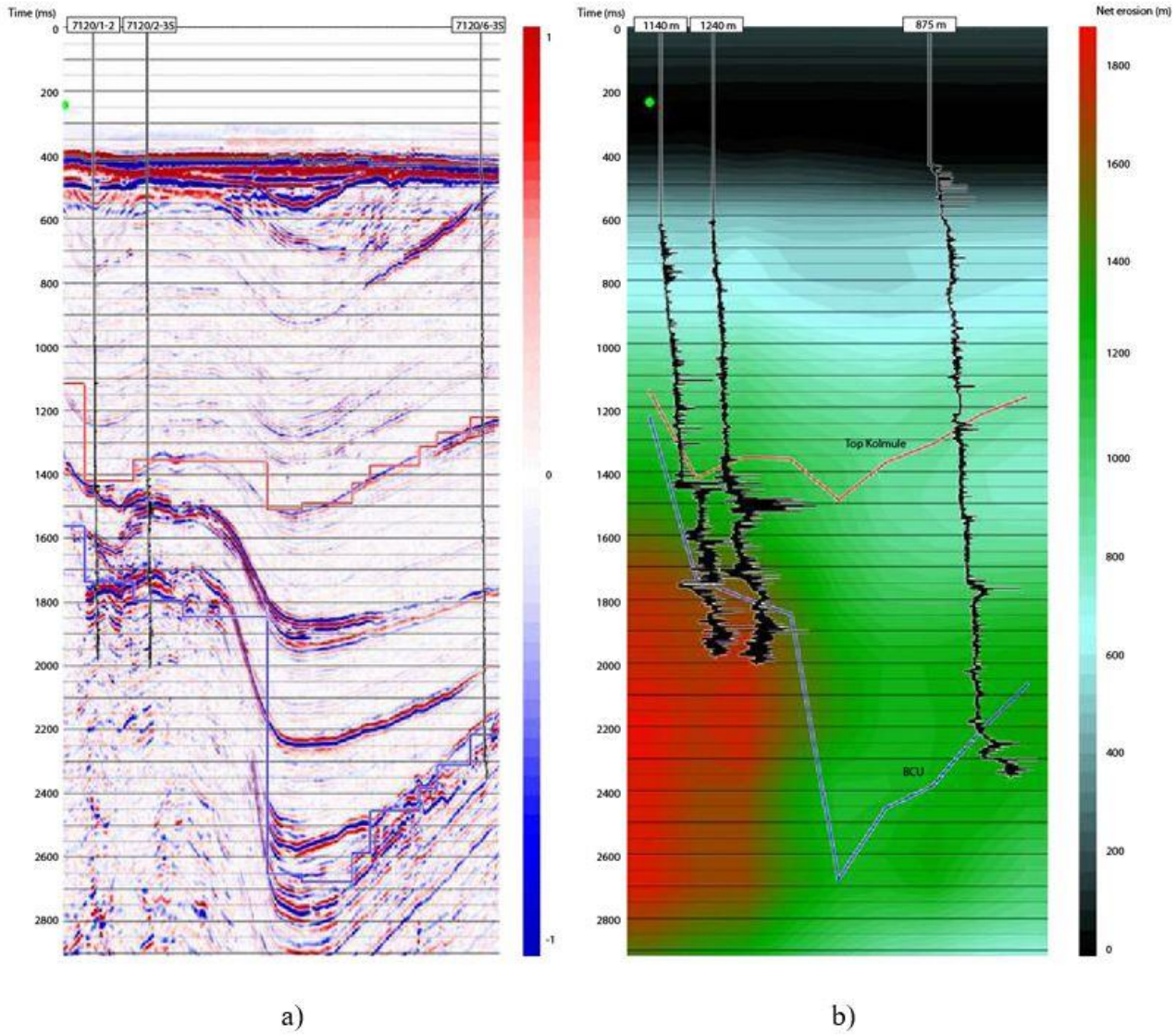

Figure 4.24: *a) Composite seismic section through the wells shown in Figure 4.25. b) A section along the same line through the net erosion cube generated form seismic velocities. The Top Kolmule- and the BCU Horizon are also shown on the section. Net erosion estimates from the sandstone modelling are shown at the well location.*

The angle stack data from the near and far stack is shown in Figure 4.25 and Figure 4.26. The general seismic responses show a weak dimming from the near to the far stack, while the Skalle gas reservoirs show a brightening effect.

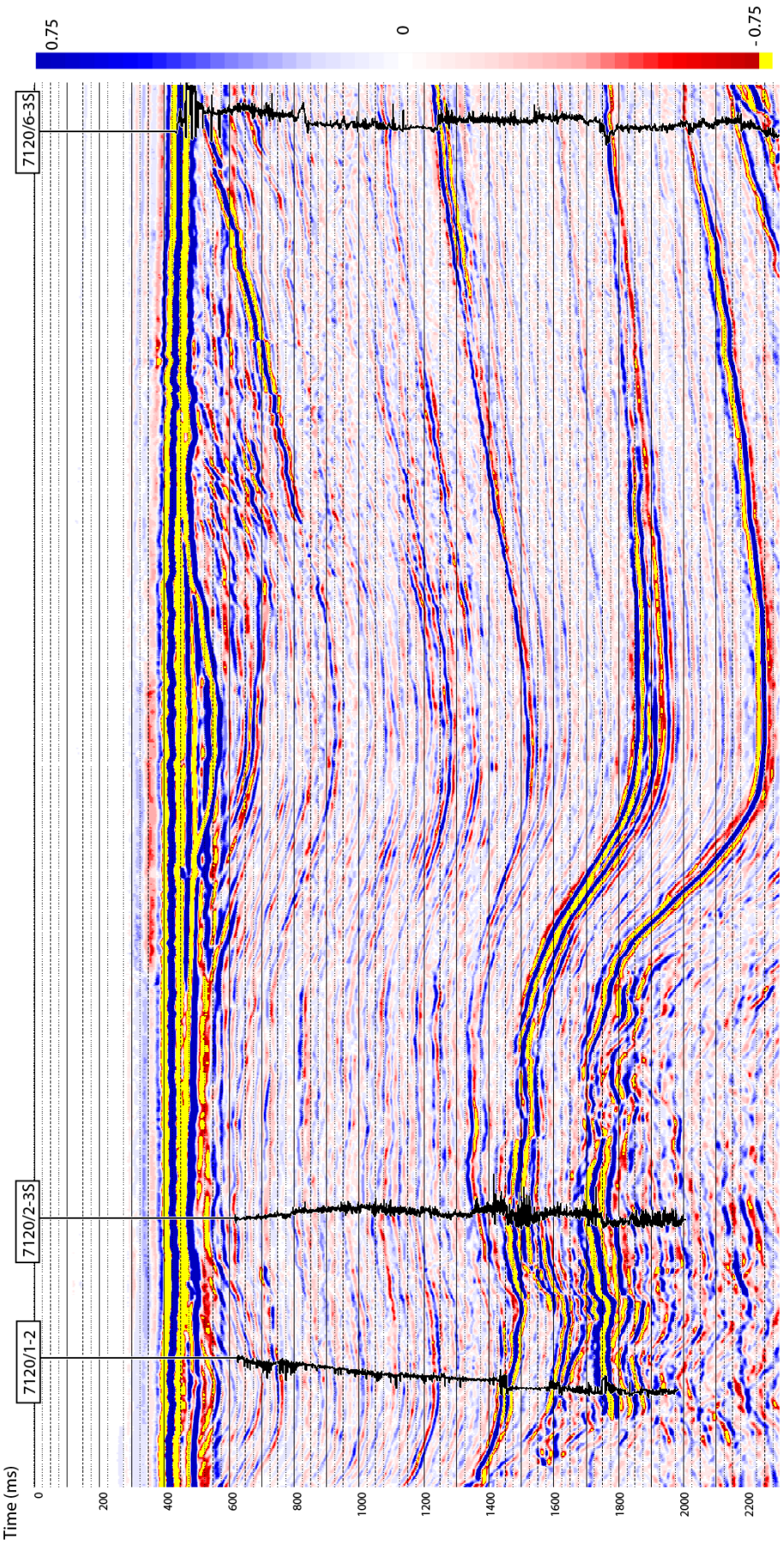

Figure 4.25: *The near stack data is represented by angles from zero to ten degrees. Location of line is shown in Figure 4.23.*

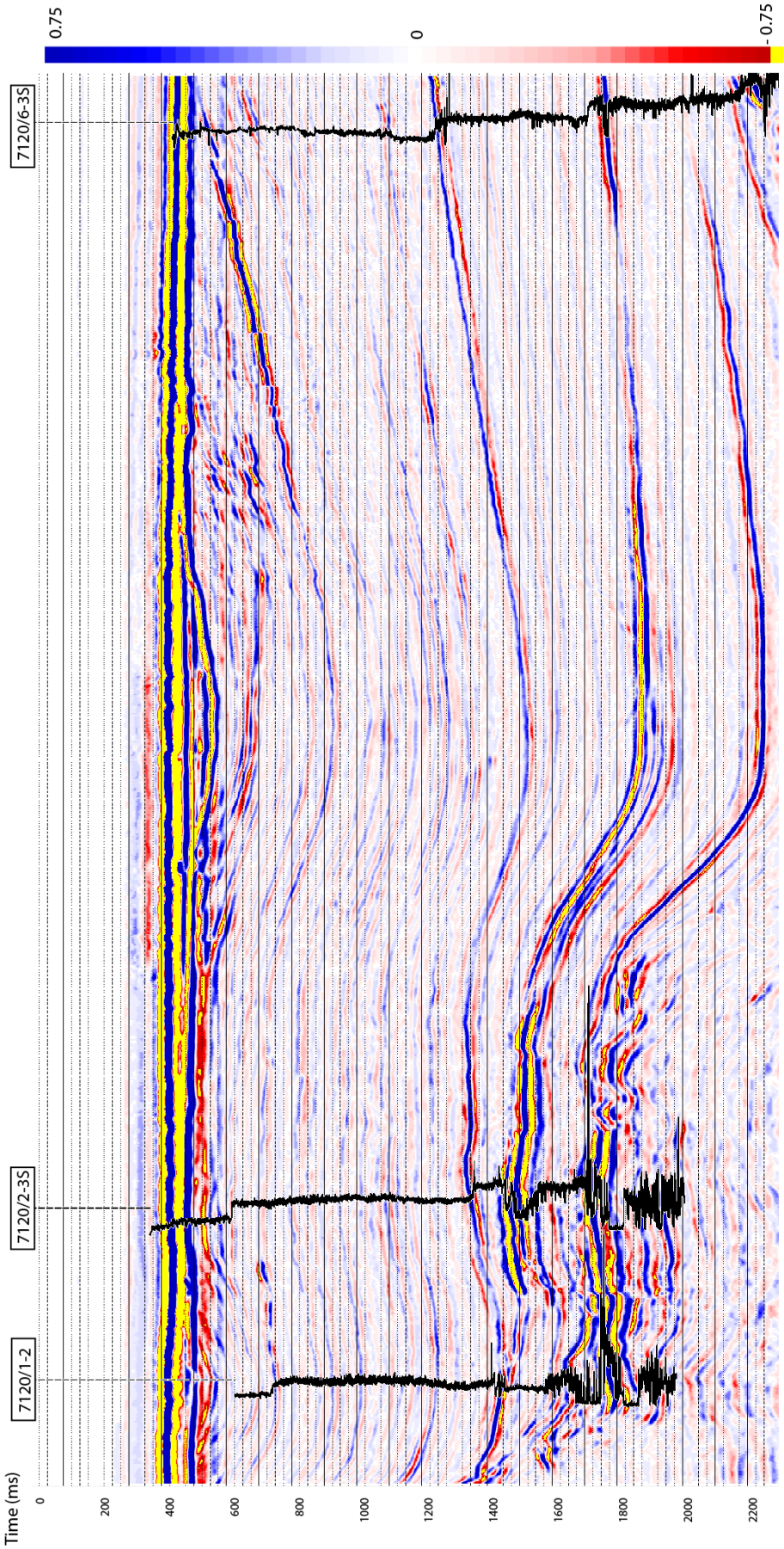

Figure 4.26: *The far stack data is represented by angles from twenty to thirty degrees. Location of line is shown in Figure 4.23.*

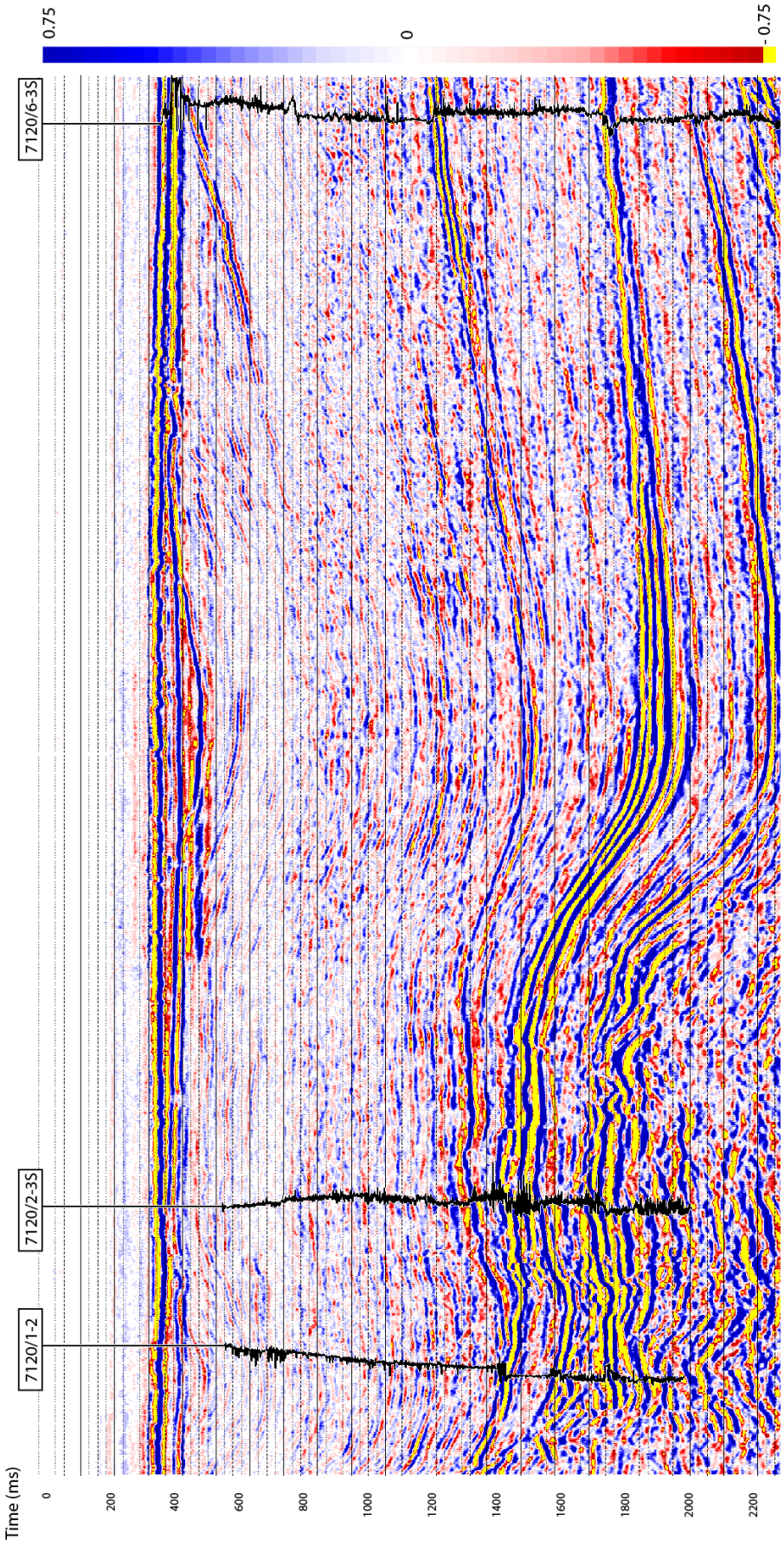

Figure 4.27: *The gradient is calculated by subtracting the near stack from the far stack. Location of line is shown in Figure 4.23.*

The gradient is shown in Figure 4.27. And, as described above, the gradient and the near stack are used to generate a gradient-intercept cross plot. Figure 4.28 shows the different AVO responses from the angle stack data in the gradient-intercept domain.

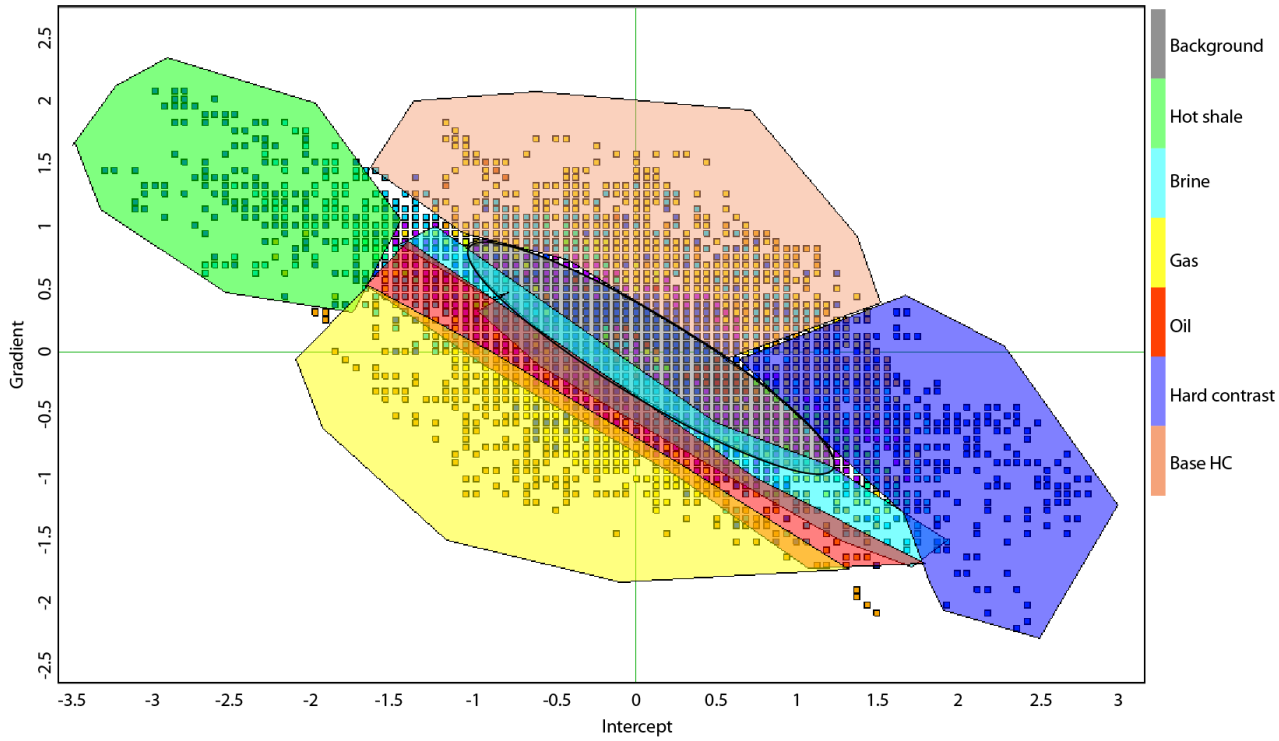

Figure 4.28: *Interpreted AVO cross plot in the gradient-intercept domain extracted from the angle stack data. The near stack is the intercept while the gradient is the far stack minus the near stack near.*

A common interpretation approach is to interpret a background trend and then look for data points that deviate from this trend (Avseth, 2015, Avseth et al., 2005). Here the interpreted background trend is plotted in grey colour. This trend is dominated by shale/shale- and shale/slit horizons, and represents the bulk of data in the section. The brine trend (light blue) is interpreted to line up along the background trend, while the data points covered by the yellow colour in the plot are interpreted to represent the top of the gas sand. See Figure 4.28 for more details.

The interpreted AVO zones from Figure 4.28 are then transferred and shown on the seismic section in Figure 4.29. The Kolmule and Stø reservoirs in the Skalle (7120/2-3 S) well show strong anomalies at reservoir levels. The interpreted AVO section indicates mainly gas, but there are also indications of oil in the Skalle well. In reality the Skalle well is a gas discovery. We see weaker responses indicating oil in the Juksa Kolmule reservoir and the Myrsildre Hekkingen reservoir. The drilling results from the two wells showed traces of oil in Kolmule (Juksa) and movable oil in Hekkingen (Myrsildre), respectively.

Such quantitative pore fluid analysis can sometimes be uncertain, especially for oil, since it is situated between the gas- and the water response in the diagram. This means that a strong water response can be interpreted as an oil response, or a "weak" gas response can be interpreted as an oil response. Also noise and interference can influence the interpretation. In this case we have calibrated the polygon classification with observations in three wells. This will improve the classifications.

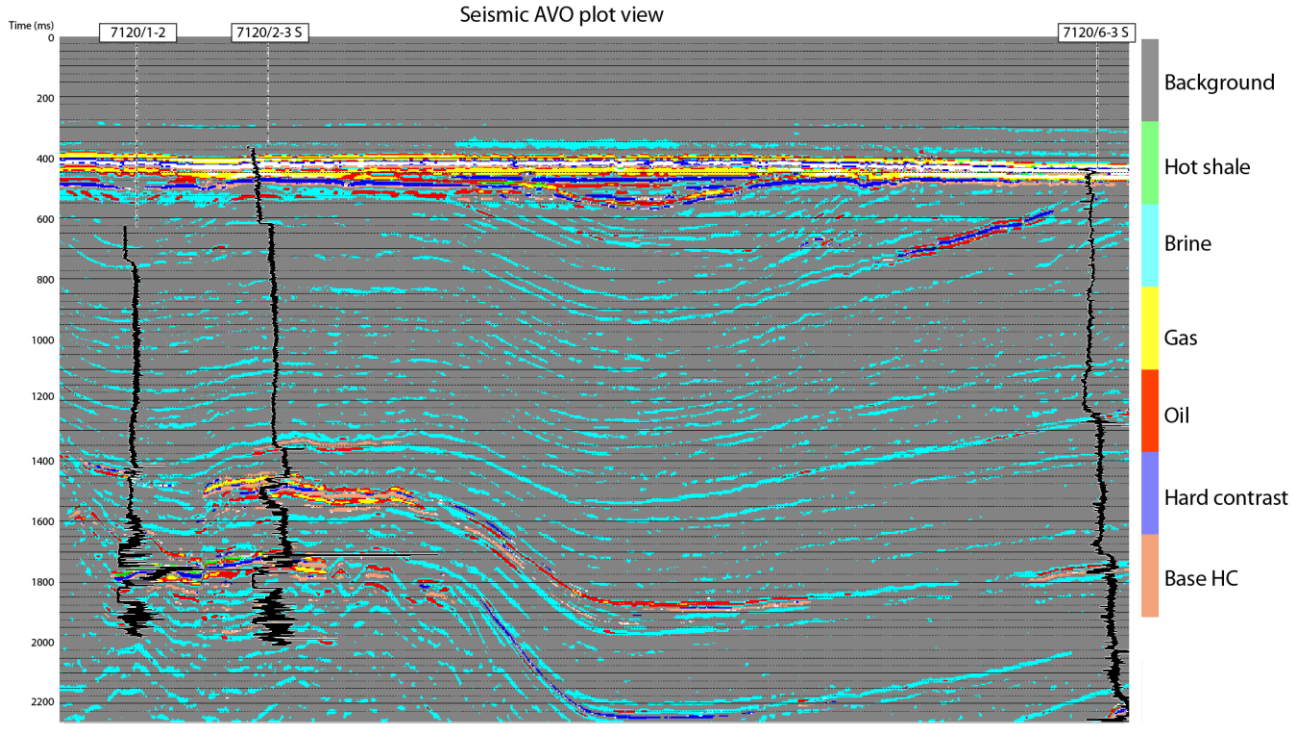

Figure 4.29: *Seismic section with the interpreted AVO zones from the cross plot in Figure 4.28. Location of the section is show in Figure 4.23.*

Below, AVO responses from the two reservoir levels shown in Figure 4.29 and Figure 4.30 were classified using the classification system describe above. For the Skalle- and Juksa well, also a more detailed analysis of the AVO responses through generation of synthetic AVO seismograms was done. For these wells the real hydrocarbon AVO responses from the angle stack data will be compared to a modelled brine response after fluid substitution. The AVO responses from the seismic data were compared to a modelled AVO response, using the sandstone diagenesis approach explained in Chapter 3.7.2, where burial history also is taken into account. The modelling of AVO using this approach was done for the intervals shown in Figure 4.30.

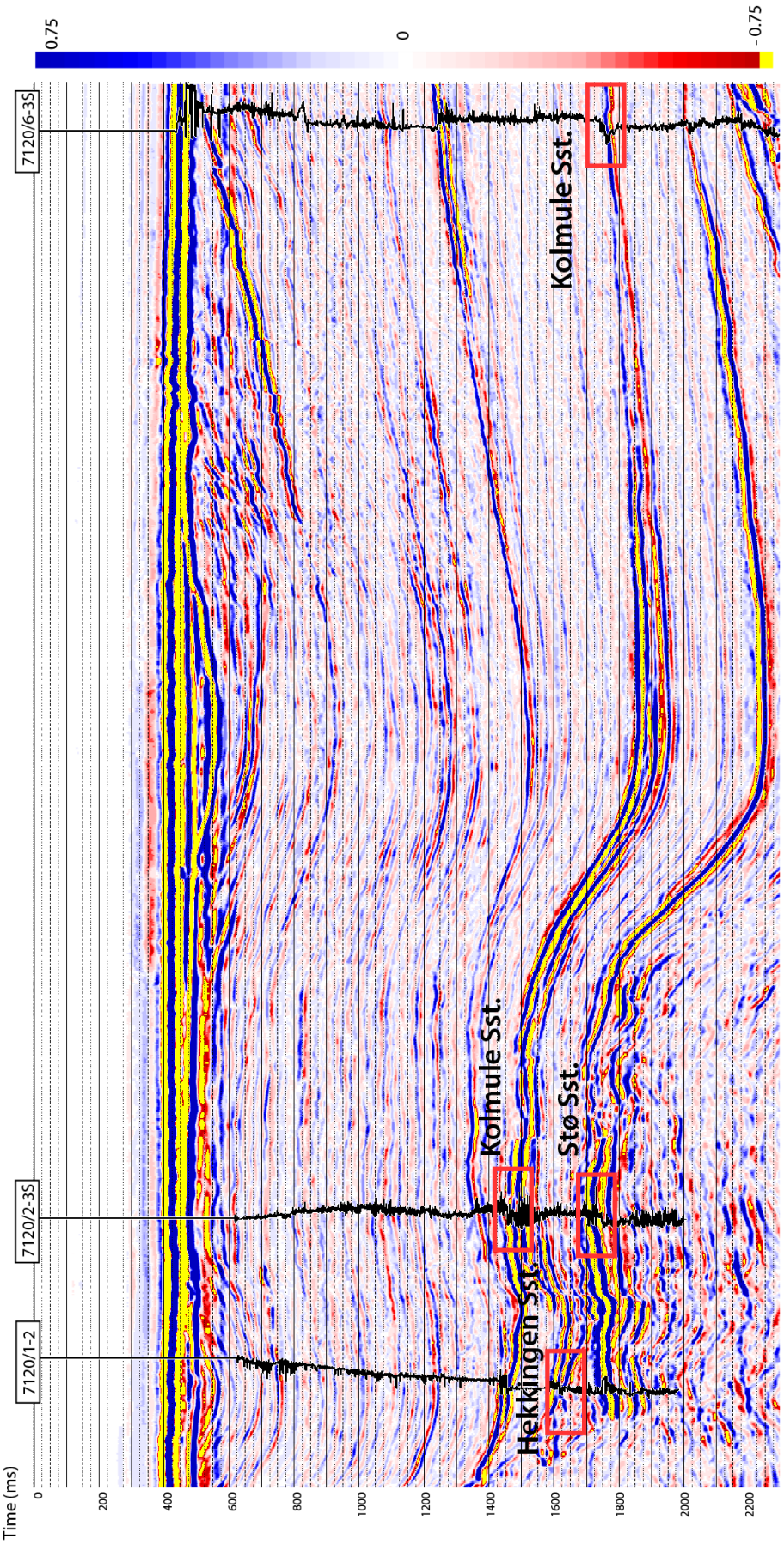

Figure 4.30: *Location of sandstone reservoirs where detailed AVO analysis were performed. Location of the section is show in Figure 4.23.*

Skalle 7120/2-3 S

The Skalle well has proven gas columns in both the Kolmule and Stø sandstones. Figure 4.31 shows a synthetic forward modelled AVO seismogram, together with the real in situ AVO seismogram, the gamma ray log, the P-wave impedance and the Vp/Vs relationship. When we tested Zoeppritz modelling in this case we got unwanted effects at far offset, most likely due to refracted energy. Therefore we did full elastic seismic modelling (Li et al., 2014) to get as realistic AVO responses as possible. It is the Kennett algorithm that in this case is implemented in the Hampson-Russell software to perform the full elastic modelling (Kennett, 1979). A brine case was modelled for comparison with the in situ gas case for both reservoir levels. Standard fluid substitution using Gassmann's equation (Gassmann, 1951) was done. The real in situ AVO response with gas is shown to the left in Figure 4.31, and the modelled AVO brine response after fluid substitution is shown to the right.

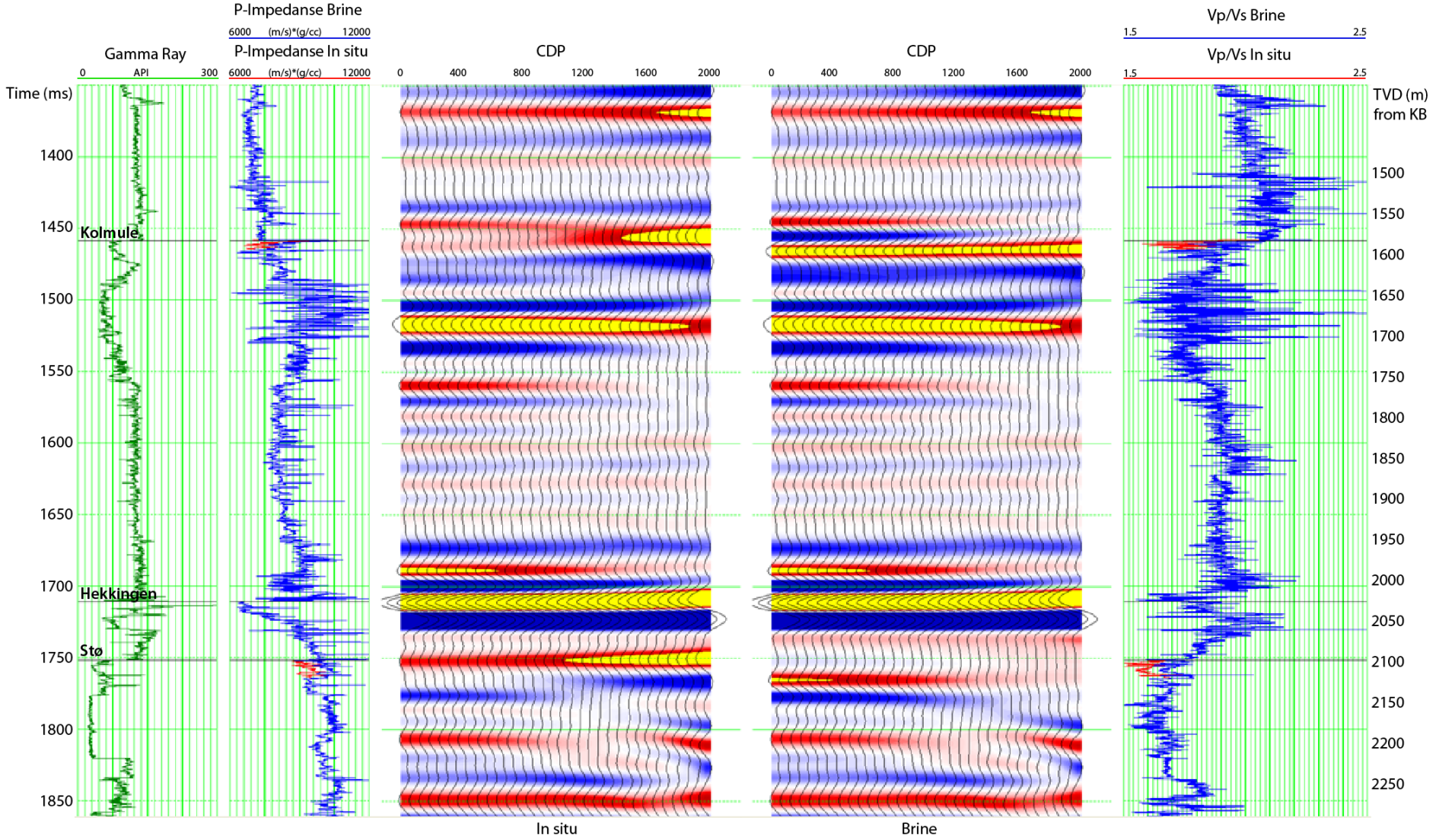
P-Impedanse Brine
6000 (m/s)*(g/cc) 12000
Gamma Ray
0 API 300
P-Impedanse In situ
6000 (m/s)*(g/cc) 12000
CDP
0 400 800 1200 1600 2000
CDP
0 400 800 1200 1600 2000
Vp/Vs Brine
1.5 2.5
Vp/Vs In situ
1.5 2.5
Time (ms)
1400
1450
1500
1550
1600
1650
1700
1750
1800
1850
Kolmule
Hekkingen
Stø
TVD (m)
from KB
1500
1550
1600
1650
1700
1750
1800
1850
1900
1950
2000
2050
2100
2150
2200
2250
In situ
Brine

Figure 4.31: *Synthetic AVO seismogram generated for the Skalle well plotted with gamma log, P-wave impedance log, Vp/Vs-ratio log and the real (in situ) seismic AVO response. The AVO modelling was done after fluid substitution, and the modelled response represents the brine case. The reservoir levels are indicated on the logs, and the fluid substitution is shown in the logs. Gas is represented by red colour and the brine case is blue. The Kolmule sandstone response is interpreted as an AVO class II for the gas, and as a class I response for the brine. The gas response for Stø is a class III and a class IIp for the brine.*

The lowered P-wave impedance and Vp/Vs-relationship represents the gas. The substitution of the gas with water, gives changes in the AVO responses in the synthetic seismogram. All the AVO responses from the top Kolmule and Stø reservoirs show a decreasing trend from near to far offsets. The Kolmule sandstone response is interpreted as an AVO class II for the gas. For the brine we get a class I response. The gas response for Stø is a class III and a class IIp for the brine.

As shown above the AVO response changes with changing fluids. But the AVO response is also influenced by the amount of net erosion, or more correctly the maximum burial depth. To be able to investigate this, the real AVO responses from the in situ fluids were compared to a rock physics based modelled AVO response.

A small window of data around the Kolmule reservoir (Figure 4.30) was chosen and plotted in an intercept – gradient cross plot (Figure 4.32). For the Kolmule sandstone the top reservoir is at approximately 1450 ms (TWT). The AVO response is interpreted as a class II. This is in agreement with the modelled synthetic seismogram for the top Kolmule reservoir. The outlined area is not accurate and will only give an indication of the AVO classification.

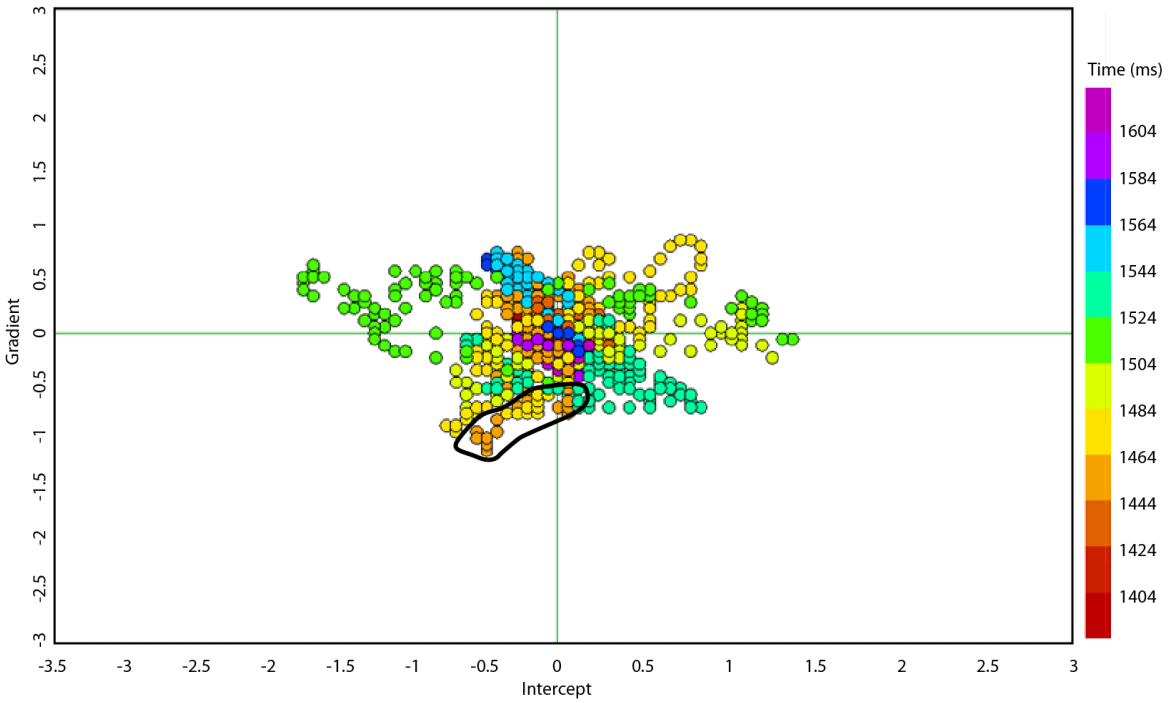

Figure 4.32: *Intercept-gradient cross plot for the response from the Kolmule reservoir in the Skalle well detected at approximately 1450 ms. The response is interpreted as a class II. Location of the reservoir is shown in Figure 4.30.*

The AVO response was then modelled using the rock physics based AVO modelling approach (Chapter 3.7.2). The modelled result from the top Kolmule sand is shown in Figure 4.33 and gives a class II for the gas case, and a class IIp for the for the brine case. This means that the AVO class for the real data and the modelled gas case are similar.

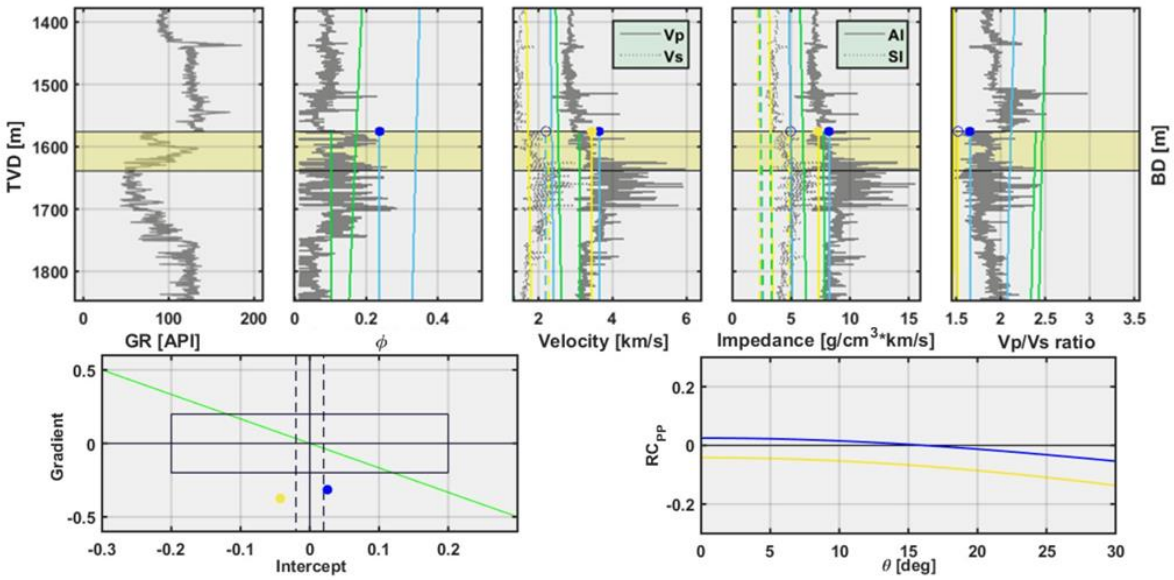

Figure 4.33: *Modelled AVO responses for the Kolmule sandstone in the Skalle (7120/2-3 S) well. The yellow curves represent the in situ gas case and the blue curves are the brine case. The green curves are the modelled cap rock shale trends. The gas case is interpreted as class II and the brine case as class IIp.*

The same procedure was repeated for the Stø sandstone. The real AVO response is shown in Figure 4.34 and the modelled AVO response in Figure 4.35. The modelled synthetic seismogram for the Stø brine case (Figure 4.31) is interpreted as a class IIp, while the in situ gas case is interpreted as a class III. The in situ AVO class from the cross plot (Figure 4.34) shows weak responses and it is difficulties to give a good classification. The modelled AVO responses from the rock physics based AVO modelling (Figure 4.35) gives a class IIp for gas case and class I for the brine case.

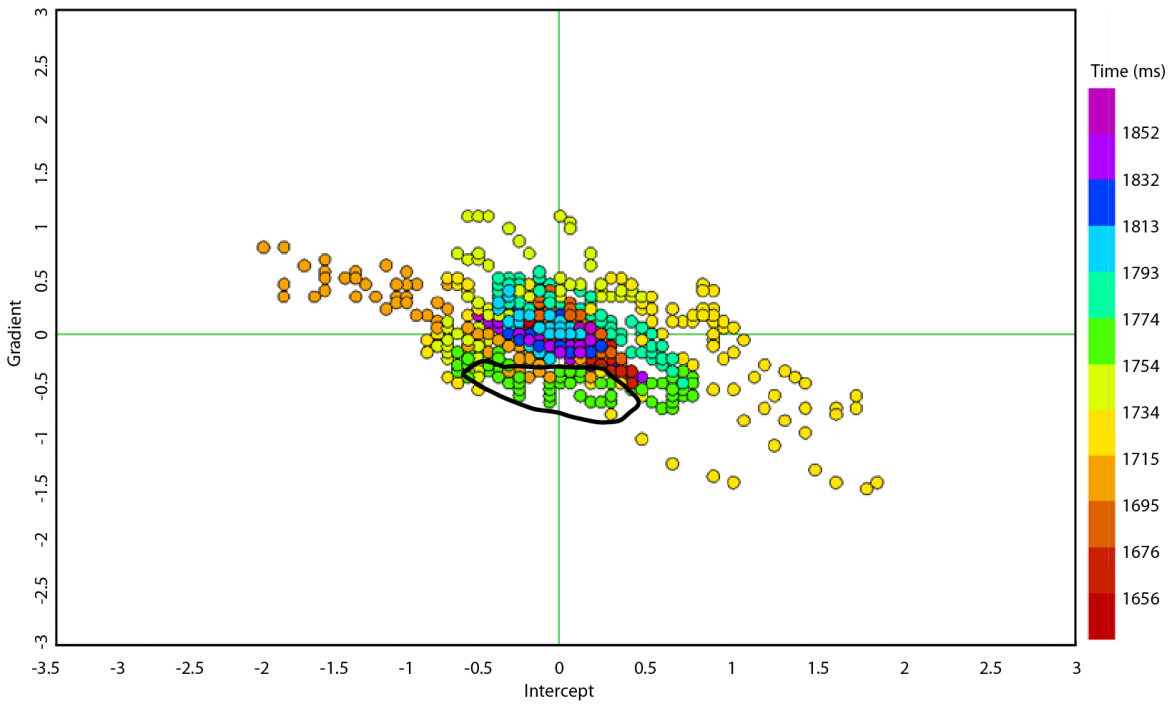

Figure 4.34: *Intercept-gradient cross plot for the response from the Stø reservoir in the Skalle well detected at approximately 1750 ms. See text for interpretation of AVO classes. Location of the reservoir is shown in Figure 4.30.*

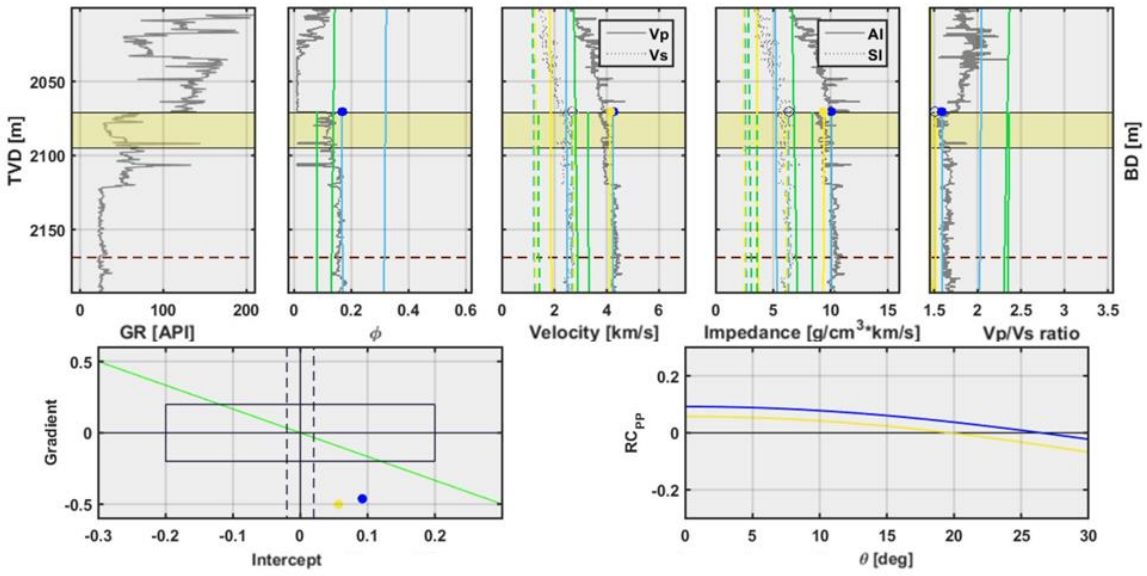

Figure 4.35: *Modelled AVO responses for the Stø sandstone in the Skalle (7120/2-3 S) well. The yellow curves represent the in situ gas case and the blue curves are the brine case. The green curves are the modelled cap rock shale trends. The gas case is interpreted as class IIp and the brine case as class I.*

Figure 4.36 shows both the Kolmule- and Stø sandstone reservoirs, the modelled compaction effects (porosity) and the corresponding rock physics properties (AI, V_p/V_s-velocities).

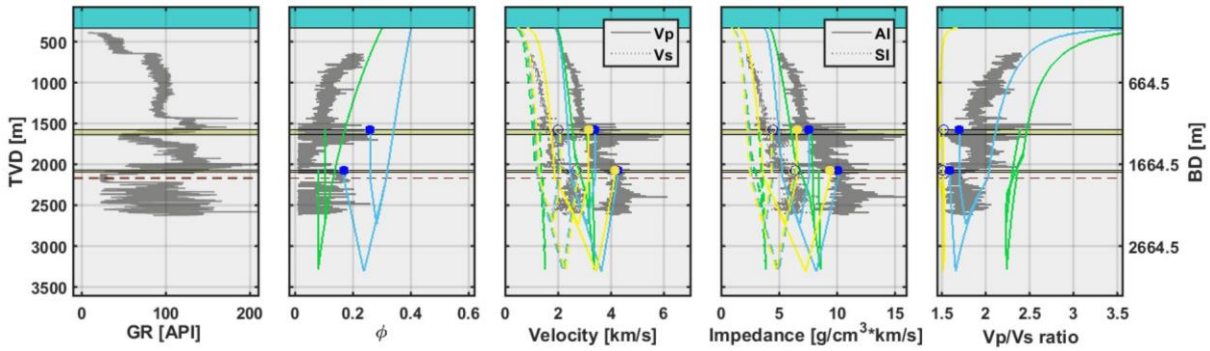

Figure 4.36: *Modelled compaction effects (porosity) and the corresponding rock physics properties (AI, V_p/V_s-velocities) for the Skalle well. The upper reservoir is the Kolmule reservoir and the lower is the Stø reservoir. The yellow curves represent the in situ gas case and the blue curves are the brine case. The green curves are the modelled cap rock shale trends.*

Myrsildre - 7120/1-2

An oil column is proven in the Hekkingen sandstone (Figure 4.30). The same procedure as for the Skalle well was used to obtain the AVO response from the angle stack data. No synthetic seismogram was generated, due to the short distance from the Skalle well. The two wells are thought to have approximately the same uplift history.

Figure 4.37shows a cross plot of intercept versus gradient made for the Hekkingen sandstone reservoir (see Figure 4.30). We see only minimal deviations from a well-defined background trend, and no obvious indications of hydrocarbons. AVO responses were modelled with rock physics based AVO modelling and the results are shown in Figure 4.38. This AVO modelling shows a class IIp response both for the brine and the in situ fluid case, which is not in full agreement with the real AVO response.

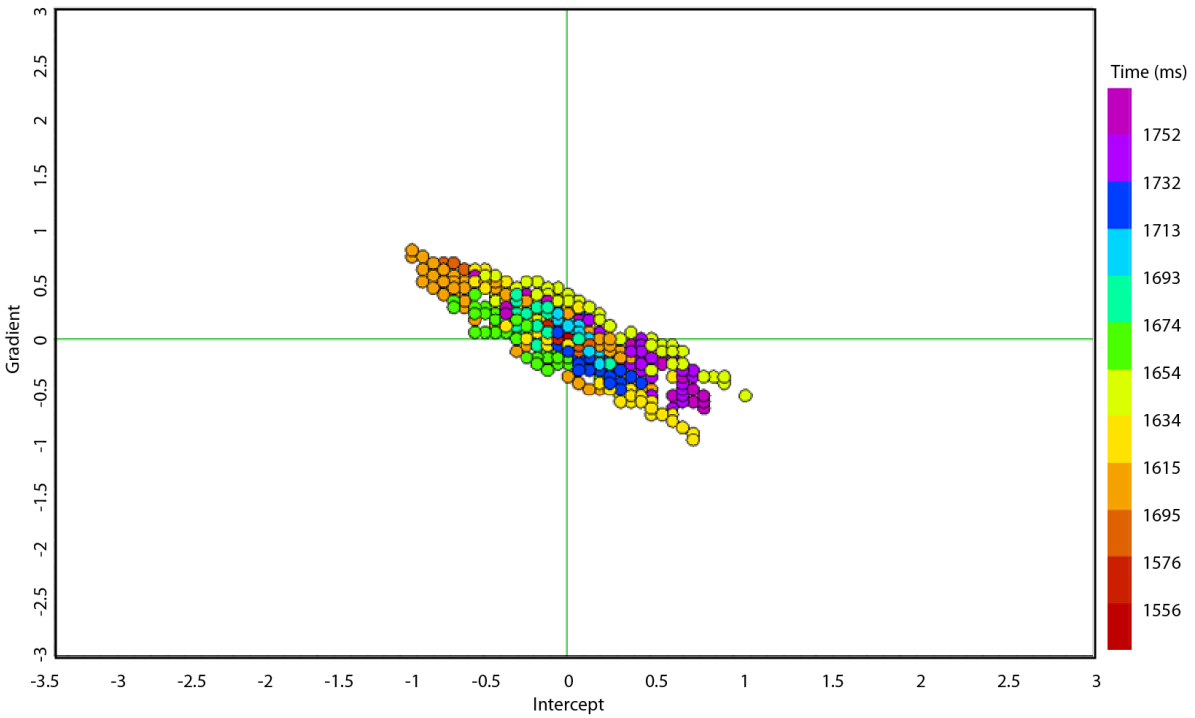

Figure 4.37: *Intercept-gradient cross plot for the response from the Hekkingen reservoir in the Myrsildre well. See text for interpretation of AVO classes. Location of the reservoir is shown in Figure 4.30.*

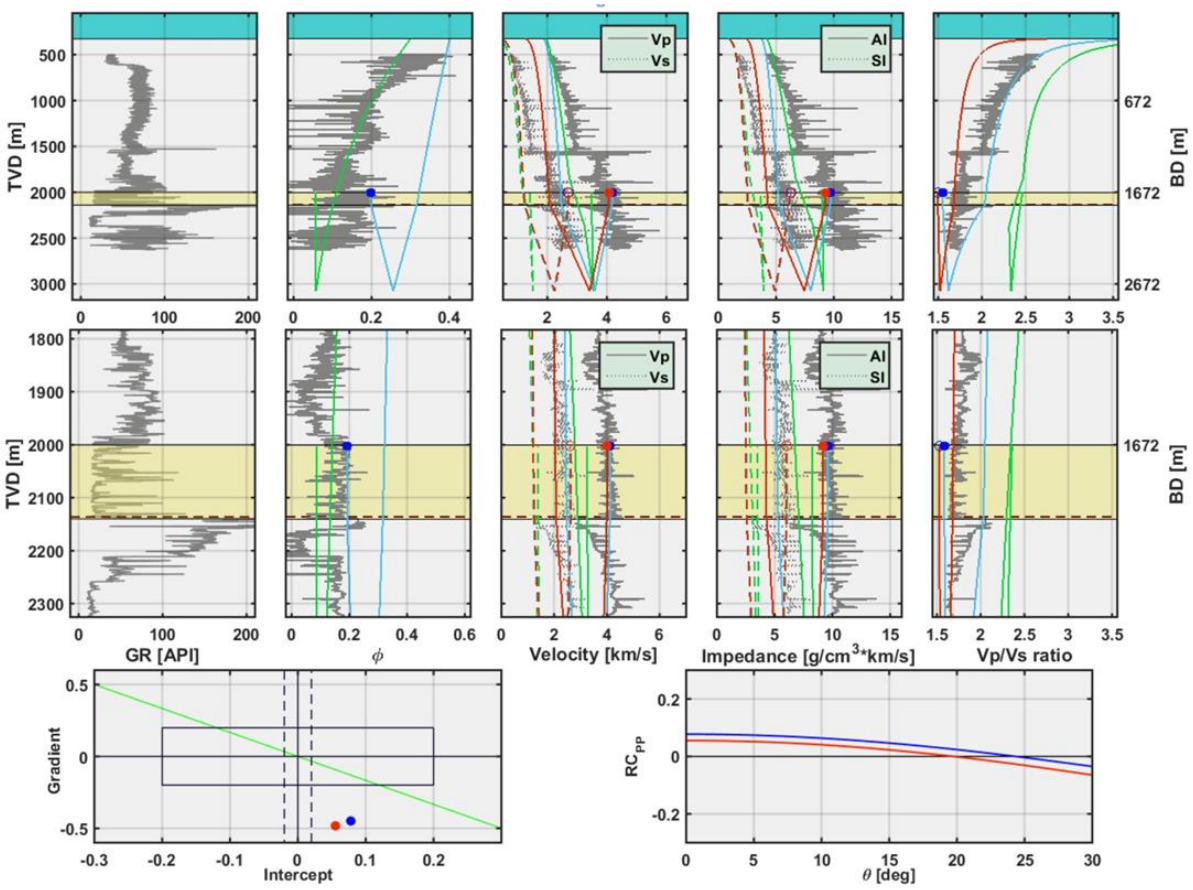

Figure 4.38: *Modelled AVO responses for the Hekkingen sandstone in the Myrsildre well. The red curves represent the in situ oil case and the blue curves are the brine case. The green curves are the modelled cap rock shale trends. Both the oil case and the brine case are interpreted as class IIp.*

Juksa – 7120/6-3 S

The Juksa well is located off the edge of the Loppa High in the Hammerfest Basin. The well encountered water with low saturation of oil (not movable) in the lower Kolmule sandstones. The same procedure was followed as for the Skalle well and a synthetic forward modelled AVO seismogram was produced Figure 4.39. In this case a simpler forward modelling (Zoeppritz-modelling) was done. The in situ AVO response from the top Kolmule sandstone is becoming increasingly negative from the near to the far stack and indicate a class II. The modelled brine response to the right gives class I to IIp, with a hard positive near that is dimming at far.

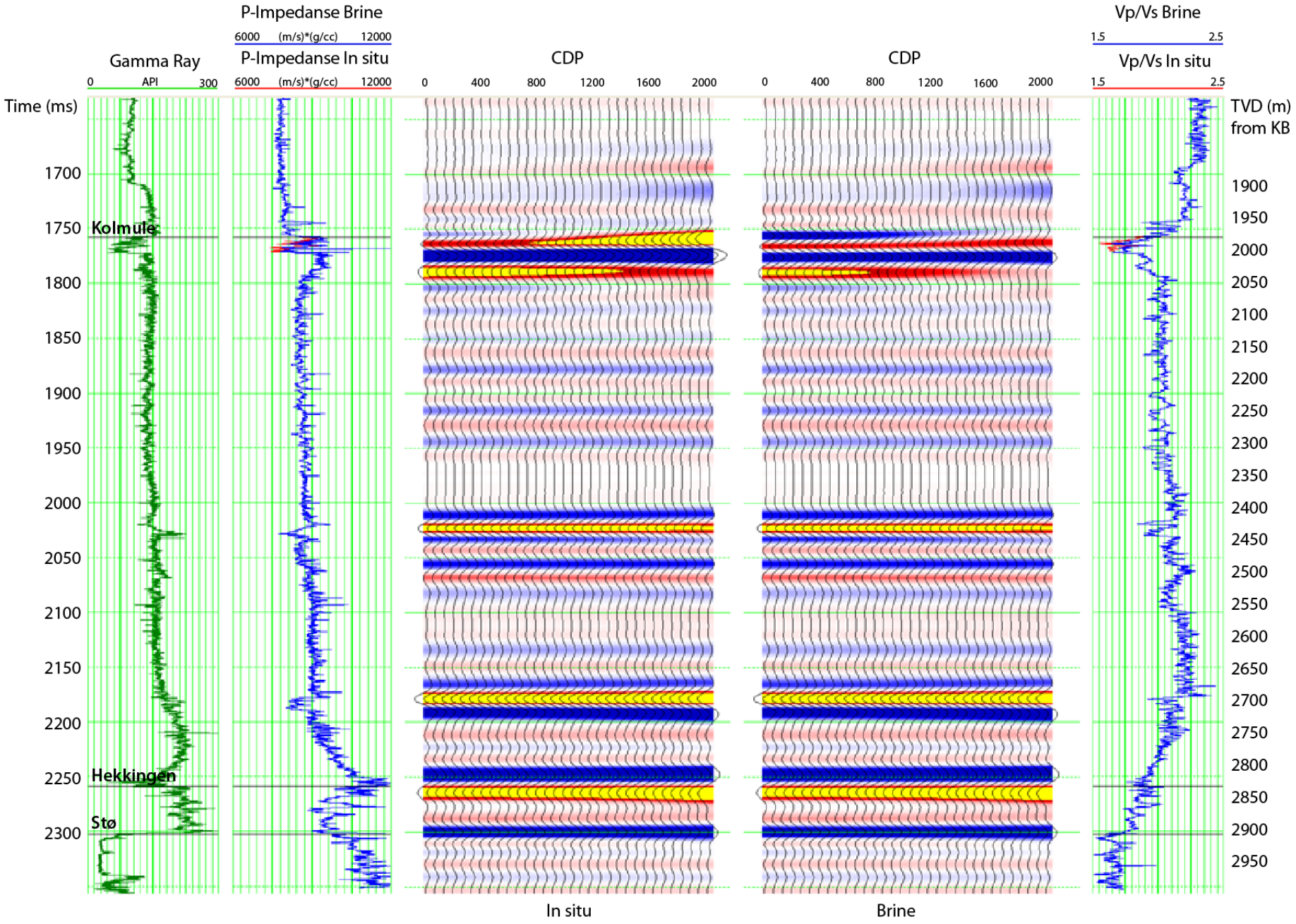
P-Impedanse Brine
6000 (m/s)*(g/cc) 12000
P-Impedanse In situ
6000 (m/s)*(g/cc) 12000
Gamma Ray
0 API 300
CDP
0 400 800 1200 1600 2000
CDP
0 400 800 1200 1600 2000
Vp/Vs Brine
1.5 2.5
Vp/Vs In situ
1.5 2.5
Time (ms)
1700
1750
1800
1850
1900
1950
2000
2050
2100
2150
2200
2250
2300
Kolmule
Hekkingen
Stø
TVD (m)
from KB
1900
1950
2000
2050
2100
2150
2200
2250
2300
2350
2400
2450
2500
2550
2600
2650
2700
2750
2800
2850
2900
2950
In situ
Brine

Figure 4.39: *Synthetic AVO seismogram generated for the Juksa well (7120/6-3 S) plotted with gamma log, P-wave impedance log, Vp/Vs-ratio log and the real (in situ) seismic AVO response. The AVO modelling was done after fluid substitution, and the modelled response represents the brine case. The reservoir levels are indicated on the logs, and the fluid substitution is shown in the logs. Oil is represented by red colour and the brine case is blue.*

The AVO response from the top Kolmule reservoir is cross plotted in Figure 4.40. The classification from the cross plot indicates a class II-IIp response. In Figure 4.41 the AVO response from rock physics based AVO modelling gives a class II and IIp for the in situ and brine case, respectively.

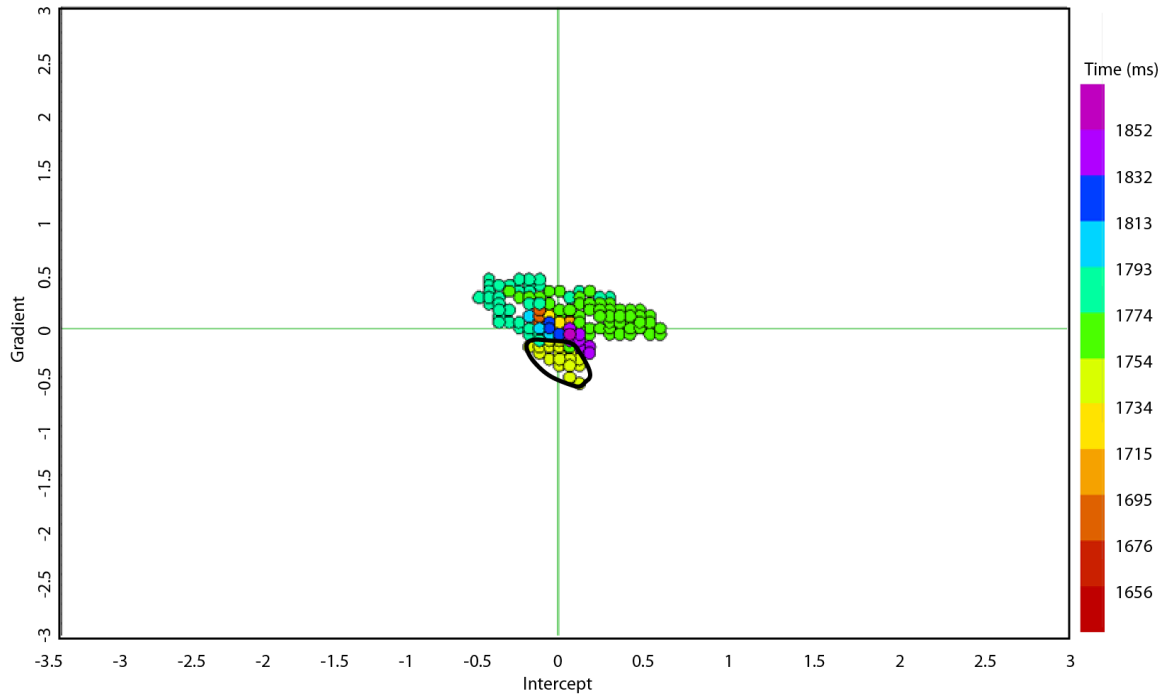

Figure 4.40: *Intercept-gradient cross plot for the response from the Kolmule reservoir in the Juksa well detected at approximately 1750 ms. See text for interpretation of AVO classes. Location of the reservoir is shown in Figure 4.30.*

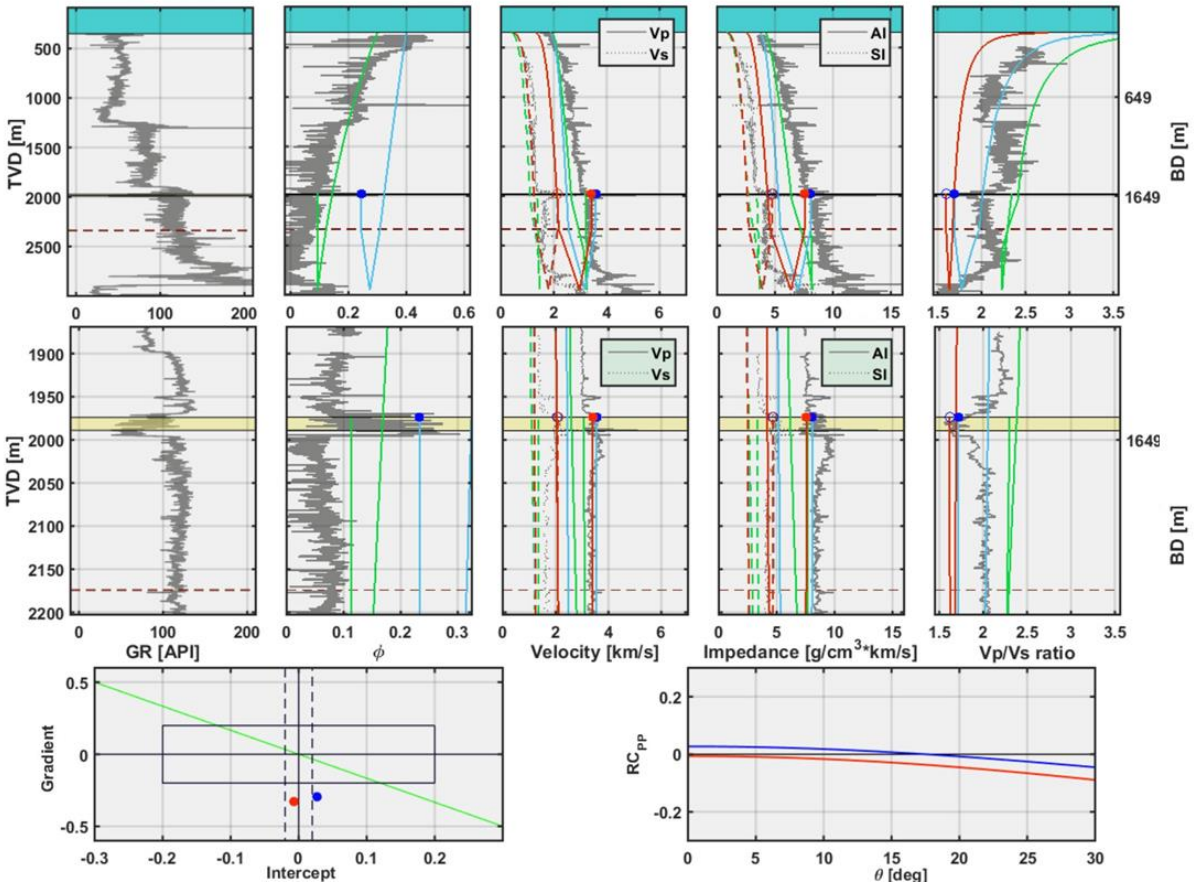

Figure 4.41: *Modelled AVO responses for the Kolmule sandstone in the Juksa well. The red curves represent the in situ oil case and the blue curves are the brine case. The green curves are the modelled cap rock shale trends. The oil case is interpreted as class II and the brine case as class IIp.*

4.6.2 Regional AVO analysis

Seismic AVO responses were modelled for the Stø reservoir sandstone using the sandstone diagenesis approach explained above. This was done for all the wells in the study area. For wells with no Stø interval, the Tubåen sandstone was chosen. The modelled AVO responses were then interpreted and classified. The modelling approach and the AVO classification are described in more detail in Chapter 3. The modelled and interpreted AVO responses are summarized in Table 4.1 along with the maximum burial depth estimates from the sandstone modelling. Figure 4.42 shows the geographical distribution for the modelled AVO responses across the western Barents Sea. Both the AVO classes and the actual fluid content in the reservoir (Stø or Tubåen Formation) are shown.

Well	AVO Class In situ	Net erosion - Sandstone modelling	Max burial - Stø TVD (BSF)
7120/9-1	II	1100 m	2597 m
7122/7-3	III	1380 m	2099 m*
7120/6-3 S	I	875 m	3004 m
7120/2-2	I	1170 m	3503 m
7120/2-3 S	IIp-I	1240 m	2976 m
7120/1-2	I	1140 m	3023 m
7220/10-1	II	1310 m	2448 m
7219/9-1	I	1230 m	2801 m
7220/8-1	II	1330 m	2250 m
7220/4-1	I	1170 m	3003 m
7321/7-1	I	1800 m	3289 m
7321/8-1	IIp-I	1805 m	2751 m
7224/6-1	II	1485 m	2200 m*
7226/2-1	IIp	1670 m	2201 m*
7324/10-1	II	1660 m	1798 m
7324/8-1	II	1760 m	1999 m
7324/7-1 S	II	1810 m	2152 m
7324/7-2	II	1735 m	1990 m
7324/8-2	IIp	1750 m	1999 m
7324/2-1	IIp	1835 m	2200 m
7324/9-1	III	1540 m	1782 m
7325/1-1	IIp	2035 m	2399 m

** Tubåen Sandstone. Used when Stø was not present.*

Table 4.1: *Modelled AVO responses for Stø sandstones along with net erosion estimates and maximum burial depth estimates from the sandstone modelling. See Figure 4.42 for location of wells.*

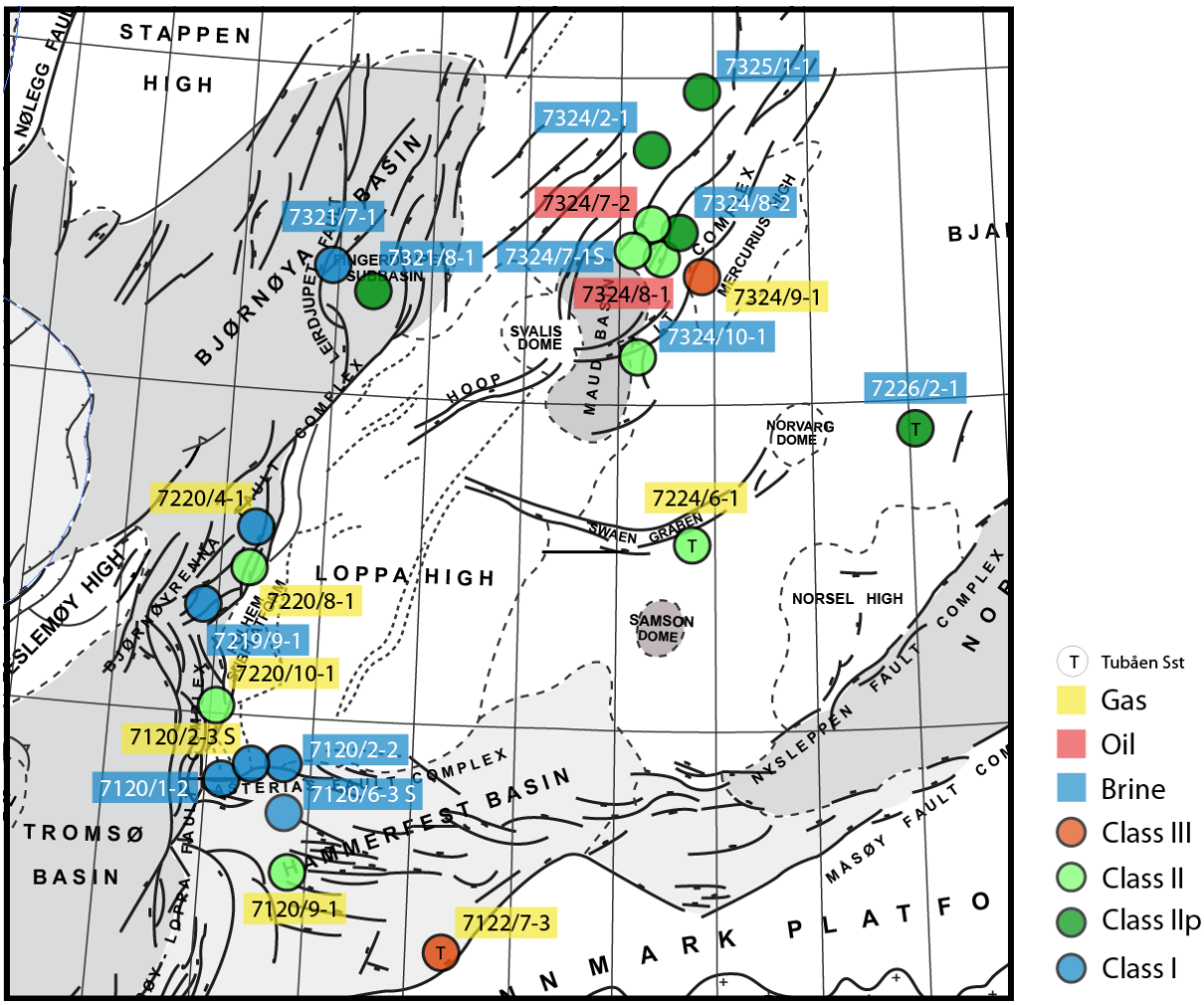

Figure 4.42: *Geographical distribution for the AVO responses from sandstone modelling. Both the modelled AVO classes and the actual fluid content in the reservoir (Stø or Tubåen Formation) are shown. The structural elements are modified from Faleide et al. (2010).*

The AVO response was modelled for the top reservoir to cap rock interface. This means that even if the response is indicating gas, in reality the reservoir can also contain oil further down in the structure. This is the case for instance in the Skrugard Field, which has a gas cap above the oil.

Most of the modelled northern and eastern wells are classes II and IIp, while the western and southern wells are class I or class II. The northern Bjarmeland Platform and the Hoop fault complex have similar classes across the area, while the Bjørnøya Basin and the western margin of the Loppa High have more variation in the interpreted classes. The Hammerfest Basin near the southern edge of the Loppa High shows class I, while the rest of the Hammerfest Basin is variable.

In Figure 4.43 all the modelled wells are plotted in an intercept versus gradient cross plot together with the corresponding in situ fluids. Both the brine filled and the hydrocarbon filled sandstones are included in the diagram. The plot also shows the interpretation of the AVO classes.

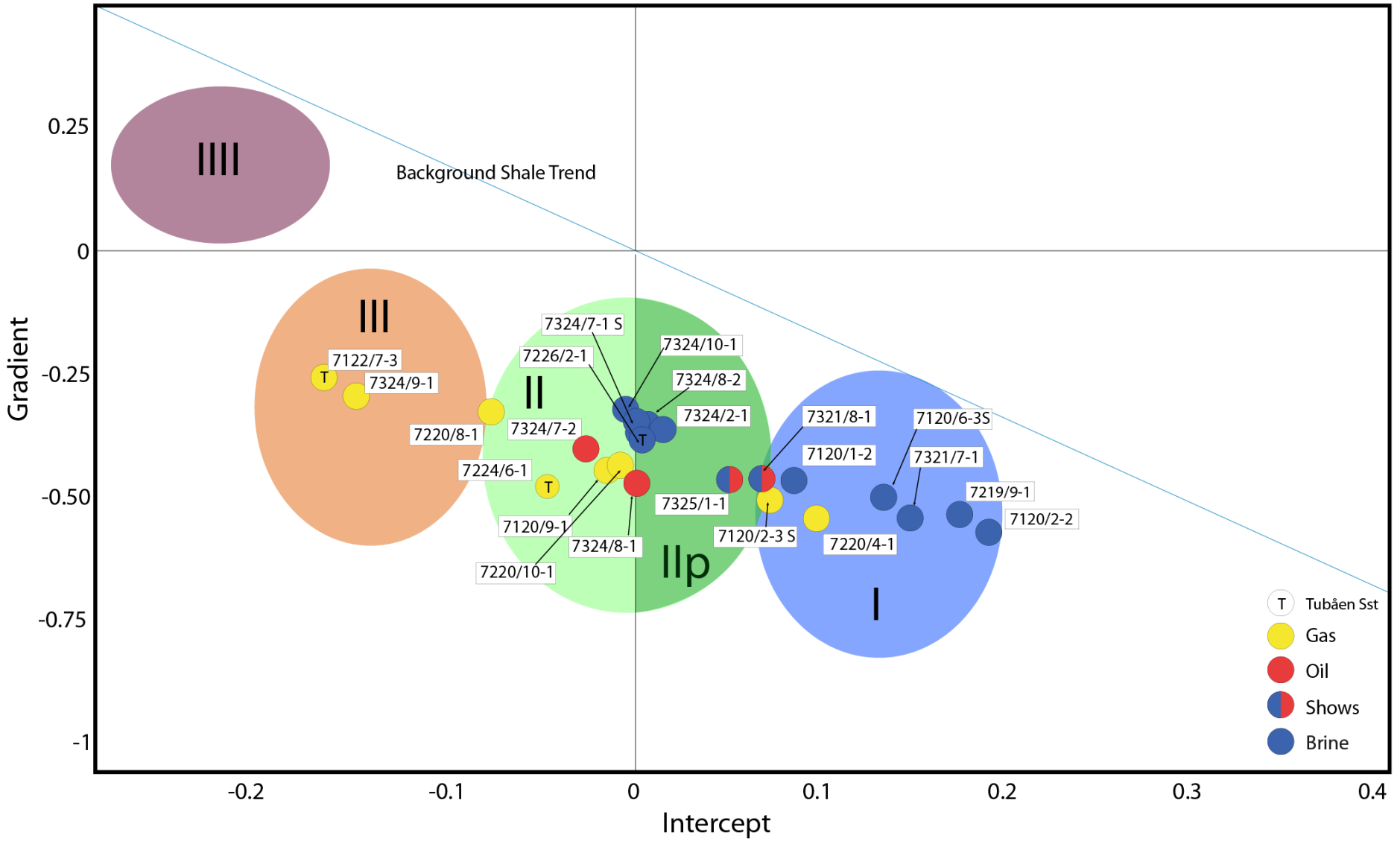
IIII
Background Shale Trend
III
II
IIp
I
7122/7-3
7324/9-1
7220/8-1
7324/7-1 S
7226/2-1
7324/10-1
7324/8-2
7324/2-1
7324/7-2
7224/6-1
7120/9-1
7324/8-1
7220/10-1
7325/1-1
7321/8-1
7120/1-2
7120/2-3 S
7120/6-3S
7321/7-1
7219/9-1
7120/2-2
7220/4-1
T
Tubåen Sst
Gas
Oil
Shows
Brine
Gradient
Intercept
0.25
0
-0.25
-0.50
-0.75
-1
-0.2
-0.1
0
0.1
0.2
0.3
0.4

Figure 4.43: *AVO responses from sandstone modelling plotted in an intercept versus gradient cross plot together with the actual fluid content in the reservoir. The interpreted AVO classes are shown as coloured ellipses. See Figure 4.42 for location of wells.*

In Figure 4.44 trend lines area suggested for brine, oil and gas. The trend lines seem to move away from a background shale trend. This change in AVO class is typical when moving from brine filled to hydrocarbon filled reservoirs (Avseth, 2015, Avseth and Lehocki, 2016).

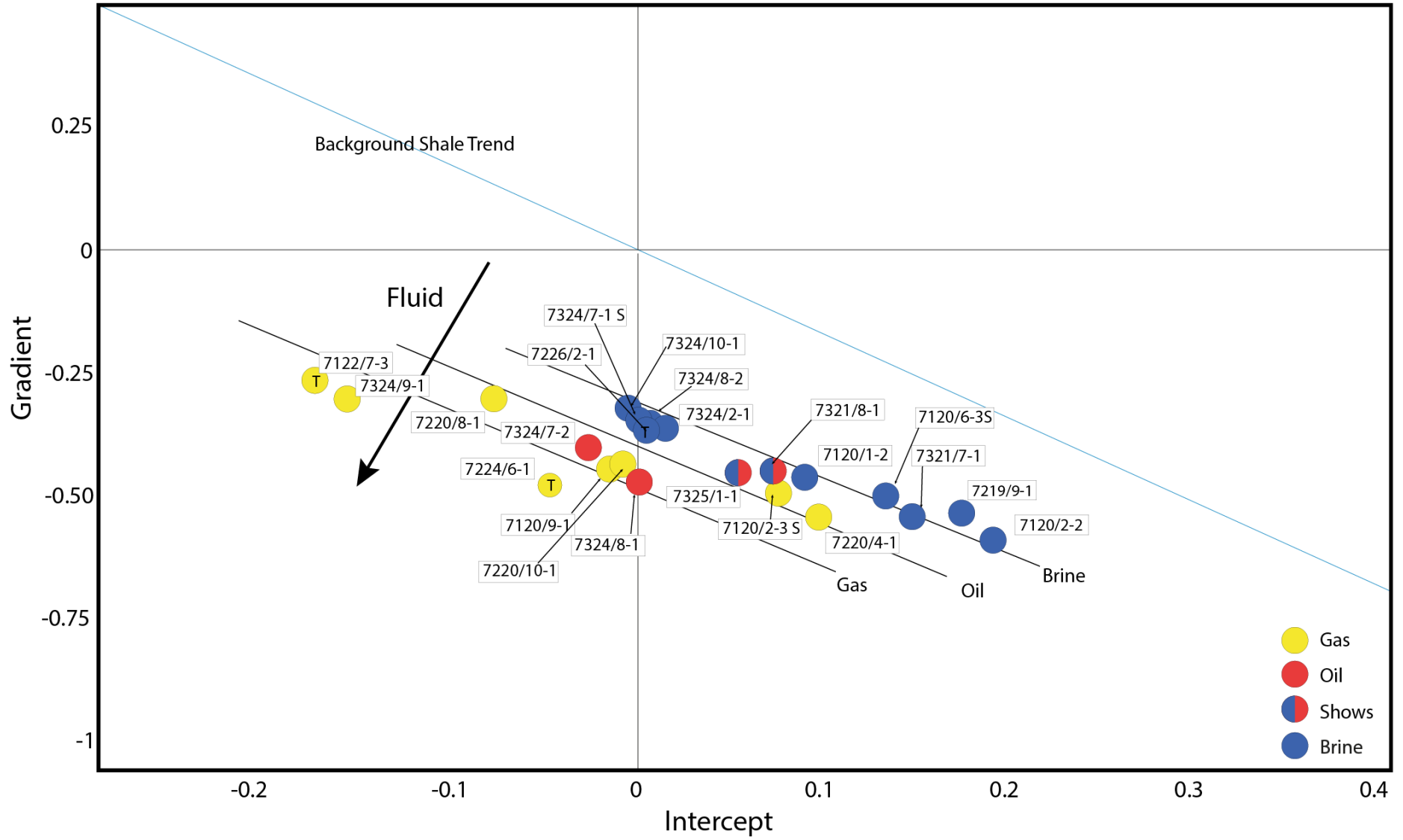
Background Shale Trend
Fluid
Gradient
Intercept
0.25
0
-0.25
-0.50
-0.75
-1
-0.2
-0.1
0
0.1
0.2
0.3
0.4
7122/7-3
7324/9-1
7220/8-1
7324/7-2
7224/6-1
7120/9-1
7220/10-1
7324/8-1
7324/7-1 S
7226/2-1
7324/10-1
7324/8-2
7324/2-1
7325/1-1
7321/8-1
7120/1-2
7120/2-3 S
7220/4-1
7120/6-3S
7321/7-1
7219/9-1
7120/2-2
Gas
Oil
Brine
Gas
Oil
Shows
Brine

Figure 4.44: *Intercept versus gradient cross plot with suggested trend lines for brine, oil and gas. The trend lines move away from the background trend when the reservoir change from brine filled to hydrocarbon filled. See Figure 4.42 for location of wells.*

For all the sandstone intervals maximum burial depth were found using the net erosion estimate from the sandstone modelling, and the maximum burial depth was assigned to each well (Figure 4.45). Now we also see a clear trend with increasing burial depth indicated by the arrow in the diagram. The observations described here will be further discussed in Chapter 5.

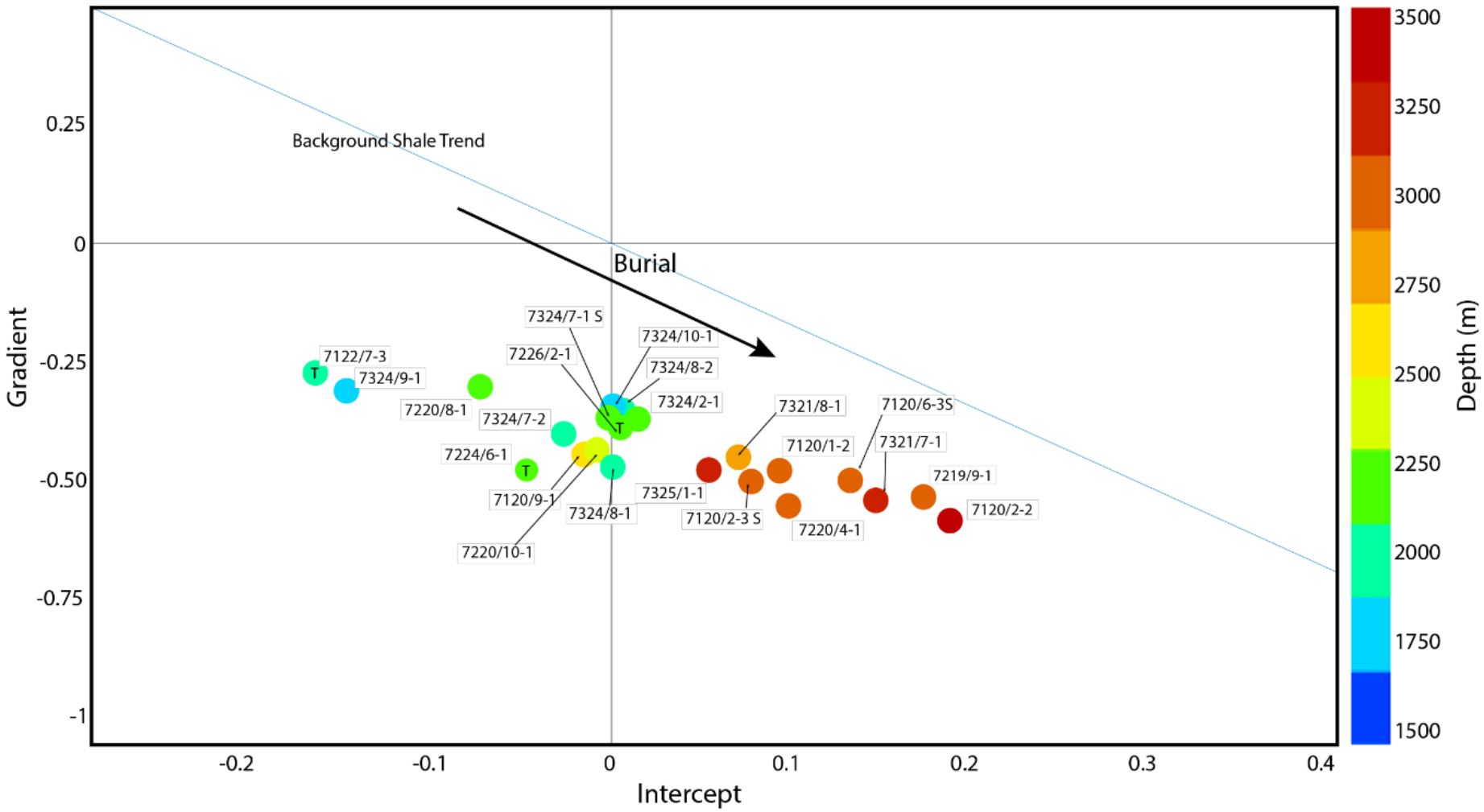
Background Shale Trend
Burial
Gradient
Intercept
Depth (m)
0.25
0
-0.25
-0.50
-0.75
-1
-0.2
-0.1
0
0.1
0.2
0.3
0.4
3500
3250
3000
2750
2500
2250
2000
1750
1500
7122/7-3
7324/9-1
7220/8-1
7324/7-2
7224/6-1
7120/9-1
7220/10-1
7324/8-1
7324/7-1 S
7226/2-1
7324/10-1
7324/8-2
7324/2-1
7325/1-1
7120/2-3 S
7321/8-1
7120/1-2
7220/4-1
7120/6-3S
7321/7-1
7219/9-1
7120/2-2
T

Figure 4.45: *Intercept versus gradient cross plot and maximum burial depths to the top of the reservoir sandstones. The arrow in the diagram indicates the trend with increasing burial depth. See Figure 4.42 for location of wells.*

Chapter 5 – Discussion

Below we discuss the various workflows for estimating net erosion including the method using resistivity. The new trend maps and the more detailed maps from seismic velocities are compared and the effects of net erosion on seismic AVO signatures are also discussed.

5.1 Comparison and validation of reference trend lines

Robust and well tested reference trends are important when doing calculations of net erosion. In this study a number of reference trend lines were tested to obtain net erosion estimates from different methods. In this chapter the reference trends will be discussed, evaluated and compared with trend lines from previous studies.

5.1.1 North Sea velocity reference trend

Due to the low density of data in areas of the Barents Sea with no or little net erosion, a reference velocity-depth trend line was established from the North Sea. The reference trend was based on data from the Viking Graben which is thought to have experienced no net erosion (Storvoll et al., 2005)

By comparing the North Sea reference trend to wells from areas in the Barents Sea with as little net erosion as possible, the trend line can be verified also for use in the Barents Sea.

In Figure 5.1 the established North Sea reference trend line is plotted with the Senja Ridge velocity log. From previous studies (Faleide et al., 2010) and from our seismic interval velocity results, the Senja Ridge is thought to have minimal net erosion (Figure 5.2). The ridge has probably experienced a net erosion of maximum 300 meters.

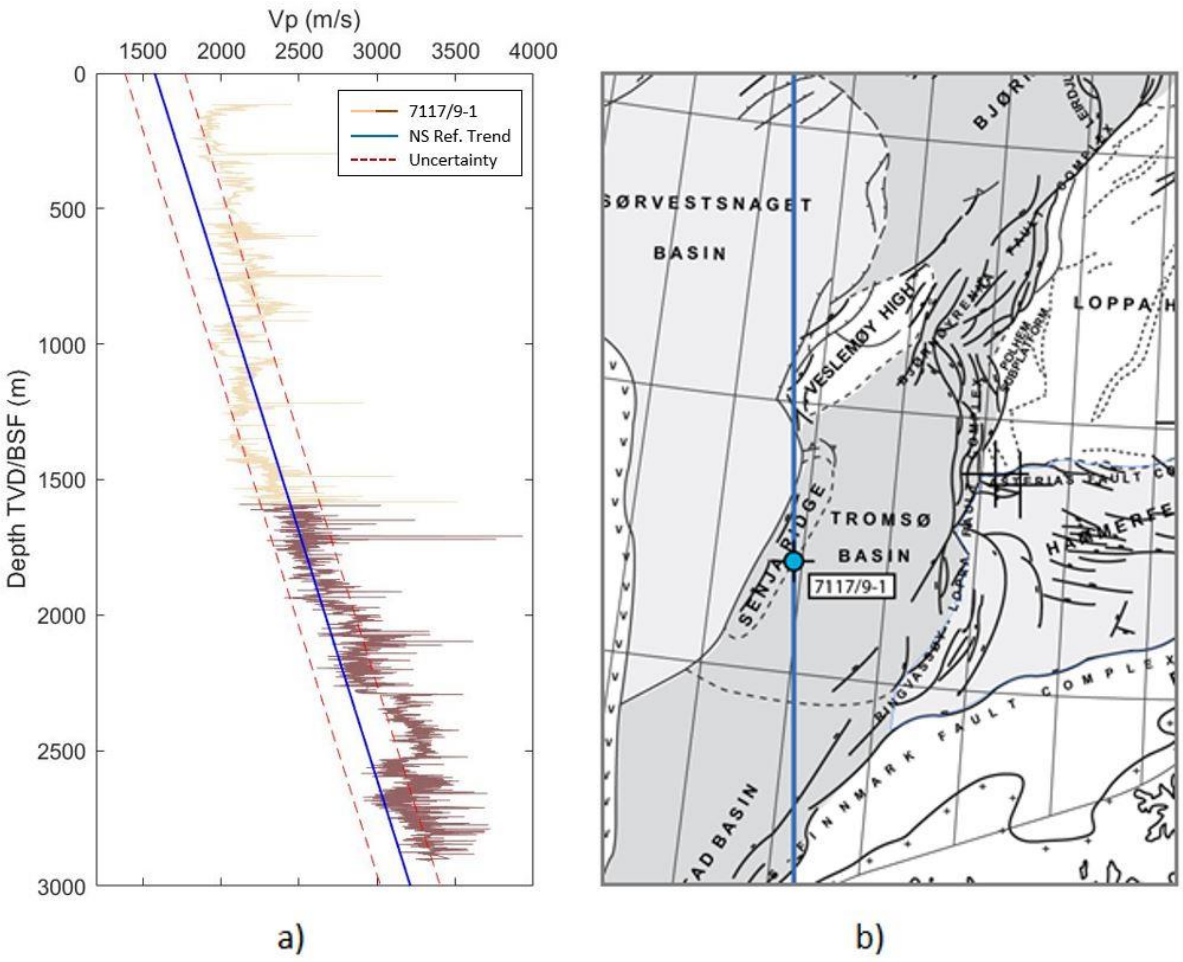

Figure 5.1: *a) The velocity log from the Senja Ridge well and the P-wave velocity reference depth trend from the North Sea. b) Location of the Senja Ridge well in the western Barents Sea. Structural elements modified from Faleide et al. (2010).*

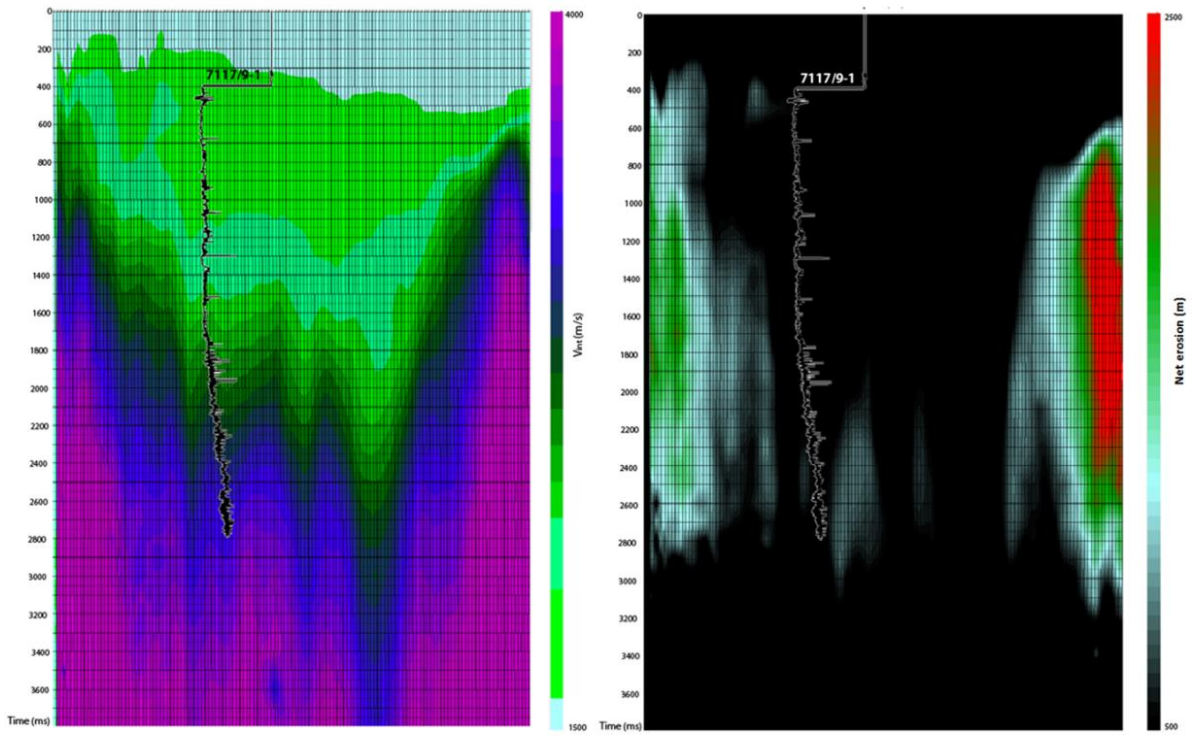

Figure 5.2: *North-south section trough the interval velocity cube (a) and the net erosion cube (b). The net erosion section indicates minimal net erosion in the well position. Location of the well is shown in Figure 5.1. See text, Figure 4.13 and Figure 4.14 for further explanations of the interval velocity- and net erosion sections. The vertical axis on the sections is TWT and the annotated time interval is 200 ms.*

A trend line established on Barents Sea data had been preferable, but since the amount of well data is not sufficient in the areas with no net erosion, we think combining the North Sea trend and the few Barents Sea wells in this way is a good approach. Although the North Sea reference trend line coincides with the Senja Ridge trend, several possible uncertainties should be kept in mind when using a trend line from another basin. These uncertainties are also related to the assumptions made in Chapter 3.1.1.

A *linear velocity-depth trend* was assumed, but in practice this is often not the case for thick well log intervals in any basin.

The *thermal history* can vary from basin to basin. Due to the size of the study- and reference areas variations in temperature gradients will exist. The thermal gradients in the Barents Sea are somewhat higher than in the North Sea and range from about 35-45ºC/km. (Ref). In the reference area in the north Viking Graben the temperature gradient can vary from 32ºC/km to 36ºC/km (Brigaud et al., 1992).

Change in *lithology* from one basin to another is not accounted for. For the net erosion estimates using well log velocities homogenous shales have been assumed. The Barents Sea shales can vary from the ones in the North Sea, and local variations in lithology both in the North Sea and the Barents Sea can occur. The amount of silt and changing clay types can alter the velocities and thereby the net erosion estimate. This is again strongly influenced by the provenance area and diagenetic processes (Figure 5.3). The velocity will increase with increasing silt content.

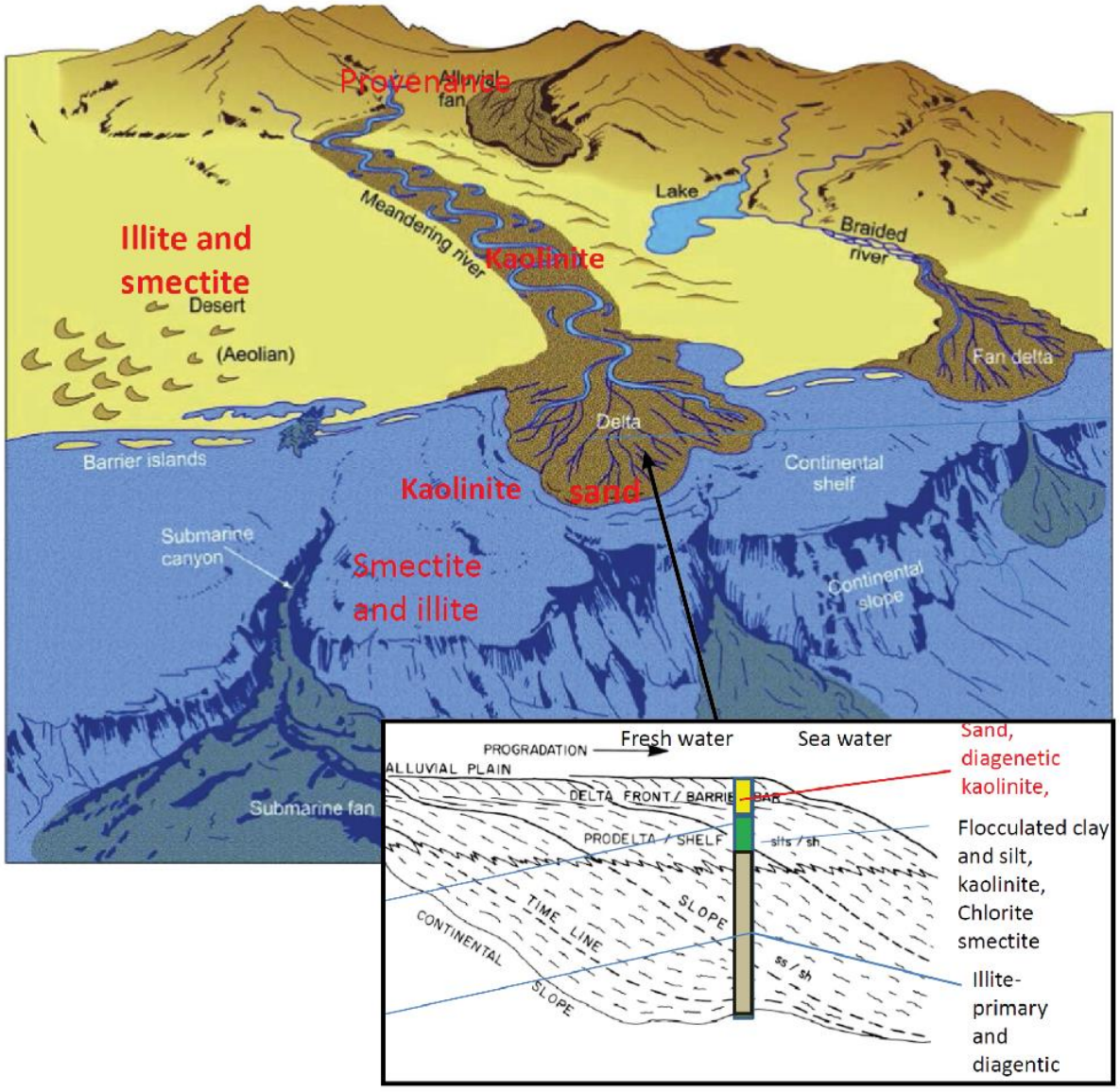

Figure 5.3: *Changing lithologies can alter the velocities of the rocks and thus the net erosion estimates. Such changes are strongly influenced by provenance (top figure) and diagenetic processes (bottom figure). Modified from Mondol et al. (2007).*

When the shale is buried diagenetic changes will alter the properties of the rock. The transformation from smectite to illite occur when the shale temperatures is above approximately 70ºC (Bjørlykke and Jahren, 2015). During illitization the shale is also prone to additional cementation. Quartz is a by-product in addition to water, and this can lead to stiffening of the rock and even higher velocities below 70ºC the illite content increases, and will thus lead to elevated velocities (Mondol et al., 2007) (Figure 5.4).

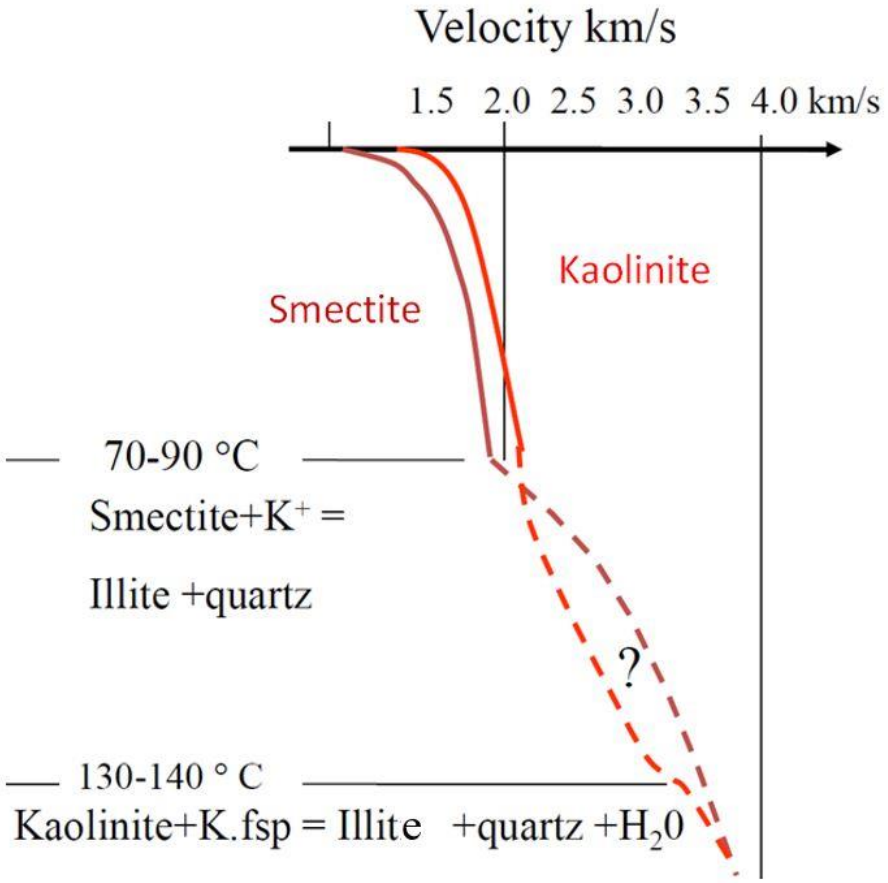

Figure 5.4: *Conceptual figure showing alteration of shale velocity with burial. When the shale is subjected to temperatures above approximately 70°C also diagenetic processes will influence the velocity change in the shale (Bjørlykke and Jahren, 2015). Modified from (Mondol et al., 2007).*

To illustrate the effect transformation from smectite to illite has on the velocities a new trend line was established by using the combination of diagenetic modelling and rock physics modelling described above (Figure 5.5). This trend line was based on input data from the North Sea. In the figure this trend line is plotted with the Senja Ridge velocity log and published trend lines. The change in the modelled line below 2000 meters depth represents the onset of illitization, as also seen in Figure 5.4.

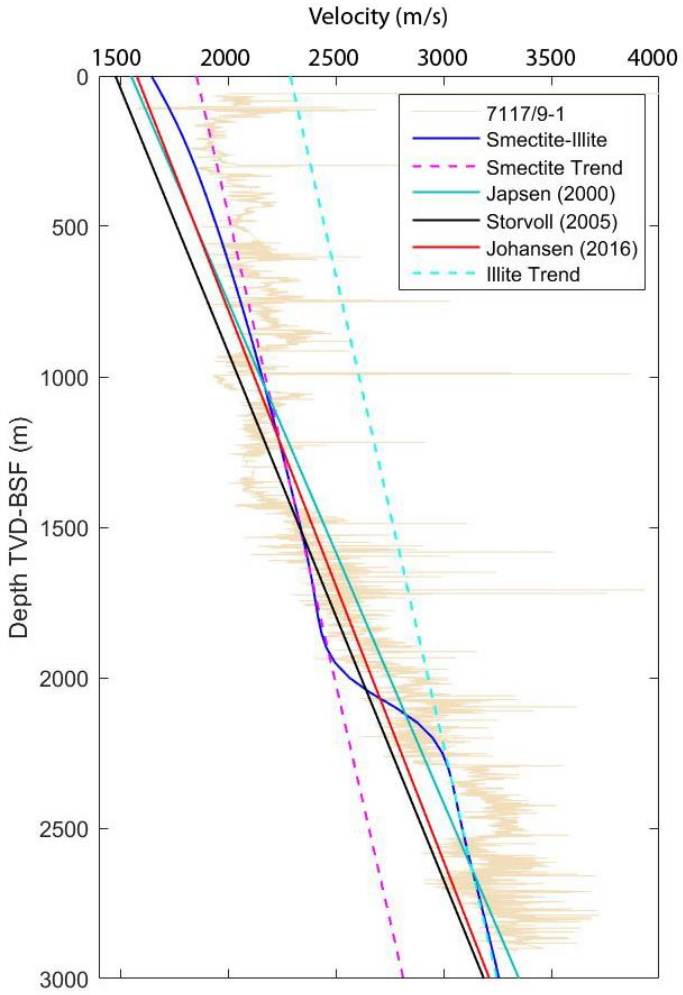

Figure 5.5: *The established illite-smectite reference trend line plotted with the Senja Ridge velocity well log and reference trend lines from the North Sea. The new reference trend line was established by the combination of diagenetic modelling and rock physics modelling described in Chapter 3. The onset of illitization occurs at approximately 2000 meters depth. See Figure 1.1 for location of well.*

Comparison with previous published studies

The established reference trend line coincides quite well with previously published trend lines from Storvoll et al. (2005), Japsen (2000) and Baig et al. (2016), but our trend line is a little steeper than for example the Japsen- and Baig lines (Figure 5.5 and Figure 5.6a).The Storvoll trend line is based on several formations including the Shetland Group, which is dominated by smectite- and illite rich shales (Storvoll et al., 2005). Our trend line is based on the Shetland Group. The Japsen trend line has somewhat higher velocities than the Storvoll trend line. This trend line is based on wells further south in the North Sea where the Shetland Group is slightly richer in carbonates (Japsen, 2000).

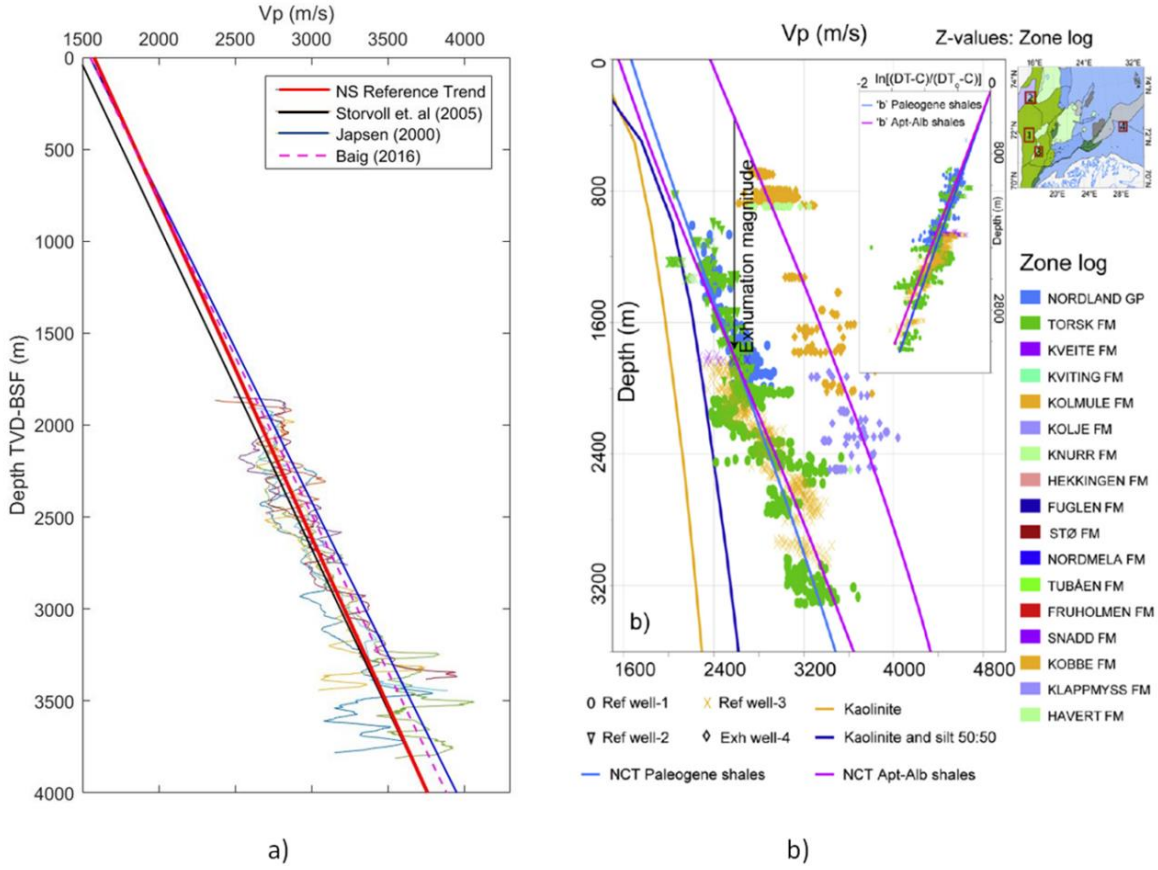

Figure 5.6: *a) Comparison of the North Sea reference trend line from this study with previous established trend lines. b) The Baig (2016) trend lines established for the Kolmule- and the Torsk Formation in the Barents Sea. Index map shows location of wells used to establish their velocity-depth trends.*

Baig et al. (2016) recently established a trend line based on three wells in the westernmost Barents Sea (Figure 5.6b). As seen in the figure the well log velocities vary significantly around the trend line. Compared to the North Sea trend lines, which are based on a large number of wells from a well-tested area, the data base is limited. However, an obvious strength with the Baig curve is that it is from the Barents Sea where the net erosion is estimated. The Baig trend is similar to the Japsen trend, and will give smaller net erosion estimates than the other trend lines. Only small changes in reference trend lines will cause changes in the net erosion estimate. We also see from Figure 5.6a that the trend lines deviate more from each other with increasing depth. Depending on the reference curve used, differences in net erosion around 200-300 m can occur. As the number of wells drilled in the western parts of the Barents Sea increases, they should be included to improve this local reference trend.

5.1.2 Resistivity shale reference trend

The same area in the North Sea was chosen for the resistivity reference trend as for the velocity reference trend line. The Shetland Group and the same processing method were used for the resistivity reference trend line as for the velocity trend line. But still, 15 wells is a relatively small number of wells compared to for example the amount of data the Storvoll velocity study is based on.

The lack of wells in areas with little or no net erosion is also in this case the reason why a resistivity reference trend from the Barents Sea was not established. Instead, as for the velocity trend, the North Sea resistivity trend line was compared to the Senja Ridge well (7117/9-1 (Figure 5.7). The reference trend line coincides well with the Senja Ridge resistivity log. This indicates that the depth-resistivity relationship established from the North Sea can be used as reference in the Barents Sea. Two wells further west were also tested to validate the trend line, and gave similar results as for the Senja Ridge.

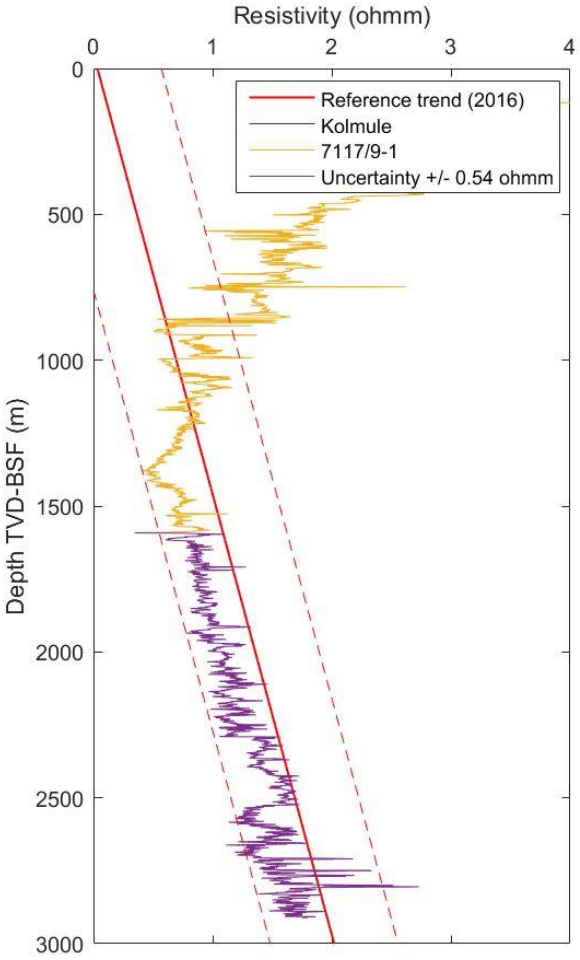

Figure 5.7: *The Senja Ridge resistivity well log (7117/9-1) compared to the North Sea resistivity reference trend. The uncertainty range is illustrated by the red stippled lines.*

5.2 Comparison and discussion of results from different methods

In this study a number of methods were used for estimation of net erosion. In total six methods were tested. Three of the methods were tested on a regional scale. The seismic velocity method was also used on regional data and is discussed further in Chapter 5.3.

P-wave velocity trends for shales, resistivity trends for shales and the sandstone diagenetic approach were tested on all the wells in the study area. The diagenetic sandstone- and shale velocity estimates gave similar results across the study area. Results from resistivity, on the other hand, deviate from the other methods. In Figure 5.8, Figure 5.9 and Table 5.1 results from all the methods are shown and compared to each other.

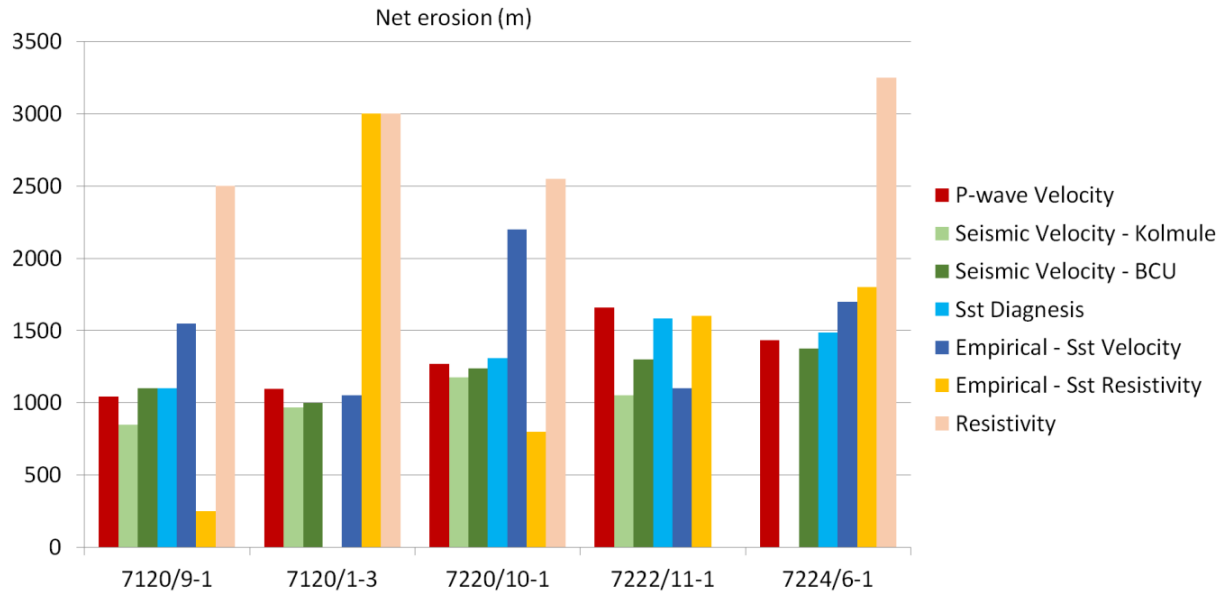

Figure 5.8: *Comparison of net erosion results from six different methods including P-wave velocity and resisitivty for shales (red and light pink), seismic velocity, sandstone diagenesis and empirical velocity- and resistivity trends for sandstones. See Figure 1.1 for location of wells.*

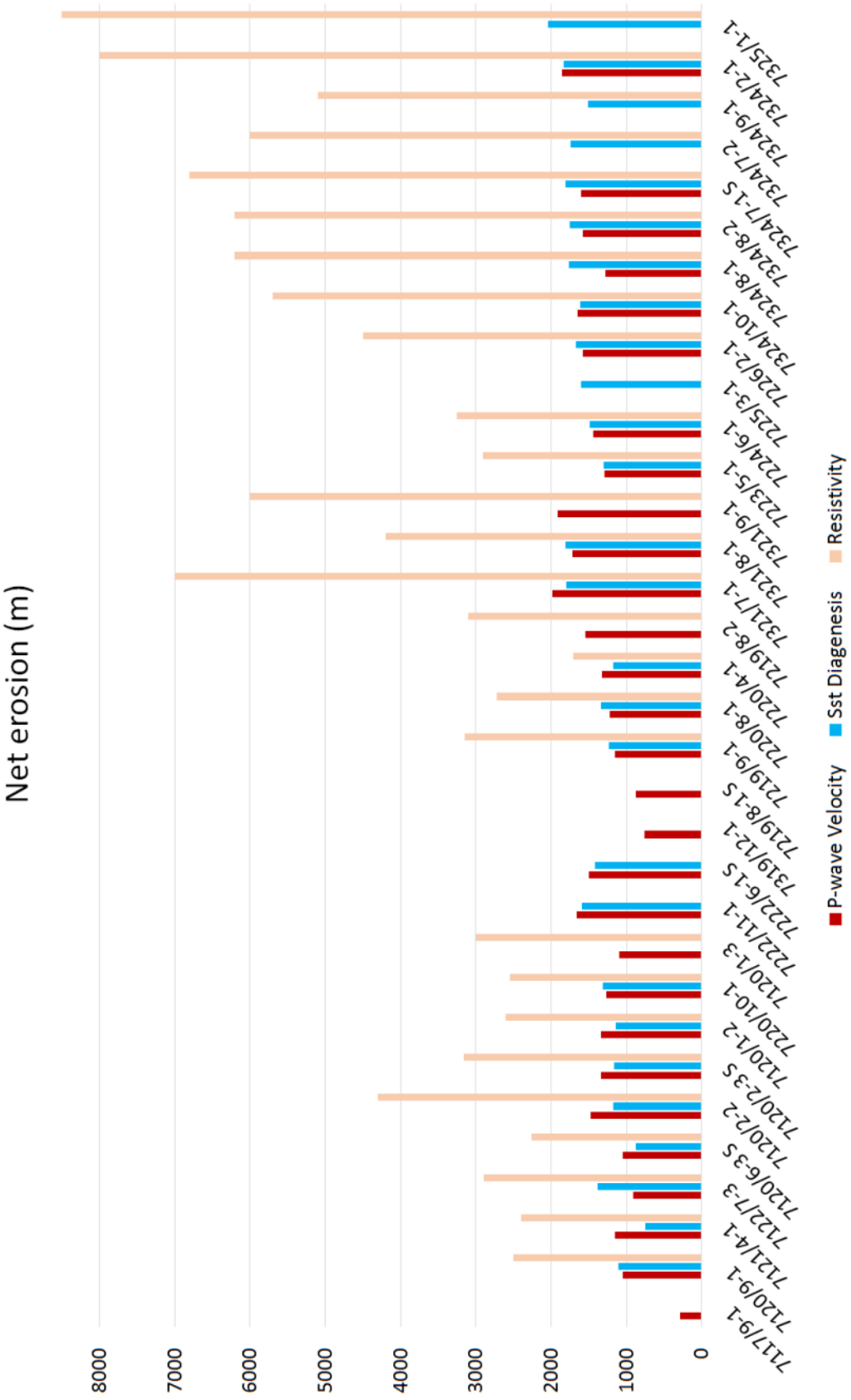

Figure 5.9: *Comparison and summary of net erosion estimates for all the wells in the data set. The P-wave velocity-, the sandstone diagenesis- and resistivity approach are included. See Figure 1.1 for location of wells.*

	Velocity data (m/s)		Resistivity data (ohm)
Well (nr. – name)	**NCT Shale**	**Sandstone diagenesis**	**NCT Shale**
Tromsø Basin			
7117/9-1 – Senja Ridge	287 m	NaN	NaN
Hammerfest Basin			
7120/9-1 – Snøhvit Albatross	1044 m	1100 m	2500 m
7121/4-1 – Snøhvit North	1149 m	750 m	2400 m
7122/7-3 – Goliat	904 m	1380 m	2890 m
7120/6-3 S – Juksa	1047 m	875 m	2260 m
7120/2-2	1468 m	1170 m	4300 m
Loppa High			
7120/2-3 S – Skalle	1338 m	1240 m	3160 m
7120/1-2 – Myrsildre	1330 m	1140 m	2600 m
7220/10-1 – Salina	1271 m	1310 m	2550 m
7120/1-3 – Gotha*	1098 m	NaN	3000 m
7222/11-1 – Caurus*	1657 m	1585 m	NaN
7222/6-1S – Obesum*	1500 m	1420 m	NaN
Bjørnøya Basin			
7319/12-1 – Pingvin	758 m	NaN	NaN
7219/8-1 S	876 m	NaN	NaN
7219/9-1	1152 m	1230 m	3150 m
7219/8-2 – Iskrystall	1545 m	NaN	3100 m
7220/8-1 – Skrugard	1223 m	1330 m	2720 m
7220/4-1 – Kramsnø	1323 m	1170 m	1700 m
Fingerdjupet Sub-basin			
7321/7-1	1981 m	1800 m	7000 m
7321/8-1	1718 m	1805 m	4200 m
7321/9-1	1907 m	NaN	6000 m
Bjarmeland Platform			
7223/5-1 – Obseum Apprisal	1291 m	1295 m	2900 m
7224/6-1 – Arenaria	1434 m	1485 m	3250 m
7225/3-1 – Norvarg*	NaN	1600 m	NaN
7226/2-1 – Ververis	1581 m	1670 m	4500 m
7324/10-1 – Alpha	1647 m	1660 m	5700 m
Hoop Fault Complex Area			
7324/8-1 – Wisting Central	1277 m	1760 m	6200 m
7324/7-1 S – Wisting Alternative	1603 m	1810 m	6800 m
7324/7-2 – Hanssen	NaN	1735 m	6000 m
7324/8-2 – Bjaaland	1579 m	1750 m	6200 m
7324/2-1 – Apollo	1858 m	1835 m	8000 m
7324/9-1 – Mercury	NaN	1510 m	5100 m
7325/1-1 – Atlantis	NaN	2035 m	9400 m

**Lacking Kolmule*

Table 5.1: *Comparison and summary of net erosion estimates for all the wells in the data set. The P-wave velocity-, the sandstone diagenesis- and resistivity approach are included. See location of wells in Figure 1.1. The net erosion results are from the same three methods as shown in Figure 5.9.*

5.2.1 Net erosion using well log velocity data from shales

As discussed above using log velocities is a well-tested method for net erosion estimation, but several factors should be kept in mind when evaluating the results.

As we saw above shale mineralogy can vary and will influence the estimations. Also the thickness of the shale unit will matter. The Kolumle Formation is present over large areas in the western Barents Sea, and the formation has similar shaly lithology in most wells, but the sand content is higher close to the Troms-Finnmark Fault Complex and in the Ringvassøy-Loppa fault Complex (Figure 1.1).

To select the best wells for estimation were important, but choosing these was not always straightforward. Some sonic logs were incomplete or missing completely, while other wells had poor gamma ray logs that made the estimation of clay content challenging. In other wells the Kolmule Formation was lacking completely. In these cases the shaly Torsk Formation was used.

On the Loppa High both the Kolmule- and Torsk Formations are missing in some of the wells. In these cases the Snadd Formation was used. After testing we found that the illite reference trend line discussed in Chapter 5.1.1 could be used. The results are displayed in Figure 5.10 and give approximately 1500-1600 meters net erosion for the two wells. Estimations in the Caurus well (7222/11-1) by Walderhaug (2012) using diagenesis of sandstones gave a similar result.

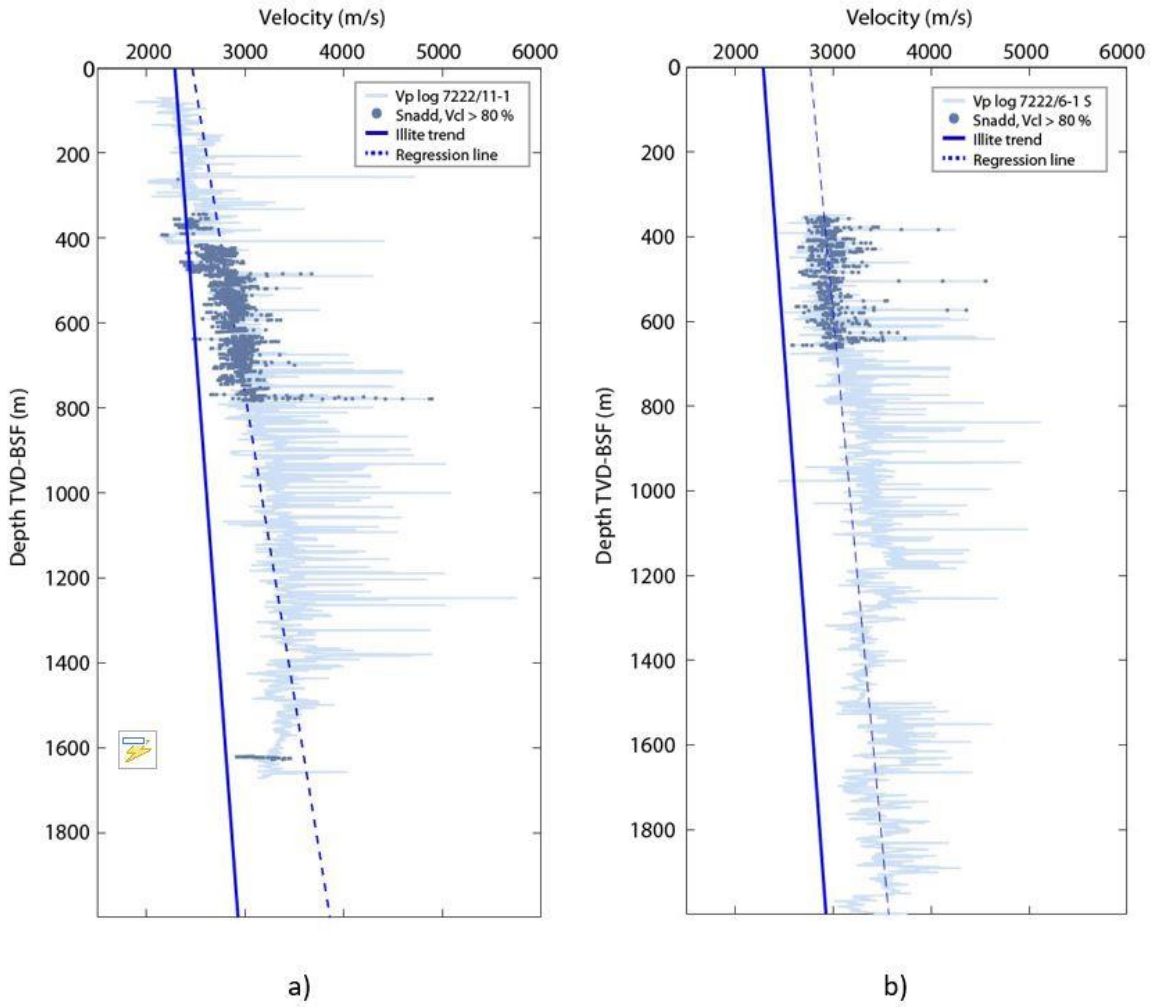

Figure 5.10: *Net erosion estimates, using an illite reference trend, for the Caurus (7222/11-1) and the Obesum (7222/6-1 S) wells on the Loppa High. The darker coloured points are clay point above 80 % clay in the Snadd Formation. Net erosion is estimated as explained in Chapter 3, and is the difference between the North Sea reference trend line and the regression line established for the specific well. Net erosion for these wells is estimated to approximately 1500-1600 meters. See Figure 1.1 for location of wells.*

5.2.2 Net erosion using well log resistivity data from shales

As we have seen and discussed above, when porosity is reduced with depth of burial the rock velocities increase. Porosity reduction is the main reason for increasing P-wave velocities with depth (Mondol et al., 2007). When rocks are uplifted, the porosity is not reversed and therefore it also keeps its velocity from maximum burial depth. This is the basis for using velocity depth trends for estimating net erosion. This method works well for standard conditions, but the results must be corrected if abnormal conditions exist.

For example, if the pore pressure is higher than normal the velocity decreases and the net erosion estimates must be corrected. Also, if the pore fluid is other than salt formation water, corrections must be made.

Also for changes in resistivity with burial depth, the porosity reduction is important. In addition, the resistivity of the pore fluids and the pore connectivity are important. And the actual lithology and local conditions must be taken into account. The resistivity of the formation water is dependent on the temperature and the salinity of the water (Figure 5.11). If the salinity is constant the resistivity of the pore fluid increases with decreasing temperature, and if the temperature is constant the resistivity increases with reduced salinity. When using resistivity of shale formations for net erosion estimates such effects should be corrected for if possible.

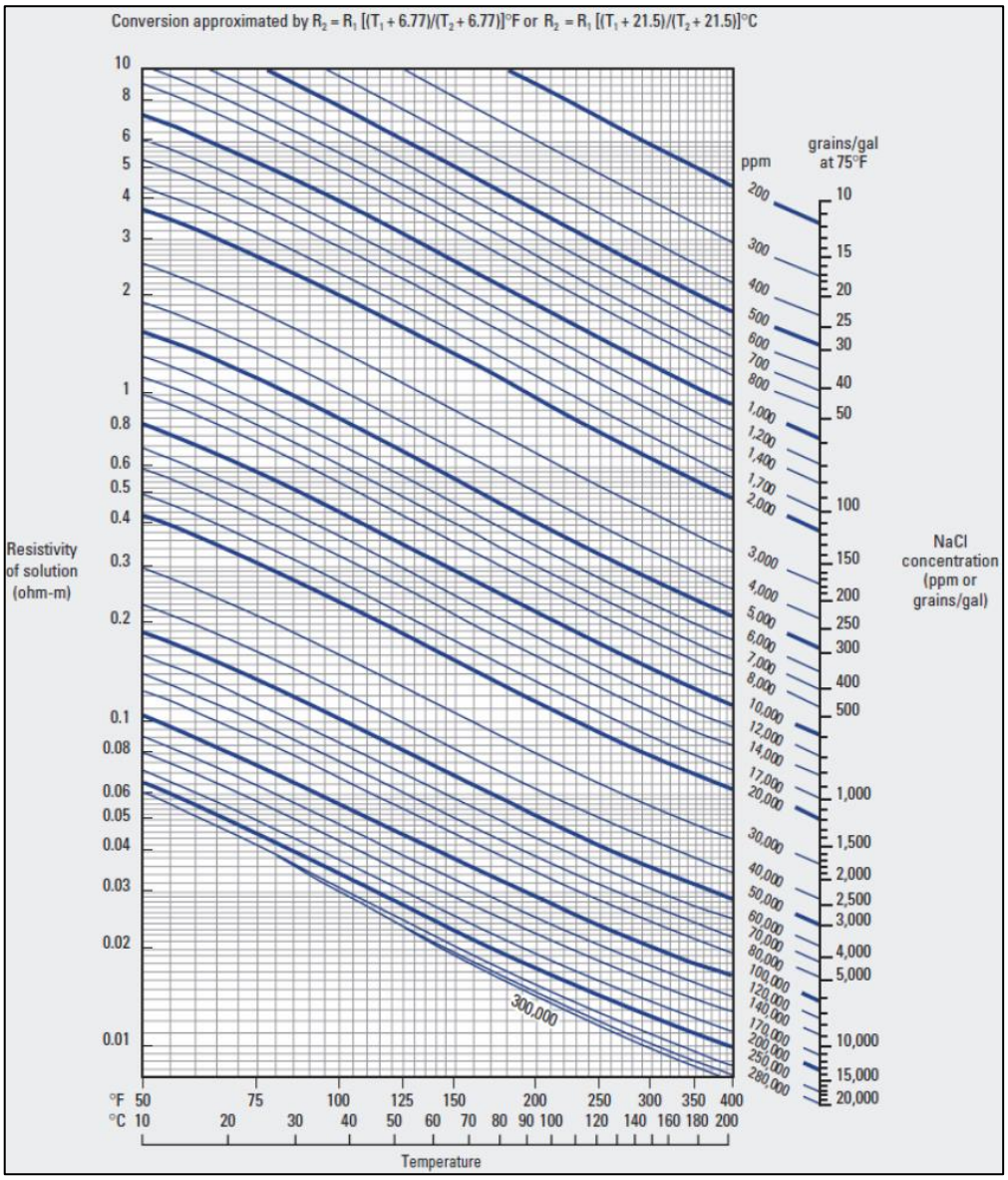

Figure 5.11: *Relationship between temperature, salinity and resistivity for formation water. Modified form Schlumberger (2015).*

When the formation is uplifted the rock resistivity will change, which is an important difference compared to the velocity. The most obvious change that will occur is that the resistivity will increase with decreasing formation temperature. In this study the Barents Sea the gradients are assumed to be between 35-42ºC/km (Khutorskoi et al., 2008, NPD, 2016). The salinity of the formation could also change, but this is more difficult to evaluate than the temperature that is mainly controlled by the temperature gradient of the actual area. The areas with known deep subsurface salt accumulations, as in the Tromsø Basin, the Nordkapp Basin and in the Maud Basin (Figure 1.1) could have elevated salinity in the nearby formations.

In Figure 4.5 and Figure 4.7 we observed that the net erosion estimated from resistivity data is increasing towards the east and north east, and also that the difference between the two methods is increasing in the same directions. Depth to the Kolmule Formation (Figure 4.8) shows a shallowing trend north- and eastwards. Combining these three observations we see that the difference between the two methods shown in Figure 4.7 is larger in the area that has the highest net erosion estimates from the velocity data. These are also the areas were the Kolmule Formation is shallowest today. This fits quite well with a hypothesis that cooling due to uplift could have increased the measured resistivity values and thereby the net erosion estimates. But as mentioned above other factors could also influence the resistivity. One possibility could be fracturing due to the uplift itself, but in the following we only discuss the effect of temperature. Salinity and pore connectivity are assumed to be constant. To understand the effect of cooling is beyond the scope of this study, but we show an example on how temperature could influence the result.

In Figure 5.12 the actual resistivity for the wells used to calculate net erosion is plotted at its present depth. Further we assume that the net erosion calculated from P-wave velocity is the best available. This net erosion for each location is now added to the present depth and plotted in Figure 5.13a. Theoretically, all the points should now plot at the reference trend line. As expected, the wells that are not affected by uplift, in the westernmost Barents Sea and the North Sea, plot close to the reference trend. The uplifted wells plot far to the right of the reference trend.

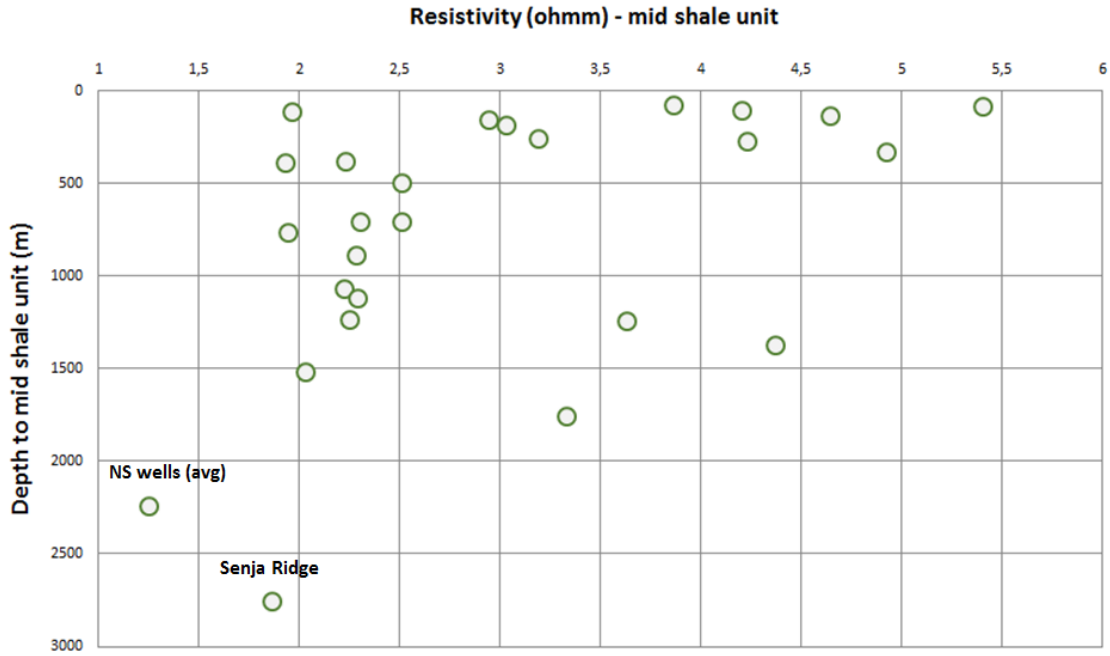

Figure 5.12: *Actual resistivity values for the wells in the data set plotted at its present depth. NS wells (average) is the average value for the North Sea wells used in the study. See Figure 1.1 for location of wells.*

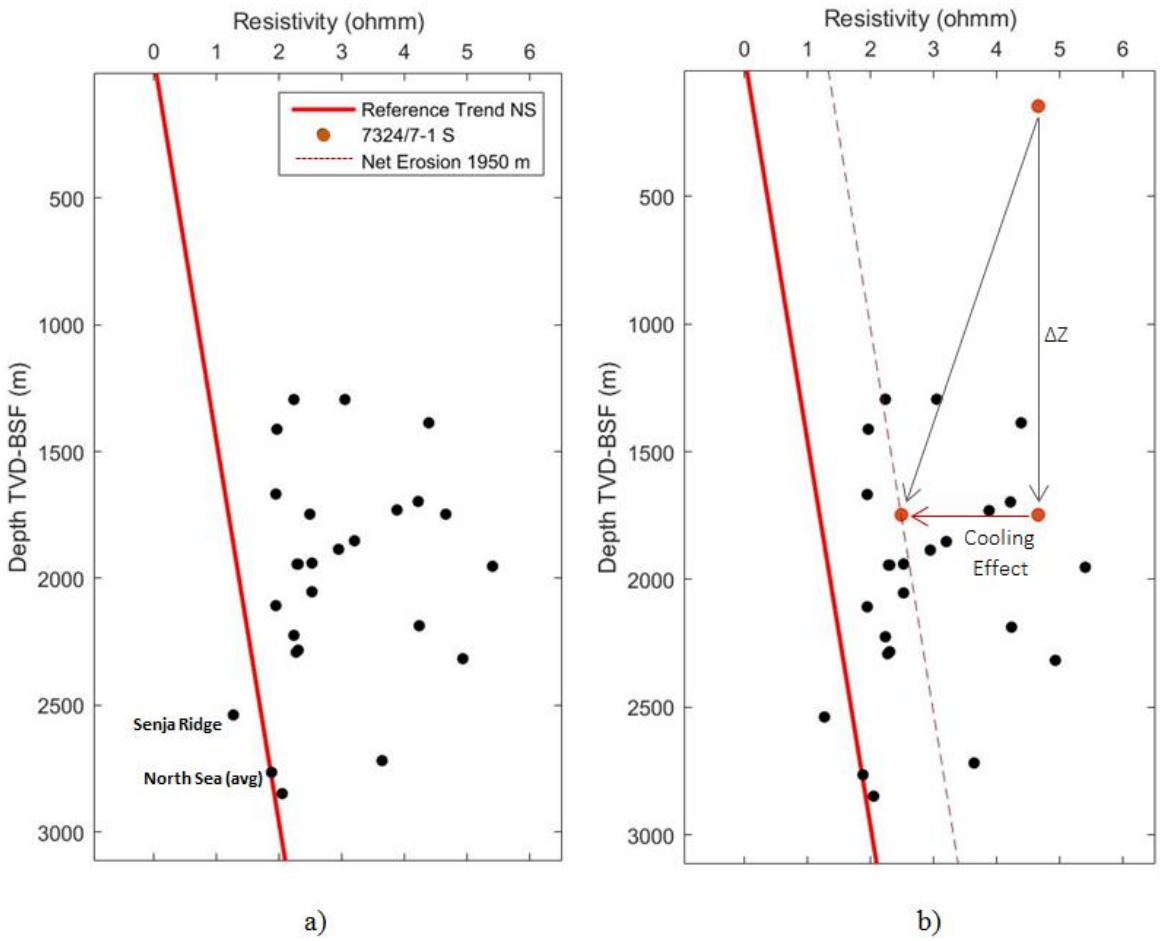

Figure 5.13: *a) The wells in the study area plotted at maximum burial depth (actual depth plus net erosion from shale velocity estimations (black circles)). b) Possible effect of cooling is illustrated by the Wisting Alternative well (red dot). See text and Figure 5.14 for a more detailed explanation. The stippled line is included to help quantifying the effect cooling has on the net erosion estimates.*

When we assume that much of this effect is caused by cooling when the formation is uplifted, it can be corrected for. The simple sketch in Figure 5.14 explains how this could be done. Such curves can be estimated based on the Archie equation (Archie, 1941). The red curve is the resistivity reference curve, and the black curve is the resistivity depth curve for the actual uplifted well location. The vertical distance between these two curves at resistivity R_1, is the uncorrected net erosion estimate from resistivity. Z_1 is the depth of the actual formation after uplift.

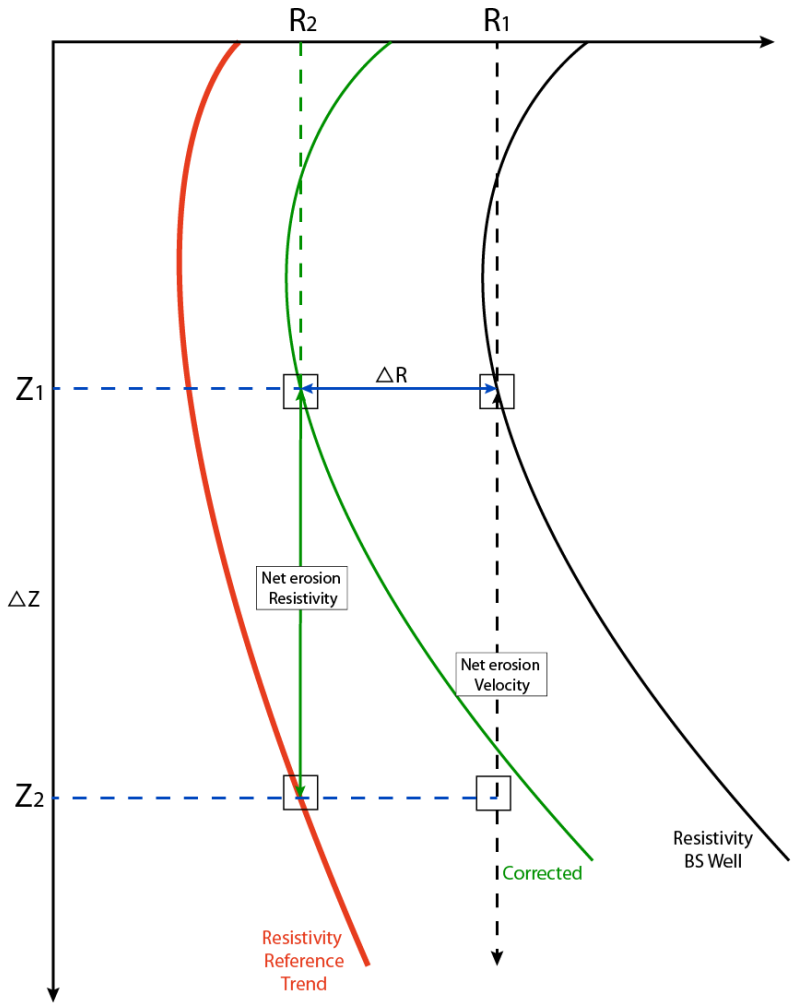

Figure 5.14: *Conceptual sketch illustrating how to correct for the effect cooling has on the resistivity of a formation. Z_1 and Z_2 are the depths after and before uplift of the formation. ΔZ is the uplift estimated from the shale velocity method for the actual well. The curves are estimated using Archie's equation (Archie, 1941). See text for a more detailed explanation.*

As discussed above this estimate is obviously too large. When corrected for cooling the resistivity curve (black) will move towards left in the diagram. In our example we suggest to use the net erosion estimate from shale velocities (ΔZ) to find the corrected curve (green). This value (ΔZ) is added to the formation depth Z_1 to find Z_2. Then if the elevated resistivity is entirely caused by cooling of the formation when uplifted, the correction for temperature is ΔR and the new corrected resistivity is R_2.

To show a simple example a curve with reference resistivities and a simplified curve for the uplifted Wisting Alternative well (7324/7-1 S) were simulated. These are not very accurate and are only meant to illustrate the effect of cooling. This was done by using Archie's Equation (1941) and the concept shown in Figure 5.14. The equation was originally made for sandstones and not for shales, but for horizontal resistivities we here assume that the equation works for shales as well.

In Figure 5.13b the Wisting Alternative well is shown at both present burial and maximum burial depths together with the other wells in the study, also at maximum burial depths. If the effect of cooling is corrected for, all the wells should theoretically move to the left in the diagram as illustrated for the Wisting Alternative well.

If the elevated resistivity was entirely caused by cooling the resistivity value for the Wisting Alternative well should move to the reference trend line (red solid line in Figure 5.13b). Since this is not the case, other effects like changing salinity and pore connectivity could also have effect in this case. The cooling effect is maybe not that interesting in itself, but since it represents the temperature of the actual area it can potentially be used to estimate the temperature gradient. Since both resistivities and velocities can be collected using geophysical data, temperature gradients could theoretically be estimated in areas lacking well data.

However, as mentioned above a more detailed study of this effect is outside the scope of this project, but could be an interesting topic for further research.

5.2.3 Net erosion using sandstones

Estimating net erosion using empirical sandstone depth trends for velocity and resistivity were tested. The method gave inconsistent and variable results compared to other methods. Both the sandstone reference velocity trends from the North Sea and most of the actual sandstones from the Barents Sea are influenced by diagenetic processes (Figure 3.11 and Figure 4.10).

The Barents Sea wells show much larger variations in properties compared to the North Sea. This is most likely the reason why using empirical velocity sandstone trends do not work well in our case. The attempt to us sandstone resistivity trends also gave inconsistent and variable results. Since the resistivity is extremely sensitive to fluids, the selected sandstone should be 100 % water saturated. Even though all the analysed sandstones in the Barents Sea were selected from the brine zone, the net erosion results were still too variable compared to estimates from the shale velocity method.

Further, estimating net erosion by combining sandstone diagenetic- and rock physics modelling was performed on most of the wells in the study area. The sandstone modelling approach is a standalone method, but is best used together with other methods. In Figure 5.15 the sandstone modelling results are compared to the estimates using P-wave velocity for shales.

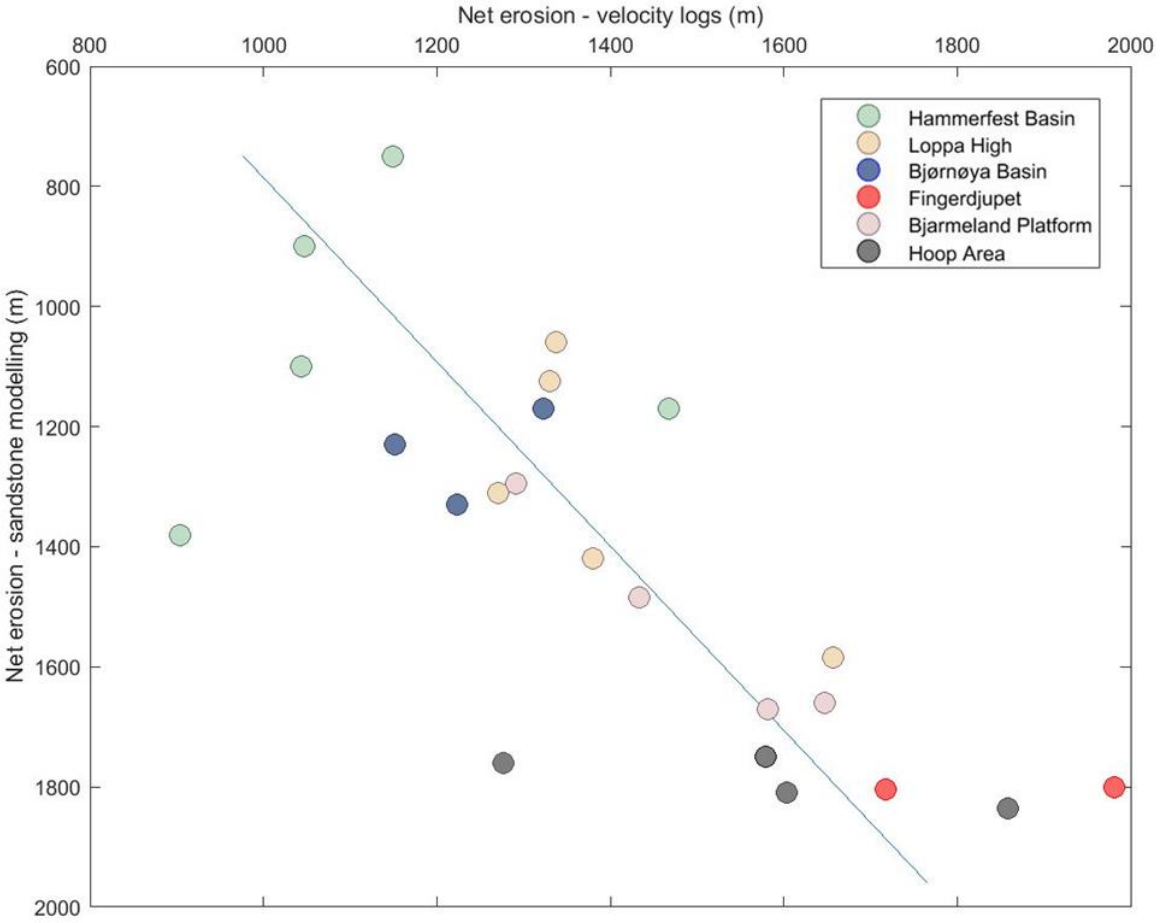

Figure 5.15: *Net erosion estimates from sandstone modelling compared to net erosion estimates using velocity depth trends for shale. The colours represent wells in sub-basins in the Barents Sea. The sandstone modelling was done for the Stø Formation and the velocity estimates were done for the Kolmule Formation. See Figure 4.10 for location of wells.*

The shale velocity estimates are based on the Kolmule Formation, and the sandstone modelling is done for the Stø Formation. Although a few variations occur in the Hammerfest Basin and in the Fingerdjupet and Hoop areas, the results from the two methods give approximately the same results. This is logical since the uplift occurred after deposition of both formations (Faleide et al., 2010).

Some shortcomings in the sandstone modelling approach should be kept in mind when evaluating the results. Different burial scenarios can result in the same net erosion result. The amount of cementation due to burial is calculated through a time and temperature dependent integral and therefore different burial scenarios can result in the same amount of in situ cement volume. This is dependent on the time the formation has been subjected to temperatures higher than approximately 70ºC (Bjørlykke and Jahren, 2015).

In Figure 5.16 three burial scenarios for are shown. Each scenario represents different amount of time below 70ºC, and thus different amounts of cement generated.

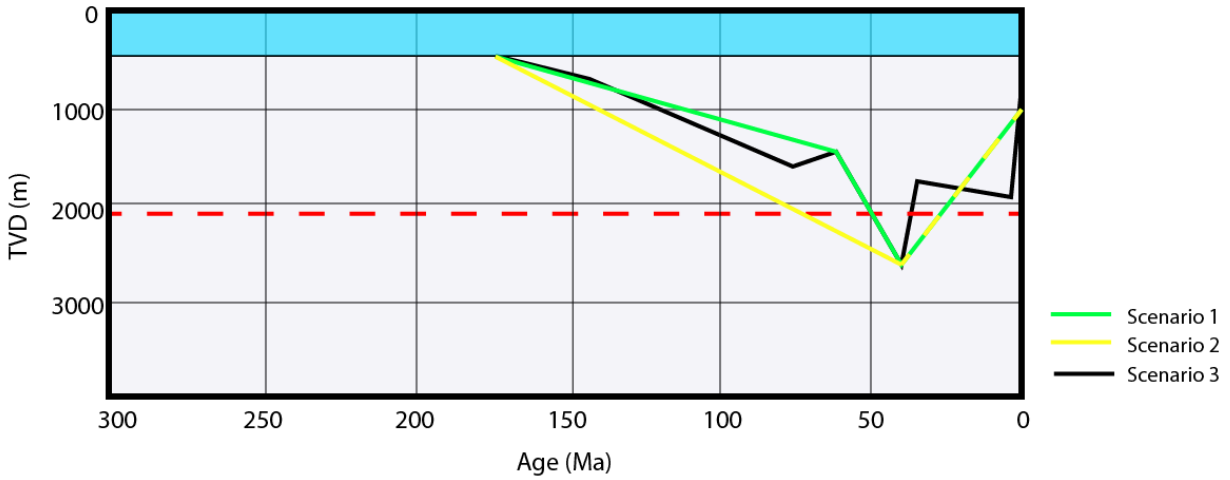

Figure 5.16: *Three burial history scenarios for the Stø sandstone in the Barents Sea. Scenario 1 (green curve): Formation is at zero depth 175 million years ago, maximum burial is approximately 40 million years ago before formation uplift. Scenario 2 (yellow curve): A simple scenario with starting point and 175 Ma, then maximum burial before uplift. Scenario 3 (black curve): This scenario is more complex, but did not give significantly different net erosion compared to the simpler green scenario.*

In burial scenario 1 (green curve) the actual formation (Stø Formation) is at zero depth 175 million years ago. After that the formation followed the green burial curve and reached maximum burial approximately 40 million years ago before it was uplifted again. In scenario 2 (yellow) a simpler burial curve is shown with only the starting point and the point of maximum burial before uplift. This burial curve should cause generation of more cement compared to scenario 1, which again will lead to a smaller net erosion estimate. The third scenario includes a more detailed burial history curve (black curve). This scenario is closest to the published burial history curves for the area (Ohm et al., 2008). This scenario generates less cement and thus the net erosion estimates will be larger.

After testing we selected scenario 1 as the standard approach for the sandstone modelling. Although it is a little simpler than scenario 3, it gives consistent results that are comparable to the empirical shale velocity estimates. A more complex burial history did not give significantly different results. The most likely explanation for this is that it is the maximum burial that is the most important factor for the modelling result.

The calculated volume of cement will also change due to changes in temperature gradient. Based on published data (NPD, 2016) average temperature gradients were estimated for each sub-basin in the western Barents Sea. The gradients vary from approximately 35ºC in the Hammerfest Basin to 42ºC in the Hoop area and the northern Bjarmeland Platform. When the temperature gradient decreases the net erosion estimate will increase. Net erosion estimates for the Wisting alternative well (7324/7-1 S) was tested with different temperature gradients. A change in the gradient from 42ºC to 33ºC/km gave an increase in net erosion of about 650 m, from 1800 m to 2460 m. The lowest estimate is comparable to the shale velocity estimate.

The examples above illustrate some of the general shortcomings when using a modelling approach. There are many factors that can influence the result, and it is always possible to match the real data by altering input parameters to the modelling. Here we have tried to minimize these effects by focusing on the most important parameters, but this will always be a weakness when using modelling.

In addition to the shortcomings with the modelling approach, there are also other sources of uncertainty that should be considered when evaluating the results. For our models a perfectly sorted and homogenous quartz sand is assumed and brine is the pore fluid. But the properties of the actual sandstones used in the modelling will always have some variations and thus these assumptions can sometimes be difficult to fulfil. Further, grain size and grain coating will also affect the generated cement volumes.

Overpressure and differential compaction is not taken into account in the modelling. Overpressure can slow down the compaction process, which will result in underestimation of the net erosion estimates.

5.3 Net erosion maps and comparison with results from previous studies

In Chapter 4 net erosion results were presented as a series of trend maps. In addition much more detailed net erosion maps were made by combining seismic velocities and interpreted seismic horizons. Here we discuss the results presented in the maps and compare them with results from earlier studies.

To use seismic velocities for estimation of net erosion is a well-known technique, and has been used by among others Baig et al. (2016) and Richardsen et al. (1993) in Barents Sea. By using regional velocity cubes and combining them with the interpreted top Kolmule Horizon and the Base Cretaceous Horizon we were able to make detailed net erosion maps compared to the simple trend maps.

These maps are useful both in regional and more detailed studies of structural development and local geological evolution. Also when evaluating and comparing hydrocarbon plays and prospects it is important to understand how the net erosion varies in general and in more detail in individual basins. The amount of net erosion in an area will influence burial and maturation of the actual source rocks. It will also affect migration into traps and possible trap leakage (Henriksen et al., 2011). This can again influence hydrocarbon prospect ranking.

The maps generated from seismic velocities give a more detailed picture compared to the trend maps made from well log data, but still there are also several limitations and uncertainties linked to the generation of such maps.

One obvious limitation is that the velocities are organized in a relatively course velocity grid (horizontal: 3x3 km, vertical: 100 ms). This will influence the results, and the velocities will only follow the general trends and will not pick up the smallest variations below the velocity grid size.

The interval velocities are based on stacking velocities, which have limited resolution decided by the resolution of the seismic data in the actual area, and in the process the data were resampled to 100 ms vertical resolution. When deriving seismic interval velocities using the Dix (1955) formula, short offsets and flat and parallel layers are assumed. These assumptions are not fulfilled for example in areas with faulting and block rotations.

Because the Kolmule Formation is not present across the entire study area, net erosion maps were made for two seismic horizons, the top Kolmule- and BCU horizons. These maps gave slightly different results, even though the uplift theoretically should have been the same for the two horizons. Possible reasons for this were explained in Chapter 4.

In spite of the possible shortcomings mentioned above, the technique using seismic interval velocities for net erosion estimation is a good method that provides valuable information about the spatial distribution of net erosion of an area. The method is especially usefully in basins with poor well control.

The trend map based on sandstone modelling gives similar trends and magnitudes as the velocity trend map (Figure 5.17). However, this map is based on forward modelling, and as discussed above several input scenarios can often explain the data. But in combination with the shale method, and in areas were other methods cannot be used, this method is still valuable.

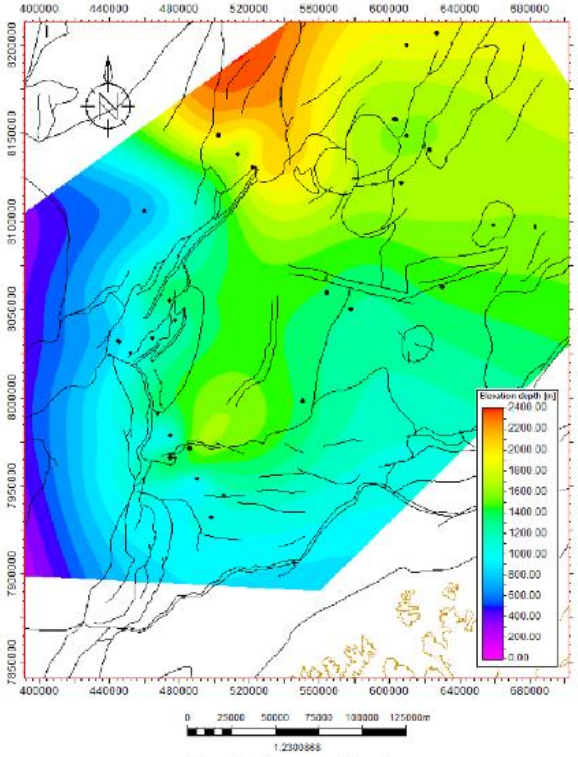

Sonic Logs - Shale

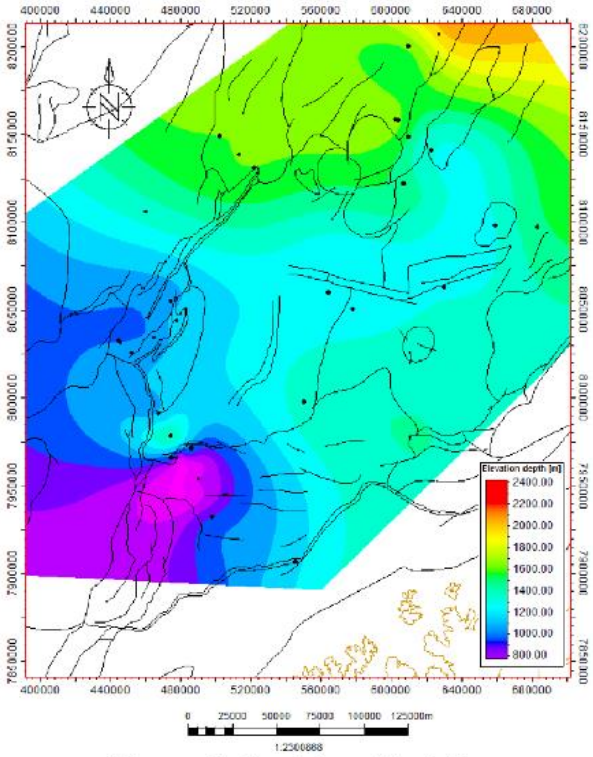

Diagenetic Sandstone Modelling

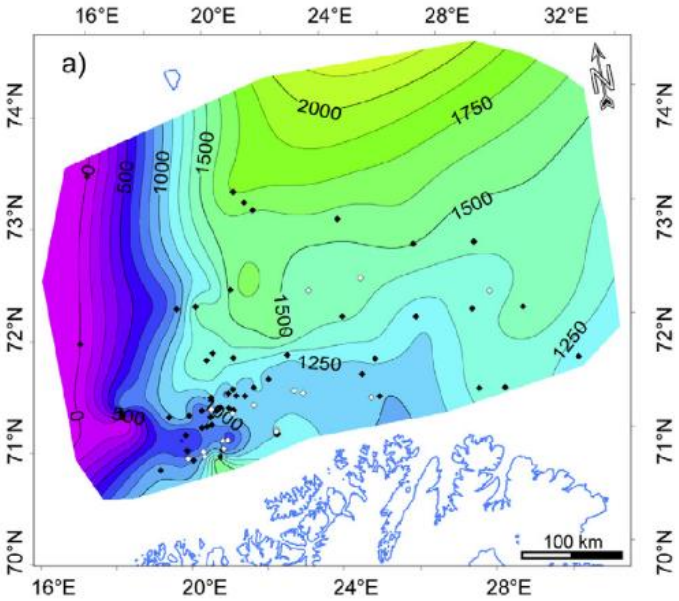

Sonic Logs - Baig (2016)

Figure 5.17: *Comparison of trend maps for net erosion estimates from this study with recent trend map from Baig et al., 2016. The black dots are the well positions where the net erosion estimations are performed. Structural elements are modified from Faleide et al. (2010).*

In Figure 5.17 our regional trend maps are compared with the most recent published trend maps from (Baig et al., 2016). Their results are good for comparison since they also evaluated earlier published estimates as well as using other methods including vitrinite reflectance. The general impression is that the trends are similar. Baig et al. (2016) looked at a larger number of wells, but we have more wells in the north-east that confirms the increasing net erosion trend in this direction.

When comparing maps made form seismic velocities, the picture is different (Figure 5.18). Here our maps have much better resolution than the map from Baig et al. (2016), but their map covers a larger area. The higher resolution in our maps is due to the dense velocity data and the combination with the mapped seismic horizons. Such detailed maps can have great value when doing play- and prospect evaluation, especially in areas were prospect parameters dependant on correct estimation of net erosion are critical.

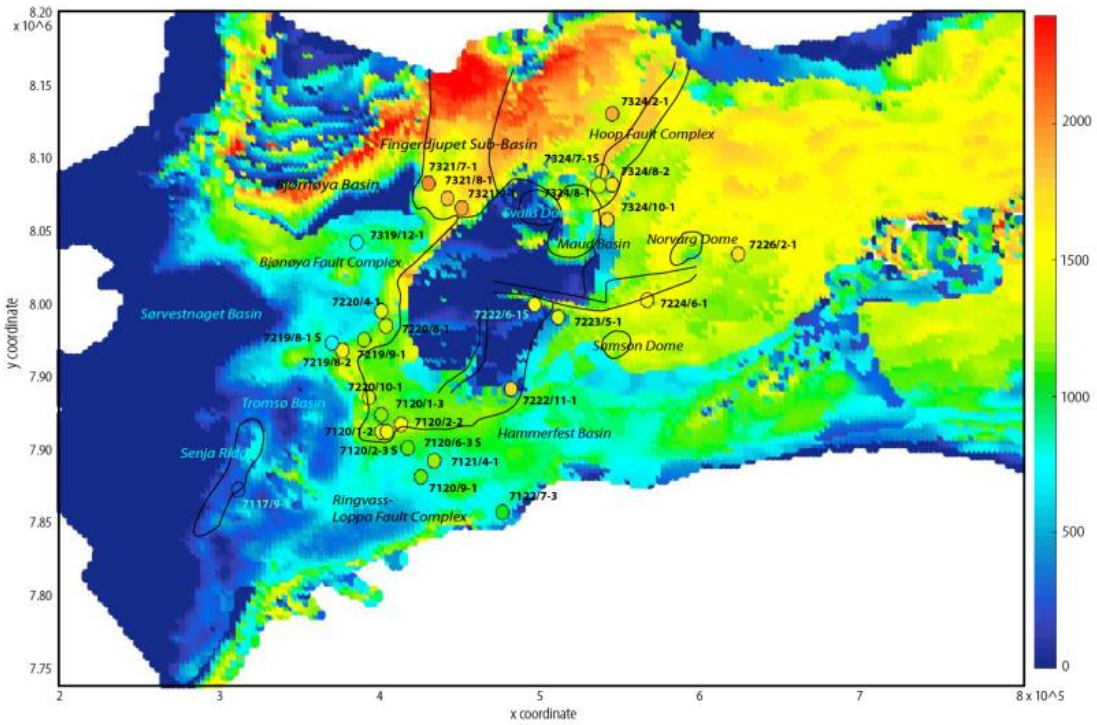

Seismic Velocity

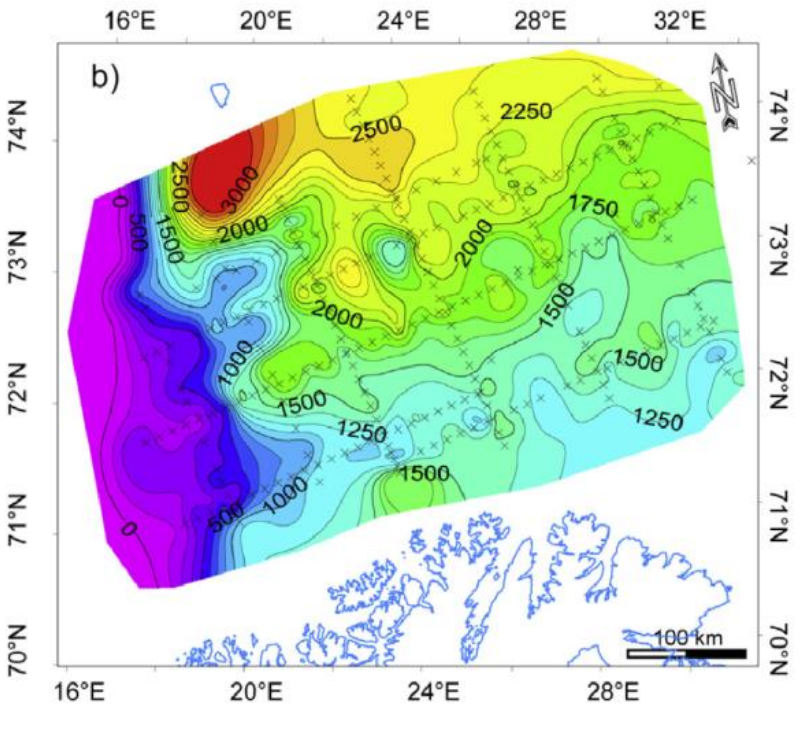

Seismic Velocity - Baig (2016)

Figure 5.18: *Comparison of net erosion estimates from seismic velocities. The left map was created by combining the seismic velocity cube, the top BCU Horizon and the Top Kolmule Horizon. Net erosion results from velocity trends in wells are included for comparison. The BCU map is shifted down 200 meters. See Figure 4.16, Figure 4.17 and text for a more detailed explanation. The apparently abrupt change in net erosion estimates in the northern Tromsø Basin is caused by the imperfect merge between the two maps. Baig et al. (2016)'s map (right) is based on an open seismic grid and is not as detailed as the maps created from the velocity cube (left). In the blue area at the Loppa High net erosion is not estimated.*

5.4 Net erosion and geological development

In Figure 5.19 to Figure 5.22 net erosion estimates from wells and seismic velocities are integrated with the geological sections from the regional seismic interpretation. By combining seismic interpretation with net erosion estimates, the results can be quality controlled in areas were all data sets are present. In the geological cross sections the erosion estimates from individual wells are shown in the well position. The interval velocities and the net erosion estimates based on seismic velocities are also shown in the figures. The geological history will be more complete by including net erosion estimates in areas where seismic interpretation is not possible.

In Figure 5.23 we have made a simplified sketch for the situation at maximum burial. This sketch is based on the net erosion estimates in this study combined with the four interpreted geological cross section. In addition we used published data from the westernmost areas Faleide et al. (2010).

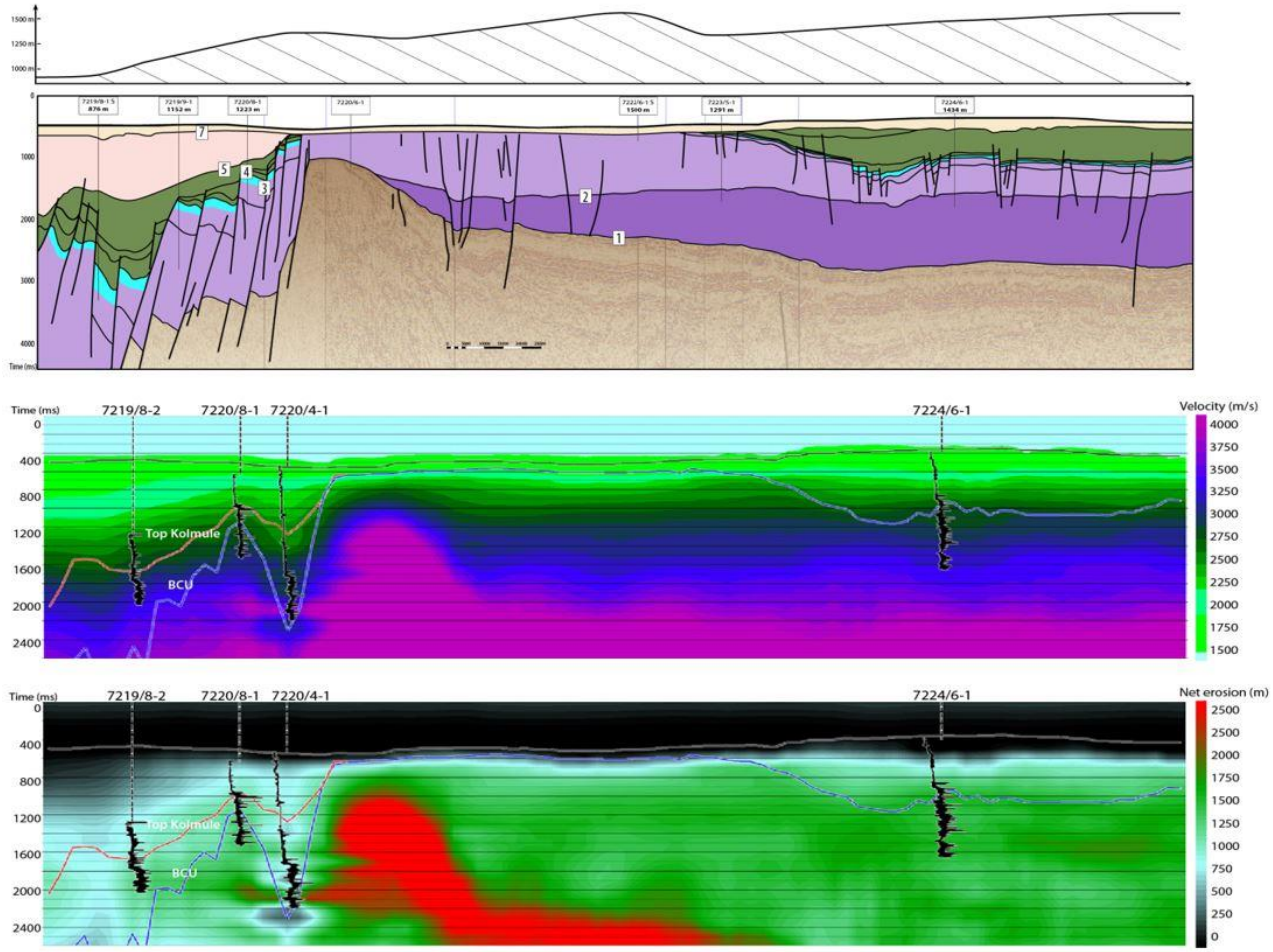

Figure 5.19: *Regional geological cross section number 1 combined with net erosion estimates from seismic velocities and velocity depth trends in wells. Net erosion estimates are included in the well position on top of the geological model (upper figure). The amount of net erosion is illustrated by the shaded area below the smoothed line on top of the model. Scale for net erosion is shown in the upper left corner of the figure. The seismic interval velocities used to estimate net erosion are included below the geological model (middle figure). The actual net erosion from seismic velocities is shown in the lower figure. In the two lower figures velocity logs are included in the well positions together with the Kolmule- (red line) and the BCU horizon. Location of regional cross sections and wells are shown in Figure 1.1. See also Figure 4.19 for well numbers and net erosion estimates.*

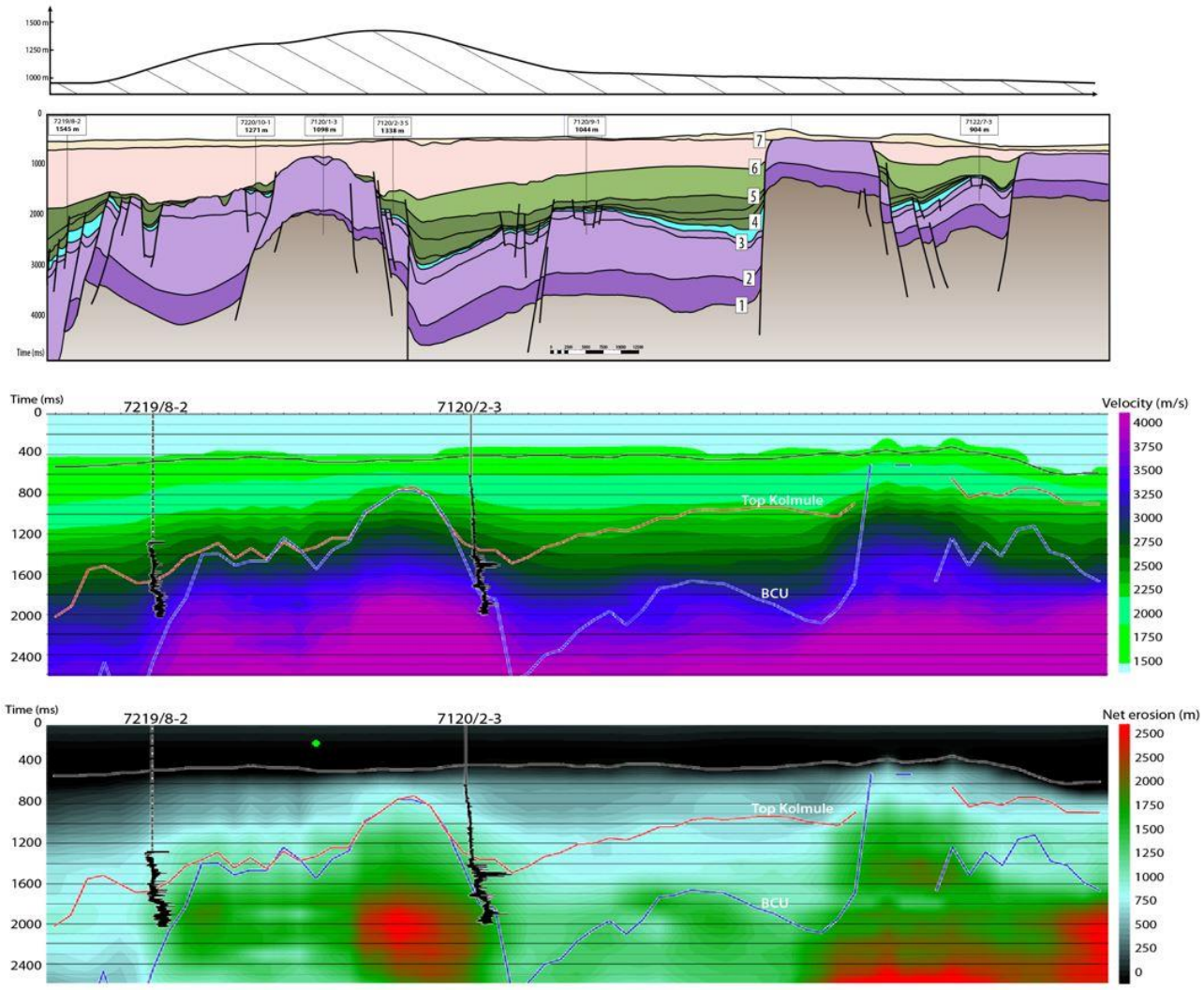

Figure 5.20: *Regional geological cross section number 2 combined with net erosion estimates from seismic velocities and velocity depth trends in wells. Net erosion estimates are included in the well position on top of the geological model (upper figure). The amount of net erosion is illustrated by the shaded area below the smoothed line on top of the model. Scale for net erosion is shown in the upper left corner of the figure. The seismic interval velocities used to estimate net erosion are included below the geological model (middle figure). The actual net erosion from seismic velocities is shown in the lower figure. In the two lower figures velocity logs are included in the well positions together with the Kolmule- (red line) and the BCU horizon. Location of regional cross sections and wells are shown in Figure 1.1. See also Figure 4.20 for well numbers and net erosion estimates.*

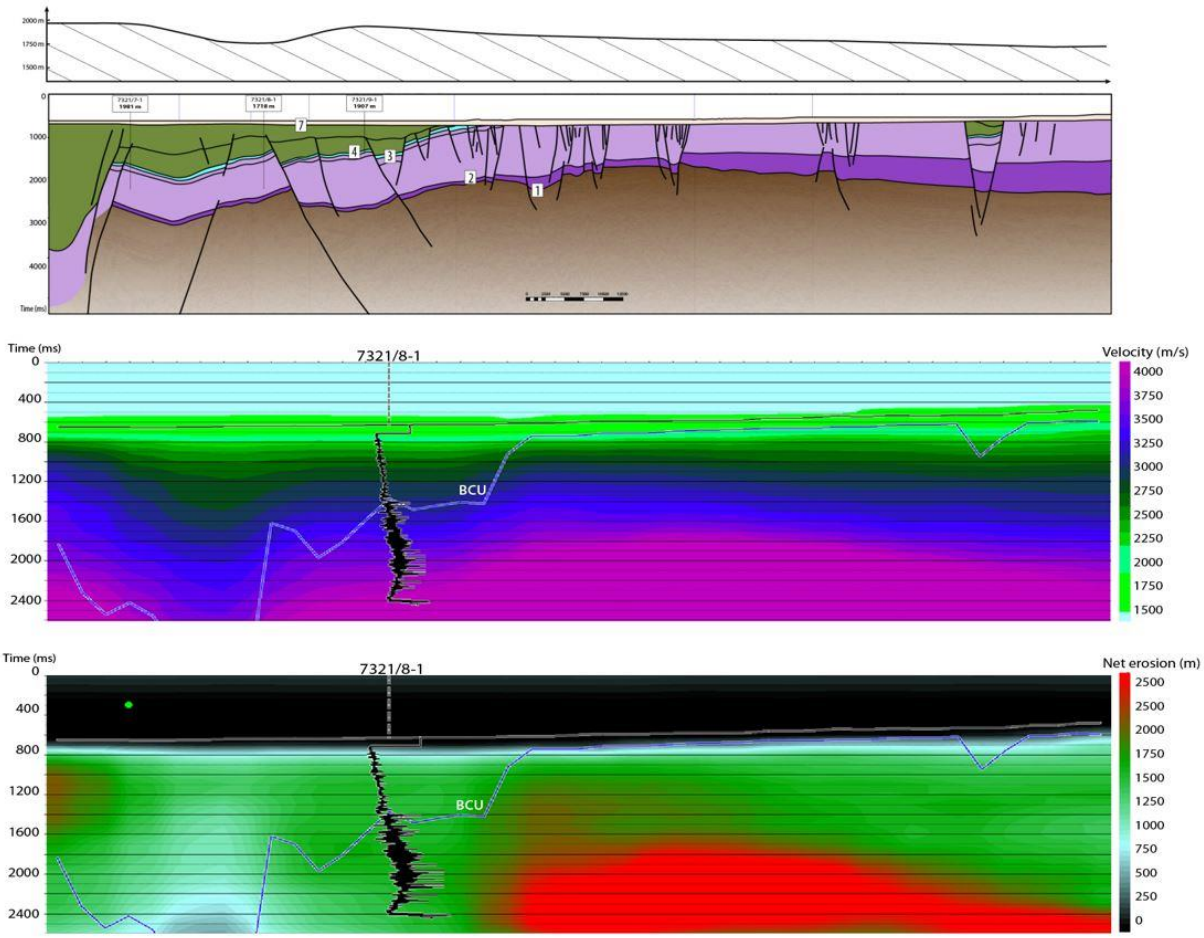

Figure 5.21: *Regional geological cross section number 3 combined with net erosion estimates from seismic velocities and velocity depth trends in wells. Net erosion estimates are included in the well position on top of the geological model (upper figure). The amount of net erosion is illustrated by the shaded area below the smoothed line on top of the model. Scale for net erosion is shown in the upper left corner of the figure. The seismic interval velocities used to estimate net erosion are included below the geological model (middle figure). The actual net erosion from seismic velocities is shown in the lower figure. In the two lower figures velocity logs are included in the well positions together with the Kolmule- (red line) and the BCU horizon. Location of regional cross sections and wells are shown in Figure 1.1. See also Figure 4.21 for well numbers and net erosion estimates.*

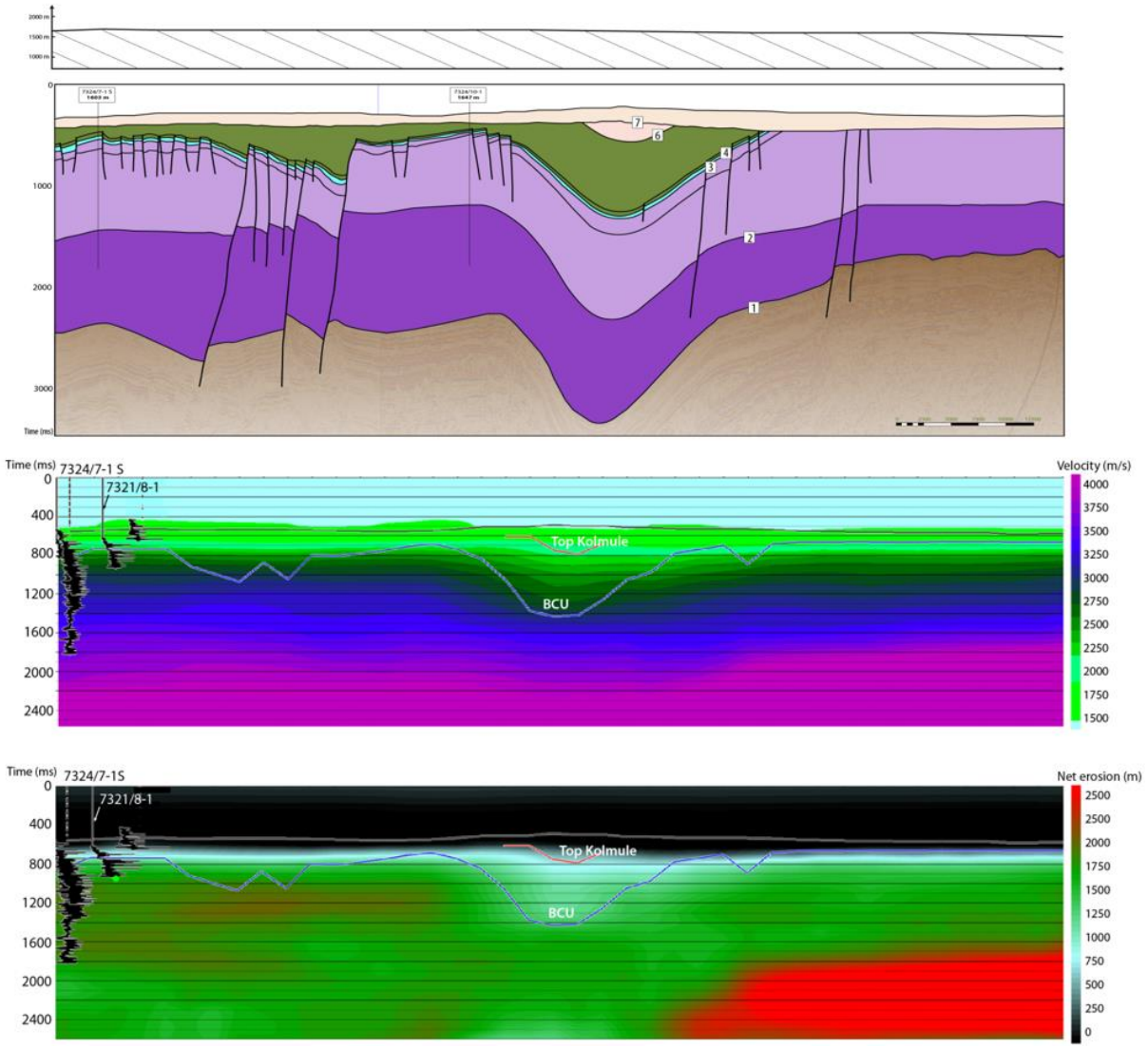

Figure 5.22: *Regional geological cross section number 4 combined with net erosion estimates from seismic velocities and velocity depth trends in wells. Net erosion estimates are included in the well position on top of the geological model (upper figure). The amount of net erosion is illustrated by the shaded area below the smoothed line on top of the model. Scale for net erosion is shown in the upper left corner of the figure. The seismic interval velocities used to estimate net erosion are included below the geological model (middle figure). The actual net erosion from seismic velocities is shown in the lower figure. In the two lower figures velocity logs are included in the well positions together with the Kolmule- (red line) and the BCU horizon. Location of regional cross sections and wells are shown in Figure 1.1. See also Figure 4.22 for well numbers and net erosion estimates.*

In the results section we saw that the study area has a complex geological history with several periods of both subsidence and uplift. The development in the Carboniferous period and in late Jurassic- to early Cretaceous times is local and linked to extensional basins. Triassic time is dominated by large scale regional subsidence, while the early Cretaceous period has both local basin subsidence and regional subsidence. The Cenozoic period also has long intervals with subsidence, and in middle Eocene time the area reached maximum burial (Faleide et al., 2010). At this time the maximum burial depth for the Kolmule Formation was almost 2000 meter deeper than today. In Figure 5.23 we also see that the depocenter at maximum burial, was in the Tromsø Basin and further to the east. During the following net erosion events the depocenter gradually moved further to the west, culminating with huge amounts of sediments deposited as a response to glacial erosion (Laberg et al., 2012, Vågnes et al., 1992).

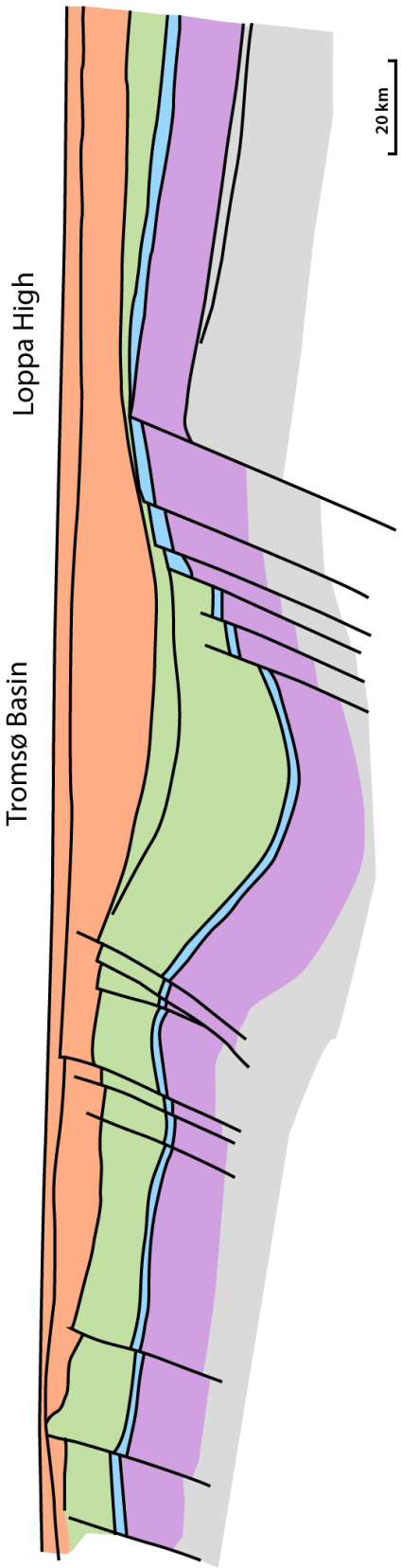

Figure 5.23: *Approximate sketch of the situation at maximum burial depth in Middle Eocene time in the Western Barents Sea. The sketch is based on the regional interpretation results and net erosion estimates in this study in addition to published regional profiles from the westernmost areas (Vågnes et al., 1992). The scales are not exact and for the vertical scale the thicknesses (TWT) should be compared to regional section 1 in Figure 5.19 – upper figure.*

5.5 Seismic AVO signatures in the Barents Sea

At the south western Loppa High real AVO responses were interpreted and compared with responses in wells. The effect of substituting brine with gas was demonstrated, and we showed results where the sandstone modelling was extended also to include the AVO response. This technique can be applied when using a reference well to constrain AVO modelling in a nearby prospect (Avseth and Lehocki, 2016) In their case they assumed that all factors at the prospect were similar to the reference well, except for the net erosion.

In the south western Loppa High area we found good agreement between the real AVO responses and the modelled AVO responses, and we expanded the AVO sandstone modelling to all the wells in our study area. Generally the sensitivity to fluids is reduced with increasing burial depth (Avseth et al., 2005). It is therefore important to understand the effect of both increasing burial depth and how the fluids affect the AVO response. Figure 4.43, Figure 4.44 and Figure 4.45 show that also in our study area maximum burial depth has a strong influence on the expected AVO signatures for different pore fluid scenarios.

We see that nearly all AVO class I responses have maximum burial deeper than approximately 2500 meters. In this class most of the reservoirs are water filled. The two gas filled reservoirs in class I are plotting slightly to the left of the water filled reservoirs, shifted along an expected fluid trend in the diagram. However, they are still interpreted as class I responses. In responses showing classes II and IIp there is a mix of brine filled and hydrocarbon filled reservoirs, but also here we see that the hydrocarbon filled reservoirs have moved along the fluid trend and lines up along a linear trend with the other discoveries (Figure 4.44). Similarly, the brined filled scenarios also line up along a clear linear trend, and hydrocarbon filled reservoirs with relatively shallow maximum burial plot as AVO class III.

In addition to maximum burial depth and fluid, lateral lithology or facies changes both in the reservoir zone and in the cap rock could influence the AVO response. Normally, in the Barents Sea, above the Stø reservoir sandstone is the shaly Fuglen cap rock formation, and above the Fuglen Formation is the Hekkingen source rock. As seen in Figure 2.6, both lithology and internal relationship vary laterally for the two formations. The Fuglen Formation is thickest, approximately 50 meters, in the south western parts of the Hammerfest Basin and thinning on to the central highs in the basin. In these areas the formation is characterized by rare, thin limestones and shales. The Hekkingen source rock can be a few hundred meters thick, but is also thinning to less than hundred meter towards basinal highs (Dalland et al., 1988). Such variations will also give lateral changes in elastic properties and AVO signatures.

Modelling tests for Top Stø Formation show that when the Fuglen Formation is pinching out, the AVO response associated with the top of the reservoir could potentially move from a class II response towards a class I response, with the Hekkingen Formation as the cap rock. These effects are not fully included in our modelling, but should be kept in mind when evaluating the results. A more detailed study is needed to fully understand such relationships in our study area.

Further, as for all seismic techniques there are several other uncertainties that also should be taken into account when using AVO results in prospect evaluation. Uncertainties related to the seismic method itself are the major one. Vertical and horizontal resolution will decrease with depth, due to geometrical spreading and frequency attenuation.

But uncertainties related to data processing are also important. Change with offset is the key with AVO analysis. Therefore the goal for all AVO processing is to maintain a true relative amplitude through the processing (Avseth et al., 2005). In addition, seismic data used for AVO analysis will have assumptions and simplifications related both to the raw and the processed data. If these are broken it will affect the final results. All these factors are important, but maybe the most important part of the AVO analysis is to evaluate if the technique is suitable for the actual area (Avseth et al., 2005). In our study we found that AVO would be an effective tool by analysing the wells at the south western Loppa High.

In this project we extended our local AVO study geographically by using AVO modelling based on the results from the diagenetic sandstone modelling. This is a very useful process, but it should always be kept in mind that modelling in itself will also have shortcomings as outlined in previous chapters.

Chapter 6 – Conclusion

The aim of this study was to quantify and understand net erosion in the south western Barents Sea and to test different approaches to be able to compare and evaluate results from the various methods. Velocity well log data and seismic data were used, and the results were further used for studies of how net erosion influence seismic AVO signatures. Also a new approach was tested - using resistivity well log data for net erosion estimation. These results gave somewhat surprising finding, and we suggest that information on temperature gradients could be derived from the estimates. There is good agreement between the results from some of the methods, for example sandstone modelling and estimations using shale velocity trends, while the results from the resistivity methods deviated from the others. Net erosion estimates from shale velocity trends provide good coverage across the study area, and probably gave the most reliable results. Below we have organized our conclusions according to the three main goals for the study as they were outlined in the introduction.

1. Quantify uplift and erosion form several techniques and compare and evaluate the results.

The study area in the western Barents Sea has a complex burial- and uplift history with both local episodes linked to extension and more regional episodes affecting a much larger area. Here we have quantified the regional Cenozoic net erosion.

The average net erosion estimates from shale velocity and sandstone diagenesis range from approximately 800 to 1400 meters within the Hammerfest Basin, 1000 to 1500 meters on the southern Loppa High, 800 to 1500 meters within the Bjørnøya Basin, around 1700 to 1900 meters in the Fingerdjupet sub-basin, 1300 to 1700 meters on the Bjarmeland Platform and 1300 to 2000 meters on the northern Bjarmeland Platform in the Hoop fault complex area. The westernmost areas are not uplifted and eroded and are at their maximum burial today.

Maximum burial occurred in Middle Eocene time approximately 40 Ma. The western areas had little or no subsidence at this time, and the main depocenter was in the Tromsø Basin. The first major net erosion episode took place during late Eocene time, and the second major net erosion event occurred during the ice ages in the Quaternary period. The main depocenters gradually moved westwards during Cenozoic time.

2. Test methods using both property-depth trends and forward modelling including methods based on well data as well as seismic data.

Integrating the net erosion estimates with regional seismic interpretation constrained the results and improved the geological understanding in areas where seismic interpretation was not possible. Detailed net erosion maps from seismic velocities and mapped depth horizons combined with net erosion trend maps improved the understanding of the lateral variation of the net erosion in the area.

The Barents Sea has few wells in areas with no net erosion. Therefore the North Sea was used to establish reference trends. New trends for shale velocity, shale resistivity, sandstone velocity, sandstone resistivity and smectite-illite shale were established. Before they were used for making estimates, the North Sea trends were compared to single wells with little or no uplift in the Barents Sea. This work flow compensates for the lack of reference wells in the study area. Also a seismic velocity trace from the Tromsø Basin was compared to the North Sea reference trend and a velocity log from the Barents Sea. We found that relatively small changes in reference trends could produce significantly different net erosion estimates.

Net erosion estimates using shale velocity trends, sandstone diagenetic modelling and seismic velocities gave consistent results across the study area. The results using empirical velocity and resistivity trends for sandstones had much large variation, and are not very reliable for net erosion estimates. Sandstone modelling worked well, but is probably even more reliable when combined with for example the shale velocity method. Generally we found that combining methods gave more credibility to the estimations.

When testing the resistivity approach we found similar variations as for the shale velocity method and the sandstone modelling method, but the estimates were unrealistically high. We interpret this as a cooling effect due to uplift of the formation. In contrast to the velocity that is "frozen" at maximum burial depth, the resistivity of the pore fluid will change with changing temperature. This effect must be corrected for if the resistivity of the formation should be used for estimating net erosion.

By combining net erosion estimated from the velocity trend method and the resistivity approach, the effect of cooling can be estimated. This correction is linked to temperature and can be used to estimate the temperature gradient for a specific area. For this suggested work flow to work in practice, the change in resistivity must be entirely caused by cooling.

3. Estimate and discuss the effects net erosion have on seismic AVO signatures.

Net erosion estimates were included when modelling seismic AVO signatures for the Stø reservoir formation. This demonstrated that AVO signatures in the western Barents Sea are strongly influenced by net erosion. To obtain reliable AVO signature from the modelling, results were compared to real well correlated AVO results from the south western margin of the Loppa High. Here the AVO modelling results gave good match with the real AVO responses.

Based on the AVO modelling we see that both the fluid content in the reservoirs and the maximum burial depth both have a strong influence on which AVO class the response is interpreted to belong to.

Chapter 7 – Suggestions for further work

In this section some suggestions for further work are proposed to improve the confidence of the results and to proceed with the work already done in the thesis.

Good reference trends are important, and it could be interesting to compare the established trends with other basins in addition to the Norths Sea. Also new reference trends can be established for the Barents Sea when more wells are drilled in the coming years.

Using mainly the Kolmule- and Torsk Formations gave good net erosion estimates, but it could also be worth to do more testing of other formation.

The diagenetic modelling approach for sandstones also provided good estimates of net erosion. The use of a wider range of lithologies, more variation in clay content, grain distribution and cement content could also be tested in an extended project.

Further, the work done on resistivity in this study has potential for more research. Additional work could be done to better understand how changes in resistivity are influenced by temperature. It is also worth testing if CSEM- or MT data can be used in this process.

Temperature gradients can vary within a basin and from one basin to another. This is an important factor that will influence net erosion estimates, and could be studied in more detail in future projects.

While the knowledge about amount and timing of uplift and erosion has improved significantly over the years, this is not the case for the mechanisms causing the uplift. Here much more work is need before a good understanding is established.

Future projects focusing on the topics mentioned about could improve both the general understanding of the geological development and the understanding of the resource potential in the Barents Sea.

References

ANDERSEN, M. S., NIELSEN, T., SØRENSEN, A. B., BOLDREEL, L. O. & KUIJPERS, A. 2000. Cenozoic sediment distribution and tectonic movements in the Faroe region. *Global Planet. Change*.

ARCHIE, G. E. 1941. The Electrical Resistivity Log as an Aid in Determining Some Reservoir Characteristics *Dallas Meeting*.

AVSETH, P. 2015. Explorational Rock Physics: The link between Geological Processes and Geophysical Observables. *In: Bjørlykke, K., Jahren, J., Petroleum Geoscience. From Sedimentary Environments to Rock Physics - Second Edition***,** 455-489.

AVSETH, P. & DRÆGE, A. 2011. Memory of rocks - how burial history controls present day seismic properties. Example from Troll East, North Sea. *In: 2011 SEG Annual Meeting. Society of Exploration Geophysics*.

AVSETH, P. & LEHOCKI, I. 2016. Combining burial history and rock-physics modeling to constrain AVO analysis during exploration. *The leading edge, June 2016***,** 528-534.

AVSETH, P., MUKERJI, T. & MAVKO, G. 2005. Quantitative seismic interpretation: Applying rock physics tools to reduce interpretation risk. *Cambridge University Press*.

AVSETH, P. & VEGGELAND, T. 2015. Seismic screening of rock stiffness and fluid softening using rock physics attributes. *The Leading Edge 33 (4)***,** SAE85-SAE93.

AVSETH, P., VEGGELAND, T. & LEHOCKI, I. 2014. Combined burial history and rock physics modeling of quartz-rich sandstones - Norwegian shelf demonstrations. *SEG Technical Program Expanded Abstracts 2014. Society of Explorational Geophysics***,** 2809-2813.

BAIG, I., FALEIDE, J., I., JAHREN, J. & MONDOL, N. H. 2016. Cenozoic exhumation on the southwestern Barents Shelf: Estimates and uncertainties constrained from compaction and thermal maturity. *Marine and Petroleum Geology 73***,** 105-130.

BATZLE, M. & WANG, Z. 1992. Seismic properties of pore fluids. *Geophysics 57 (11)***,** 1396–1408.

BJØRLYKKE, K. & JAHREN, J. 2015. Sandstones and Sandstone Reservoirs. *In: Bjørlykke, K., Jahren, J., Petroleum Geoscience. From Sedimentary Environments to Rock Physics - Second Edition***,** 119-149.

BREVIK, I., CALLEJON, A., KAHN, P., JANAK, P. & EBRON, D. 2011. Rock physicists step out of the well location, meet geophysicists and geologists to add value in exploration analysis. *The Leading Edge 30 (12***,** 1382-1391.

BRIGAUD, F., VASSEUR, G. & CAILLET, G. 1992. Thermal state in the north Viking Graben (North Sea) determined from oil exploration well data. *GEOPHYSICS, VOL. 57, NO. 1***,** 69-88.

BULAT, J. & STOKER, S. J. 1987. Uplift determination from interval velocity studies, UK, southern North Sea. *Brooks , J., Glennie, K.W. (Eds.), Petroleum Geology of North West Europe. Graham and Trotman, London***,** 293-305.

CANNON, S. 2016. Petrophysics: A Practical guide. *West Sussex, John Wiley & Sons, Ltd*.

CASTAGNA, J. P. & SMITH, S. W. 1994. Comparison of AVO indicators: A modeling study. *Geophysics 59 (12)***,** 1849-1855.

CASTANGA, J. P. & SMITH, S. W. 1994. Comparison of AVO indicators: A modeling study. *Geophysics 59 (12)***,** 1849-1855.

CGG HRS-9/R2.

CHALMERS, J. A. 2000. Offshore evidence for Neogene uplift in central West Greenland. *Global Planet. Change 24***,** 311-318.

CLAUSEN, O. R., NIELSEN, O. B., HUUSE, M. & MICHELSEN, O. 2000. Geological indications for Palaeogene uplift in the eastern North Sea Basin. *Global Planet. Change 724***,** 175-187.

DALLAND, A., WORSLEY, D. & OFSTAD, K. 1988. A lithostratigraphic scheme for the Mesozoic and Cenozoic succession offshore mid- and northern Norway. *NPD-Bulletin No. 4***,** 65.

DIX, C. H. 1955. Seismic velocities from surface measurements. *Geophysics 20 (1)***,** 68-86.

DORÉ, A. G. 1992. The base Tertiary surface of southern Norway and the northern North Sea. *Nor. Geol. Tidsskr. 72***,** 259-265.

DORÉ, A. G. & JENSEN, L., N. 1996. The impact of late Cenozoic uplift and erosion on hydrocarbon exploration. *Global and Planetary Change 321. Special Issue: Impact of glaciations on basin evolution: data and models from the Norwegian Margin and adjacent areas.*

DRÆGE, A., DUFFAUT, K., WIIK, T. & HOKSTAD, K. 2015. Linking rock physics and basin history - Filling gaps between wells in frontier basins. *The Leading Edge 33 (3)***,** 240-246.

DVORKIN, J. & NUR, A. 1996. Elasticity of high-porosity sandstones: Theory for two North Sea data sets. *Geophysics 61 (59***,** 1363-1370.

DVORKIN, J., NUR, A. & YIN, H. 1994. Effective properties of cemented granular materials. *Mechanics of materials 18 (4)***,** 351-366.

ENGLAND, P. & MOLNAR, P. 1990. Surface uplift, uplift of rocks, and exhumation of rocks. *Geology 18***,** 1173-1177.

EVANS, D., MCGIVERON, S., MCNEILL, A. E., HARRISON, Z. H., ØSTMO, S. R. & WILD, J. B. L. 2000. Plio-Pleistocene deposits on the mid-Norwegian margin and their implications for late Cenozoic uplift of the Norwegian mainland. *Global Planet. Change 24***,** 233-237.

FALEIDE, J., I., BJØRLYKKE, K. & GABRIELSEN, R., H. 2010. Geology of the Norwegian Continental Shelf. *Petroleum Geoscience: From Sedimentary Environment to Rock Physics*, 467-499.

FIEDLER, A. & FALEIDE, J. I. 1996. Cenozoic sedimentation along the southwestern Barents Sea margin in relation to uplift and erosion of the shelf. *Glob. Planet. Change, 12*, 75–93.

FJELDSKAAR, W. & AMANTOV, A. 2016. Om årsakene til erosjonen i Barentshavet – del 2

GALLAGHER, K. 2012. Uplift, denudation, and their causes and constraints over geological timescales. *Principles of Geologic Analysis, 10, 30*.

GASSMANN, F. 1951. Über die elastizität poröser medien. *Vierteljahrss-chrift der Naturforschenden Gesellschaft in Zurich 96*, 1-23.

GATEMANN, J. H. M. 2016. Relationship between burial history and seismic signatures in the Horda Platform area, Norwegian North Sea. *Master Thesis, Department of Geosciences, University of Oslo*.

GLØRSTAD-CLARK, E., FALEIDE, J. I., LUNDSCHIENB, B. A. & NYSTUENA, J. P. 2010. Triassic seismic sequence stratigraphy and paleogeography of the western Barents Sea area. *Marine and Petroleum Geology 24 (7)*, 1448–1475.

GRADSTEIN, F., M., OGG, J., G., SCHMITZ, M. & OGG, G. 2012. The Geologic Time Scale 2012. *Elsevier*.

GREEN, P. F. 1989. Thermal and tectonic history of the East Midlands shelf onshore UK and surrounding regions assessed by apatite fission track analysis. *J. Geol. Soc. London 146*, 755-774.

HANSEN, K. 2000. Tracking thermal history in East Greenland: an overview. *Global Planet. Change 24*, 303-309.

HANSEN, S. 1996. Quantification of net uplift and erosion on the Norwegian Shelf south of 66°N from sonic transit times of shale. *Norsk Geologisk Tidsskrift, Vol. 76*, 245-152.

HENRIKSEN, E., BJØRNSETH, H. M. & HEIDE, T. K. 2011. Uplift and erosion of the greater Barents Sea: impact on prospectivity and petroleum systems. *Artic Petroleum Geology, geological Society, Chapter 17*, 271-281.

HERMANRUD, C., WENSAAS, L., TEIGE, G. M. G., BOLAS, H. M. N., HANSEN, S. & VIK, E. 1998. Shale porosities from well logs on Haltenbanken (offshore mid-Norway) show no influence of overpressuring. *In: LAW, B. E., ULMISHEK, G. F. & SLAVIN, V. I. (eds.) Abnormal pressures in hydrocarbon environments: AAPG Bulletin.*

JAPSEN, P. 2000. Investigation of multi-phase erosion using reconstructed shale trends based on sonic data. Sole Pit axis, North Sea. *Global Planet. Change 24*, 189-210.

JAPSEN, P. & CHALMERS, J. A. 2000. Neogene uplift and tectonics around the North Atlantic: Overview. *Elsevier: Global and Planetary Change 24 (2000) 165-173*.

JENSEN, L. N. & SCHMIDT, B. J. 1992. Late Tertiary uplift and erosion in the Skagerrak area; magnitude and consequences. *Nor. Geol. Tidsskr. 72***,** 275-279.

JOHANSEN, S. E. & GABRIELSEN, P. T. 2015. Interpretation of Marine CSEM and Marine MT Data for Hydrocarbon Prospecting. *In: Bjørlykke, K., Jahren, J., Petroleum Geoscience. From Sedimentary Environments to Rock Physics - Second Edition***,** 515-544.

JOHNSON, C. & GALLAGHER, K. 2000. A preliminary Mesozoic and Cenozoic denudation history of the North East Greenland onshore margin. *Global Planet. Change 24***,** 261-274.

JORDT, H., FALEIDE, J. I., BJØRLYKKE, K. & IBRAHIM, M. T. 1995. Cenozoic sequence stratigraphy of the central and northern North Sea Basin: tectonic development, sediment distribution and provenance areas. *Mar. Pet. Geol. 12***,** 845-879.

KENNETT, B. 1979. Theoretical reflection seismograms for elastic media. *Geophysical Prospecting*, 27**,** 301-321.

KHUTORSKOI, M. D., VISKUNOVA, K. G., PODGORNYKH, L. V. & AKHMEDZYANOV, V. R. 2008. A temperature model of the crust beneath the Barents Sea: Investigations along geotraverses *Geotectonics 42 (2)***,** 125-136.

LABERG, J. S., ANDREASSEN, K. & VORREN, T. O. 2012. Late cenozoic erosion of the high-latitude southwestern barents sea shelf revisited. *Bull. Geol. Soc. Am., 124***,** 77–88.

LANDER, R. H. & WALDERHAUG, O. 1999. Predicting porosity through simulating sandstone compaction and quartz cementation *AAPG bulletin 83 (3)***,** 433-449.

LI, Y., DOWNTON, J. & XU, Y. 2014. AVO Modeling in Seismic Processing and Interpretation II. Methodologies. *Recorder*, 29.

LIDMAR-BERGSTRØM, K., OLLIER, C. D. & SULEBAK, J. C. 2000. Landforms and uplift history of southern Norway. *Global Planet. Change 24***,** 211-231.

MARCUSSEN, Ø., MAAST, T. E., MONDOL, N., H., JAHREN, J. & BJØRLYKKE, K. 2009. Changes in physical properties of a reservoir sandstone as a function of burial depth – The Etive Formation, northern North Sea. *Marine and Petroleum geology (2010)* 1-11.

MARION, D. P. 1990. Acoustical, mechanical, and transport properties of sediments and granular materials. *Ph.D. thesis, Stanford University, Department of Geophysics*.

MATHIESEN, A., BIDSTRUP, T. & CHRISTIANSEN, F. G. 2000. Denudation and uplift history of the Jameson Land Basin, East Greenland — constrained from previous maturity and new apatite fission track data. *Global Planet. Change B 24***,** 275-301.

MATHWORKS R2015a. Matlab. *1994-2016: The MathWorks, Inc.*

MAVKO, G. 1987. In: Bourbie et al 1987, Acoustics of porous Media, Gulf Publishing Co.

MINDLIN, R. D. 1949. Compliance of Elastic Bodies in Contact. *Journal of Applied Mechanics 16*, 259–268.

MONDOL, N. H., BJØRLYKKE, K., JAHREN, J. & HØEG, K. 2007. Experimental mechanical compaction of clay mineral aggregates – Changes in physical properties of mud- stones during burial. *Marine and Petroleum Geology 24(5)*, 289–311.

MORK, M. B. E. 1999. Compositional variations and provenance of Triassic sandstones from the Barents Shelf. *Journal of Sedimentary Research 69 (3)*, 690-710.

NPD 2014. Lithostratigrapic summary for the North Sea.

NPD 2016. Factpages, Norwegian Petroleum Directorate. Accessed 2016-09-01.

NYLAND, B., JENSEN, L., N., SKAGEN, J., SKARPNES, O. & VORREN, T. 1992. Tertiary uplift and erosion in the Barents Sea: magnitude, timing and consequences. *Struct. Tect. Model. its Appl. Petrol. Geol.*, 153–162.

OHM, S. E., KARLSEN, D. A. & AUSTIN, T. 2008. Geochemically driven exploration models in uplifted areas: Examples from the Norwegian Barents Sea. *AAPG bulletin 92 (9)*, 1191-1223.

RICHARDSEN, G., VORREN, T. & TØRUDBAKKEN, B. O. 1993. Post-Early Cretaceous uplift and erosion in the southern Barents Sea: a discussion based on analysis of seismic interval velocities. *Norsk Geologisk Tidsskrift. Vol. 73*, 3-20.

RIDER, M. 2000. The geological interpretation of well logs. *Rider-french Consulting*.

RIIS, F. 1996. Quantification of Cenozoic vertical movements of Scandinavia by correlation of morphological surfaces with offshore data. *Global Planet. Change 12*, 331-357.

ROHRMAN, M., VAN DER BEEK, P., ANDRIESSEN, P. & CLOETINGH, S. 1995. Meso-Cenozoic morphotectonic evolution of southern Norway: Neogene domal uplift inferred from apatite fission track thermochronology. *Tectonics*, 700-714.

ROSS, C. P. & KINMAN, D. L. 1995. Nonbright-spot AVO: Two examples. *Geophysics 60 (5)*, 1398–1408.

ROSS, C. P. & KINMAN, D. L. 1995b. Nonbright-spot AVO: Two examples. *Geophysics 60 (5)*, 1398-1408.

RUTHERFORD, S. R. & WILLIAMS, R. H. 1989. Amplitude-versus-offset variations in gas sands. *Geophysics 54 (6)*, 680–688.

SCHLUMBERGER 2015.

SHUEY, R. 1985. A simplification of the Zoeppritz equations. *Geophysics 50 (4)*, 609–614.

SORKHABI, R. 2015. Ph.D, Fracture, Fracture Everywhere - Part II, How and why do fractures occur in rocks? . *GEO ExPro, Vol. 11, No. 3*.

STORVOLL, V., BJØRLYKKE, K. & MONDOL, N. H. 2005. Velocity-depth trends in Mesozoic and Cenozoic sediments from the Norwegian Shelf. *AAPG Bulletin, 89*, 359-381.

STUEVOLD, L. M. & ELDHOLM, O. 1996. Cenozoic uplift of Fennoscandia inferred from a study of the mid-Norwegian margin. *Global Planet. Change 12*, 359-389.

THYBERG, B., JAHREN, J., WINJE, T., BJØRLYKKE, K. & FALEIDE, J. I. 2009. From mud to shale: rock stiffening by micro-quartz cementation. *First Break, Vol. 27*, 53-59.

VÅGNES, E., FALEIDE, J. I. & GUDLAUGSSON, S., T. 1992. Glacial erosion and tectonic uplift in the Barents Sea. *Norsk Geologisk Tidsskrift 72 (3)*, 333-338.

WALDERHAUG, H. P. 2012. Petrography, diagenesis and reservoir quality of the Triassic Fruholmen, Snadd and Kobbe formations, southern Barents Sea. *Master Thesis, Norwegian University of Science and Technology*.

WALDERHAUG, O. 1996. Kinetic modeling of quartz cementation and porosity loss in deeply buried sandstone reservoirs. *AAPG bulletin 80 (5)*, 731-745.

ØDEGAARD, E. & AVSETH, P. 2004. Well log and seismic data analysis using rock physics templates. *First Break 22 (10)*, 37-43.